frontiers | Research Topics

Petroleum generation, migration and storage in shale system

Edited by
Xiaomin Xie, Feng Yang, Jianhua Zhao, Juan Teng, Tao Hu, Chunqing Jiang and Jun Wang

Published in
Frontiers in Earth Science

ISSN 1664-8714
ISBN 978-2-8325-3818-0
DOI 10.3389/978-2-8325-3818-0

About Frontiers

Frontiers is more than just an open access publisher of scholarly articles: it is a pioneering approach to the world of academia, radically improving the way scholarly research is managed. The grand vision of Frontiers is a world where all people have an equal opportunity to seek, share and generate knowledge. Frontiers provides immediate and permanent online open access to all its publications, but this alone is not enough to realize our grand goals.

Frontiers journal series

The Frontiers journal series is a multi-tier and interdisciplinary set of open-access, online journals, promising a paradigm shift from the current review, selection and dissemination processes in academic publishing. All Frontiers journals are driven by researchers for researchers; therefore, they constitute a service to the scholarly community. At the same time, the *Frontiers journal series* operates on a revolutionary invention, the tiered publishing system, initially addressing specific communities of scholars, and gradually climbing up to broader public understanding, thus serving the interests of the lay society, too.

Dedication to quality

Each Frontiers article is a landmark of the highest quality, thanks to genuinely collaborative interactions between authors and review editors, who include some of the world's best academicians. Research must be certified by peers before entering a stream of knowledge that may eventually reach the public - and shape society; therefore, Frontiers only applies the most rigorous and unbiased reviews. Frontiers revolutionizes research publishing by freely delivering the most outstanding research, evaluated with no bias from both the academic and social point of view. By applying the most advanced information technologies, Frontiers is catapulting scholarly publishing into a new generation.

What are Frontiers Research Topics?

Frontiers Research Topics are very popular trademarks of the *Frontiers journals series*: they are collections of at least ten articles, all centered on a particular subject. With their unique mix of varied contributions from Original Research to Review Articles, Frontiers Research Topics unify the most influential researchers, the latest key findings and historical advances in a hot research area.

Find out more on how to host your own Frontiers Research Topic or contribute to one as an author by contacting the Frontiers editorial office: frontiersin.org/about/contact

Petroleum generation, migration and storage in shale system

Topic editors

Xiaomin Xie — Yangtze University, China
Feng Yang — China University of Geosciences Wuhan, China
Jianhua Zhao — China University of Petroleum (East China), China
Juan Teng — Yangtze University, China
Tao Hu — China University of Petroleum, Beijing, China
Chunqing Jiang — Geological Survey of Canada, Canada
Jun Wang — Yunnan University, China

Citation

Xie, X., Yang, F., Zhao, J., Teng, J., Hu, T., Jiang, C., Wang, J., eds. (2023). *Petroleum generation, migration and storage in shale system*. Lausanne: Frontiers Media SA. doi: 10.3389/978-2-8325-3818-0

Table of contents

04 Multiple experimental studies of pore structure and mineral grain sizes of the Woodford shale in southern Oklahoma, USA
Chen Zhao, Qinhong Hu, Qiming Wang, Jan Ilavsky, Min Wang, Xiaobei Zhang and Jianping Yan

25 Study on fault sealing of the Lishui West Sag in the East China Sea Basin
Bing Yang, Qiang Fu, Jinshui Liu, Wenrui Ma and Shijie Zhao

36 Characteristics and controlling factors of the Upper Permian Dalong Formation in northwestern Sichuan Basin, China
Lu Wang, Xiaodong Guan, Jianyong Wang, Zuoyu Sun and Huiyuan Xu

51 Discovery of solid bitumen in the Cambrian reservoirs and its geological implications in the Ordos Basin, China
Junping Huang, Xiangbo Li, Kaijun Tan, Nijiao Xiang and Yan Zhang

60 Hydrocarbon generation and expulsion modeling of different lithological combination source rocks from the Funing Formation in the Subei Basin
Jinning Peng, Longlong Li, Chongjiao Du, Xu Liu, Jianhui Zhu, Shiyou Liang, Qi Qiu and Dongyan Wang

74 A review of possible mechanisms for mercury migration in diagenesis: Clay to pyrite
Huan Xu, Bo Ran, Shugen Liu, Tong Sun, Chao Luo, Yi Li and Yiqing Zhu

80 Sealing of oil-gas reservoir caprock: Destruction of shale caprock by micro-fractures
Ye Tao, Youbin He, Zhongxiang Zhao, Dongsheng Wu and Qiao Deng

85 Pore characteristics and preservation mechanism of over-6000-m ultra-deep shale reservoir in the Sichuan Basin
Guoliang Xie, Kun Jiao, Bin Deng, Weiduo Hao and Shugen Liu

99 A method for evaluating resource potential and oil mobility in liquid-rich shale plays—An example from upper Devonian Duvernay formation of the Western Canada Sedimentary Basin
Zhuoheng Chen, Chunqing Jiang, Julito Reyes, Xiaojun Liu and Edward Little

115 Fatty acids, alkanones and alcohols from a major lower Triassic low-permeability petroleum reservoir
Jaime Cesar, Rachel Robinson, Sebastian Naeher, Marina Milovic and Omid H. Ardakani

frontiers | Frontiers in Earth Science

TYPE Original Research
PUBLISHED 26 September 2022
DOI 10.3389/feart.2022.1019951

OPEN ACCESS

EDITED BY
Jianhua Zhao,
China University of Petroleum, China

REVIEWED BY
Yang Wang,
Chang'an University, China
Mengdi Sun,
Northeast Petroleum University, China

*CORRESPONDENCE
Qinhong Hu,
maxhu@uta.edu

SPECIALTY SECTION
This article was submitted to Geochemistry, a section of the journal Frontiers in Earth Science

RECEIVED 15 August 2022
ACCEPTED 06 September 2022
PUBLISHED 26 September 2022

CITATION
Zhao C, Hu Q, Wang Q, Ilavsky J, Wang M, Zhang X and Yan J (2022), Multiple experimental studies of pore structure and mineral grain sizes of the Woodford shale in southern Oklahoma, USA.
Front. Earth Sci. 10:1019951.
doi: 10.3389/feart.2022.1019951

Multiple experimental studies of pore structure and mineral grain sizes of the Woodford shale in southern Oklahoma, USA

Chen Zhao[1,2], Qinhong Hu[1]*, Qiming Wang[1,2], Jan Ilavsky[3], Min Wang[2], Xiaobei Zhang[2] and Jianping Yan[4]

[1]Department of Earth and Environment Sciences, The University of Texas at Arlington, Arlington, TX, United States, [2]Shandong Provincial Key Laboratory of Deep Oil and Gas, China University of Petroleum (East China), Qingdao, China, [3]X-ray Science Division, Advanced Photon Source, Argonne National Laboratory, Lemont, IL, United States, [4]School of Geoscience and Technology, Southwest Petroleum University, Chengdu, China

Pore structure study is an important part of unconventional shale reservoir characterization, since the pore system provides the primary petroleum storage space and fluid flow pathways. Previous studies have suggested that the pore structure is related to the total organic carbon (TOC) content, mineral compositions, and the maturity of the organic matter (OM). However, few studies have focused on the mineral grains, the primary grains being deposited but before cementation, which are the building blocks of shale. Eight Woodford Shale outcrop samples from southern Oklahoma were chosen to study the effects of mineral grain size on the pore structure characterization, using multiple and complementary experimental approaches, including laser diffraction, mineralogy, TOC, pyrolysis, liquid immersion porosimetry, mercury intrusion porosimetry, gas physisorption, (ultra) small angle X-ray scattering, scanning electron microscopy, and spontaneous imbibition. The results from different experiments of eight samples show that the Woodford Shale has the mean mineral grain diameters at 3–6 μm, a wide range of porosity at 3–40% and pore diameters at 50–1,000 nm, and various pore connectivity. Grain size variation was probably caused by the sea-level fluctuation during its deposition, which affect the porosity, pore size distribution, and pore connectivity. With decreasing mineral grain sizes, the porosity tends to increase while the pore connectivity worsens. The results also indicate that OM and carbonates in this low-maturity Woodford Shale could block the pores and decrease the porosity. Coupling with the grain size analyses, the control of depositional environment on grain sizes and subsequent effects on pore structure is identified. The pore structure characteristics over a wide pore-diameter range provided by multiple experiments could improve the understanding of storage space and fluid flow in the Woodford Shale to further increase its petroleum production.

KEYWORDS

woodford shale, pore structure, characterization methods, connectivity, grain size, deposition

Introduction

Shales have fine-grained matrices, low porosities and very low permeabilities, and very slow fluid flow rates; as a consequence, hydraulic fracturing is needed for the petroleum production in shale reservoirs. To understand the fluid-matrix interactions, pore structure characterization of shale has been carried out in recent decades (Ross and Bustin, 2009; Curtis et al., 2010; Clarkson et al., 2013; Cao et al., 2016; Sun et al., 2017; Kibria et al., 2018). Pore size distribution, pore types, and pore connectivity are key aspects of shale pore structure studies (Parker et al., 2009; Wang et al., 2016; Gao et al., 2018; Sun et al., 2019; Wang et al., 2021a; Wang et al., 2022). The factors that control pore structure properties of both marine and lacustrine shales include TOC content, mineral compositions, and thermal maturity. Increasing TOC content and thermal maturity both increase the formation of secondary pores in OM, which can lead to an increase in the porosity and specific pore surface area (Curtis et al., 2012; Cao et al., 2015). The contents of silica minerals also increase the porosity in both marine and lacustrine shale (Fu et al., 2015; Dong and Harris, 2020; Iqbal et al., 2021).

Mineral grain sizes can also be a factor controlling the pore structure. In this study, we define the mineral grains as the primarily deposited grains, which can be measured after the dissolution of cements and OM. Several studies have shown that quartz grain sizes in sandstones are positively correlated with porosity, pore throat size, and pore connectivity (Cao et al., 2016; Li et al., 2018; Qiao et al., 2020). However, few studies have focused on the effects of mineral grain sizes on pore structure in shale. The full section Woodford Shale outcrop at southern Oklahoma is a good option to study this topic. The samples collected from the bottom to the top of the section deposited at the same basin with a continuous environment change, under which the changes of mineral grain size could have a rule to follow (Catuneanu, 2006). Moreover, Woodford Shale in Oklahoma is an important unconventional source rock, and its pore structure study could provide more geologic supports to improve the petroleum production. In this work on eight Woodford Shale outcrop samples collected from Oklahoma in USA, the effects of mineral grain size on pore structure have been studied using various experiments of X-ray diffraction on mineralogy (XRD), TOC, pyrolysis, liquid immersion porosimetry (LIP), mercury intrusion porosimetry (MIP), gas physisorption (GP), (ultra) small angle X-ray scattering [(U)SAXS)], scanning electron microscopy (SEM), spontaneous imbibition (SI), and grain size distribution (GSD) by laser diffraction. The results from different experiments of these eight samples are discussed to illustrate the effects of grain size on pore structure, including porosity, pore size distribution, pore connectivity, and tortuosity.

Geological background

The Late Devonian to Early Mississippian marine Woodford Shale is widely distributed in the Midwest USA, including western Texas, southeastern New Mexico, and southern Oklahoma (Comer, 1991; Romero and Philp, 2012). The Woodford Shale in Oklahoma contains OM of mostly algal/bacterial origin, which is oil- and associated gas-prone, and contains reserves of more than 644 billion cubic feet of gas and 460 million barrels of oil (Cardott, 2012; Cardott, 2017). Like most shale reservoirs, the extremely low permeability and other complex petrophysical properties lead to a rapid decline in petroleum production in the Woodford Shale and make economic development difficult to sustain. However, the studies on the Woodford Shale have not attracted much attention of petrophysicists since the production is not prominent, and only a few research studies focus on the basic aspects of pore structure characteristics (Slatt and O'Brien, 2011; Kibria et al., 2018; Ojha et al., 2018; Cullen, 2020).

The Woodford Shale in Oklahoma is mainly present in the Anadarko, Arkoma, Ardmore, and Marietta Basins (Cardott, 2017). The samples in this study were collected from the outcrop in the McAlister Cemetery quarry, in the western Ardmore Basin, to the south of Ardmore city near the exit off Interstate 35 (Bernal et al., 2012; Ekwunife, 2017). The Ardmore Basin is the consequence of compression by a series of tectonic events in Pennsylvanian to Permian (Granath, 1989). Eight samples collected in this work were from the 100 m-thick vertical section. The Hunton Group and Sycamore Limestone contact with the Woodford Shale unconformably on the top and bottom, respectively (Figure 1; Comer, 2008; Ekwunife, 2017). The Woodford Shale is unofficially subdivided into three units: Lower, Middle, and Upper Woodford; the Lower and Middle units were deposited in a transgressive environment, and the Upper Woodford Shale was formed under a regressive environment (Bernal et al., 2012).

Samples and methods

Woodford samples

From these eight samples, WFD-4, WFD-5, and WFD-6 were collected from Middle Woodford, while samples WFD-7, WFD-8, WFD-9, WFD-11, and WFD-328 came from the Upper Woodford (Figure 1). Since the shale from Lower Woodford is too fragile to collect as chunky samples, only Middle and Upper Woodford were covered in this work. These samples were processed into various shapes and sizes for different laboratory experiments detailed below.

Mineralogy, organic geochemistry, and SEM imaging

Samples were pulverized into powder with particle sizes <75 μm and oven-dried at 60°C for 48 h before the

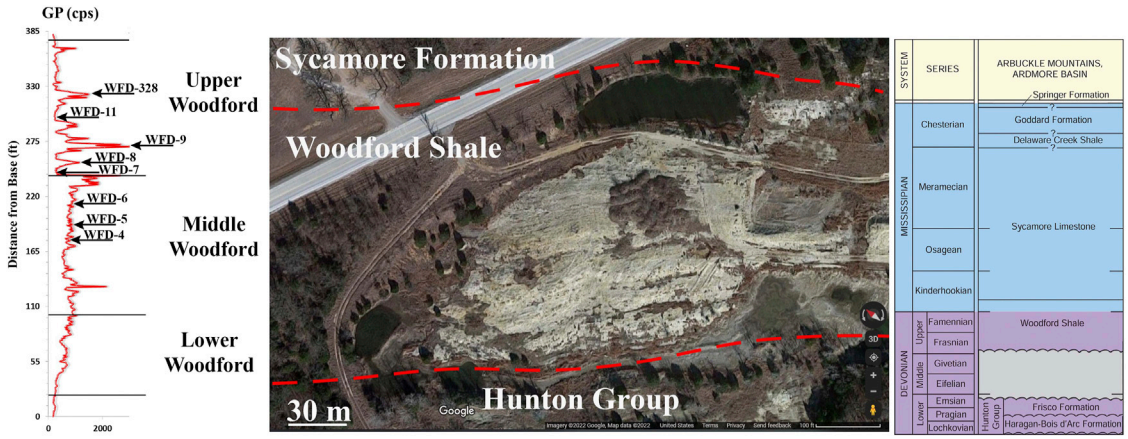

FIGURE 1
Outcrop sample locations and lithostratigraphy (modified after Ekwunife, 2017).

mineralogy and organic geochemistry analyses. The mineral analyses by XRD were performed using a Shimadzu MAXima X XRD-7000 X-ray Diffractometer with the 2θ from 2° to 70°. The mineralogical compositions were semi-quantitatively calculated in weight percentage with an approximate uncertainty of ±10% (Moore and Reynolds, 1997). TOC content and pyrolysis were conducted by GeoMark Research Ltd with a LECO TOC and HAWK pyrolysis instruments, respectively. The TOC content, T_{max} and other geochemical parameters (e.g., S1 and S2) were obtained from these two measurements.

Pore types were studied using images generated by SEM. Images are created using a variety of radiation signals, including X-rays, backscattered electrons, secondary electrons, and Auger electrons emitted from the sample surface. Backscattered electrons (BSE) and secondary electrons (SE) are two commonly used signals in SEM image generation. The BSE images reflect the atomic number differences in the sample and show the compositional difference at different grayscales. The SE signals produce a visual information of the surface topography of the sample. Both Hitachi S-4800 and Hitachi N-3000 instruments were applied in this study for different observational scales of samples and containing pores. Before scanning, all the samples were oven-dried at 60°C for 48 h and coated with metal Pt for 1–2 min with Hummer VI Sputtering System.

Liquid immersion porosimetry

LIP was carried out after vacuum pulling to evacuate the air from the connected pore space, followed by a liquid immersion to ensure full liquid saturation of the pore systems connected to the sample surface. Samples as 1-cm^3 cubes with a side length of 1 cm were vacuumed under a pressure of 0.1 Torr for over 12 h, after that samples were flushed with CO_2 for 30 min. The aim of CO_2 injection was to use this gas to replace the residual air, in order to improve the water saturation of the pores since CO_2 dissolves more readily in water than air during the subsequent water immersion. Samples were evacuated again under a similar vacuum pressure for 12 h before the release of deionized water (DIW) into the sample/vacuum chamber to occupy the evacuated pore space. The water-saturated sample was then submerged under boiled and cooled DIW to obtain the bulk volume and pore volume, using the Archimedes' principle (Hu et al., 2012, 2015; Kuila et al., 2014). Porosity, bulk density, and grain density were calculated from the sample weight, bulk volume, and pore volume.

Spontaneous imbibition

SI can be applied to characterize the combined influence of capillarity and relative permeability on the extent and rate of fluid flow in porous media. The capillary force-driven SI is a process in which the wetting fluid (e.g., water) expels a non-wetting fluid (e.g., air or oil) in a water-wet material. Imbibition can be regarded as diffusion mathematically (Philip, 1957). Hu et al. (2012) proved that the fitting slope of imbibed mass and imbibed time in log-log space could describe the pore connectivity of the shale rocks. The experimental procedure of imbibition tests follows Hu et al. (2001). One 1-cm^3 cubic sample was hung under a bottom-weighing electronic balance with the bottom end in contact with the imbibing liquid which is DIW. Except for the bottom and top faces, the other four faces of the cube were covered by epoxy to minimize the adsorption of DIW vapor. The imbibition direction was transverse (T direction) to the bedding layers, without the restriction of either top or bottom faces of the sample. For samples without stratifications, the imbibition

direction was not specified. Every sample was tested for 24 h. The porosity measured from LIP method was used in SI for imbibed liquid volume calculation, because both methods use DIW as the testing fluid.

Mercury intrusion porosimetry

MIP method uses non-wetting liquid mercury to invade pores under an applied pressure, and the data can be used to measure the pore-throat diameter distribution. 1-cm^3 cubes with side length of 1 cm were used and oven-dried for 48 h before the MIP tests by following the procedure of Gao and Hu (2013) and Hu et al. (2017). The Washburn equation describes the relationship between the applied pressure and pore throat size being intruded (Eq. 1)

$$\Delta P = \frac{-2\gamma \cos\theta}{r} \tag{1}$$

where ΔP is the applied pressure, γ is the surface tension of mercury, θ is the contact angle, and r is the radius of the pore throat (Washburn, 1921). The surface tension and contact angle are commonly selected as 0.485 Nm^{-1} and 140° (Baiker and Reithaar, 1982; Giesche, 2006). The Washburn equation is the basic theory of the MIP approach in converting the applied mercury pressure to the pore-throat diameter. The maximum pressure that the MIP instrument (Micromeritics AutoPore IV 9520) used in this study could achieve is 413 MPa, corresponding to the pore-throat diameter of ~3 nm (Gao et al., 2018). Related to the sample holder and initial filling pressure of 1.38 KPa, the maximum pore-throat diameter that can be detected by MIP in this work is 1,000 μm.

In addition to porosity and pore throat diameter distribution, tortuosity and permeability of the pore system can be obtained by the MIP method. Tortuosity is the ratio of the actual distance the fluid travels and the shortest distance between the start and end points of the fluid flow. Eq. 2 shows the calculation of tortuosity (ξ) using the pressure-volume data collected during the MIP tests:

$$\xi = \sqrt{\frac{\rho}{24k(1+\rho V_{tot})} \int_{\eta=r_{c,min}}^{\eta=r_{c,max}} \eta^2 f_v(\eta) d\eta} \tag{2}$$

where ρ is the density, k is the permeability, V_{tot} is the total pore volume, and $\int_{\eta=r_{c,min}}^{\eta=r_{c,max}} \eta^2 f_v(\eta) d\eta$ is the probability density function of the pore throat volume (Micromeritics Instrument Inc, 2015). Permeability (k) can be calculated using Eq. 3 (Katz and Thompson, 1986):

$$k = \frac{1}{89}(L_{max})^2 \left(\frac{L_{max}}{L_c}\right) \varnothing S_{(L_{max})} \tag{3}$$

where L_{max} is the pore throat diameter under the maximum hydraulic conductance, L_c is the pore throat diameter corresponding to the threshold pressure, $\varnothing$ is the porosity, and $S_{(L_{max})}$ is the mercury saturation (Katz and Thompson, 1986; Micromeritics Instrument Inc, 2015).

Gas physisorption

Hand-crushed granular samples with diameter between 500–840 μm were used in GP tests, as nitrogen gas was used with a Micromeritics ASPS 2460 system. The Langmuir equation expresses the relationship between the volume of nitrogen gas adsorbed and the relative pressure, from which pore surface area, pore diameter distribution, and pore shape can be calculated (Bardestani et al., 2019). At the beginning of the adsorption process, the gas molecules start to form a monolayer on the pore walls at low relative pressures. The specific surface area can be calculated based on a monolayer coverage of nitrogen molecules using the Brunauer-Emmett-Teller (BET) equation (Thommes, 2010; Lowell et al., 2012). An isotherm plot can be obtained by plotting adsorption volume against relative pressure at a constant experimental temperature. During the desorption process, the nitrogen in pores is released with decreasing pressure. The Barrett-Joyner-Halenda (BJH) method was used to calculate the pore diameter distribution (Barrett et al., 1951). The experimental temperature was 77.3K, while the absolute pressure range was 0.210–102 KPa and the relative pressure range was 0.002–0.998.

(Ultra) small angle X-ray scattering

To understand the effect of OM on pore structure characteristics, both solvent-extracted and non-extracted samples were measured by (U)SAXS methods. Two wafers were made from every sample with a thickness of ~0.8 mm: one wafer was soaked in a mixture of dichloromethane and methanol at a volume ratio of 9:1 under 70°C for 48 h (Zhang et al., 2019), and another wafer was made without soaking in solvent.

In (U)SAXS analyses, the X-ray passes through the sample and scatters differently, and the contrast of the scattering intensity measured by the detector is used to characterize the spatial pore data of porous materials (Li et al., 2016; Sun et al., 2020). The (U)SAXS experiments were performed at beamline 9-ID of the Advanced Photon Source at Argonne National Laboratory in Illinois. The detectable pore diameter range is ~1 Å-6 μm, and the range of scattering vector Q is $8\times10^{-5} < Q < 6$ A^{-1}. Each sampling spot was scanned by ultra-SAXS for 90 s and by (U)SAXS for 10 s with an X-ray energy of 21 keV, yielding the combined (U)SAXS data (Wang et al., 2021b). Calibration and background subtraction were needed during (U)SAXS experiments for

TABLE 1 Mineralogical, petrophysical, and geochemical properties from XRD, and rock pyrolysis results (HC: hydrocarbons; wt.%: weight percentage).

Sample ID	Mineralogy (wt.%)						TOC (%)	Ro (%)	T_{max} (°C)	S1 (mg HC/g)	S2 (mg HC/g)
	Quartz	Feldspar	Dolomite	Gypsum	Clays	Pyrite					
WFD-4	13.7	0.30	84.9	—	0.0	1.50	4.05	0.29	414	1.6	24.7
WFD-5	25.8	14.6	15.0	11.5	31.3	1.70	7.40	0.22	410	2.9	49.7
WFD-6	40.8	—	18.0	12.3	21.6	7.30	10.6	0.18	408	4.1	62.1
WFD-7	75.6	—	2.30	—	22.1	—	0.07	0.00	374	0.06	0.05
WFD-8	17.9	1.20	72.8	—	5.9	0.20	8.35	0.27	413	4.4	61.6
WFD-9	68.1	—	—	13.5	17.1	1.40	15.7	0.49	425	9.1	135
WFD-11	26.5	—	—	—	73.5	—	0.06	0.29	414	0.10	0.04
WFD-328	92.2	—	—	—	7.80	—	1.21	0.31	415	0.37	3.99

consequent data reduction. The data were processed by Igo Pro software following Ilavsky and Jemian (2009) and Ilavsky et al. (2018). Porosity, pore diameter distribution, and pore surface area were thus calculated, and pore volume obtained using the bulk density results obtained from MIP tests.

Particle size analyses by laser diffraction

The particle size is related to the diffraction angle when the X-ray passing through the particle, and the particle size distribution is related to the diffracted light intensity. During the measurement, samples are carried by being suspended in DIW, and flowing through a monochromatically parallel X-ray beam in the sample cell. The scatter patterns and light intensity are measured by the detector after the scattered light passes through a focal lens and is captured by the detector (;McCave et al., 1986; Ma et al., 2000; Wen et al., 2002).

With a detectable range from 10 nm to 300 μm, a Shimadzu SALD-7101 laser diffraction particle size analyzer was applied in this study to measure the grain size distribution. Eight hand crushed and sieved samples with a particle diameter of 500–841 μm were dissolved in sequence in 10% HCl and 30% H_2O_2 to dissolve the carbonate cement and pyrite, which can disaggregate the mineral grains. The residual grains were carried by 0.5 g/L NaH_2PO_4 solution, which was applied for better dispersion of the grains for grain size measurement (Penner and Lagaly, 2001; Sato et al., 2019). In this study, to simplify the analysis and discussion, we define a particle as the aggregation of primarily-deposited crystal grains being cemented (i.e., by carbonates), and a grain as the primary crystals. In other word, the sizes of the grains that remain in the HCl and H_2O_2 solutions are regarded as the primarily deposited crystal grains.

Results

Basic rock properties from XRD, rock pyrolysis, and LIP

Table 1 shows the mineralogical compositions from XRD analyses. Quartz, dolomite, and clays are the major minerals in these eight samples of the Woodford Shale. The quartz content varies from 13.7 wt.% to 92.2 wt.%, the dolomite content ranges from 2.30 wt.% to 84.9 wt.%, and clays content varies from 0-73.5 wt.%. Sample WFD-328 has the highest quartz content, WFD-8 has the highest dolomite content, and WFD-11 has the highest clays content.

The TOC content varies from 0.06 to 15.7%. T_{max} values range from 408 to 425°C, indicating that all samples are thermally immature with respect to oil generation. The low value of 374°C for sample WFD-7 is unreliable due to its low TOC and S2 values.

SEM observations

From the SEM images, both interparticle, intraparticle, and OM pores were identified in the samples. Interparticle pores formed between mineral grains, such as rigid quartz grains, are the primary contributors to the pore volume (Figures 2A,B). Intraparticle pores are defined as pores inside the grain boundary (Loucks et al., 2012). Intraparticle pores are common in clay minerals, such as kaolinite and illite (Figure 2C). The pores in OM are also a type of intraparticle pore (Figure 2D); however, in this study, they are called OM pores. WFD-6 has well-connected OM pores with diameters of 30–50 nm (Figures 2E,F). The particles of OM were obviously detected by the SEM in samples with TOC contents >4%, such as WFD-4, WFD-5, WFD-8, and WFD-9; nevertheless, not all OM has pores inside. Some non-porous OM filled in partial interparticle pores could block the interparticle pores and decrease the pore volume. Both samples WFD-4 and WFD-8 are dominated by carbonates. In Figure 2G, non-porous carbonates are likely serving

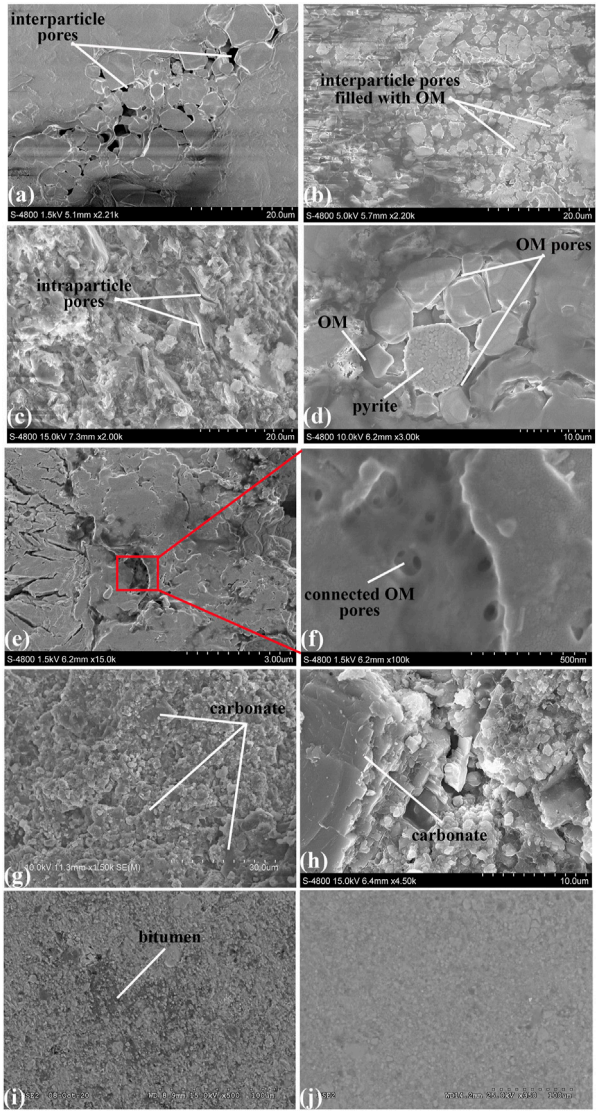

FIGURE 2
Pore types identified in SEM images; **(A,B)** interparticle pores in WFD-4 and WFD-9; **(C)** intraparticle pores in WFD-5; **(D)** OM pores and pyrite in WFD-4; **(E,F)** connected OM pores in WFD-6; **(G)** carbonate in WFD-8; **(H)** carbonate in WFD-4; **(I)** BSE image of WFD-6 before solvent extraction; **(J)** BSE image of WFD-6 after solvent extraction.

as the cements. The sizes of mineral grains, including quartz, clay minerals, and feldspar, can also be estimated from the SEM images with a mean size of 3–4 μm.

Pore structure from MIP, GP, and LIP methods

Porosity, pore-throat size distribution, and tortuosity can be obtained from MIP (Table 2). The average porosity of MIP is 22.9%, within the range of 3.72–50.3%. Figure 3 shows the pore-throat diameter distribution from the MIP analyses. Most samples have pore-throat diameters smaller than 1 μm. WFD-4 and WFD-8 have lower peaks with the smallest porosities compared with other samples (Figure 3). Samples WFD-5, WFD-6, and WFD-9 are dominated by pores with a diameter of 0.02 μm, while WFD-7, WFD-11, and WFD-328 primarily have pore diameters of 0.1–1 and ~1,000 μm. The total pore volume varies from 0.02 cm^3/g to 0.58 cm^3/g. The total pore surface areas range from 2.69 m^2/g to 26.2 m^2/g, and tortuosity calculated from the MIP method changes from 3.00 to 3,341.

From the GP analyses, hysteresis loops apparently exist between the adsorption and desorption isotherms due to both pore blocking and cavitation (Figure 4) (Thommes et al., 2015; Schlumberger and Thommes, 2021). The adsorption isotherms suddenly increase after P/P_0 = 0.8. No horizontal plateau exists when P/P_0 approaches to 1 in these samples, which indicates that the diameters of many pores are over the upper detectable range of GP method (Ravikovitch and Neimark, 2002), which is 300 nm in this work. The desorption isotherms show a step-down behavior and overlap with the adsorption isotherms at P/P_0 = 0.4–0.5. Based on the classification of IUPAC (Thommes et al., 2015), the hysteresis loops for these eight Woodford Shales are identified as Type H3, which indicates a primary presence of slit-shaped pores. Figure 5 shows the dominant pore diameter is 2–3 nm. The total pore volume within the GP-measurable range of 1–300 nm varies from 0.01 cm^3/g to 0.05 cm^3/g, and over 50% of the total pore volume is provided by pores with a diameter smaller than 50 nm. In addition, the specific pore surface area varies from 1.96 m^2/g to 13.0 m^2/g. Porosities range from 3.94 to 40.3% from the LIP analyses, and the bulk density varies from 1.66 g/cm^3 to 2.44 g/cm^3. LIP and MIP show similar porosities and bulk densities. Total pore volume and total pore surface area from MIP and GP were compared under the same pore range from 1–300 nm (Table 2). For its wide measurable pore size range, MIP results have higher values of total pore volume and pore surface area than these from GP.

Pore structure from (U)SAXS analyses

The pore structure analyses by (U)SAXS method were applied to both non-extracted and solvent-extracted samples. For non-extracted samples, the range of porosities is from 2.84 to 8.93% (Table 3). The pore diameter distributions are characterized by multiple peaks in Figure 6. All samples have similar pore diameter distribution patterns with a dominance at 50–100 nm and 250–700 nm, in additional to a minor presence of pores at 2–10 nm in diameters.

For solvent-extracted samples, the porosity varies from 4.93 to 11.1%. The pore diameter distribution patterns of solvent-extracted samples are similar to the non-extracted samples but with greater incremental porosities. The pore

diameter distribution curves of solvent-extracted samples WFD-5, WFD-7, WFD-11, and WFD-328 show little differences compared to the results of non-extracted samples (Figures 6A,B). The curves of solvent-extracted samples WFD-4, WFD-6, WFD-8, and WFD-9 show a significant increase in incremental porosities at diameters of 40–150 nm and 300–1,000 nm. The porosity differences [(solvent-extracted–non-extracted)/non-extracted) ×100%] among these samples vary from 7.72 to 94.1% with an average of 46.5% (Table 3), which indicates the dramatic porosity increase after the solvent extraction.

Pore connectivity from SI method

As mentioned in *Spontaneous imbibition* Section, SI can estimate the pore connectivity associated with LIP result. The DIW volume imbibed by the eight samples varies from 0.03 to

TABLE 2 Porosity, pore volume, surface area, and tortuosity obtained from three methods, (-) means dimensionless.

Sample ID	LIP		MIP							GP	
	Porosity	Bulk density	Porosity	Bulk density	Total pore volume	Total pore surface area	Total pore volume for 1–300 nm interval	Total pore surface area for 1–300 nm interval	Tortuosity (-)<	Total pore volume	Total pore surface area
	(%)	(g/cm³)	(%)	(g/cm³)	(cm³/g)	(m²/g)	(cm³/g)	(m²/g)		(cm³/g)	(m²/g)
WFD-4	3.94	2.44	3.72	2.47	0.02	9.75	0.01	9.75	28.5	0.01	1.96
WFD-5	19.5	1.88	16.9	1.95	0.09	19.1	0.08	19.1	8.84	0.04	12.1
WFD-6	18.0	1.79	16.5	1.81	0.09	26.2	0.08	26.2	5.15	0.04	10.4
WFD-7	40.3	1.57	50.3	1.60	0.58	2.69	0.03	1.37	3.00	0.04	10.2
WFD-8	7.96	2.34	6.64	2.40	0.03	5.65	0.02	5.65	20.2	0.01	1.92
WFD-9	13.8	1.83	13.3	1.89	0.07	21.7	0.07	21.7	3.21	0.03	5.89
WFD-11	37.1	1.66	43.2	1.46	0.30	13.1	0.06	12.0	1,544	0.05	13.0
WFD-328	31.1	1.81	33.0	1.72	0.19	13.7	0.10	13.2	3,341	0.03	8.87

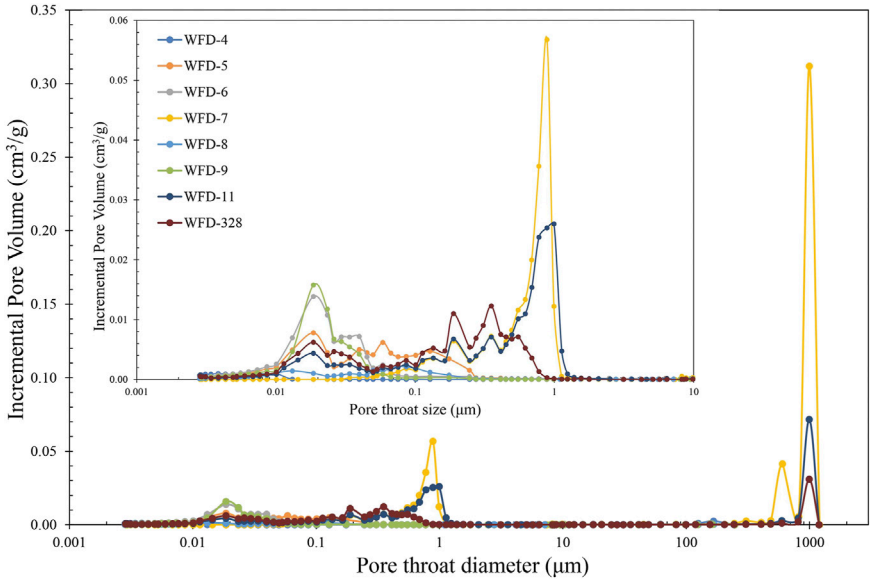

FIGURE 3
Pore-throat size distribution from MIP analyses with complete (0.3 nm-1000 μm) and zoomed (0.3 nm-2 μm) regions.

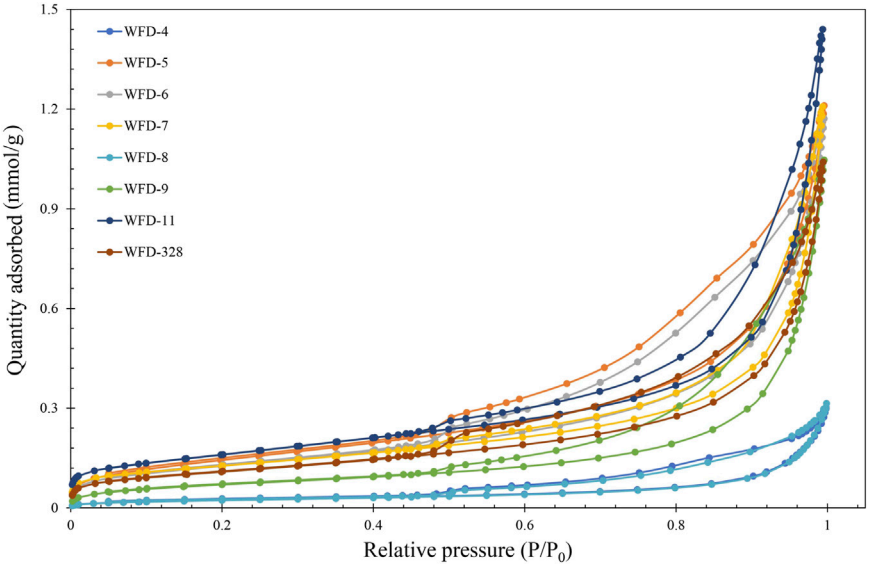

FIGURE 4
Isotherm plots from the GP method.

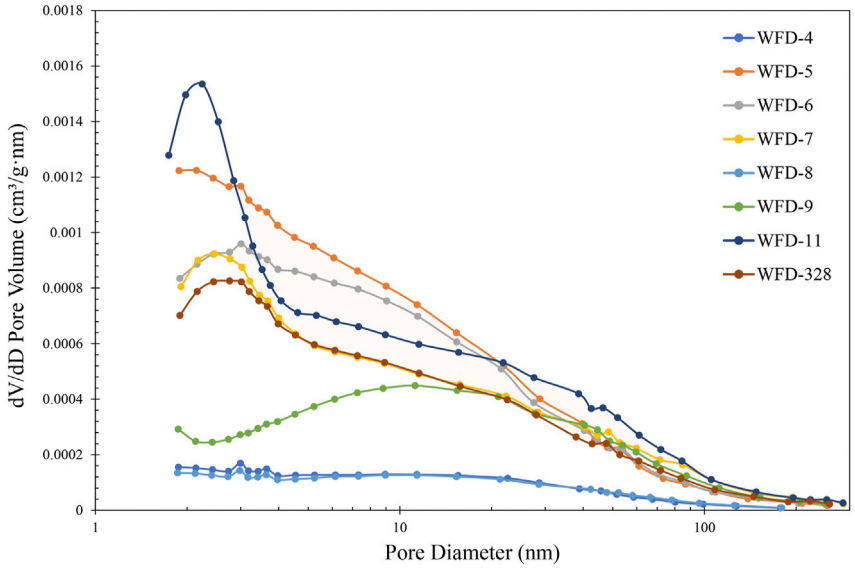

FIGURE 5
Pore diameter distribution from the GP method.

0.45 cm^3. Since the sample dimension of LIP and SI are the same which is a cube with a length of ~1 cm, the pore volume and porosity measured by LIP can be used to calculate the imbibed DIW volume in SI. The imbibed DIW volumes from SI are only 0.34–0.86% of the total pore volumes (Table 4). In the log-log plot of imbibition time against cumulative imbibition volume, these eight samples can be separated into two groups based on the imbibition behaviors (Figure 7). Group 1 contains samples WFD-4, WFD-5, WFD-6, WFD-8, and WFD-9, which have no or a very short plateau during the experimental duration of the SI tests. The fitted imbibition slopes vary from 0.10 to 0.38 (Table 4). In addition, samples WFD-5 and WFD-6 show an

TABLE 3 Porosity before and after solvent extraction.

Sample ID	Porosity from (U)SAXS (%)		Porosity difference (%)
	Non-extracted	Solvent-extracted	
WFD-4	3.24	4.93	51.9
WFD-5	8.66	9.33	7.72
WFD-6	5.21	9.36	79.7
WFD-7	7.86	11.1	40.6
WFD-8	2.84	5.51	94.1
WFD-9	4.56	7.62	67.0
WFD-11	6.79	7.39	8.80
WFD-328	8.93	10.9	22.1

increase in the fitted slope after 2 and 4 h of imbibition, respectively.

Group 2 contains samples WFD-7, WFD-11, and WFD-328 which have fast and large cumulative imbibition with a long plateau after 40 min of imbibition test time. The fitted slopes vary from 0.52 to 0.59 (Table 4).

Particle size distribution analyses

Table 5 shows the mean grain size and sorting of eight Woodford Shale samples, which were calculated by Eq. 4 reported by Folk (1980) for sedimentary rocks:

$$\text{Mean particle size} = \frac{D_{16} + D_{50} + D_{84}}{3} \tag{4a}$$

$$\text{Sorting} = \frac{D_{84} - D_{16}}{4} + \frac{D_{95} - D_5}{6.6} \tag{4b}$$

where D is the grain diameter in micrometers and the numbers in subscript represent the cumulative percentage in particle size distribution. For these eight samples, the mean grain size varies from 1.72 to 6.42 μm, with an average of 3.82 μm; in addition, the sorting parameter varies from 2.56 to 5.87 (Table 5). Based on the sorting classification by Folk (1980), these eight samples fall in the categories of being very poorly sorted to extremely poorly sorted, which will affect the wide range of pore size distribution. Figure 8 shows that the GSD obtained from the laser diffraction method. Most samples are dominated by grains with sizes at 3 μm, except for WFD-7 which has a second maximum at 0.06 μm. The mean grain size estimated from SEM images (3–4 μm) also shows similar results to the laser diffraction analyses.

Discussion

In this Section, the comparison of experimental methods, pore structure characterization, and effect of grain sizes on pore structure will be discussed. As no single experiment can measure the complete spectrum of the pore structure, through measuring shale by multiple experiments, the pore structure can be characterized credibly and comprehensively, and the pros and cons of each experiment can be compared. With a well-justified pore structure characterization, the discussion on the effect of grain sizes on pore structure can be more reasonable.

Comparison of GP, MIP, LIP and (U)SAXS methods

In Results *Results* Section, the similar porosities and bulk densities between MIP and LIP indicate the accuracy of the LIP and increase the credibility of SI results, since the porosities from LIP were used to calculate the imbibed DIW volume percentage in SI. Both GP and MIP are fluid-intrusion methods which use fluids to probe pore structures. GP uses nitrogen gas based on the Kelvin equation and MIP uses high-pressure liquid mercury based on the Washburn equation. For GP method, only pore volume and specific surface area of the samples can be obtained. Moreover, the measurable pore range of GP is 2–300 nm which is too narrow to fully characterize the pore structure of shale with a nm-μm spectrum. For MIP method, more petrophysical properties can be probed compared with GP, including pore volume, specific surface area, densities, and the wide measurable pore-throat range from 3 nm to ~1,000 μm. This makes the MIP the most popular method in pore structure characterization. However, the samples cannot be reused after MIP, since mercury will pollute them; in addition, there are some concerns that high pressure intrusion may deform the pore structure of porous media Unlike the fluid-intrusion methods, (U)SAXS measures both isolated and connected pores in 1–1,000 nm on ~800 μm intact wafers which can be tested repeatably.

The pore volumes measured by GP, MIP, and (U)SAXS methods were compared in the pore range of 2–300 nm which

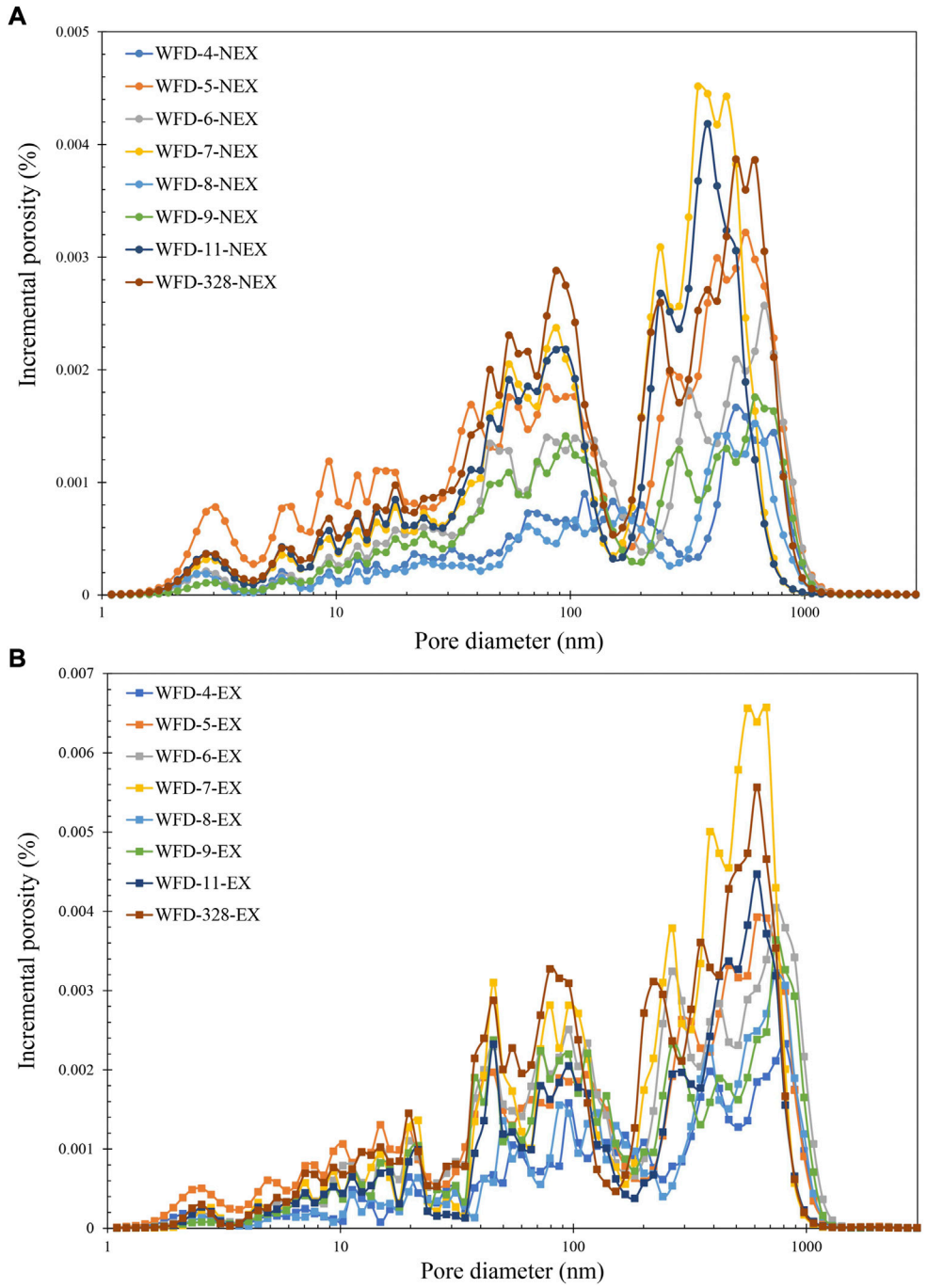

FIGURE 6
Pore diameter distributions of non-extracted **(A)** and solvent-extracted **(B)** samples.

is the overlapping range of the three methods (Figure 9). The results show that GP has similar pore volume with (U)SAXS in 2–300 nm, which indicate the creditability of both methods. MIP shows no data in <2.8 nm and slightly higher pore volume than GP and (U)SAXS in the pore interval of 2.8–300 nm, which could be mainly caused by the ink-bottle effect in the MIP method, as the MIP method measures the pore-throat distribution with the pore volume associated with larger-sized pore body being ascribed to smaller pore throats. The systematic bias in (U)SAXS and sample heterogeneity will also need to be considered in the result comparison among different methods. The data interpretation model for pore volume calculation in (U)SAXS

TABLE 4 Results of imbibition to T directions of Woodford Shale samples.

Sample ID	SI slope (-)	Imbibed DIW volume in SI	Expected pore volume from LIP	Ratio of imbibed DIW volume
		(cm^3)	(cm^3)	(%)
WFD-4	0.38	0.03	5.70	0.56
WFD-5	0.26	0.13	30.0	0.42
WFD-6	0.10	0.08	24.3	0.34
WFD-7	0.59	0.33	38.1	0.86
WFD-8	0.16	0.04	9.72	0.43
WFD-9	0.21	0.08	18.7	0.41
WFD-11	0.52	0.45	67.7	0.67
WFD-328	0.54	0.29	35.2	0.83

was applicable for samples with porosities smaller than 10%, while the Woodford Shale outcrop samples have large porosities with an average of 21.5% to potentially introduce systematic bias to the pore volume results. The sample dimension in MIP is 1-cm^3 cube and in (U)SAXS is 0.8 mm-thick wafer with X-ray scanning area of 0.64 mm^2. The measurable volume in (U)SAXS is much smaller than in MIP, which may enlarge the effect of sample heterogeneity and show smaller pore volume in (U)SAXS.

Pore body with small throat cannot be filled until the throat was intruded under high pressure. In such condition, the mercury volume being filled into pore body will be accounted as the volume corresponding to a smaller size of pore throat. Because the Washburn equation links the intrusion pressure to pore throat size (Wardlaw and McKellar, 1981; Gao et al., 2018; Zhang, et al., 2019). Therefore, the volume of pore-throats in nanometers are higher than GP and (U)SAXS. No single experiment can characterize the complete spectrum of pore structure in shale because of the limitations and different principles of each experiment. For MIP, higher pressures are needed to measure pores in nanometers, while the high pressure could potentially change the original pore structure and introduce errors to the results (Tang et al., 2016; Li et al., 2018). Compared with MIP, the GP method will not distort the pore structures and keep the samples reusable. However, the measurement range of GP is only from 2–300 nm which is much smaller than the range in MIP which is from 3 nm to ~1,000 μm. Therefore, the combined data from both methods can be the best option to cover more pores and obtain a better and holistic characterization of the connected pores, with the ability of assessing the ink-bottle effect.

In summary, MIP is the most economic and popular test in pore structure characterization. Though GP could measure nano-sized pores in 2–300 nm by using theoretical data interpretation models, this relatively narrow range make the GP not as effective as MIP. (U)SAXS could measure nano-sized pores in the range of 1–1,000 nm, which is more powerful than GP. However, the small sample size and the accessibility to (U)SAXS instruments in national facilities are the two major limitation, along with the upper testable limit of 1 μm in diameter that is relatively not sufficient to cover many shale samples.

Pore structure characterization by MIP, GP, (U)SAXS and SI methods

In this section, pore structure will be discussed in the context of pore size distribution and pore connectivity. Pore size distribution are based on the combined data of GP and MIP methods. To avoid the errors introduced by the deformation in pores <50 nm under high mercury pressure, GP provides the pore data in 1–50 nm and MIP provides data in the 50 nm-1000 μm range. In addition, the pore connectivity of the Woodford Shale is to be discussed from imbibition slopes (SI) and tortuosity (MIP) results.

In this study, the pore diameter classification by Loucks et al. (2012) was applied. Loucks et al. (2012) proposed three categories of pores: nanopores (1 nm-1 μm), micropores (1–62.5 μm), and mesopores (62.5 μm-4 mm). Figure 10 shows the domination of nanopores in the eight samples. WFD-7, WFD-11, and WFD-328 with porosities over 30% (from MIP) have large pore volumes in nanopores and mesopores. For other samples with porosities at 3–17% (from MIP), only nanopores have the domination. The large pore volumes in large porosity samples may be caused by the weathering and dissolution of the outcrops.

These eight Woodford Shale samples were also tested by (U)SAXS method for solvent-extracted and non-extracted samples. The pore volume distribution of non-extracted samples from (U)SAXS shows similar distribution behavior (Figure 10A), which

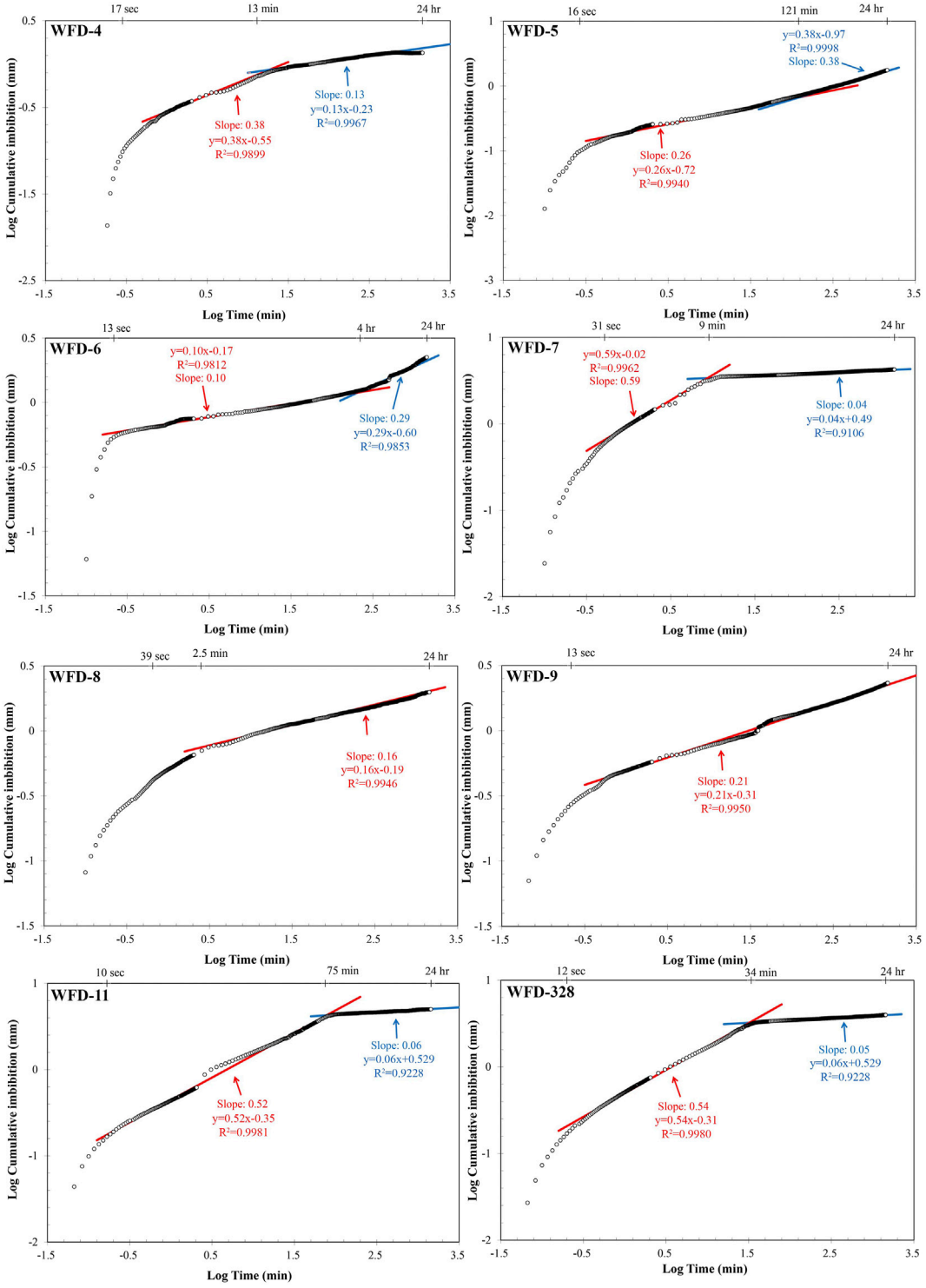

FIGURE 7
Plots of imbibition time vs. cumulative imbibition volume of SI results with fitted imbibition slopes.

indicates the consistency among GP, MIP, and (U)SAXS methods (Figure 10B). In Table 3, the porosities of solvent-extracted samples increase 46% on the average compared to the non-extracted samples. Samples with high TOC contents, such as WFD-8 and WFD-9, tend to have greater porosity differences after the solvent extraction. Pore diameter distributions of WFD-

TABLE 5 Mean grain size from laser diffraction analyses (TST: transgressive system tract; HST: highstand system tract).

Depositional environment	Sample ID	Mean grain size (μm)	Soring (-)
TST	WFD-4	6.42	5.87
	WFD-5	5.06	5.02
	WFD-6	2.95	2.95
HST	WFD-7	1.72	2.56
	WFD-8	4.10	3.22
	WFD-9	3.22	3.23
	WFD-11	3.07	2.67
	WFD-328	4.04	4.66

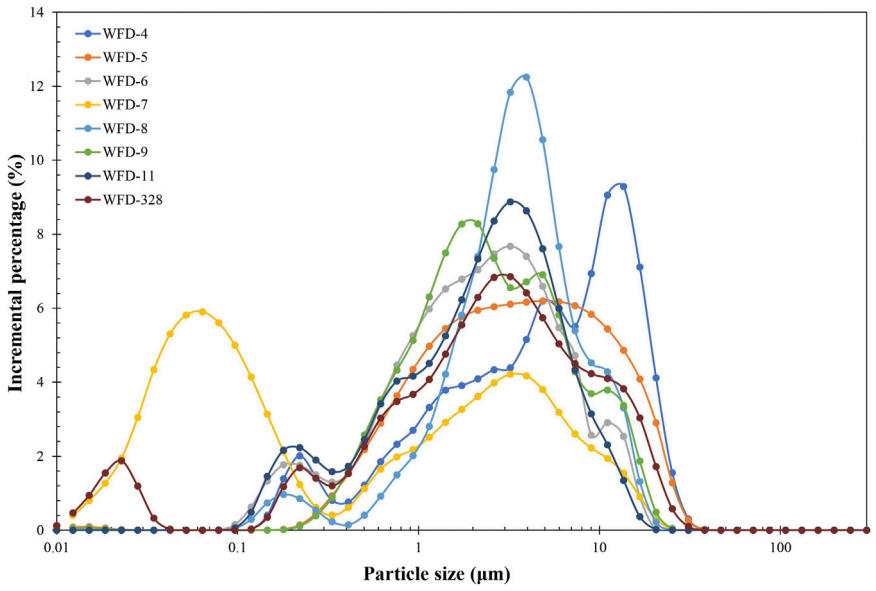

FIGURE 8
Laser diffraction-derived GSD results of eight Woodford Shale sample.

4, WFD-6, WFD-8, and WFD-9 show a volume increase in nanopores after the solvent extraction, especially at the intervals of 50–100 nm and 400–1,000 nm (Figure 6B). Through the comparison of SEM images, bitumen which is soluble to the solvent decreases obviously with the solvent extraction (Figures 2I,J). Therefore, it is reasonable to speculate that the bitumen which is accounted as OM could block pores and may affect the pore connectivity (Tissot and Welte, 1984).

The fitted slope can indicate the pore connectivity based on the classification by Hu et al. (2002). The values of fitted slope at ~0.26 indicates poor pore connectivity, ~0.5 for good pore connectivity, and 0.26–0.5 for intermediate pore connectivity. The fitted slopes from SI method show that the pore connectivities of these eight samples are different. Samples WFD-6, WFD-8, and WFD-9 have poor pore connectivity, WFD-4 and WFD-5 have intermediate pore connectivity, and WFD-7, WFD-11, and WFD-328 have good pore connectivity. The increase in fitted slope for samples WFD-5 and WFD-6 indicates the pore connectivity changing from poor pore connectivity to intermediate connectivity during the imbibition process. To find the factors that influence the pore connectivity, crossplots of

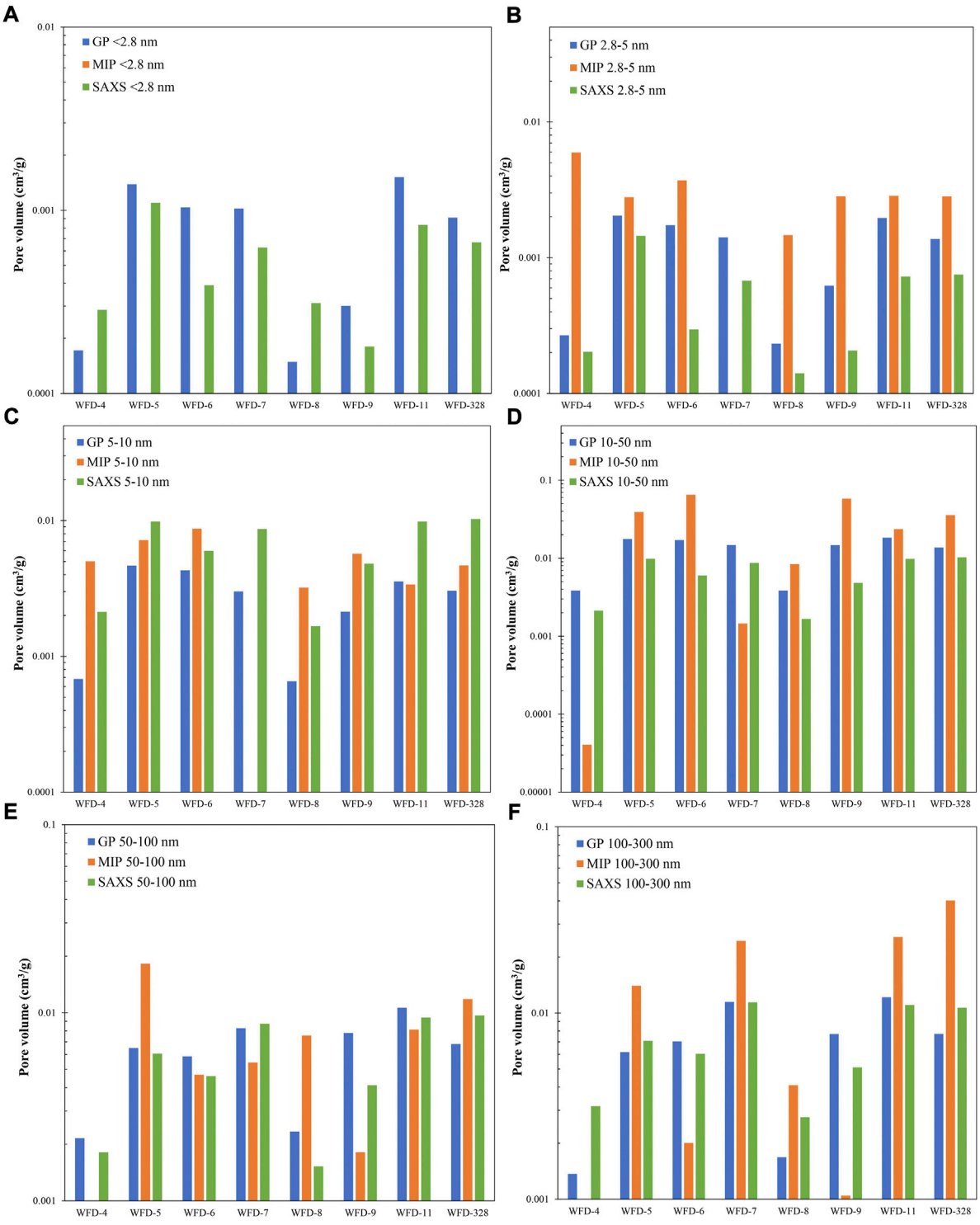

FIGURE 9
Pore volume comparison of GP, MIP, and (U)SAXS methods in six ranges; **(A)** < 2.8 nm; **(B)** 2.8–5 nm; **(C)** 5–10 nm; **(D)** 10–50 nm; **(E)** 50–100 nm; **(F)** 100–300 nm.

fitted slopes with other results were presented (Figure 11A). Group 1 samples (WFD-4, WFD-5, WFD-6, WFD-8, and WFD-9) in SI show a positive relationship between mean grain size and the fitted slope. This correlation could indicate

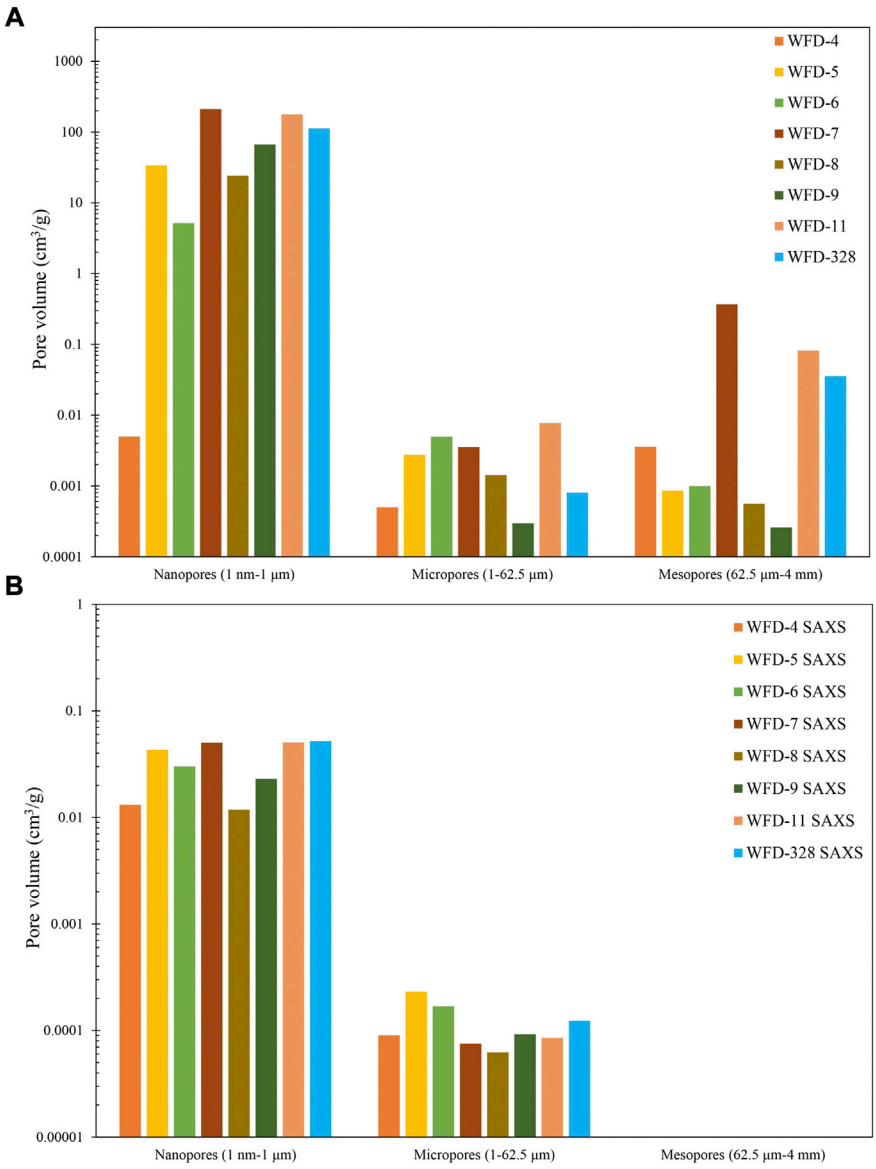

FIGURE 10
(A) Combined pore diameter distribution of MIP and GP method; **(B)** pore diameter distribution of (U)SAXS method.

that the increase in grain diameter could help to improve the pore connectivity. Wang X. et al. (2021) pointed out that pores with diameter >50 nm provide the major driving force in SI process. In Table 6, the percentages of pores in 0.05–1 μm for samples WFD-5, WFD-8, WFD-9, WFD-11, and WFD-328 are over 50%. The cross-plot of percentage of pore volume in 0.05–1 μm and mean grain size also have a positive relationship (Figure 11B). Therefore, we reasonably expect that shales with grain sizes greater than 4 μm have a higher possibility to create more nanopores with diameters over 50 nm and provide better pore connectivity. Samples in Group 2 (WFD-7, WFD-11, and WFD-328) in SI show less correlation with mean grain sizes. Tortuosity is also an important property in shale pore structure studies, which could affect the formation factor in Archie's Law and fluid flow behavior (Archie, 1941; Tsang, 1984). The tortuosity values in the eight Woodford Shale samples are lower than 30, except for samples WFD-11 and WFD-328 which are extremely high (Table 2). Results from Rao and Bai (2020) show a negative linear relationship between tortuosity and porosity in granular soil simulation. However, no relationship exists between tortuosity and porosity in Figure 11C, which could be caused by the complexity of the pore structure in shale.

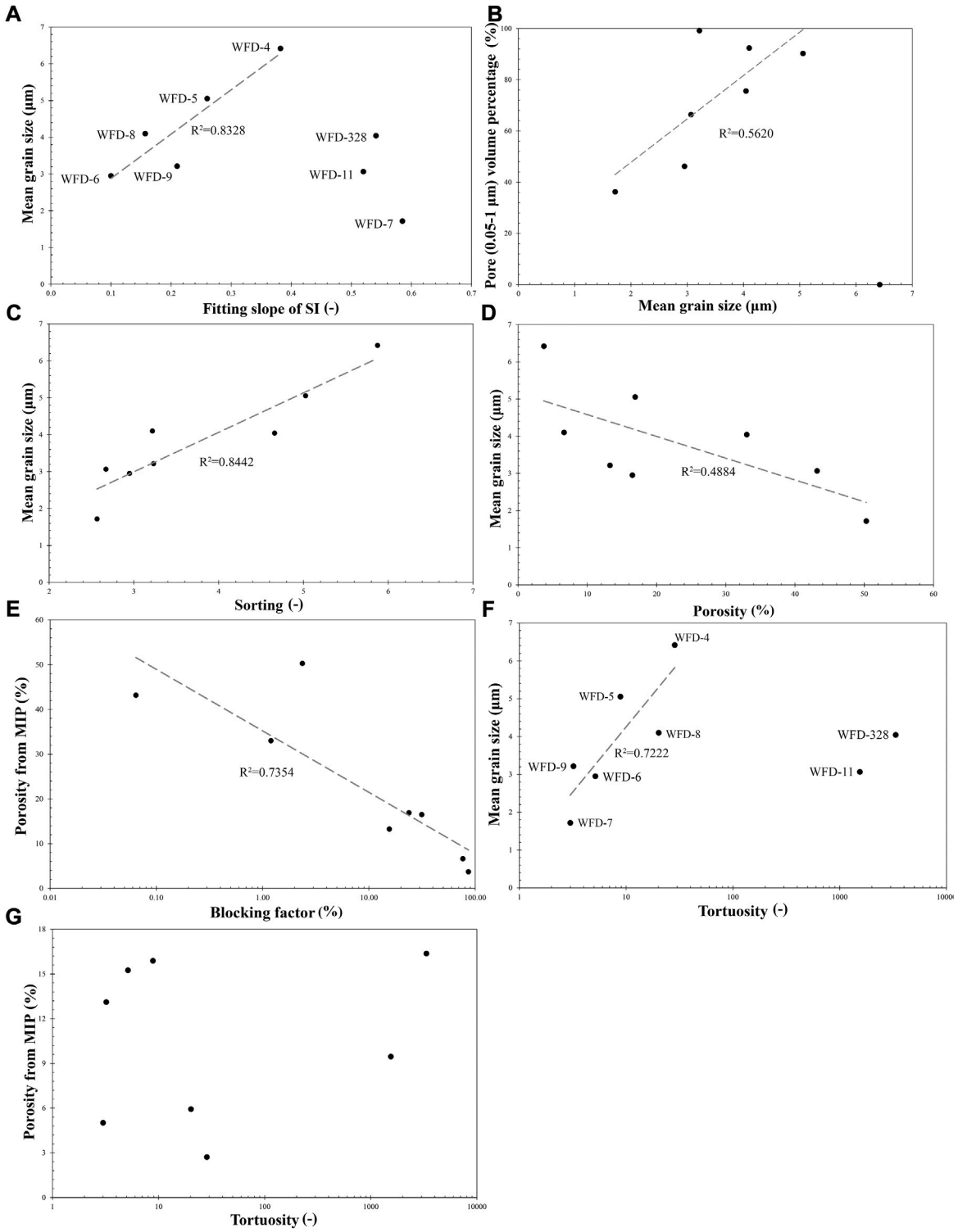

FIGURE 11
Cross plots of **(A)** mean grain size vs. fitting slopes; **(B)** nanopore percentage vs. mean grain size; **(C)** porosity vs. tortuosity; **(D)** porosity vs. blocking factor; **(E)** mean grain size vs. sorting; **(F)** mean grain size vs. porosity; and **(G)** mean grain size vs. tortuosity; (-) means dimensionless.

TABLE 6 Pore volume percentages from the combined GP-MIP data.

Sample ID	Pore diameter from GP (μm)				Pore diameter from MIP (μm)				
	<0.0028	0.0028–0.005	0.005–0.01	0.01–0.05	0.05–0.1	0.1–1	1–10	10–100	>100
WFD-4	0.0042	0.0066	0.0168	0.0949	0.00	0.00	1.19	18.20	80.5
WFD-5	0.0037	0.0054	0.0125	0.0471	59.5	30.8	3.66	4.44	1.57
WFD-6	0.0093	0.0156	0.0386	0.1534	46.2	0.02	16.6	31.7	5.32
WFD-7	0.0002	0.0002	0.0005	0.0025	1.21	35.0	0.39	0.28	63.1
WFD-8	0.0006	0.0009	0.0025	0.0147	80.3	12.1	2.27	3.78	1.54
WFD-9	0.0004	0.0009	0.0032	0.0218	97.7	1.53	0.04	0.45	0.29
WFD-11	0.0006	0.0007	0.0013	0.0069	4.27	62.1	2.62	0.35	30.6
WFD-328	0.0006	0.0009	0.0021	0.0092	9.60	66.0	0.25	0.36	23.8

TABLE 7 Blocking factors of the eight Woodford Shale samples.

Sample ID	Blocking factor (%)
WFD-4	86.4
WFD-5	23.8
WFD-6	31.4
WFD-7	2.36
WFD-8	76.4
WFD-9	15.6
WFD-11	0.06
WFD-328	1.20

Effects of grain size and pore blocking factors on pore structure

In this section, the influence of grain sizes, pore blocking factors, and paleo-depositional environment on the pore structure of Woodford Shale will be discussed. The results of solvent extraction and (U)SAXS analyses, as well as SEM imaging, show that the bitumen could block the pore space and decrease the porosity as reported by Wei et al. (2014). In addition, Taghavi et al. (2006) and Ehrenberg et al. (2006) showed that the compaction and recrystallization of carbonates can decrease the porosity. From XRD results, the carbonate percentages in WFD-4 & WFD-8 are over 70%, and both samples have the smallest porosities in the eight samples. Moreover, the carbonates in WFD-4 & WFD-8 are observed to be non-porous in SEM images (Figures 2G,H). Therefore, we speculate that both bitumen and carbonates in the Woodford Shale act as pore blocking materials. To quantify the potential contribution of these pore blocking materials, a blocking factor is introduced in this study (Eq. 5) (Table 7). To simplify the weight percent calculation of bitumen, we used TOC% as the replacement in calculating the blocking factor.

$$\text{Blocking factor} = \frac{carbonate\% + TOC\%}{clays\% + carbonates\% + qtz\% + TOC\%} \times 100\% \quad (5)$$

where qtz% is the total percentage of quartz, feldspars, and other trace minerals from the XRD results. The blocking factor varies from 0.06 to 86.4% (Table 1), and the negative relationship between porosity (from MIP) and blocking factor prove the effect of carbonates and OM on porosity (Figure 11D). Mean grain sizes of eight samples show positive and negative relationships with sorting values and porosity (from MIP) (Figures 11E,F). Samples with small grain sizes tend to be well-sorted, and well-sorted samples tend to have greater porosities (McLean and Kirk, 1969; Edwards, 2001; Ogolo et al., 2015). Grain sizes also have direct relationships with the depositional environment of the Woodford Shale. Middle Woodford Shale was deposited in a transgressive environment with increasing water depth, and Upper Woodford Shale was deposited in a highstand system with relatively stable water level (Figure 1) (Comer, 1991; Kirkland et al., 1992; Philp and DeGarmo, 2020). As a water depth increases, the grains deposited at the same place tend to have smaller diameters (Catuneanu, 2006). Therefore, the grain size will decrease upward in the stratigraphic column (from older to younger rocks). In Figure 12, such grain size decrease can be observed in Middle Woodford Shale with the sea-level increase. The changing pattern in the grain size in the Upper Woodford Shale is irregular as the grain sizes decrease first and then increase, which should show grain size increase upward in high-stand system (Figure 12).

The paleo-location of the Ardmore Basin was near the equator and subtropical area (Comer, 1991). The oxygen-bearing surface water could not sink due to its high temperature, which finally formed a thermocline and created the anoxic bottom water environment (Kirkland et al., 1992). Moreover, the dilution of the OM by the sediments was weak due

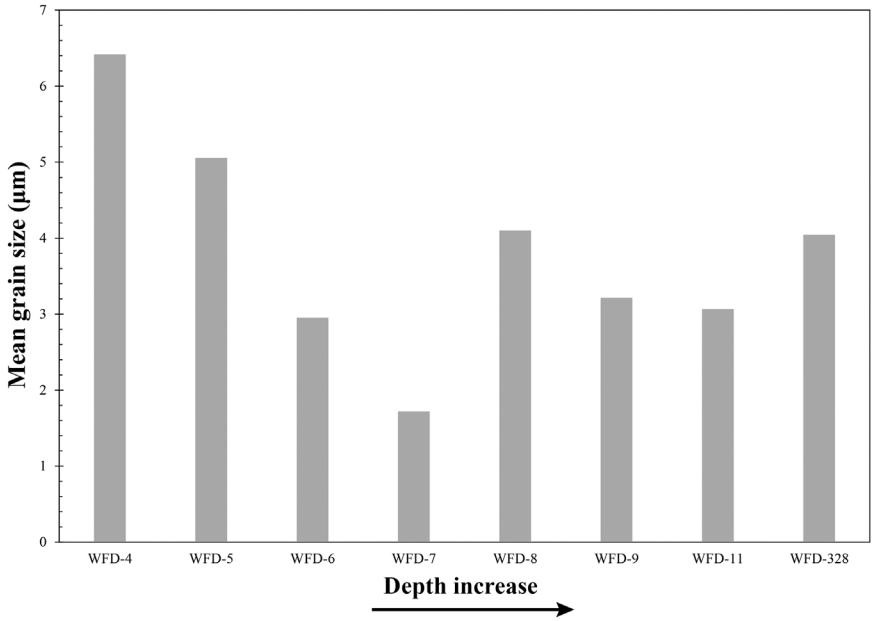

FIGURE 12
Grain size changes with sample depths.

to the less input of sediments during the deposition (Kirkland et al., 1992). Therefore, the anoxic environment and low dilution resulted in higher preservation of the OM in the Woodford Shale. Compared with the Middle Woodford Shale, the TOC% preserved in the Upper Woodford Shale is much lower. In the Upper Woodford Shale, quartz and feldspars are the major minerals and the Upper Woodford Shale has a smaller average blocking factor than the Middle Woodford Shale.

In Woodford Shale samples, positive relationships exist between tortuosity vs. mean grain size, rather than in tortuosity vs. porosity (Figures 11C,G). As discussed before, samples with greater grain sizes tend to be poorly sorted, which has also been suggested by Khabbazi et al. (2015) and Rezende and Pope (2015). Compared with well-sorted samples, smaller sized grains fill in the pores in poorly-sorted samples, resulting in more barriers to fluid movement and an increase in the tortuosity. Therefore, the Woodford Shale outcrop samples with greater grain size tend to be poorly sorted and have higher tortuosity than smaller sized samples.

Conclusion

Multiple experiments were applied on eight Woodford Shale outcrop samples to characterize the pore structure, with a particular emphasis on grain sizes and their distributions. Through a comparison of integrated and complementary experiments, the associated (U)SAXS, MIP, and GP methods are a good combination for shale pore structure study. The results indicate that (1) the nanopores (1 nm-1 μm) dominated Woodford Shale outcrop samples have porosities in 3–40% with poor-to-good pore connectivity; 2) carbonate and OM can decrease the porosity; and 3) porosity, pore connectivity, and tortuosity have close relationships with the grain size which is affected by the sea-level fluctuation in the Woodford Shale. With the sea-level increase, the grain size will decrease, which makes the porosity and tortuosity increase and improves the pore connectivity. This study presents the advantages of the application of multiple experiments on shale. The multiple experiments tested the shales on different aspects to probe the pore structures as comprehensive as possible. This study also built a connection between pore structure and grain size. Since the pores are created based on the grains, such as the interparticle pores, the studies on grains can provide more understandings on pore structures and the pore structure can be further connected with depositional environment in the future.

Data availability statement

The data analyzed in this study is subject to the following licenses/restrictions: The datasets generated during and/or analyzed during the current study are available from the corresponding author on reasonable request. Requests to

access these datasets should be directed to Qinhong Hu, maxhu@uta.edu.

Author contributions

CZ: Investigation, Formal analysis, Writing-Ordinal draft preparation. QH: Conceptualization, Methodology, Resources, Supervision, Writing-Reviewing and Editing. QW: Investigation, Software, Writing-Reviewing and Editing. JI: Investigation, Software. MW: Investigation, Visualization, Resources. XZ: Investigation; Formal analysis. JY: Visualization, Investigation.

Funding

Financial assistances for this work are provided by the National Natural Science Foundation of China (Nos. 41830431 and 41821002), Shandong Provincial Major Type Grant for Research and Development from the Department of Science and Technology of Shandong Province (No. 2020ZLYS08), and AAPG Foundation's Grants-in-Aid Program. The X-ray scattering data were collected at the X-ray Science Division beamline of 9-ID, a resource of the Advanced Photon Source, a U.S. Department of Energy (DOE) Office of Science User Facility operated for the DOE Office of Science by Argonne National Laboratory under Contract No. DE-AC02-06CH11357.

Conflict of interest

The authors declare that the research was conducted in the absence of any commercial or financial relationships that could be construed as a potential conflict of interest.

Publisher's note

All claims expressed in this article are solely those of the authors and do not necessarily represent those of their affiliated organizations, or those of the publisher, the editors and the reviewers. Any product that may be evaluated in this article, or claim that may be made by its manufacturer, is not guaranteed or endorsed by the publisher.

References

Baiker, A., and Reithaar, A. (1982). Contact angle of mercury against catalyst materials for use in intrusion porosimetry. *Ind. Eng. Chem. Prod. Res. Dev.* 21 (4), 590–591. doi:10.1021/i300008a015

Bardestani, R., Patience, G. S., and Kaliaguine, S. (2019). Experimental methods in chemical engineering: Specific surface area and pore size distribution measurements—BET, BJH, and DFT. *Can. J. Chem. Eng.* 97 (11), 2781–2791. doi:10.1002/cjce.23632

Barrett, E. P., Joyner, L. G., and Halenda, P. P. (1951). The determination of pore volume and area distributions in porous substances. I. Computations from nitrogen isotherms. *J. Am. Chem. Soc.* 73 (1), 373–380. doi:10.1021/ja01145a126

Bernal, A. S., Mayorga, L. C., Prada, A. G., and Slatt, R. M. (2012). *Geological characterization of the Woodford shale*. McAlester Cemetery quarry, 63. Oklahoma, 202–213. Shale Shaker.

Brunauer, S., Emmett, P. H., and Teller, E. (1938). Adsorption of gases in multimolecular layers. *J. Am. Chem. Soc.* 60 (2), 309–319. doi:10.1021/ja01269a023

Cao, T., Song, Z., Wang, S., and Xia, J. (2015). A comparative study of the specific surface area and pore structure of different shales and their kerogens. *Sci. China Earth Sci.* 58 (4), 510–522. doi:10.1007/s11430-014-5021-2

Cao, Z., Liu, G., Zhan, H., Li, C., You, Y., Yang, C., et al. (2016). Pore structure characterization of Chang-7 tight sandstone using MICP combined with N_2GA techniques and its geological control factors. *Sci. Rep.* 6 (1), 36919–37013. doi:10.1038/srep36919

Cardott, B. J. (2017). Oklahoma shale resource plays. *Okla. Geol. Notes* 76 (2), 21–30.

Cardott, B. J. (2012). Thermal maturity of Woodford Shale gas and oil plays, Oklahoma, USA. *Int. J. Coal Geol.* 103, 109–119. doi:10.1016/j.coal.2012.06.004

Catuneanu, O. (2006). *Principles of sequence stratigraphy*. 1st ed. Amsterdam: Elsevier, 375.

Clarkson, C. R., Solano, N., Bustin, R. M., Bustin, A. M. M., Chalmers, G. R., He, L., et al. (2013). Pore structure characterization of North American shale gas reservoirs using USANS/SANS, gas adsorption, and mercury intrusion. *Fuel* 103, 606–616. doi:10.1016/j.fuel.2012.06.119

Comer, J. B. (2008). "Distribution and source-rock characteristics of Woodford Shale and age-equivalent strata," in *Poster panel presented at 2008 AAPG annual convention held in san antonio* (USA: Texas).

Comer, J. B. (1991). "Stratigraphic analysis of the upper devonian Woodford formation, permian basin, west Texas and southeastern New Mexico," in *Bureau of Economic Geology* (Austin: University of Texas at Austin). Report of Investigations Number 201, 66.

Craddock, P. R., Le Doan, T. V., Bake, K., Polyakov, M., Charsky, A. M., and Pomerantz, A. E. (2015). Evolution of kerogen and bitumen during thermal maturation via semi-open pyrolysis investigated by infrared spectroscopy. *Energy fuels.* 29 (4), 2197–2210. doi:10.1021/ef5027532

Cullen, A. (2020). Woodford shale mercury anomalies from the McAlister Cemetery quarry, Oklahoma: A north American test of the volcanic-trigger hypothesis for late devonian mass extinctions. *Shale Shak.* 71 (5). September-October.

Curtis, M. E., Ambrose, R. J., Sondergeld, C. H., and Rai, C. S. (2010). in Structural characterization of gas shales on the micro- and nano-scales: Canadian Unconventional Resources and International Petroleum Conference, October 19-21, 2010 (Calgary, Alberta: Canada), 15. SPE Paper 137693.

Curtis, M. E., Cardott, B. J., Sondergeld, C. H., and Rai, C. S. (2012). Development of organic porosity in the Woodford Shale with increasing thermal maturity. *Int. J. Coal Geol.* 103, 26–31. doi:10.1016/j.coal.2012.08.004

Dong, T., and Harris, N. B. (2020). The effect of thermal maturity on porosity development in the Upper Devonian–Lower Mississippian Woodford Shale, Permian Basin, US: Insights into the role of silica nanospheres and microcrystalline quartz on porosity preservation. *Int. J. Coal Geol.* 217, 103346. doi:10.1016/j.coal.2019.103346

Edwards, A. C. (2001). Grain size and sorting in modern beach sands. *J. Coast. Res.*, 38–52.

Ehrenberg, S. N., Eberli, G. P., and Baechle, G. (2006). Porosity-permeability relationships in miocene carbonate platforms and slopes seaward of the great barrier reef, Australia (ODP leg 194, marion plateau). *Sedimentology* 53 (6), 1289–1318. doi:10.1111/j.1365-3091.2006.00817.x

Ekwunife, I. C. (2017). *Assessing mudrock characteristics, high-resolution chemostratigraphy, and sequence stratigraphy of the Woodford shale in the McAlister Cemetery quarry, Ardmore Basin*. Oklahoma, Master Thesis: University of Oklahoma.

Folk, R. L. (1980). *Petrology of sedimentary rocks*. Austin, Texas: Hemphill's.

Forsmo, S. P. E., and Vuori, J. P. (2005). The determination of porosity in iron ore green pellets by packing in silica sand. *Powder Technol.* 159 (2), 71–77. doi:10.1016/j.powtec.2005.05.032

Freeman, V. L. (1961). Contact of boquillas flags and austin chalk in val verde and terrell counties, Texas. *AAPG Bull.* 45 (1), 105–107.

Fu, H., Wang, X., Zhang, L., Gao, R., Li, Z., Xu, T., et al. (2015). Investigation of the factors that control the development of pore structure in lacustrine shale: A case study of block X in the ordos basin, China. *J. Nat. Gas Sci. Eng.* 26, 1422–1432. doi:10.1016/j.jngse.2015.07.025

Gao, Z., and Hu, Q. (2013). Estimating permeability using median pore-throat radius obtained from mercury intrusion porosimetry. *J. Geophys. Eng.* 10, 025014. doi:10.1088/1742-2132/10/2/025014

Gao, Z., Hu, Q., and Hamamoto, S. (2018). Using multicycle mercury intrusion porosimetry to investigate hysteresis phenomenon of different porous media. *J. Porous Media* 21 (7), 607–622. doi:10.1615/jpormedia.2018017822

Giesche, H. (2006). Mercury porosimetry: A general (practical) overview. *Part. Part. Syst. Charact.* 23 (1), 9–19. doi:10.1002/ppsc.200601009

Granath, J. W. (1989). Structural evolution of the Ardmore Basin, Oklahoma: Progressive deformation in the foreland of the ouachita collision. *Tectonics* 8 (5), 1015–1036. doi:10.1029/tc008i005p01015

Hall, P. L., Mildner, D. F., and Borst, R. L. (1986). Small-angle scattering studies of the pore spaces of shaly rocks. *J. Geophys. Res.* 91 (B2), 2183–2192. doi:10.1029/jb091ib02p02183

Hu, H., Zhang, T., Wiggins-Camacho, J. D., Ellis, G. S., Lewan, M. D., and Zhang, X. (2015). Experimental investigation of changes in methane adsorption of bitumen-free Woodford Shale with thermal maturation induced by hydrous pyrolysis. *Mar. Petroleum Geol.* 59, 114–128. doi:10.1016/j.marpetgeo.2014.07.029

Hu, Q., Ewing, R. P., and Dultz, S. (2012). Low pore connectivity in natural rock. *J. Contam. Hydrology* 133, 76–83. doi:10.1016/j.jconhyd.2012.03.006

Hu, Q., Persoff, P., and Wang, J. S. (2001). Laboratory measurement of water imbibition into low-permeability welded tuff. *J. Hydrology* 242 (1-2), 64–78. doi:10.1016/s0022-1694(00)00388-7

Hu, Q., Zhang, Y., Meng, X., Li, Z., Xie, Z., and Li, M. (2017). Characterization of micro-nano pore networks in shale oil reservoirs of paleogene shahejie formation in dongying sag of bohai bay basin, east China. *Petroleum Explor. Dev.* 44 (5), 720–730. doi:10.1016/s1876-3804(17)30083-6

Ilavsky, J., and Jemian, P. R. (2009). Irena: Tool suite for modeling and analysis of small-angle scattering. *J. Appl. Crystallogr.* 42 (2), 347–353. doi:10.1107/s0021889809002222

Ilavsky, J., Zhang, F., Andrews, R. N., Kuzmenko, I., Jemian, P. R., Levine, L. E., et al. (2018). Development of combined microstructure and structure characterization facility for *in situ* and operando studies at the Advanced Photon Source. *J. Appl. Crystallogr.* 51 (3), 867–882. doi:10.1107/s160057671800643x

Iqbal, O., Padmanabhan, E., Mandal, A., and Dvorkin, J. (2021). Characterization of geochemical properties and factors controlling the pore structure development of shale gas reservoirs. *J. Petroleum Sci. Eng.* 206, 109001. doi:10.1016/j.petrol.2021.109001

Jarvie, D. M., Claxton, B. L., Henk, F., and Breyer, J. T. (2001). *Oil and shale gas from the barnett shale*. Denver: AAPG Annual Meeting Program 10, A100.

Katz, A. J., and Thompson, A. H. (1986). Quantitative prediction of permeability in porous rock. *Phys. Rev. B* 34 (11), 8179–8181. doi:10.1103/physrevb.34.8179

Khabbazi, A. E., Hinebaugh, J., and Bazylak, A. (2015). Analytical tortuosity–porosity correlations for Sierpinski carpet fractal geometries. *Chaos, Solit. Fractals* 78, 124–133. doi:10.1016/j.chaos.2015.07.019

Kibria, M. G., Hu, Q., Liu, H., Zhang, Y., and Kang, J. (2018). Pore structure, wettability, and spontaneous imbibition of Woodford shale, Permian Basin, West Texas. *Mar. Petroleum Geol.* 91, 735–748. doi:10.1016/j.marpetgeo.2018.02.001

Kirkland, D. W., Denison, R. E., Summers, D. M., Gormly, J. R., Johnson, K. S., and Cardott, B. J. (1992). Geology and organic geochemistry of the Woodford shale in the criner hills and Western arbuckle mountains, Oklahoma. *Okla. Geol. Surv. Circ.* 93, 38–69.

Kuila, U., McCarty, D. K., Derkowski, A., Fischer, T. B., and Prasad, M. (2014). Total porosity measurement in gas shales by the water immersion porosimetry (WIP) method. *Fuel* 117, 1115–1129. doi:10.1016/j.fuel.2013.09.073

Li, T., Senesi, A. J., and Lee, B. (2016). Small angle X-ray scattering for nanoparticle research. *Chem. Rev.* 116 (18), 11128–11180. doi:10.1021/acs.chemrev.5b00690

Li, X., Kang, Y., and Haghighi, M. (2018). Investigation of pore size distributions of coals with different structures by nuclear magnetic resonance (NMR) and mercury intrusion porosimetry (MIP). *Measurement* 116, 122–128. doi:10.1016/j.measurement.2017.10.059

Li, Z., Wu, S., Xia, D., He, S., and Zhang, X. (2018). An investigation into pore structure and petrophysical property in tight sandstones: A case of the yanchang formation in the southern ordos basin, China. *Mar. Petroleum Geol.* 97, 390–406. doi:10.1016/j.marpetgeo.2018.07.014

Loog, A., Kurvits, T., Aruvali, J., and Petersell, V. (2001). Grain size analysis and mineralogy of the Tremadocian Dictyonema shale in Estonia. *Oil Shale* 18 (4), 281–297.

Loucks, R. G., Reed, R. M., Ruppel, S. C., and Hammes, U. (2012). Spectrum of pore types and networks in mudrocks and a descriptive classification for matrix-related mudrock pores. *Am. Assoc. Pet. Geol. Bull.* 96 (6), 1071–1098. doi:10.1306/08171111061

Loucks, R. G., and Reed, R. M. (2014). Scanning-electron-microscope petrographic evidence for distinguishing organic-matter pores associated with depositional organic matter versus migrated organic matter in mudrock. *Gulf Coast Assoc. Geol. Soc.* 3, 51–60.

Lowell, S., Shields, J. E., Thomas, M. A., and Thommes, M. (2012). *Characterization of porous solids and powders: Surface area*, 16. New York City, USA: Springer Science & Business Media. pore size and density.

Ma, Z., Merkus, H. G., de Smet, J. G., Heffels, C., and Scarlett, B. (2000). New developments in particle characterization by laser diffraction: Size and shape. *Powder Technol.* 111 (1-2), 66–78. doi:10.1016/s0032-5910(00)00242-4

McCave, I. N., Bryant, R. J., Cook, H. F., and Coughanowr, C. A. (1986). Evaluation of a laser-diffraction-size analyzer for use with natural sediments. *J. Sediment. Res.* 56, 561–564. doi:10.1306/212f89cc-2b24-11d7-8648000102c1865d

McLean, R. F., and Kirk, R. M. (1969). Relationships between grain size, size-sorting, and foreshore slope on mixed sand-shingle beaches. *N. Z. J. Geol. Geophys.* 12 (1), 138–155. doi:10.1080/00288306.1969.10420231

Micromeritics Instrument Inc. (2015). AutoPore V series mercury intrusion porosimetry calculations, 19 pp.

Moore, D. M., and Reynolds, R. C. (1997). *X-Ray diffraction and the identification and analysis of clay minerals*. 2nd Edition. New York: Oxford University Press.

Muller, P. (1994). Glossary of terms used in physical organic chemistry (IUPAC Recommendations 1994). *Pure Appl. Chem.* 66 (5), 1077–1184. doi:10.1351/pac199466051077

Ogolo, N. A., Akinboro, O. G., Inam, J. E., Akpokere, F. E., and Onyekonwu, M. O. (2015). "Effect of grain size on porosity revisited," in *SPE Nigeria annual international conference and exhibition* (Lagos: SPE-178296-MS).

Ojha, S. P., Misra, S., Sinha, A., Dang, S., Tinni, A., Sondergeld, C., et al. (2018). Relative permeability and production-performance estimations for bakken, wolfcamp, eagle ford, and Woodford shale formations. *SPE Reserv. Eval. Eng.* 21 (02), 307–324. doi:10.2118/189983-pa

Parker, M. A., Buller, D., Petre, J. E., and Dreher, D. T. (2009). Haynesville shale-petrophysical evaluation. SPE Rocky Mountain Petroleum Technology Conference. SPE-122937-MS.

Penner, D., and Lagaly, G. (2001). Influence of anions on the rheological properties of clay mineral dispersions. *Appl. Clay Sci.* 19 (1-6), 131–142. doi:10.1016/s0169-1317(01)00052-7

Philip, J. R. (1957). The theory of infiltration: 4. Sorptivity and algebraic infiltration equations. *Soil Sci.* 84 (3), 257–264. doi:10.1097/00010694-195709000-00010

Philp, R. P., and DeGarmo, C. D. (2020). Geochemical characterization of the devonian-mississippian Woodford shale from the McAlister Cemetery quarry, criner hills uplift, Ardmore Basin, Oklahoma. *Mar. Petroleum Geol.* 112, 104078. doi:10.1016/j.marpetgeo.2019.104078

Qiao, J., Zeng, J., Jiang, S., Zhang, Y., Feng, S., Feng, X., et al. (2020). Insights into the pore structure and implications for fluid flow capacity of tight gas sandstone: A case study in the upper paleozoic of the ordos basin. *Mar. Petroleum Geol.* 118, 104439. doi:10.1016/j.marpetgeo.2020.104439

Ravikovitch, P. I., and Neimark, A. V. (2002). Experimental confirmation of different mechanisms of evaporation from ink-bottle type pores: Equilibrium, pore blocking, and cavitation. *Langmuir* 18 (25), 9830–9837. doi:10.1021/la026140z

Rezende, M. F., and Pope, M. C. (2015). Importance of depositional texture in pore characterization of subsalt microbialite carbonates, offshore Brazil. *Geol. Soc. Lond. Spec. Publ.* 418 (1), 193–207. doi:10.1144/sp418.2

Romero, M. A., and Philp, R. P. (2012). Organic geochemistry of the Woodford Shale, southeastern Oklahoma: How variable can shales be. *Am. Assoc. Pet. Geol. Bull.* 96 (3), 493–517. doi:10.1306/08101110194

Sato, Y., Ishihara, M., Nakamura, S., Fukuda, K., Takayama, T., Hiruma, S., et al. (2019). Preparation and application of bioshell calcium oxide (BiSCaO)

nanoparticle-dispersions with bactericidal activity. *Molecules* 24 (18), 3415. doi:10.3390/molecules24183415

Schlumberger, C., and Thommes, M. (2021). Characterization of hierarchically ordered porous materials by physisorption and mercury porosimetry—a tutorial review. *Adv. Mat. Interfaces* 8 (4), 2002181. doi:10.1002/admi.202002181

Slatt, R. M., and O'Brien, N. R. (2011). Pore types in the Barnett and Woodford gas shales: Contribution to understanding gas storage and migration pathways in fine-grained rocks. *Am. Assoc. Pet. Geol. Bull.* 95 (12), 2017–2030. doi:10.1306/03301110145

Sun, M., Yu, B., Hu, Q., Yang, R., Zhang, Y., Li, B., et al. (2017). Pore structure characterization of organic-rich Niutitang shale from China: Small angle neutron scattering (SANS) study. *Int. J. Coal Geol.* 186, 115–125. doi:10.1016/j.coal.2017.12.006

Sun, M., Zhang, L., Hu, Q., Pan, Z., Yu, B., Sun, L., et al. (2019). Multiscale connectivity characterization of marine shales in southern China by fluid intrusion, small-angle neutron scattering (SANS), and FIB-SEM. *Mar. Petroleum Geol.* 112, 104101. doi:10.1016/j.marpetgeo.2019.104101

Sun, M., Zhao, J., Pan, Z., Hu, Q., Yu, B., Tan, Y., et al. (2020). Pore characterization of shales: A review of small angle scattering technique. *J. Nat. Gas Sci. Eng.* 78, 103294. doi:10.1016/j.jngse.2020.103294

Taghavi, A. A., Mork, A., and Emadi, M. A. (2006). Sequence stratigraphically controlled diagenesis governs reservoir quality in the carbonate Dehluran Field, southwest Iran. *Pet. Geosci.* 12 (2), 115–126. doi:10.1144/1354-079305-672

Tang, X., Jiang, Z., Jiang, S., Wang, P., and Xiang, C. (2016). Effect of organic matter and maturity on pore size distribution and gas storage capacity in high-mature to post-mature shales. *Energy fuels.* 30 (11), 8985–8996. doi:10.1021/acs.energyfuels.6b01499

Thommes, M., Kaneko, K., Neimark, A. V., Olivier, J. P., Rodriguez-Reinoso, F., Rouquerol, J., et al. (2015). Physisorption of gases, with special reference to the evaluation of surface area and pore size distribution (IUPAC Technical Report). *Pure Appl. Chem.* 87 (9-10), 1051–1069. doi:10.1515/pac-2014-1117

Thommes, M. (2010). Physical adsorption characterization of nanoporous materials. *Chem. Ing. Tech.* 82 (7), 1059–1073. doi:10.1002/cite.201000064

Tissot, B. P., and Welte, D. H. (1984). *Petroleum formation and occurrence*. New York: Springer-Verlag, 699.

Tsang, Y. W. (1984). The effect of tortuosity on fluid flow through a single fracture. *Water Resour. Res.* 20 (9), 1209–1215. doi:10.1029/wr020i009p01209

Wang, P., Jiang, Z., Chen, L., Yin, L., Li, Z., Zhang, C., et al. (2016). Pore structure characterization for the Longmaxi and Niutitang shales in the Upper Yangtze Platform, South China: Evidence from focused ion beam–He ion microscopy, nano-computerized tomography and gas adsorption analysis. *Mar. Petroleum Geol.* 77, 1323–1337. doi:10.1016/j.marpetgeo.2016.09.001

Wang, Q., Hu, Q., Larsen, C., Zhao, C., Sun, M., Zhang, Y., et al. (2021a). Microfracture-pore structure characterization and water-rock interaction in three lithofacies of the Lower Eagle Ford Formation. *Eng. Geol.* 292, 106276. doi:10.1016/j.enggeo.2021.106276

Wang, Q., Hu, Q., Ning, X., Ilavasky, J., Kuzmenko, I., and Tom, T. (2021b). Spatial heterogeneity analyses of pore structure and mineral composition of Barnett Shale using X-ray scattering techniques. *Mar. petroleum Geol.* 134, 105354. doi:10.1016/j.marpetgeo.2021.105354

Wang, X., Wang, M., Li, Y., Zhang, J., Li, M., Li, Z., et al. (2021c). Shale pore connectivity and influencing factors based on spontaneous imbibition combined with a nuclear magnetic resonance experiment. *Mar. Petroleum Geol.* 132, 105239. doi:10.1016/j.marpetgeo.2021.105239

Wang, Y., Cheng, H., Hu, Q., Liu, L., Jia, L., Gao, S., et al. (2022). Pore structure heterogeneity of Wufeng-Longmaxi shale, Sichuan Basin, China: Evidence from gas physisorption and multifractal geometries. *J. Petroleum Sci. Eng.* 208, 109313. doi:10.1016/j.petrol.2021.109313

Wardlaw, N. C., and McKellar, M. (1981). Mercury porosimetry and the interpretation of pore geometry in sedimentary rocks and artificial models. *Powder Technol.* 29 (1), 127–143. doi:10.1016/0032-5910(81)85011-5

Washburn, E. W. (1921). Note on a method of determining the distribution of pore sizes in a porous material. *Proc. Natl. Acad. Sci. U. S. A.* 7 (4), 115–116. doi:10.1073/pnas.7.4.115

Wei, L., Mastalerz, M., Schimmelmann, A., and Chen, Y. (2014). Influence of Soxhlet-extractable bitumen and oil on porosity in thermally maturing organic-rich shales. *Int. J. Coal Geol.* 132, 38–50. doi:10.1016/j.coal.2014.08.003

Wen, B., Aydin, A., and Duzgoren-Aydin, N. S. (2002). A comparative study of particle size analyses by sieve-hydrometer and laser diffraction methods. *Geotechnical Test. J.* 25 (4), 434–442.

Zhang, H., Huang, H., Li, Z., and Liu, M. (2019). Oil physical status in lacustrine shale reservoirs–A case study on Eocene Shahejie Formation shales, Dongying Depression, East China. *Fuel* 257, 116027. doi:10.1016/j.fuel.2019.116027

Zhang, L., Deng, Z., Sun, M., Lin, J., Ukaomah, C. F., Hu, Q., et al. (2021). Characterization of closed pores in Longmaxi Shale by synchrotron small-angle x-ray scattering. *Energy fuels.* 35 (8), 6738–6754. doi:10.1021/acs.energyfuels.1c00190

Zhang, Y., Yang, B., Yang, Z., and Ye, G. (2019). Ink-bottle effect and pore size distribution of cementitious materials identified by pressurization–depressurization cycling mercury intrusion porosimetry. *Materials* 12 (9), 1454. doi:10.3390/ma12091454

frontiers | Frontiers in Earth Science

TYPE Original Research
PUBLISHED 09 January 2023
DOI 10.3389/feart.2022.1012324

OPEN ACCESS

EDITED BY
Juan Teng,
Yangtze University, China

REVIEWED BY
Jianhua He,
Chengdu University of Technology, China
Saipeng Huang,
Northeast Petroleum University, China

*CORRESPONDENCE
Qiang Fu,
fuqiang@tongji.edu.cn

SPECIALTY SECTION
This article was submitted to Geochemistry, a section of the journal Frontiers in Earth Science

RECEIVED 05 August 2022
ACCEPTED 16 September 2022
PUBLISHED 09 January 2023

CITATION
Yang B, Fu Q, Liu J, Ma W and Zhao S (2023), Study on fault sealing of the Lishui West Sag in the East China Sea Basin.
Front. Earth Sci. 10:1012324.
doi: 10.3389/feart.2022.1012324

Study on fault sealing of the Lishui West Sag in the East China Sea Basin

Bing Yang[1], Qiang Fu[1]*, Jinshui Liu[2], Wenrui Ma[2] and Shijie Zhao[1]

[1]State Key Laboratory of Marine Geology, Tongji University, Shanghai, China, [2]Shanghai Branch Company of CNOOC (China) Ltd., Shanghai, China

The property of fault sealing is a critical controlling factor for hydrocarbon transportation. To date, the sealing property of the complex fault system in the Lishui West Sag is still not clear, meaning it is essential to study regional hydrocarbon transportation and reservoir formation. In this study, we use an integrated method to quantitatively analyze and characterize several important index parameters that affect the sealing property of the faults in the Lishui West Sag based on regional logs and seismic data. We calculated the shale smear factor (SSF), shale gouge ratio (SGR), and clay smear potential (CSP) to characterize the lateral sealing property of the main faults covered with the giant thick shale cap in the Lishui West Sag. We used the vertical shale smear factor Q to clarify the vertical sealing property of these faults quantitatively as a comparison. The results show that the shale cap has a strong smear ability in the Lishui West Sag, while the active fault could moderate the smear. A high fault activity in this area benefits hydrocarbon transportation at the same time. The lateral sealing property and the vertical sealing property of the main faults in the Lishui West Sag have negative correlations.

KEYWORDS

fault sealing, shale smear, quantitative evaluation, Lishui West Sag, East China Sea Basin

Introduction

Fault sealing has confused geologists in reservoir theory and exploration practice, who have tried to evaluate the fault sealing property since the 1960s. Smith (1966) established a model of sand–clay docking to clarify sealing and non-sealing faults. Engelder (1974) studied the relationship between cataclasis and the formation of fault gouge. The existence and distribution range of fault gouges were then confirmed using the ring-shear test by Weber et al. (1978). Through field observations and sample tests, Smith (1980) showed the strong sealing ability of the shale smear layer. Downey (1984) pointed out that the fault sealing properties should be considered as vertical sealing and lateral sealing.

Based on these research studies, Bouvier et al. (1989) came up with the concept of clay smear potential (CSP) and the calculating method. Lindsay et al. (1993) used the shale smear factor (SSF) to calculate the fault sealing property quantitatively. During this

period, Allan (1989) proposed a conceptual model to study the state of sand–clay docking between two fault plates using the cross-sectional profile graphical method based on the theoretical basis of sand–clay docking sealing.

Quantitative evaluation of the fault sealing property started to be put into practice in 1996 (Lyu et al., 1996). Yielding et al. (1997) started to evaluate fault sealing quantitatively by calculating the shale gouge ratio (SGR). After Yielding's attempt, there were more and more articles on the quantitative evaluation of fault sealing and its related parameters. Bretan et al. (2003) pointed out that the SGR can be used to estimate the maximum hydrocarbon column height supported by faults based on sorting a large amount of fault data worldwide. Lyu et al. (2009) considered using the displacement pressure contrast of fault rock against a reservoir to evaluate the fault lateral sealing property quantitatively.

In recent years, an increasing number of scholars have adopted a comprehensive research approach to investigate fault sealing. Wang et al. (2019) undertook an integrative study using core, wireline logs, and seismic data to analyze the architecture of reservoirs and seals of the Lower Jurassic System in the Surat Basin. He et al. (2021) studied the variability in fault reactivation models according to differences in fault throw potential influences across-fault juxtaposition of strata and sealing potential for CO_2 storage of overlying strata in the Surat Basin. The study provides a framework to understand fault architecture and predict which parts of the basin are more prone to the juxtaposition of strata forming transmissive versus sealing relationships. Peng et al. (2021) discussed the evolution, sealing, and damage mechanism of the normal fault in the Yanchang Formation of the Jinhe oilfield, Ordos Basin, based on a series of physical simulation experiments and the particle image velocimetry (PIV) technique.

A series of geotectonic features have been studied in the Lishui Sag. Based on the analyses of gravity and magnetic data by Ma et al. (2018) and Jiang et al. (2019), it is considered that the main control faults in the Lishui Sag are NE–SW trending. Inside the sag, multiple sets of strike-slip faults with nearly east–west strikes have developed. The existence of this series of faults divides the sag into several small sub-sags. Wang et al. (2000), Yang and Wang (2002), and Zhang et al. (2014a) made a comprehensive discussion on the extension characteristics of the Lishui Sag through various technical means such as balanced section technology and pointed out that there are some differences in the extension of different regions and different geological stages in the sag. In the late Cretaceous–Paleocene stage, the extension of the sag was dominated by the multi-stage and progressive "curtain" horizontal extension. At the same time, in the fault depression period, due to the influence of tensile stress, a series of normal faults appeared. The lateral distance of normal faults and a tilt in block faults appeared. The early Lishui fault depression basin is mainly composed of small and relatively independent fault depressions. Based on geological and seismic data on the Lishui Sag, scholars have identified the main petroleum geological conditions in the sag. However, due to its complex structural features, rich structural styles, and complex sedimentary distribution, few studies have examined the hydrocarbon migration channels and transportation systems, which has affected the prediction and evaluation of hydrocarbon resources in the Lishui Sag.

Regional geologic setting

Located in the southwestern part of the East China Sea Shelf Basin, the Lishui Sag is a part of the Taipei Depression. The Lishui Sag is distributed in a NE–SW striking, on the east of the Minzhe Uplift. The Yandang Uplift is on the east of the Lishui Sag, while the Jiaojiang Sag is on the north. The area of the Lishui Sag is about 15,000 square kilometers, and the maximum sedimentary thickness is about 15,000 m (Figure 1).

The Lishui Sag is a Cenozoic rift basin formed of Mesozoic residual basins. Controlled by the NE–SW trending faults, the Lishui Sag developed with a typical "east-fault and west-overlap" feature. The whole sag can be divided into northern and southern sections, while the different tectonic appearances show between the west and east zones. The west part of the Lishui West Sag connects with the Minzhe Uplift by a gentle slope zone, while the east part connects with the Lingfeng Uplift through edge faults of the steep slope zone. The Lishui East Sag also presents the structural characteristics of the western gentle slope zone and eastern steep slope zone. The Lishui Sag has experienced three tectonic evolution stages: the syn-rift stage (the Yueguifeng Formation and Lingfeng Formation in Pliocene), transition stage (the Mingyuefeng Formation in Pliocene), and post-rift stage (after Eocene). The Cenozoic strata from bottom to top are the lower Paleocene Yueguifeng Formation (E_1y), the upper Paleocene Lingfeng Formation (E_1l), the Mingyuefeng Formation (E_1m), the lower Eocene Oujiang Formation (E_2o), the middle Eocene Wenzhou Formation (E_2w), and Miocene, Pliocene, and the Quaternary. The upper Eocene and the Oligocene strata are missing (Figure 2). As the vital exploration target area, the area of the Lishui West Sag is about 6,900 km^2, and the upper Paleozoic Lingfeng Formation and the Mingyuefeng Formation are the primary exploration target intervals.

The China National Offshore Oil Corporation, Primeline Energy Holdings Inc., and many other companies have carried out a series of hydrocarbon explorations in the Lishui Sag since the 1970s. The exploration discovered the L Gas Field and gained a large number of seismic data and log data (Ge et al., 2019). However, the exploration work has been stagnant, and no breakthroughs have been made since the discovery of the L Gas Field at the end of the last century (Cui and Zhao, 2015; Zhong et al., 2018).

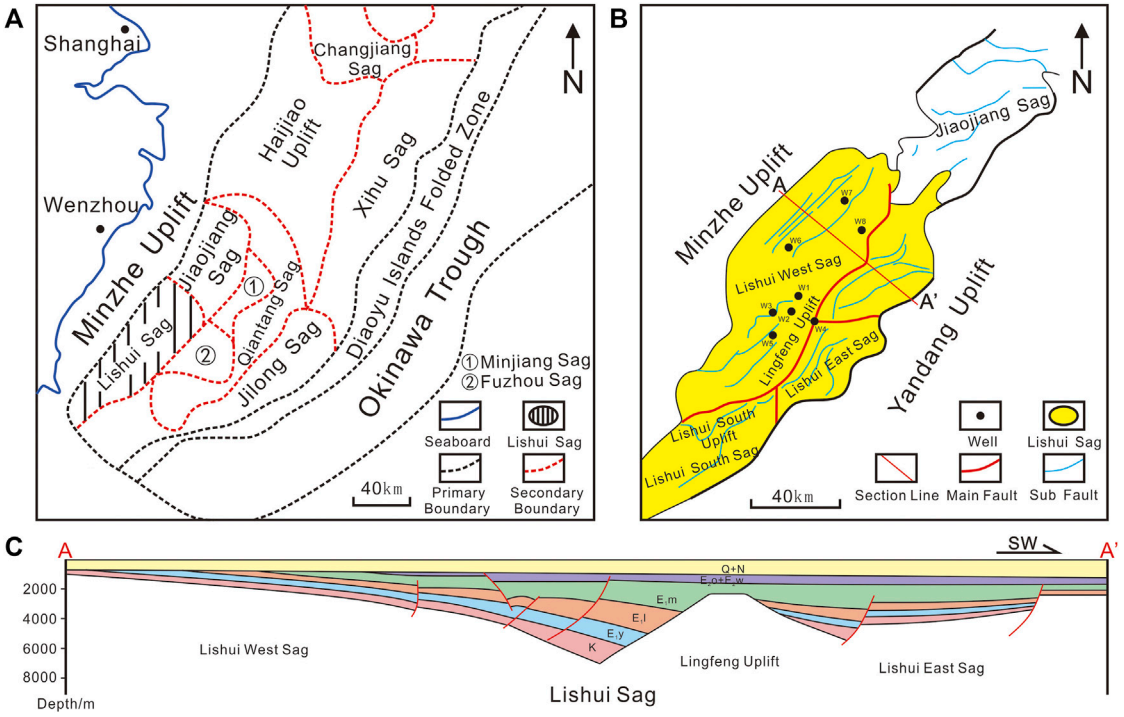

FIGURE 1
Regional geologic setting of the Lishui Sag. **(A)** The Lishui Sag, located in the west–south part of the East China Sea Basin, on the west of the Yandang Uplift, east of the Minzhe Uplift, and south of the Jiaojiang Sag. **(B)** Lishui Sag, containing five tectonic units. The extension causes a series of NE- to NNE-striking normal faults in this area. **(C)** Geological section, showing the basic tectonic features in the Lishui Sag.

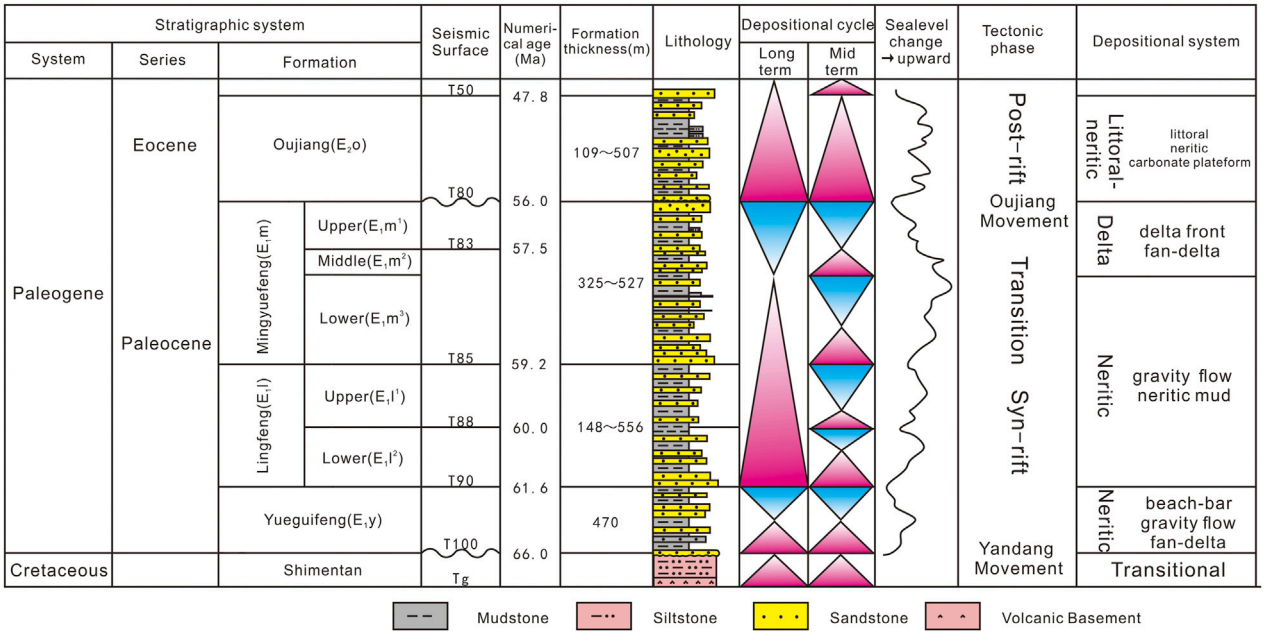

FIGURE 2
Comprehensive histogram of early Paleogene in the Lishui Sag.

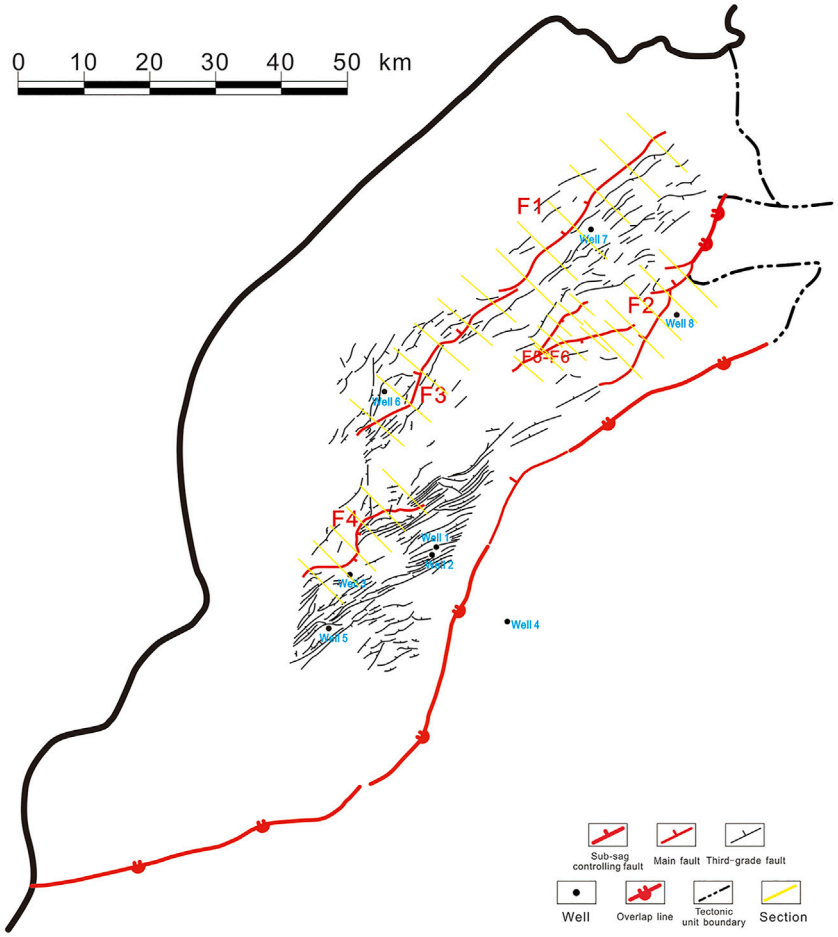

FIGURE 3
Fault system of the T90 reflector in the Lishui West Sag.

Methodology

Fault activity

The seismic data on the Lishui West Sag show that 135 faults developed in the Pliocene strata, including six main faults (Figure 3). There are 26 faults in the north, 23 faults in the middle transfer zone, 33 faults in the southeast area (L block), 25 faults in the south depression zone, and 28 faults in the south slope zone (the western gentle slope zone), and all faults are normal faults.

This study uses the fault activity rate (V) method to calculate the fault activity intensity of all six main faults in the Lishui West Sag. Based on the accuracy of the existing seismic profile interpretation results and the practical demand for Paleocene hydrocarbon research, a series of deposition periods are selected. There are faults F1, F2, F3, F5, and F6 in the northern section, while F4 is in the southern section. We chose K_2s, E_1y, E_1l^2, E_1l^1, E_1m, and E_2o+E_2w formations' deposition period to calculate the fault activity rate in the northern section. In the southern section, we chose K_2s+E_1y, E_1l^2, E_1l^1, E_1m^2+E_1m^3, E_1m^1, and E_2o+E_2w formations' deposition period to calculate the activity rate of fault F4.

Combined with the actual seismic and geological characteristics, the unit of the main fault activity rate in the Lishui West Sag is selected as a meter per million years (m/Ma). Based on the quality of seismic data, six section lines of faults F1, F3, and F4 were selected, and five section lines of faults F2, F5, and F6 were selected (Figure 3). According to the calculation results, we plotted the activity rate curves of six main faults corresponding to the deposition period. We quantitatively described the activity intensity of the main faults in the Lishui West Sag (Figure 4).

What can be seen from the evolution curve of V is that the main active periods of the main faults in the Lishui West Sag are in the range of the Paleocene (the rifting stage). Since the beginning of the Eocene, the intensity of the fault activity has been significantly reduced, while the Oligocene strata are absent in the Lishui West Sag. From Miocene to the Quaternary, the V of

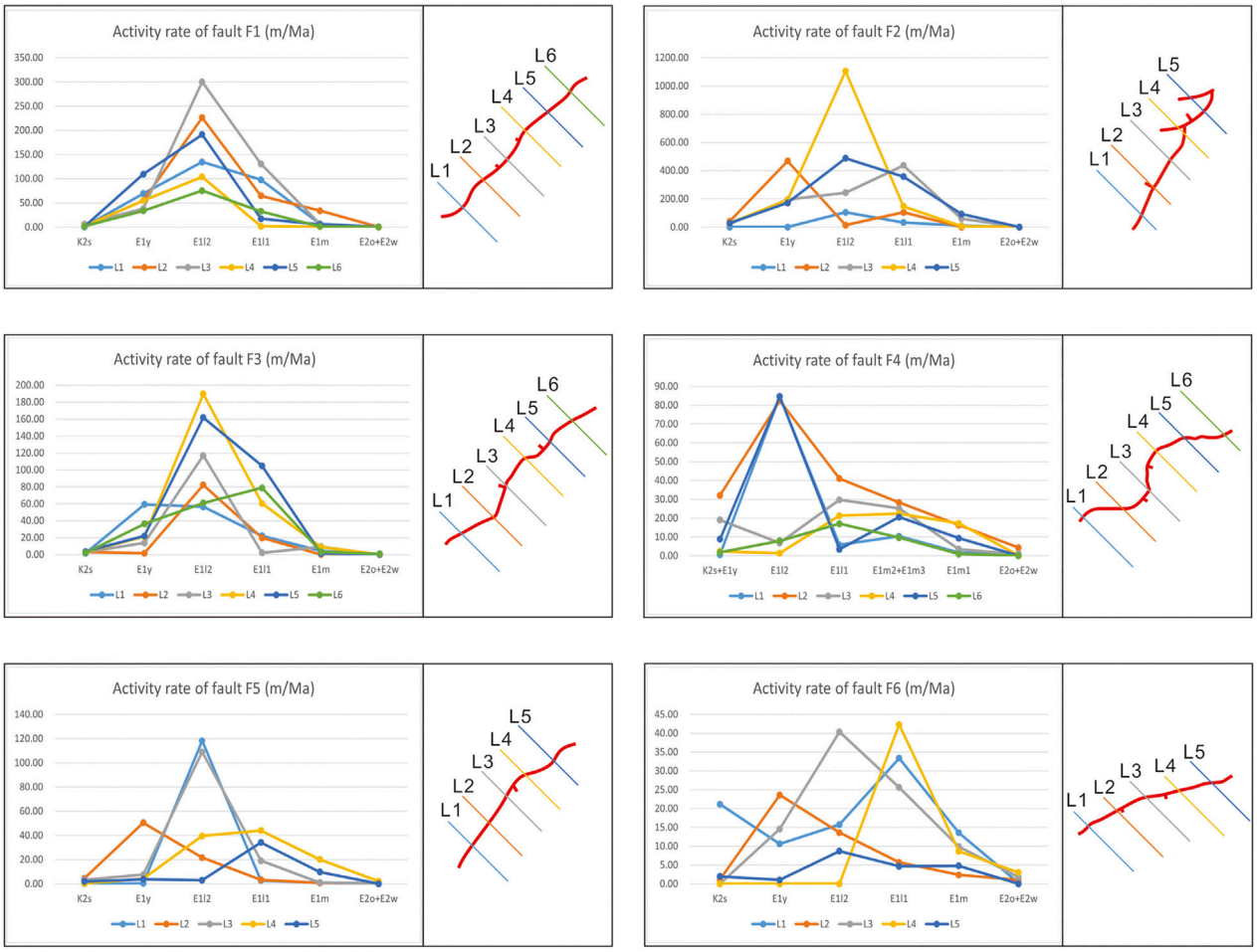

FIGURE 4
V of main boundary faults in the Lishui West Sag.

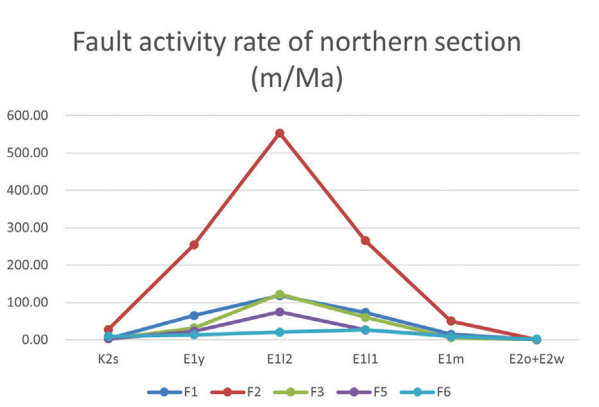

FIGURE 5
RMS V of main boundary faults of the northern section in the Lishui West Sag.

main faults in the Lishui West Sag is almost zero. In other words, the activity of the main faults in the Lishui West Sag stopped at that time.

In order to ensure the accuracy of the data and facilitate the comparison of the difference in the activity intensity of each main fault, the main faults in the southern section and the northern section are respectively processed by the root mean square (RMS) method (Figures 5, 6).

Data processing indicates that the main active period of the main fault in the west sub-depression of the Lishui Sag is from E_1y to E_1l. In the period of E_1l^2, the value of main faults reached the highest. In other words, during the E_1l, the fault rift in the Lishui West Sag reached its climax, meaning the regional tectonic activity in the Lishui West Sag had the most significant impact on terrain development during this period.

Among the value of RMS V in the northern section, we discovered that the V of fault F2 is higher than the others. The reason for this is the syn-deposition of fault F2 and the only sub-sag

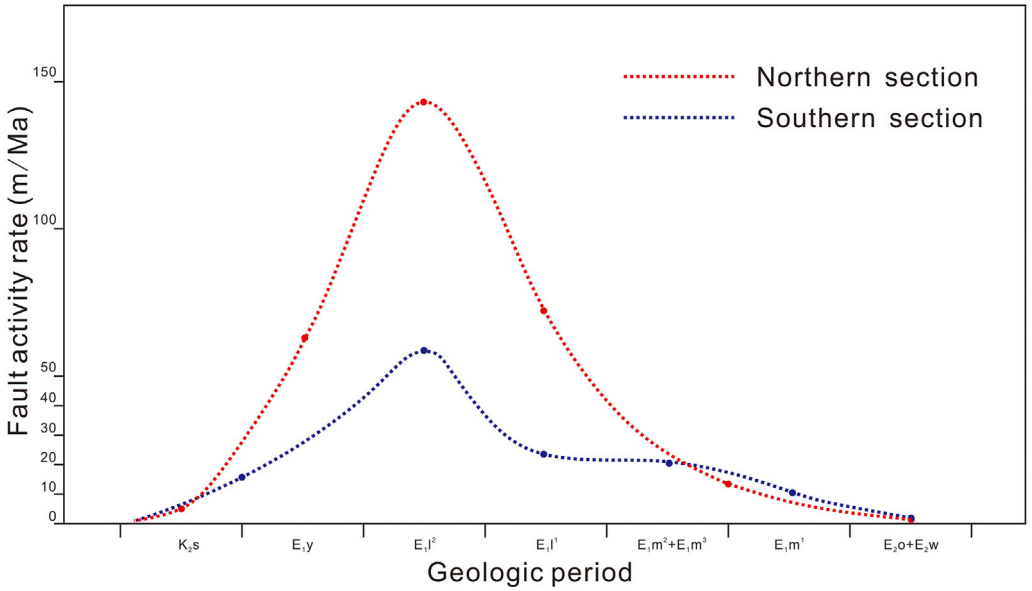

FIGURE 6
RMS V of main boundary faults of northern and southern sections in the Lishui West Sag.

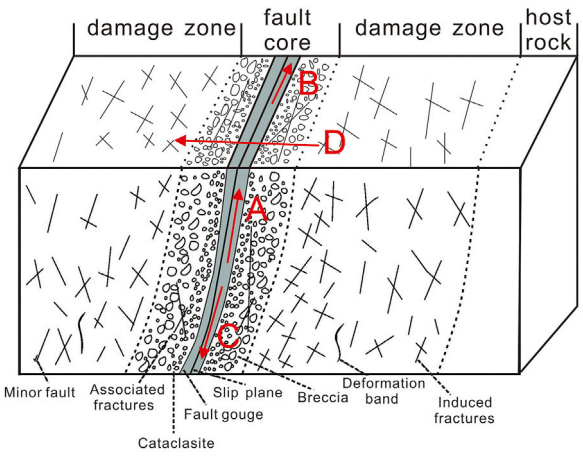

FIGURE 7
Different transporting forms of fault hydrocarbon transportation. **(A)** The vertical upward migration of hydrocarbon along the fault plane. **(B)** The migration of hydrocarbon along the fault strike. **(C)** The vertical downward migration of hydrocarbons along the fault plane. **(D)** The migration of hydrocarbon through the fault plane.

controlling fault in the Lishui West Sag. In the E_1l^2 period, the activity intensity of fault F2 was 26.74 times that of fault F6. Therefore, in the analysis of the active intensity of the main faults in the northern section of the Lishui West Sag, we removed data on fault F2 for statistics to ensure the accuracy of data on the active intensity of the northern main faults. After the removal operation, the activity intensity of the main faults in the northern section was weakened (Figure 6). However, the value of the northern section is still higher than that of the southern section. This shows that in this period, the comprehensive activity intensity of faults in the northern section was more vital than that in the southern section.

Furthermore, we note that the main faults in the southern section still have high activity in the late deposition period of E11, and that the fault activity intensity was further weakened after the transition stage (Figure 6).

Fault hydrocarbon transporting

The forms of hydrocarbon transportation related to faults can be divided into two types; one is along the fault plane (Figures 7A–C), and the other is through the fault plane (Figure 7D). The hydrocarbon transportation which forms along the fault plane can be divided into three types. The most important type is the vertical upward migration of hydrocarbon along the fault plane, which is often accompanied by the diffusion and migration of hydrocarbons across the fault plane on both sides. The second type is the form of hydrocarbon transportation along the fault strike, which has specific requirements for transportation conditions. First, the fault zone should maintain the advantages of transportation. Second, there are fluid potential differences or structural potential differences along the fault strike. The third is the sealing of the cap rock in the upper

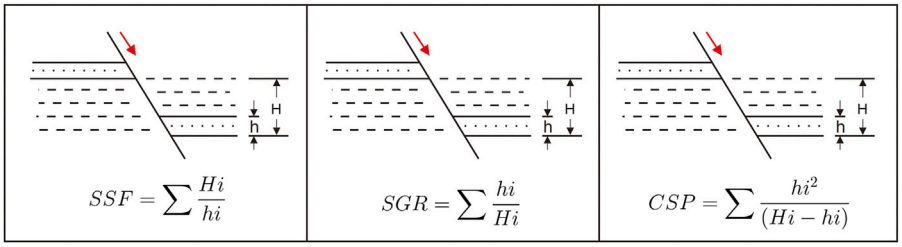

FIGURE 8
Quantitative methods of the shale smear.

part of the fault zone, so vertical upward transportation cannot be realized. The last type is the vertical downward migration of hydrocarbons along the fault plane.

This type of transportation requires that the downward abnormal pressure of the hydrocarbon source rock is much greater than the buoyancy, strata gradient force, and other vertical upward forces (Zha et al., 2002). At present, there are a large number of research examples of this kind of "Reversed Migration" reservoir, such as the Sanzhao Depression in the northern Songliao Basin, which proves the universality of this kind of hydrocarbon transportation form (Fu et al., 2009; Yu, 2021).

Results

Shale smear sealing

Combined with previous studies, we believe that three dimensions affect the fault zone transporting capacity under the cap rock of the Lishui West Sag. The first is the lithology configuration relationship of the fault zone in the Lishui West Sag, that is, the lithology juxtapositional sealing. The second is the influence of the sealing layer on the shale smearing mode in the Lishui West Sag; the third is the pressure-bearing mode of fault rock, that is, the pressure effect of the hydrocarbon-bearing system (Lei et al., 2019).

The caprock of the Lingfeng Formation in the Lishui West Sag is shale. Lindsay et al. (1993) believed that the shale smear factor (SSF) could quantitatively evaluate the sealing property of the caprock (Yielding et al., 2010). At the same time, there are also indicators such as the shale gouge ratio (SGR), shale smear potential (CSP), clay content ratio (CCR), and many other indicators to quantitatively analyze the smear effect of shale caprock (Downey, 1984; Yielding et al., 1997; Yielding et al., 1999; Zhang et al., 2014b) (Figure 8).

Macroscopically, the shale caprock of the Lingfeng Formation in the Lishui West Sag has prominent sectional characteristics: the upper Lingfeng Formation (E_1l^1) is mainly thick shale; the lower Lingfeng Formation (E_1l^2) shows the characteristics of multi-group thin sediment stack and sand-mud interbeds in the vertical sedimentary sequence. Liu and Li (2015), through physical simulation, found that the number of shale layers in the caprock has a significant influence on the deformation characteristics of shale. When the thickness of shale and sandstone is uniform, there are more layers of shale, and the smearing effect of the shale appears to be worse. For single-layer shales, the greater the thickness and depth of the shale, the stronger the smearing effect appears (Lyu et al., 2000).

Based on existing data on the study area, this study calculates the main characterization parameters related to the shale sealing of the main faults (Table 1). The rock lithology and thickness of the four main faults F1–F4 (F5 and F6 data missing) from the lower Lingfeng Formation to the Mingyuefeng Formation are clarified and statistically analyzed combined with logging data.

Fault lateral sealing

When the fault is in the active stage, the lateral hydrocarbon transport of the fault zone is not apparent. When the fault is in a relatively static stage, the lateral hydrocarbon transportation of the fault zone depends mainly on the juxtapositional sealing of lithology. The lithology juxtapositional sealing rate(e)of a specific stratum is equal to the ratio of the total thickness of unconnected sandstone to the total thickness of sandstone. The e value is negatively correlated with the hydrocarbon transportation effect, but it is challenging to carry out practical statistics in exploration and development practice (Figure 9).

We collected the published data on the sand ratio and lithology juxtapositional sealing rate in Daqing, Liaohe, and many other oilfields (Table 2). These data show a specific relationship between the sand ratio and the lithology juxtapositional sealing rate, so we use the mathematical method to fit the formula (Lyu et al., 1996).

Based on the collected data, we fitted and obtained the empirical formula of the lithology juxtapositional sealing rate:

$$e = -38.79\,ln(\sigma) + 5.4405.$$

In this formula, e denotes the lithology juxtapositional sealing rate, dimensionless, and σ denotes the formation sand ratio, dimensionless. R^2=0.7076 after fitting the formula shows a

TABLE 1 Shale smear of main faults in the Lishui West Sag.

Fault	Formation	Strata thickness(m)	Shale layer	SSF	SGR	CSP	Remark
F1	E1m	695	68	5.29	0.19	0.23	
	E1l1	409	44	5.35	0.19	0.23	
	E1l2	427.8	50	5.98	0.17	0.20	
F2	E1m	442	60	3.52	0.28	0.40	
	E1l1	165	30	1.74	0.58	1.36	
	E1l2	*					No data
F3	E1m	437	28	2.08	0.48	0.92	
	E1l1	259	23	3.42	0.29	0.41	
	E1l2	384	40	2.50	0.40	0.67	
F4	E1m	951	73	3.01	0.33	0.50	
	E1l1	267	20	5.40	0.19	0.23	
	E1l2	*					No data

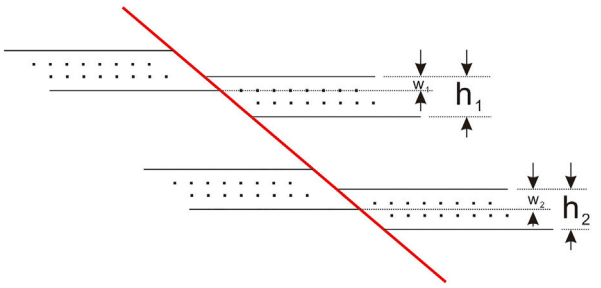

FIGURE 9
Definition of the lithology juxtapositional sealing rate (e). $e = \sum \frac{hi-wi}{hi}$.

TABLE 2 Published data on similar basins in East China.

No.	Facies	Sand ratio	e (%)
1	Fluvial	0.205	48.1
2	Fluvial	0.185	73.2
3	Fluvial	0.105	91.5
4	Fluvial	0.165	85.4
5	Delta	0.49	26.6
6	Delta	0.28	49.3
7	Fluvial	0.33	72
8	Delta	0.385	38.8

corresponding good relationship. Therefore, we can use this method to connect the sand ratio with the connectivity efficiency to deduce the approximate effect of the lateral sealing of the fault and approximately describe the lateral sealing of the fault according to the characteristics of the insufficient data on the Lishui West Sag.

TABLE 3 Lithology juxtapositional sealing rate (e) of main faults in the Lishui West Sag.

Fault	Formation	Depth(m)	Sand ratio	e (%)
F1	E_1m	2,936	0.19	69.86
	E_1l^1	3,345	0.19	69.86
	E_1l^2	3,772.8	0.17	74.17
F2	E_1m	2,761	0.28	54.82
	E_1l^1	2,926	0.58	26.57
	E_1l^2	*		No data
F3	E_1m	1761	0.48	33.91
	E_1l^1	2020	0.29	53.46
	E_1l^2	2,404	0.40	40.98
F4	E_1m	2,641	0.33	48.45
	E_1l^1	2,908	0.19	69.86
	E_1l^2	*		No data

Based on the empirical formula of the lithology juxtapositional sealing rate, we calculated the lateral fault sealing of faults F1–F4, and the results are shown in Table 3:

Fault vertical sealing

The vertical sealing of the fault is mainly indirectly controlled by the fault plane's normal pressure. Furthermore, the fault plane normal pressure directly controls the diagenetic degree of the fractured fragments, such as the fault rock on the fault plane. Ultimately, the diagenetic degree of fractured fragments directly determines the displacement pressure. Therefore, the displacement pressure (Pd) at the fault plane can be used to quantitatively characterize the vertical sealing of the fault. The greater the fault displacement pressure, the worse the vertical fault sealing (Lyu et al., 2007).

Zhang et al. (2014b) came up with the concept of the vertical shale smear evaluation parameter (Q) of the main faults in 2014.

With this parameter, we can quantitatively evaluate the vertical sealing of growing faults. The relationship between the vertical shale smear coefficient (Q) and the shale gouge ratio (SGR) is expressed as follows:

$$Q = \frac{P_1}{P_1 - P_2} \times SGR.$$

In this formula, P_1 is the fault plane normal pressure, MPa; P_2 is the fracture pressure of shale, MPa; SGR is the shale gouge ratio, dimensionless; and Q is the vertical shale smear coefficient, dimensionless.

In this formula, the greater the fault plane normal pressure, the greater the vertical shale smear coefficient Q, and the stronger the vertical fault sealing. The more significant the difference between the fault plane normal pressure and the fracture pressure of shale, the weaker the smearing ability of the shale, and the weaker the vertical sealing of the fault.

According to the obtained SRG of the main faults in the Lishui West Sag (Table 1), we calculate the fracture pressure of the shale by Eaton's method (Eaton, 1969), and the calculation expression is as follows:

$$P_2 = G_f \times D = \left[\frac{\nu}{1-\nu}(G_b - G) + G\right] \times D.$$

In this formula, P_2 is the fracture pressure of the shale, MPa; G_f is the fracture pressure gradient of the shale, MPa/m; D is the depth, m; ν is the Poisson ratio, dimensionless; G_b is the pressure gradient of overlying strata, MPa/m; and G is the pore fluid pressure gradient of strata, MPa/m.

Based on previous research studies (Fu et al., 2003; Lyu et al., 2007; Lyu and Wang, 2010; Tan et al., 2018; Li et al., 2020), we conclude that the fault plane's normal pressure is the component of the strata on the fault plane, indicating that the fault plane normal pressure of the main faults in the Lishui West Sag is

$$P_1 = 0.009876(\rho - \rho_w)\cos\theta D.$$

In this formula, P_1 is the fault plane's normal pressure, MPa; ρ is the average density of overlying strata, g/cm^3; ρ_w is the density of strata water, g/cm^2; θ is the dip of the fault plane; and D is the breaking point depth, m.

By referring to the related parameters of similar faults in adjacent areas (Xiang, 2008; Xie et al., 2021; Zhao et al., 2021; He et al., 2022), aiming at the fault development in the Lishui West Sag, we assigned a Poisson ratio of 2.0. We used the hydrostatic column pressure gradient instead of the pore fluid pressure gradient, G=0.0107 MPa/m; and the average pressure gradient instead of the overlaying pressure gradient, Gb =0.0231 MPa/m. Through conversion, the average density of overlaying formation can be obtained as 2.357 g/cm^3. The density of strata water of the Lishui West Sag is 1.092 g/cm^3.

The fracture pressure of the shale of the main faults F1–F4 in the Lishui West Sag is calculated by referring to the aforementioned formula and index parameters. Because the fault plane normal pressure is not equal everywhere, to keep the relative rationality of the results and the value of the relative consistency, the fault dip angle was calculated using the average dip angle of the selected sections of the main faults in this study. Based on the horizontal–vertical proportional relationship of the profile, we increased the proportional coefficient r = 2.2 to correct the data results.

According to the calculation results of P1, P2, and SGR, we further calculated the vertical shale smear evaluation parameter (Q) of the main faults F1–F4 in the Lishui West Sag. The calculation results are shown in Table 4:

TABLE 4 Vertical shale smear evaluation parameter (Q) of the main faults in the Lishui West Sag.

Fault	Formation	P_1 (MPa)	P_2 (MPa)	SGR	Q
F1	E_1m	53.08	40.52	0.19	0.25
	E_1l^1	63.72	46.16	0.19	0.26
	E_1l^2	56.03	52.06	0.17	0.18
F2	E_1m	61.93	38.10	0.28	0.46
	E_1l^1	72.67	40.38	0.58	1.04
	E_1l^2	*			No data
F3	E_1m	49.51	24.30	0.48	0.98
	E_1l^1	50.90	27.88	0.29	0.53
	E_1l^2	60.57	33.18	0.40	0.73
F4	E_1m	60.05	36.45	0.33	0.55
	E_1l^1	69.55	40.13	0.19	0.32
	E_1l^2	*			No data

Discussion

Shale smear sealing

From the calculation results in Table 1, it can be concluded that the layer number of shale strata in E_1l^1 of each main fault is relatively tiny. However, the thickness is relatively large, indicating that the sealing ability is better than the overlying strata. This shows that the smearing effect of the shale caprock in E_1l^1 is strong and the sealing effect of hydrocarbon transportation is better in E_1l^1. The abnormal characteristics of fault F2 may be due to the lack of data collection of E_1l^2 and part of E_1l^1. Other possible reasons are that fault F2 is located in the steep slope zone, the geological structure is relatively complex, and the mutation is strongly correlated.

Fault lateral sealing

From the data analyses in Table 3, it can be concluded that among all the main faults, the lateral sealing of the main fault

F1 is the best, followed by F4 and F3. In the E_1l period, the lateral sealing of fault F2 was the worst, which reflected that F2 was an extension fault of the regional control fault to some extent. During the E_1l period, the scale of the activity intensity of F2 was significantly stronger than that of other main faults, which was extraordinary.

In the longitudinal time series, the lateral sealing of the E_1l period of faults F1, F3, and F4 is stronger than that of the E_1m period, indicating the critical influence of lithology difference on the lateral sealing of faults. This is typical in the longitudinal comparison of fault F3. Large sets of thick shale developed in the E_1l^1 period of fault F3 and its lateral sealing property is better than that of the underlying E_1l^2 and the overlying E_1m.

We also note that fault F1 in the E_1l period has no apparent advantage in the lateral sealing of E_1m. The lateral sealing of fault F2 in the E_1l period is worse than that of the E_1m period. These phenomena, to some extent, reflect the weakening effect of the fault activity intensity on fault lateral sealing during this period. Based on this assumption, we can reasonably explain why the fault activity intensity of fault F2 in the E_1l period is significantly stronger than that of fault F1 and other faults. The lateral sealing of the main faults in the Lishui West Sag is ranked as F1 > F4 > F2 > F3.

Fault vertical sealing

The results in Table 4 show that the Q of the main faults in the Lishui West Sag is almost less than 1.0. The maximum value appears at 1.04 of E_1l^1 on fault F2, and the minimum value appears at 0.1 of E_1l^2 on fault F1. It indicates that the vertical sealing of the fault is not strong in general and has relatively good vertical hydrocarbon transportation capacity. The main faults are the possible dominant channels for hydrocarbon migration.

From the point of view of the time series, the vertical sealing of the E_1m period is better than that of the E_1l period, reflecting a more vital tectonic activity of the E_1l. The open faults are conducive to hydrocarbon transportation and migration at that time. From the perspective of spatial distribution, the vertical sealing property of fault F3 near the structural transfer zone of the Lishui West Sag is relatively good, while the vertical sealing of fault F1 in the western slope zone of the northern section is the worst. The overall vertical sealing property of the main faults in the Lishui West Sag is in the order of F3 > F2 > F4 > F1 from good to poor, which is precisely the opposite of the lateral sealing property of the main faults.

Conclusions

(1) Through the calculation of the relevant parameters of shale smear, our findings indicate that the shale caprock of the Lingfeng Formation in the Lishui West Sag has a strong smear effect and that the sealing effect of hydrocarbon transportation is better, which is helpful for the occurrence of hydrocarbons in the Lishui West Sag.

(2) The sealing ability of the main fault in the Lishui West Sag was quantitatively calculated. The shale filling of the fault helps enhance the lateral sealing ability of the fault, and the activity of the fault will weaken the lateral sealing ability of the fault. The activity intensity of the fault has a positive control effect on the vertical sealing ability of the fault, and the shale filling of the fault can weaken the influence of the fault activity intensity.

(3) The vertical sealing order and the lateral sealing order of the main faults in the Lishui West Sag are precisely the opposite, indicating that there is a specific negative correlation between the vertical sealing ability dominated by the fault activity intensity and the lateral sealing ability dominated by the fault shale filling, and the relationship between them needs to be further explored.

Data availability statement

The original contributions presented in the study are included in the article/supplementary material; further inquiries can be directed to the corresponding author.

Author contributions

BY processed data and wrote the manuscript. QF, JL, and WM provided funding and helped with the conception of the idea. BY compiled the data, drew plots, and edited the manuscript. SZ contributed to the conception, and reviewed and edited the manuscript. QF contributed to data processing and participated in discussion. QF reviewed and edited the manuscript.

Funding

This work is supported by the CNOOC seven-year action plan project (Grant No. CCL2020SHPS023RSI).

Conflict of interest

Authors JL and WM are employed by the Shanghai Branch Company of CNOOC (China) Ltd.

The remaining authors declare that the research was conducted in the absence of any commercial or financial relationships that could be construed as a potential conflict of interest.

Publisher's note

References

Allan, U. S. (1989). Model for hydrocarbon migration and entrapment within faulted structures[J]. *AAPG Bull.* 73 (07), 803–811.

Bouvier, J., Kaars-Sijpesteijn, C., Kluesner, D., Onyejekwe, C., and Van Der Pal, R. (1989). Three-dimensional seismic interpretation and fault sealing investigations, Nun River Field, Nigeria[J]. *AAPG Bull.* 73 (11), 1397–1414. doi:10.1306/44B4AA5A-170A-11D7-8645000102C1865D

Bretan, P., Yielding, G., and Jones, H. (2003). Using calibrated shale gouge ratio to estimate hydrocarbon column heights. *Am. Assoc. Pet. Geol. Bull.* 87 (03), 397–413. doi:10.1306/08010201128

Cui, M., and Zhao, Z. (2015). Constraint analysis of Lishui sag hydrocarbon accumulation in donghai basin[J]. *Special Oil Gas Reservoirs* 22 (02), 18–21+151.

Downey, M. W. (1984). Evaluating seals for hydrocarbon accumulations[J]. *AAPG Bull.* 68 (11), 1752–1763.

Eaton, B. A. (1969). Fracture gradient prediction and its application in oilfield operations. *J. petroleum Technol.* 21 (10), 1353–1360. doi:10.2118/2163-pa

Engelder, J. T. (1974). Cataclasis and the generation of fault gouge. *Geol. Soc. Am. Bull.* 85 (10), 1515–1522. doi:10.1130/0016-7606(1974)85<1515:catgof>2.0.co;2

Fu, G., Lyu, Y., Ma, F., and Fu, X. (2003). Comprehensive evaluation method for vertical sealing of fault and its application[J]. *Xinjiang Pet. Geol.* (05), 451–454.

Fu, X., Ping, G., Fan, R., and Liu, Z. (2009). Research on migration and accumulation mechanism of hydrocarbon "reversed migration" in fuyu and yangdachengzi Formation in Sanzhao depression[J]. *Acta Sedimentol. Sin.* 27 (03), 558–566.

Ge, H., Gao, S., Zhou, P., and Diao, H. (2019). Fault structural characteristics and its petroleum geological significance of Lishui sag in donghai basin[J]. *Adv. Geosciences* 9 (11), 1025–1035.

He, J., La Croix, A. D., Gonzalez, S., Pearce, J., Ding, W., Underschultz, J. R., et al. (2021). Quantifying and modelling the effects of pre-existing basement faults on folding of overlying strata in the Surat Basin, Australia: Implications for fault seal potential. *J. Petroleum Sci. Eng.* 198, 108207. doi:10.1016/j.petrol.2020.108207

He, Y., Zheng, J., and Zhang, M. (2022). Calculation method and application of formation fracture pressure in Baiyun deepwater area[J]. *Mar. Geol. Front.* 38 (05), 41–50.

Jiang, Z., Ming, Y., and Yao, G. (2019). Study on fault division of Lishui sag in East China Sea basin[J]. *Prog. Geophys.* 34 (01), 310–315.

Lei, Z., Xu, H., Liu, Q., Li, W., Yan, D., Li, S., et al. (2019). The influence of multiple-stage oil emplacement on deeply buried marine sandstone diagenesis: A case study on the devonian donghe sandstones, tabei Uplift, tarim basin, NW China. *Mar. Petroleum Geol.* 110 (C), 299–316. doi:10.1016/j.marpetgeo.2019.07.030

Li, H., Wu, J., Huang, J., Wang, Y., and Li, Z. (2020). Quantitative analysis of fault vertical sealing ability and its application in an oil field of Bohai Bay Basin[J]. *Bull. Geol. Sci. Technol.* 39 (04), 125–131.

Lindsay, N., Murphy, F., Walsh, J., and Watterson, J. (1993). Outcrop studies of shale smears on fault surfaces[J]. *Geol. Model. hydrocarbon reservoirs outcrop analogues* 15, 113–123.

Liu, X., and Li, H. (2015). Physical simulation of clay layer effect on clay smear and evolution [J]. *Fault-Block Oil and Gas Field.* 22 (06), 722–728. doi:10.6056/dkyqt201506009

Lyu, Y., Huang, J., Fu, G., and Fu, X. (2009). Quantitative study on fault sealing ability in sandstone and mudstone thin interbed[J]. *Acta Pet. Sin.* 30 (06), 824–829.

Lyu, Y., Li, G., Wang, Y., and Song, G. (1996). Quantitative analyses in fault sealing properties[J]. *Acta Pet. Sin.* (03), 39–45.

Lyu, Y., Sha, Z., Fu, X., and Fu, G. (2007). Quantitative evaluation method for fault vertical sealing ability and its application[J]. *Acta Pet. Sin.* (05), 34–38.

Lyu, Y., and Wang, S. (2010). Quantitative evaluation of fault seal[J]. *J. Northeast Petroleum Univ.* 34 (05), 35–41+166.

Lyu, Y., Zhang, S., and Wang, Y. (2000). Research of quantitative relations between sealing ability and thickness of cap rock[J]. *Acta Pet. Sin.* (02), 27–30+4.

Ma, G., Ming, Y., and Huang, D. (2018). Distribution characteristics study of cenozoic basement of lishui-jiaojiang sag based on gravity and magnetic anomalies [J]. *J. Jilin University(Earth Sci. Edition)* 48 (05), 1493–1500.

Peng, X., Deng, H., He, J., Chen, H., and Zhang, Y. (2021). Research on the evolution and damage mechanism of normal fault based on physical simulation experiments and Particle image Velocimetry technique. *Energies* 14 (10), 2825. doi:10.3390/en14102825

Smith, D. A. (1980). Sealing and nonsealing faults in Louisiana Gulf Coast salt basin[J]. *AAPG Bull.* 64 (02), 145–172.

Smith, D. A. (1966). Theoretical considerations of sealing and non-sealing faults [J]. *AAPG Bull.* 50 (02), 363–374.

Tan, L., Xie, H., Zhang, H., Zhao, J., and Guo, Y. (2018). A quantitative research method on the sealing of growth faults: A case study of JX1-1 oil field in liaozhong sag, Liaohe depression[J]. *Petroleum Geol. Exp.* 40 (02), 268–273.

Wang, J., La Croix, A. D., Gonzalez, S., He, J., and Underschultz, J. (2019). Sequence stratigraphic analysis of the lower jurassic precipice sandstone and evergreen Formation in the Surat Basin, Australia: Implications for the architecture of reservoirs and seals for CO_2 storage[J]. *Mar. Petroleum Geol.* 102, 829–843. doi:10.1016/j.marpetgeo.2019.01.038

Wang, Y., Jiang, L., and Yang, W. (2000). Kinematical analysis on faults in the Lishui Jiaojiang sag[J]. *Sci. Geol. Sin.* (04), 441–448.

Weber, K., Mandl, G., Pilaar, W., Lehner, F., Precious, R., et al. (1978). "The role of faults in hydrocarbon migration and trapping in Nigerian growth fault structures [C]," in Offshore Technology Conference. doi:10.4043/3356-ms

Xiang, L. (2008). Quantitatively analyze the main controlling factors of mudstone fracture in Jiyang Depression[J]. *Petroleum Geol. Recovery Effic.* (05), 31–33+37+113.

Xie, J., Wu, H., Lou, Y., and Zhai, Y. (2021). Fracture pressure prediction model of high temperature and high-pressure formation in deep water area of the South China Sea[J]. *Fault-Block Oil Gas Field* 28 (03), 378–382.

Yang, W., and Wang, Y. (2002). The analysis of the basin's extension in the Lishui Jiaojiang Sag[J]. *J. Southwest Petroleum Inst.* (03), 8–10+5.

Yielding, G., Bretan, P., and Freeman, B. (2010). fault seal calibration: A brief review. *Geol. Soc. Lond. Spec. Publ.* 347 (01), 243–255. doi:10.1144/sp347.14

Yielding, G., Freeman, B., and Needham, D. T. (1997). Quantitative fault seal prediction[J]. *AAPG Bull.* 81 (06), 897–917.

Yielding, G., Øverland, J., and Byberg, G. (1999). Characterization of fault zones for reservoir modeling: An example from the Gullfaks field, northern North Sea[J]. *AAPG Bull.* 83 (06), 925–951.

Yu, Y. (2021). Predicting method of migration and accumulation space of the hydrocarbon reversed in upper source-lower reservoir combination and its application[J]. *Petroleum Geol. Oilfield Dev. Daqing* 40 (06), 44–51.

Zha, M., Qu, J., and Zhang, W. (2002). The relationship between overpressure and reservoir forming mechanism[J]. *Petroleum Explor. Dev.* (01), 19–23.

Zhang, T., Zhang, J., Zhang, S., Yu, Y., Tang, X., et al. (2014). An application of the balanced cross-section technique: The tectonic evolution of Lishui sag, the east China Sea Shelf basin[J]. *Shanghai Land & Resour.* 35 (01), 92–96.

Zhang, W., Zhang, W., and Zhang, Q. (2014). An improved method of shale smear evaluation[J]. *Xinjiang Oil Gas* 10 (01), 19–22+4.

Zhao, L., Liu, J., Yao, Y., Zhong, K., Ma, J., Zou, C., et al. (2021). Quantitative seismic characterization of source rocks in lacustrine depositional setting using the Random Forest method: An example from the Changjiang sag in East China Sea basin[J]. *Chin. J. Geophys.* 64 (02), 700–715.

Zhong, K., Zhu, W., Gao, S., and Fu, X. (2018). Key geological questions of the formation and evolution and hydrocarbon accumulation of the east China Sea Shelf basin[J]. *Earth Sci.* 43 (10), 3485–3497.

frontiers | Frontiers in Earth Science

TYPE Original Research
PUBLISHED 12 January 2023
DOI 10.3389/feart.2022.1024357

OPEN ACCESS

EDITED BY
Jianhua Zhao,
China University of Petroleum, China

REVIEWED BY
Li Tian,
China University of Geosciences Wuhan, China
Shipeng Huang,
Research Institute of Petroleum Exploration and Development (RIPED), China

*CORRESPONDENCE
Xiaodong Guan,
guanxd@sinopec.com

SPECIALTY SECTION
This article was submitted to Geochemistry, a section of the journal Frontiers in Earth Science

RECEIVED 21 August 2022
ACCEPTED 31 October 2022
PUBLISHED 12 January 2023

CITATION
Wang L, Guan X, Wang J, Sun Z and Xu H (2023), Characteristics and controlling factors of the Upper Permian Dalong Formation in northwestern Sichuan Basin, China.
Front. Earth Sci. 10:1024357.
doi: 10.3389/feart.2022.1024357

Characteristics and controlling factors of the Upper Permian Dalong Formation in northwestern Sichuan Basin, China

Lu Wang[1,2], Xiaodong Guan[3]*, Jianyong Wang[4], Zuoyu Sun[1] and Huiyuan Xu[2]

[1]School of Earth and Space Sciences, Peking University, Beijing, China, [2]State Key Laboratory of Shale Oil and Gas Enrichment Mechanisms and Effective Development, Beijing, China, [3]Department of science and Technology Development, Sinopec, Beijing, China, [4]Department of Oilfield Exploration and Production, Sinopec, Beijing, China

It has been generally accepted that the Permian shale is an important target for shale oil and gas exploration. In order to precisely predict the distribution of potential excellent source rocks of shale oil and gas, it is necessary to reveal the forming process and mechanism of high-quality source rocks, such as the Dalong Formation in the Scihuan Basin. In this study, 17 samples were collected from the Dalong Formation in Longfeng Quarry, Northwest Guangyuan City, Sichuan Province. The lithofacies, organic geochemistry, and pyrolysis of these samples were analyzed to evaluate the main factors controllingthe source rock formation. In particular, the influences of hydrothermal and paleoenvironmental conditions on the accumulation of organic matter were analyzed. The total organic carbon (TOC) content of the samples, which ranges from 0.05% to 12.21%, is closely related to the lithology. High TOC has been generally observed in rock intervals developed in a deep-water sedimentary environment, including siliceous rock, dark shale, and siliceous shale. The peak pyrolysis temperature of the samples ranges from 444°C to 462°C, indicating a mature stage. Thin-section observation, combined with the results of previous studies, has confirmed that the source of the organic matter is mainly marine phytoplankton, such as algae and radiolarians, ostracods, and other marine organisms, which consist of these high-quality source rocks. The ratio of trace elements, such as Ni/Co, V/Cr, U/Th, and V/(V + Ni) indicate that high-quality source rocks are mainly formed in anoxic restricted environments. The hydrothermal activity of submarine volcanoes provided many nutrients and compounds, resulting biological prosperity and improving primary productivity. This is simultaneously conducive to the formation of anoxic environments and the preservation of organic matter.

KEYWORDS

sichuan basin, paleoenvironment, trace elements, hydrocarbon source rocks, hydrothermal effects, organic-inorganic interaction

1 Introduction

Shale gas is an important unconventional natural gas, and its commercial production in some countries has attracted worldwide attention. The United States describes shale gas revolution as "a revolution that can change the world's energy pattern" (Curtis and Montgomery, 2002; Bowker, 2007). Since the commencement of shale gas revolution in the United States in 2010, China's fundamental research and industrial development of shale gas have been developing gradually; and many sets of organic-rich black shales have been developed in China (Nie et al., 2011; Zou et al., 2016; Mei et al., 2022). According to many predictions from different institutes, shale gas resources amount up to 83.3–134.4 × 10^{12} m^3, and of which 10.0–36.1 × 10^{12} m^3 are economical recoverable in China.

Recently, the drilling depth of oil and gas exploration in the northern Sichuan Basin has reached 7000 m, and confirmed that the Dalong Formation has a huge oil and gas potential (Dong et al., 2015). Previous studies conducted on the Dalong Formation found that the total organic carbon (TOC) was very high, and silicalite and mudstone in the Dalong Formation contained good types of organic matter, making it a set of high-quality marine source rocks (Chen et al., 2012; Shao et al., 2016; Liu et al., 2017; Peng et al., 2021; Xiao et al., 2021).

Previous studies have also evaluated the distribution characteristics of organic matter and its hydrocarbon generation potential of the Dalong Formation (Guo et al., 2016; Qiao et al., 2016; Dai et al., 2018; Li et al., 2019). However, the preservation and rock formation conditions are poorly understood (Xia et al., 2010; Yin et al., 2012; Yin and Song, 2013; Wei et al., 2018a; Wei et al., 2018b). To this end, this study conducted petrographic, organic geochemical, and pyrolysis analyses on the Dalong Formation samples collected from the Longfeng Quarry in Northwest Township, Guangyuan, the Sichuan Basin. The controlling factors on the forming of the Dalong Formation to be source rock, particularly the influence of hydrothermal action and paleosedimentary environment on the accumulation of organic matter, were investigated.

2 Geological background

Located in northwest of the Yangtze Platform, the large sedimentary Sichuan Basin covers a rhombic-shaped area of approximately18 × 10^4 km^2 (Figure 1A). Surrounded by high mountains, the basin is divided into three major districts. The east one is a low mountain with an altitude of 250–1000 m, the west one is a plain, and the middle one is a hill with an altitude of −250–750 m (Mingyi et al., 2012; Wei et al., 2018a). The Sichuan Basin, as an extremely important onshore gas-producing area in China, has been affected by multiperiod, superimposed structural changes since the Sinian Period. During the Sinian, the Sichuan Basin was a large-scale depression, into which a thick purple-red sandstone shale was deposited during the Mesozoic (Xie et al., 2007; Yin et al., 2012; Xie et al., 2017), making an overlying thick marine Sinian-Middle Triassic interval up to −3000–6000 m. Main sedimentary interval in the Sichuan Basin, of which neritic carbonate platforms are dominant, with marine and continental interfacies containing coal measures and terrigenous clasts (Jin et al., 2000; Liu et al., 2018; Liu et al., 2019a). The source rocks, which are widely distributed organic-rich shale, were developed in the main strata and considered to be the source of natural gas in many large- and medium-sized gas fields in Permian-to Triassic-aged strata.

The Guangyuan area within the study area is located at the intersection of the Dabashan fold belt and the Longmenshan fault belt (Figure 1B). The Changxing, Dalong, and Feixianguan Formations are successive deposits on the profile taken in the Longfeng Quarry, Northwest Township, Guangyuan. Observation of the field outcrop indicates that there is a −5-m-thick light-gray limestone containing layered flint nodules in the Permian Changxing Formation underlying the Dalong Formation, and in whose upper part there is a −50-cm-thick light-gray layered flint-nodule limestone.

The lower part of the Dalong Formation (Figure 2A) is composed of, from the bottom to the top, thick-layered gray-black siliceous rock; thin-layered gray-white volcanic ash; thin-layered gray-black siliceous rock; thin-layered gray-black siliceous rock with lamellar siliceous shale; middle-layered siliceous limestone; thin-layered gray-black platy siliceous shale; middle-layered dark-gray siliceous limestone with interbeds of thin-layered gray-black siliceous shale; thick-layered light-gray limestone; and middle-layered gray-black siliceous with thin-layered siliceous shale.

The middle part of the Dalong Formation (Figure 2B) is composed of, from the bottom to the top, thin-layered gray-black siliceous shale; middle-layered light-gray limestone whose top and bottom are gray-black siliceous rock interbedded with thin siliceous shale; thin-layered gray-white tuff; gray-black medium-to thin-layered siliceous rock with thin-layered gray-white volcanic ash 0.7 m from the bottom; middle-layered gray-black siliceous limestone; thin-layered gray-black siliceous rock containing asphalt; middle-layered gray-black siliceous rock; thin-layered gray-black siliceous rock; and middle-layered gray-black siliceous rock with bituminous at the top; middle-layered gray-black siliceous shale sandwiched with a limestone 2.0 × 0.8 m lens (Figure 2C); medium-to thin-layered gray-black siliceous rock containing numerous ammonite fossils up to a maximum diameter of 8 cm and containing asphalt.

The upper part of the Dalong Formation (Figure 2D) is composed of middle-layered dark-gray siliceous limestone interlayered with layered siliceous limestone and thin (3 cm) volcanic ash (the siliceous limestone becomes thick upward); middle-layered gray-white limestone and thin-layered dark-gray siliceous limestone interbeds with thin siliceous shale containing

double-shell fossils; thin-layered light-yellow tuff whose surface is weathered to gray-white and blue-gray middle-layered nodular argillaceous limestone with purple tumor-like protrusion on the surface, and numerous ammonite fossils. The Feixianguan Formation, located near the Dalong Formation, contains light-gray middle tuff intercalated with carbonate nodules in an upward sequence. The surface of the nodules is oxidized to purple-red, and the middle-thin blue-gray nodular limestone is intercalated with middle light-gray (30 cm thick) limestone. The surface is fractured and contains limestone concretions, light-gray middle-thick lamellar marl, and light-gray middle-thick limestone.

Various types of biota were observed in the Dalong Formation, including algae, calcispheres, ostracods, gastropods, foraminifera, crinoids, ammonites, brachiopods, radiolarians, and conodonts (Xie et al., 2017). Few flints occur in layered siliceous rocks. In addition to pyrite, fossilized foraminifera, phytoplankton, ammonite siliceous radiolarians and thin bivalves, were observed. Some calcareous bioshells have been intensely silicified. Radiolarians, mainly concentrated in the lower part of the Dalong Formation, are fragmented and difficult to identify. Algae exhibit detrital and leaf-like morphologies. Calcium globules are mainly round to oval, with the highest content in the middle, but less in both ends.

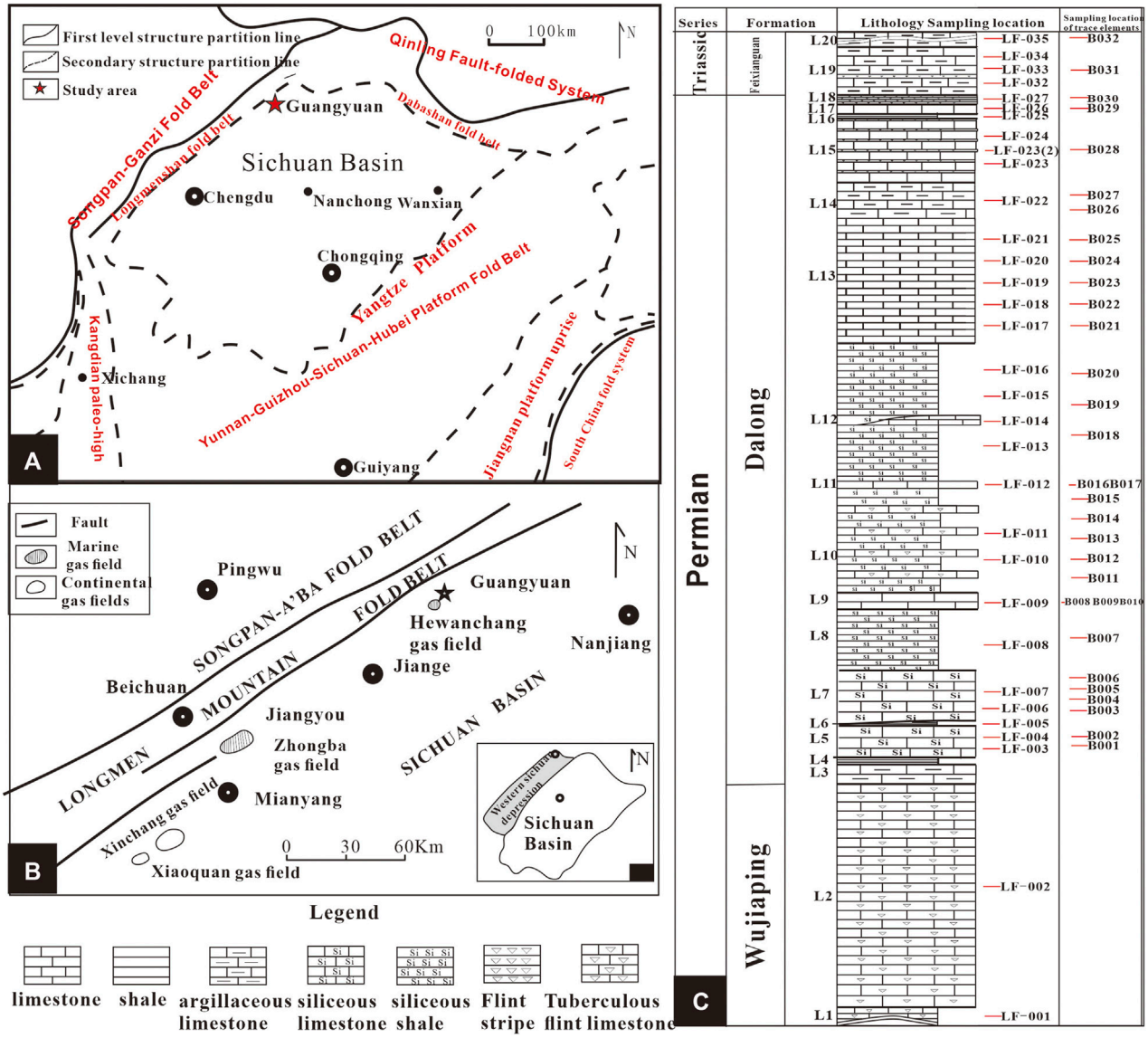

FIGURE 1
Geographical map of Sichuan Basin and sampling location **(A)** Geographical map of the Sichuan Basin. **(B)** Distribution of gas fields in the Sichuan Basin. **(C)** Lithological column of the Dalong Formation in Guangyuan and this study's sampling locations.

Ostracods, concentrated in the lower to middle sections, are thick shelled and mostly fragmented. Gastropods are mainly snails, particularly in the middle section, and they are well preserved. Foraminifera organisms are mostly concentrated in the upper section. Crinoids appear in the middle section, and there are many ammonite fossils that can be observed in the outcrops, mainly in the middle and upper sections (Xiao et al., 2017; Xie et al., 2017).

The role of episodic volcanic or intrusive magmatic activity in triggering global-scale perturbations during the Early Triassic, the ~5-million-year interval following the latest Permian mass extinction (LPME) is suspected but has not been strongly evidenced to date. Shen et al.(2019) investigate the record of volcanism through the Early Triassic (with a focus on the Smithian-Spathian Boundary, or SSB) using mercury (Hg) concentrations in marine sediments as a proxy. Shen et al.(2010) reported Late Permian igneous rocks in the Dalong Formation, Guangyuan. Similarly, this study found three layers of volcanic ash, confirming the occurrence of volcanic activities in the Dalong Formation.

3 Experimental methods

3.1 Samples

Rock samples were obtained from the Longfeng Quarry, Northwest Township, Guangyuan, the Sichuan Basin. The sampling interval was −50 cm. The sampling locations are shown in Figure 1C, and the test methods are listed in Table 1. 14 samples were selected for pyrolysis to analyze TOC and total sulfur (TS); 24 samples were selected for making thin-sections; 12 samples were analyzed for trace elements; 2 samples were analyzed for major elements; and 4 samples were tested for biomarker compounds.

3.2 Test methods

The pollution-free fragmentation and major element testing of whole-rock samples were undertaken at the Institute of Geology and Geophysics, Chinese Academy of Sciences (Beijing, China). Specifically, the rock samples were coarsely crushed, washed, and dried. The samples were subsequently crushed to <8 mm with a nonpolluting agate crusher, placed in the agate tank of a nonpolluting agate ball mill, and ground to <200 mesh for X-ray fluorescence spectrometry.

A Gas chromatography-mass spectrometry (GC-MS) was employed (HP 5890 II; Hewlett Packard). Trace element analysis was performed in the State Key Laboratory of Biogeology and Environmental Geology, China University of Geosciences (Wuhan, China). Trace element analysis was performed by inductively coupled plasma-mass spectrometry (ICP-MS). Approximately 50 mg of powdered sample was accurately weighed, ground to 200 mesh, and placed in a Teflon crucible. The sample was subsequently wetted with 1–2 drops of high-

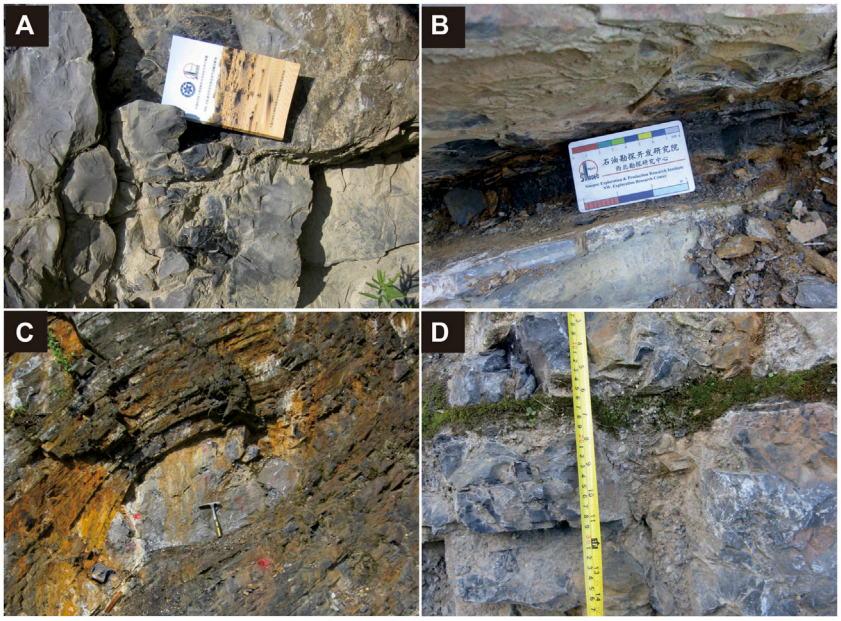

FIGURE 2
Field outcrops in the study area **(A)** Thick-layered gray-black siliceous rock. **(B)** Thin-layered gray-black siliceous shale. **(C)**Middle-layered gray-black siliceous shale sandwiched with a limestone 2.0 m × 0.8 m lens. **(D)** Middle-layered dark-gray siliceous limestone.

TABLE 1 Pyrolysis parameters of the source rocks of the Dalong Formation from Longfeng Quarry, Northwest Township, Guangyuan.

	S1 (mg/g)	S2 (mg/g)	Tmax (°C)	S1+S2 (mg/g)	TOC (%)	PI	HI (mg/g)	PC (%)	D (%)	HC (mg/g)
LF-001	0.02	0.03	462	0.05	0.05	0.40	54.67	0.00	0.00	36.45
LF-003	3.42	15.59	449	19.01	11.68	0.18	133.48	1.58	13.53	29.28
LF-004	2.03	6.44	447	8.47	8.28	0.24	77.82	0.70	8.46	24.53
LF-006	2.81	14.55	448	17.36	5.75	0.16	252.87	1.44	25.03	48.84
LF-007	0.08	0.16	454	0.24	12.21	0.33	1.31	0.02	0.16	0.66
LF-008	1.66	8.72	447	10.38	9.78	0.16	89.14	0.86	8.79	16.97
LF-009	0.02	0.03	552	0.05	0.13	0.40	22.64	0.00	0.00	15.09
LF-010	3.63	13.54	445	17.17	4.02	0.21	336.98	1.43	35.59	90.34
LF-011	0.92	3.77	444	4.69	6.62	0.20	56.99	0.39	5.90	13.91
LF-013	1.28	5.81	449	7.09	4.96	0.18	117.09	0.59	11.89	25.80
LF-016	1.10	6.94	449	8.04	4.57	0.14	151.99	0.67	14.67	24.09
LF-018	0.93	3.10	452	4.03	3.49	0.23	88.93	0.33	9.47	26.68
LF-019	0.36	1.41	459	1.77	1.10	0.20	127.83	0.15	13.60	32.64
LF-020	0.50	4.06	452	4.56	3.88	0.11	104.67	0.38	9.80	12.89

S_1, soluble hydrocarbon; S_2, pyrolytic hydrocarbon; Tmax, temperature of maximum rate of pyrolysis; TOC, total organic carbon; PI, production index (S1/[s1 + s2]); HI, hydrogen index; PC, available carbon; D, degradation rate; HC = (S1 × 100)/TOC.

purity water, 1 ml of HNO_3 and 1 ml of HF were added successively, and the sample was placed in an open Teflon beaker. The Teflon crucible was placed in a tightly-screwed steel jacket and put into an oven at 195°C for over 48 h. After the dissolving bomb was cooled and the acid completely evaporated, the lid was opened, and the sample was placed on an electric hot plate (115°C) to evaporate to dry. Thereafter, 1 ml of HNO_3 was added, and the sample was evaporated to dry again. During this process, we ensured that there was no liquid on the wall of the Teflon crucible. If black suspended matter was present, 1–2 drops of $HClO_4$ were added after evaporating to dry, and the sample was evaporated to dry again. After this, 3 ml of 30% HNO_3 was added, and the Teflon crucible was placed in a steel jacket, tightened, placed in an oven, and heated to 195°C for over 12 h. The solution was subsequently transferred into a polyethylene vial, diluted with 2% HNO_3 to −100 g, and stored under airtight conditions in preparation for ICP time-of-flight MS. To determine the analytical precision and the precision of trace element data, GBW07105 (GSR-3) was used as the standard. Each sample was analyzed three times, and the final average result was used. The analytical precision of the trace elements was estimated to be 5%. A total of 35 elements were detected in the solid samples using the high-temperature and high-pressure closed digestion method.

TOC and TS were tested at China University of Petroleum (Beijing). After treatment with 10% hydrochloric acid to remove carbonates, the samples were subjected to TOC and TS analysis using a carbon/sulfur analyzer (CS-344; LECO) with analytical precision of ±0.1%. The samples were ground to 80–100 mesh and extracted with chloroform for 72 h. After distilling the solvent, the asphalt fraction was separated by petroleum ether precipitation, and the aliphatic and aromatic fractions were eluted by n-hexane, benzene, and ethanol silica gel-alumina column chromatography and resin fractions.

The biomarker compounds were tested at the Massachusetts Institute of Technology (Massachusetts, United States). All the samples were decontaminated, pulverized to powders, and extracted with dichloromethane. The extracts were separated into paraffinic, aromatic, and polar component paraffinic fractions using silica gel chromatography for GC (gas chromatography) and C-C-MS (Capillary gas chromatography-mass spectrometry) analysis. The compounds

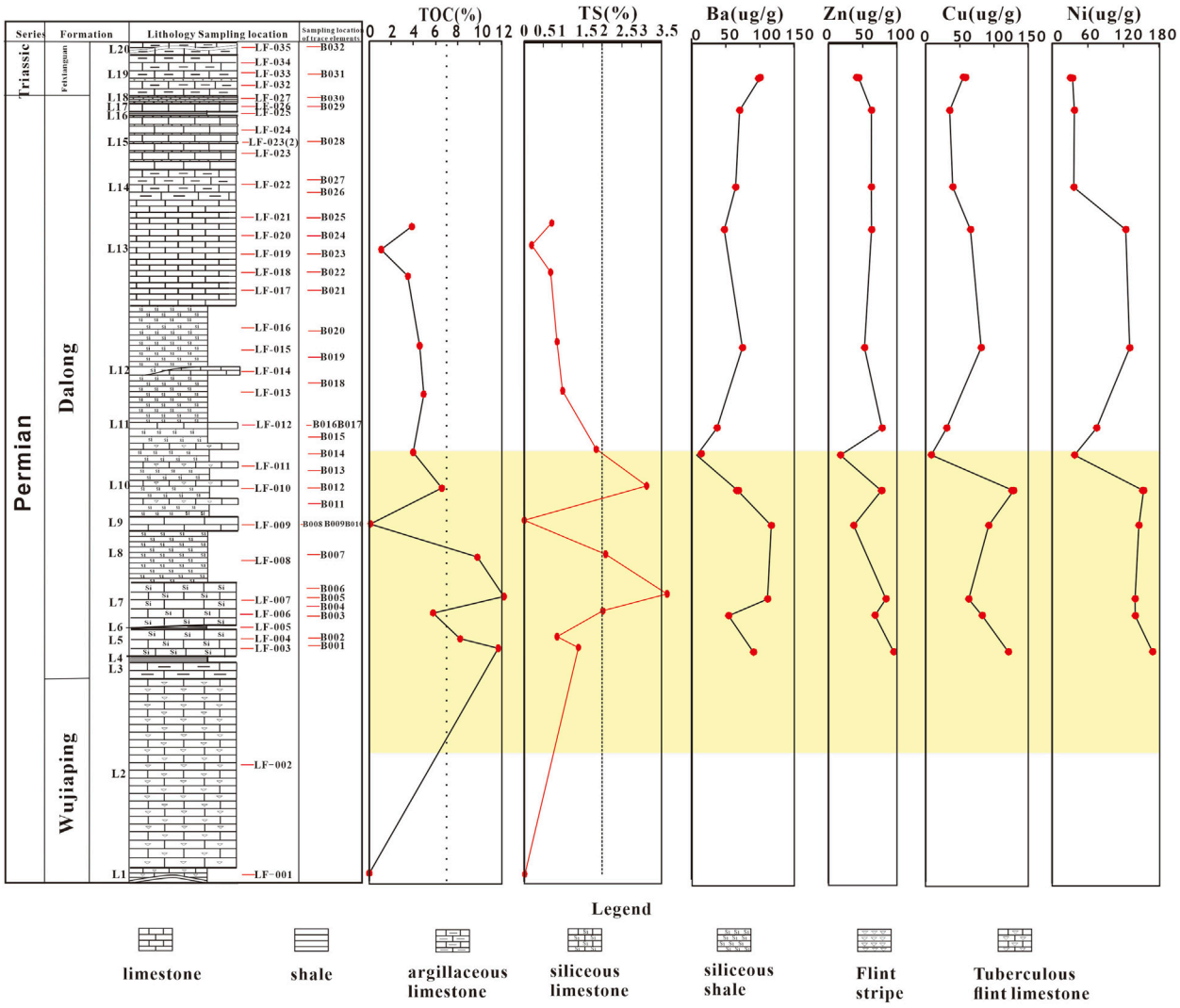

FIGURE 3
Vertical trends in TOC, redox indicators, and paleoproductivity proxies of the Dalong Formation. TS, total sulfur.

were identified by comparison with standard chromatograms. The n-alkane parameters were calculated based on the m/z 85 mass chromatogram, and the hopane series compounds were calculated based on the m/z 191 mass chromatogram.

4 Results

4.1 Abundance of organic matter

The results of the organic geochemical test are presented in Table 1.

The TOC of 14 of the Permian Dalong Formation samples was analyzed. To study the changes in the TOC of the mudstone/limestone or mudstone/siliceous rocks (mudstone or marl) in certain interbeds, individual samples of thin and lenticular layers, such as strips or thin layers within the limestone layers, were collected. The TOC results are presented in Figure 3; Table 1. The TOC varies from 0.05% to 12.21%, with an average of 5.62% and a maximum of 12.21% in layer 7.

First, the TOC is closely related to the lithology of the host (siliceous shale). As shown in Figure 3; Table 1, the TOC varies significantly: the TOC in the bioclastic siliceous shale generally exceeds 10%; the TOC of the siliceous shale with no or extremely little bioclastic material is generally between 4.5% and 9%; and the TOC of the bioclastic limestone is extremely low, at only 0.13%. The TOC of thick limestone in the Changxing Formation is only 0.05%. Second, there is a relationship between the TOC

and the layer thickness. In the Dalong Formation, the TOC in the thick limestone is generally lower than 0.5%. However, in the corresponding layered or siliceous marl, the TOC exceeds 4%. Generally, the thickness of the limestone layer is inversely proportional to the TOC (i.e., the thinner the limestone layer, the greater the TOC). More organic matters accumulate in the layered mudstone and thin limestone.

The hydrogen index (HI) of the Dalong Formation source rocks ranges from 1.31 to 336.98 mg/g, with an average of 115.46 mg/g. Their hydrocarbon generation potential is between 0.05 and 19.01 mg/g, with an average of 7.35 mg/g. The hydrocarbon generation potential was roughly at two peaks: 19.01 mg/g and 17.07 mg/g, corresponding to samples LF-003 and LF-010, respectively. In addition, in general, the hydrocarbon generation potential of the lower Dalong Formation source rock is greater. The available carbon (PC) of the Dalong Formation exhibits a similar double-peak shaped distribution. The two peaks, 1.58 and 1.43, correspond to samples LF-003 and LF-010, respectively. The PC of the source rock in the lower part of the Dalong Formation is higher, indicating that the lower part of the Dalong Formation contains high-potential hydrocarbon-generating organic carbon. The histogram for each S1/TOC interval shows that LF-010 has the largest value (0.90), indicating that the proportion of potential soluble hydrocarbons in the TOC still exceeds that of LF-010.

4.2 Total sulfur

TS in the Upper Permian Dalong Formation shale ranges between 0.01% and 3.65%, with an average of 1.26%, a maximum of 3.65% in layer 7, and a minimum of 0.01% in layer 1, as shown in Table 1. In layer 9, a minimum TS of 0.03% was found with a minimum TOC. The bioclastic siliceous shale (siliceous mudstone) has a high TS content, while the thick bioclastic limestone (thick siliceous limestone) has a low TS content. Figure 3 shows that TS and TOC are roughly positively correlated with each other. It has also confirmed that the rock formation with the highest TOC has a high TS content, which indicates that the rock formation with the highest TOC may undergo a high degree of reduction.

4.3 Source of organic matter

Thin sections of the organic matter indicate that the lower part of the Dalong Formation comprises bioclastic siliceous shale (Figure 4A), microcrystalline limestone, and weakly silicified, interbedded bioclast-bearing carbonaceous mudstone containing ostracods, radiolarians, and calcium globules. Subhorizontal and discontinuous carbonaceous shale laminae were observed, and local asphaltization was observed in fractures. Carbonaceous shale, calcium spheres (Figure 4B), and bioclastic limestone as well as weak silicification were observed in the middle part of the Dalong Formation. Many types of organisms were observed inside the calcium spheres, such as foraminifera, brachiopod, ostracod, and gastropod (Figure 4C). It was speculated that a siliceous calcium sphere in the mudstone was a siliceous radiolarian (Figure 4D). The top part of the Dalong Formation comprises micrite limestone, bioclastic micrite limestone, silicified carbonaceous and shaly calcium spheres, and micrite limestone with horizontal bedding and containing algal debris and radiolarians. A few of the samples contain asphalt, and yellow iron ore in the siliceous rocks, along with less flint. In addition, pyrite and fossils of foraminifera and phytoplankton, such as ammonites, siliceous radiolarians, and thin bivalves, were observed. In the siliceous radiolarian mudstone, some radiolarians were filled with organic matter to varying degrees (Figure 4E).

Biomarker compounds can be used to infer the source of organic matter, such as terrestrial or marine and algae, bacteria, or higher plants (Xiao et al., 2017). (Xiaoyan et al., 2008).confirmed the predominance of low-molecular-weight n-alkanes in the Upper Permian Dalong Formation, leading to the speculation that the origin of the marine organic matter in the Dalong Formation in Shangsi, Guangyuan, was mainly from algae and bacteria. Wei et al. (2018b) found that the C_{12}^{+} n-alkanes in the Dalong Formation shale are mainly nonwaxy congeners, which are typical marine organisms produced by local phytoplankton. Herein, the results of standard biological compounds tested in samples LF-006, LF-008, LF-011, and LF-013 (Figure 5A) led to the speculation that the source of the organic matter was mainly lower aquatic organisms, bacteria, and algae.

We analyzed the source of the organic matter (i.e., the type of kerogen) according to the cross-plot of Tmax and HI (Figure 5B). Most of the organic matters belong to types II_1-II_2, namely sapropel, which is common in source rocks. This type of sapropel is mainly derived from bacteria and phytoplankton in catchment basins and has a high hydrocarbon generation potential of −0.3–0.5.

4.4 Thermal maturity

Tmax can be used as an indicator of maturity. As shown in Figure 5B, most samples have Ro in the range of 0.8–1.2, indicating a high-maturity stage. The Tmax values of the samples, presented in Table 2, range from 444°C to 462°C, except for sample LF-009, where the Tmax value is 552°C. Sample LF-009 is bioclastic limestone with a TOC of 0.3%. It is not a source rock, so it is not discussed further herein. Therefore, the organic-rich Dalong Formation in Longfeng Quarry is at a high-maturity stage.

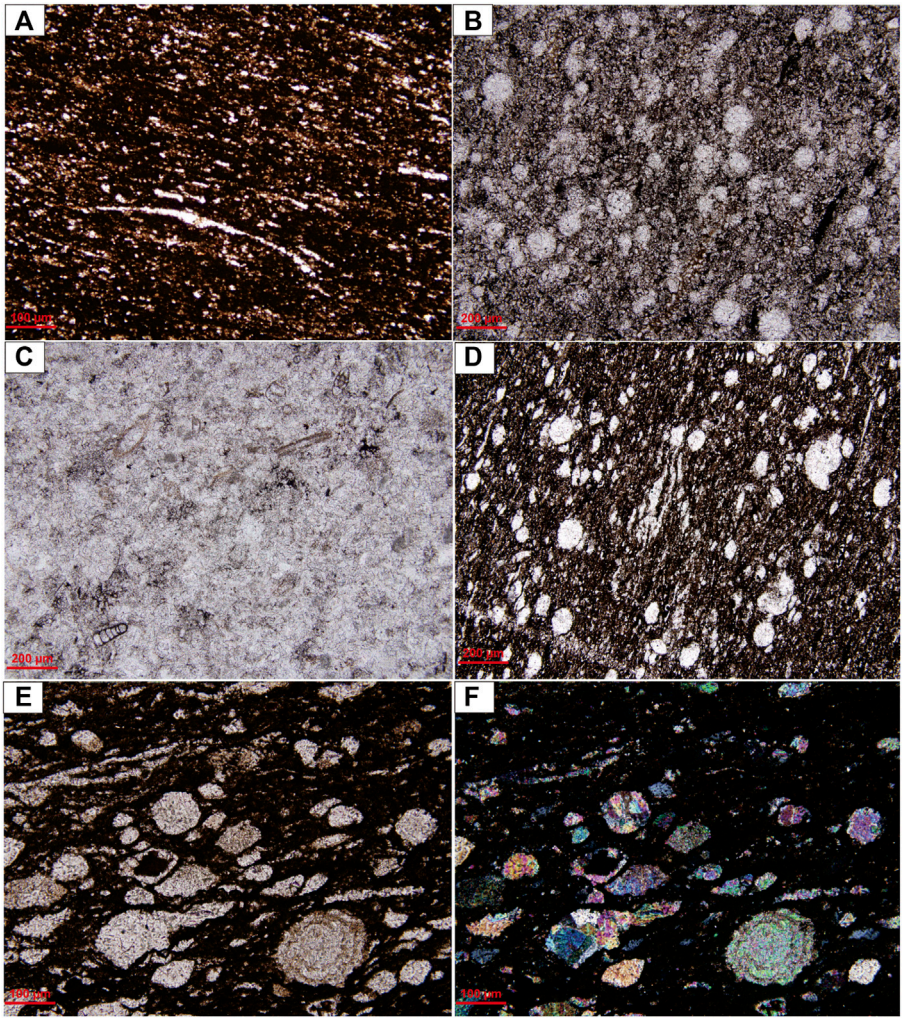

FIGURE 4
Lithological microscopic photos of the Dalong Formation. **(A)** Bioclastic siliceous shale, biodetritus aligned in a directional manner. **(B)** Calcium spheres, the calcium spheres are not uniform in size. **(C)** Bioclastic limestone, such as foraminifera, brachiopod, ostracod, and gastropod. **(D)** Radiolarian, and **(E)** Spherules filled with organic matter by polarizing microscope with plane polarized light. **(F)** spherules filled with organic matter by polarizing microscope with perpendicular polarized light.

5 Discussion

5.1 Controlling factors on high-quality source rocks

Many factors control the formation of high-quality source rocks, including productivity, the effect of the depositional environment on the preservation of organic matter, and hydrothermal activity (Song et al., 2016; Song et al., 2019; Meng et al., 2022). We studied the sedimentary paleoenvironment and the hydrothermal activity associated with the Dalong Formation high-quality source rocks.

5.1.1 Paleoenvironment for source rock deposition

In black shale, metal elements combine with sulfide and organic matter through symbiotic mineralization. Factors affecting the content of metal elements include redox conditions, organic matter type, deposition rate, diagenesis, and subsequent mineralization. Previous studies have shown that certain metals exhibit high fluxes and mobilities under anoxic conditions, leading to a significant enrichment of these metals in sediments (Meng et al., 2013). Therefore, organic-rich sediments are usually enriched with sulfide metal elements through redox reactions. The trace elements in the Dalong Formation samples are presented in Table 2. Several

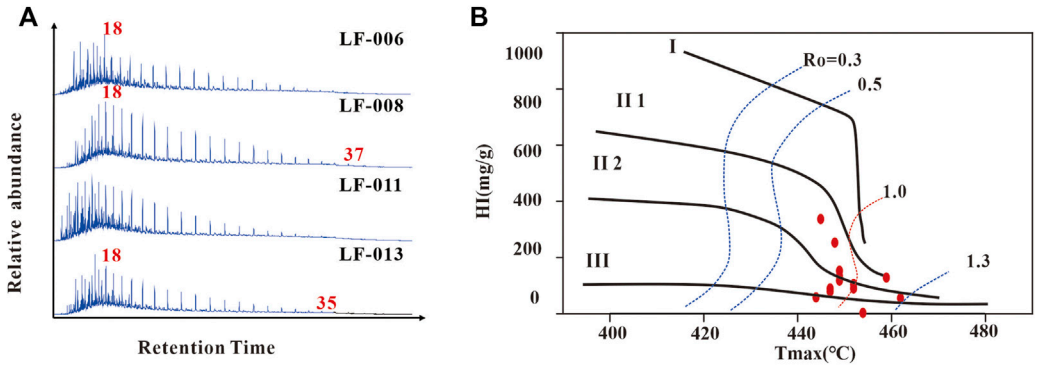

FIGURE 5
Analysis of the source of the organic matter in Dalong Formation. **(A)** Normal alkane distribution of the source rocks, and **(B)** crossplot of Tmax with HI of the source rocks.

trace elements, including Mo, Re, U, and V, are regarded as signs of hypoxia in paleosedimentary environments. The ratios of certain trace elements, such as V/(V + Ni), V/Cr, Ni/Co, and U/Th, indicate reducing conditions to restore the depositional environment. Reduction-sensitive trace elements, such as Mo, U, and V, are enriched in anoxic environments, rendering element concentrations and ratios useful indicators for paleoreduction reconstructions.

Previous studies have observed that V/(V + Ni), V/Cr, Ni/Co, and U/Th can be used to indicate ancient redox environments (Wei et al., 2018b). Although there is no consensus among these redox indicators, Ni/Co, V/Cr, U/Th, and V/(V + Ni) show an overall downward trend with increasing water oxidation· Previous studies have established standard values for Ni/Co, V/Cr, U/Th, and V/(V + Ni) ratios to distinguish oxygen-rich, oxygen-poor, and anoxic conditions (Francois, 1988). Therefore, using the sample test data, the standard values for various Ni/Co, V/Cr, U/Th, and V/(V + Ni) ratios were used to distinguish oxygen-rich, oxygen-poor, and anoxic conditions, as shown in Figure 6. Generally, samples B002, B004, B006, B008, B013, B015, B016, B018, and B021 from the middle and lower sections of the Dalong Formation are within the hypoxia-hypoxia region, while samples B026, B029, and B031 from the top of the Dalong and Feixianguan Formations are within the oxygen-enriched region. Therefore, we speculated that the organic matter in the lower part of the Dalong Formation was mainly deposited under semianoxic to anoxic conditions, while the top of the Dalong Formation was deposited in an oxygen-rich environment. This is consistent with the sedimentary history of the Permian. In the Early Permian, transgression occurred in the Sichuan Basin, and at the end of the Permian, the Sichuan Basin experienced regression. It was then entirely uplifted, denuded, and remained under oxygen-rich conditions. Therefore, the Early Permian is significantly different from the Late Permian.

The Ni/Co, V/Cr, and U/Th ratios strongly correlate with TOC (Figure 7). Peaks were observed at L7 and L10, and the values were higher in the middle and lower sections of the Dalong Formation. However, the values were lower at the top of the Permian Dalong and Triassic Feixianguan Formations. Thus, it's confirmed that the rock layers with high TOC (i.e., the rock layers with abundant organic matter) are related to the preservation conditions for organic matter.

High-resolution biomarker profiles from Shangsi can help to identify the succession of environmental and related microbial community changes that occurred during the PTB (Permian-Triassic boundary) crisis. Xie et al. (2017) reveal major differences in the microbial communities and environmental conditions by biomarker records. The first episode of the PTB mass extinction was probably associated with massive soil erosion ($C_{30}M/C_{30}HP$ >0.20; Pr/Ph >2), expansion of oceanic anoxia (r/C_{30} HP >0.1), and blooms of marine red algae (C_{27}/C_{27-29} sterane ratio >0.4) and nitrogen-fixing bacteria (C_{31} 2-MHP >0.05, decrease in $\delta^{15}N_{org}$). The Pr/Ph ratio is frequently used to judge redox conditions (Chen et al., 2012). A Pr/Ph value of <1 indicates an anoxic environment. When the value is between 1 and 3, it indicates a subanoxic environment. When the value is >3, it indicates that the organic debris was deposited in a full-oxygen terrestrial environment. Figure 5A shows the distribution of n-alkanes in Longfeng Quarry samples. The Pr/Ph ratio of the Dalong Formation high-quality source rocks ranges from 0.8 to 1.0, so we speculate that their depositional environment may have been anoxic. The DBT/P shown in Figure 8A represents depositional environments. The depositional environments of samples LF-006, LF-011, and LF-013 were similar, while the depositional environment represented by sample LF-008 was more reduced. Figure 8 presents the biological compound spectra of samples LF-006, LF-008, LF-011, and LF-013 and shows (A) the m/z 178 + 184 distribution and (B) aromatic distribution characteristics of the samples.

As shown in Figure 8B, in four samples LF-006, LF-008, LF-011 and LF-013, the abundance of dimethylnaphthalene is similar, while

TABLE 2 Trace elements (μg/g) of the source rocks of Dalong and Changxing formations in northwestern Sichuan basin.

Samples	B002	B004	B006	B008	B013	B015	B015	B016	B018	B021	B026	B029	B031-2	B031-2
Be	2.29	1.09	1.63	1.28	0.23	0.9	0.85	0.23	0.82	0.94	0.63	0.88	1.37	1.27
Sc	7.33	5.49	6.45	4.68	1.45	6.11	6.08	1.43	4.24	3.76	3.43	6.97	8.62	8.35
V	309	403	1112	972	128	1136	1116	287	581	1130	37	34.8	48.7	47.2
Cr	190	169	216	350	15.8	132	138	78.4	169	173	22.2	53.9	40.3	42.4
Co	15.3	14.7	20.7	21.4	4.7	18.8	18.7	60.5	21.7	12.9	12.3	16.3	16.7	19.2
Ni	169	140	138	146	37.6	152	154	75.4	131	124	35.8	37.3	30	32.5
Cu	121	63.2	82.9	92.3	7.51	129	126	30.5	80.5	64.9	38.8	34.8	52.9	56.3
Zn	95.1	83.7	68.2	37.2	17.6	77.2	77.9	23.7	52.6	62.9	38	53.5	44.3	41
Ga	8.72	4.96	7.05	7.73	0.38	4.62	4.45	1.68	4.69	3.93	3.62	5.69	9.21	8.76
Rb	42.1	20.2	47.4	40.3	1.6	34.4	34.6	7.06	22.5	25.9	20.7	40.2	59.1	57.9
Sr	883	1575	359	71.4	467	1520	1512	243	721	372	2995	702	539	514
Y	15.4	50.4	11.3	5.32	4.08	28.6	28.4	8.4	13.3	11.2	6.91	9.09	17.3	16.8
Zr	76.4	65	68.9	57.2	8.33	48	47.5	25.6	37.9	33.1	35.4	39.6	73.3	68.9
Nb	15	4.68	8.06	6.12	0.63	4.79	4.68	1.42	3.11	3.05	2.93	4.07	7.38	7.14
Cs	2.42	1.07	2.52	2.33	0.06	1.63	1.6	0.58	1.51	1.33	1.28	2.28	3.4	3.25
Ba	89.8	54.4	111	117	7.59	67.4	66.3	37.2	73.9	47.3	64.7	70.7	99.7	95
La	13.3	48.3	14.2	7.81	2.71	23	22.6	6.99	13.4	8.27	7.81	10.9	22.4	21.4
Ce	17.6	60.4	25	12.1	3.43	34.4	33.8	11.9	22.7	14.8	14.6	21.8	41.7	40.3
Pr	2.49	7.29	3.24	1.51	0.46	4.91	4.77	1.64	3	1.85	1.65	2.43	5.02	4.8
Nd	9.12	27.2	12.1	5.15	1.75	18.8	18.2	6.47	11.1	7.22	6.05	9.11	18.9	18.1
Sm	1.63	5.32	2.09	0.77	0.35	4.07	4.03	1.35	2.02	1.53	1.18	1.79	3.59	3.49
Eu	0.32	0.98	0.35	0.16	0.07	0.72	0.7	0.2	0.34	0.29	0.22	0.3	0.68	0.67
Gd	1.68	6.08	1.76	0.7	0.38	4.27	4.29	1.33	2.13	1.59	1.2	1.62	3.49	3.39
Tb	0.3	1.02	0.29	0.12	0.07	0.73	0.73	0.24	0.37	0.27	0.19	0.27	0.55	0.53
Dy	1.85	5.96	1.59	0.71	0.41	4.16	4.13	1.37	2.04	1.6	1.07	1.5	2.95	2.85
Ho	0.42	1.25	0.34	0.17	0.10	0.84	0.83	0.28	0.43	0.34	0.23	0.31	0.58	0.55
Er	1.46	3.78	1.11	0.62	0.3	2.42	2.35	0.83	1.27	1.02	0.66	0.9	1.66	1.63
Tm	0.26	0.56	0.2	0.12	0.05	0.35	0.35	0.14	0.21	0.16	0.1	0.14	0.26	0.24
Yb	1.83	3.24	1.3	0.87	0.34	2.16	2.1	0.9	1.37	1.04	0.68	0.94	1.55	1.53
Lu	0.3	0.51	0.21	0.15	0.06	0.34	0.33	0.14	0.21	0.16	0.11	0.14	0.23	0.23
Hf	1.76	1.05	1.68	1.44	0.16	1.18	1.16	0.42	1.19	0.84	0.95	1.1	2.03	1.9
Ta	0.47	0.26	0.54	0.4	0.05	0.31	0.29	0.17	0.44	0.24	0.23	0.3	0.54	0.53
Pb	10.6	7.25	12.1	8.2	1.36	15.5	15.2	3.8	9.12	8.63	69.6	12.2	9.57	9.24
Th	4.19	2.21	5.39	3.24	0.44	3.24	3.18	0.84	10.8	2.75	2.24	3.49	6.19	5.94
U	5.68	29.7	6.98	5.95	8.53	19	18.8	5.78	12.5	22.6	6.38	3.8	2.27	2.17

the abundance of 1,2,5-trimethylnaphthalene is different, indicating that the source rocks were affected by biogenesis, particularly the influence of low microbial activities or the input of higher plants. The 2-/1-methylphenanthrene parameters indicate the similar maturity of all the samples.

5.2 Hydrothermal influence

South China as a whole was likely covered frequently by felsic ash beds around the PTB time. 21 fine-grained tuff beds of centimeter scale occer in the 12-m-thick PTB interval. These indicate that rhyodacitic volcanism was active, and that northern Sichuan often experienced ash falls at the end of the Permian. This implies that the eruptions of felsic volcanoes may have played a certain role in environmental change relevant to the mass extinction at the end of Permian (Isozaki et al., 2007). Direct evidence of intense chemical weathering induced by volcanism is rare in sedimentary successions. Shen et al. undertake a multiproxy analysis (including organic carbon isotopes, mercury (Hg) concentrations and isotopes, chemical index of alteration (CIA), and clay minerals) of two well-dated Triassic-Jurassic (T-J) boundary sections. Both sections show increasing CIA in association with Hg peaks near the T-J boundary, reflecting volcanism-induced intensification of continental chemical

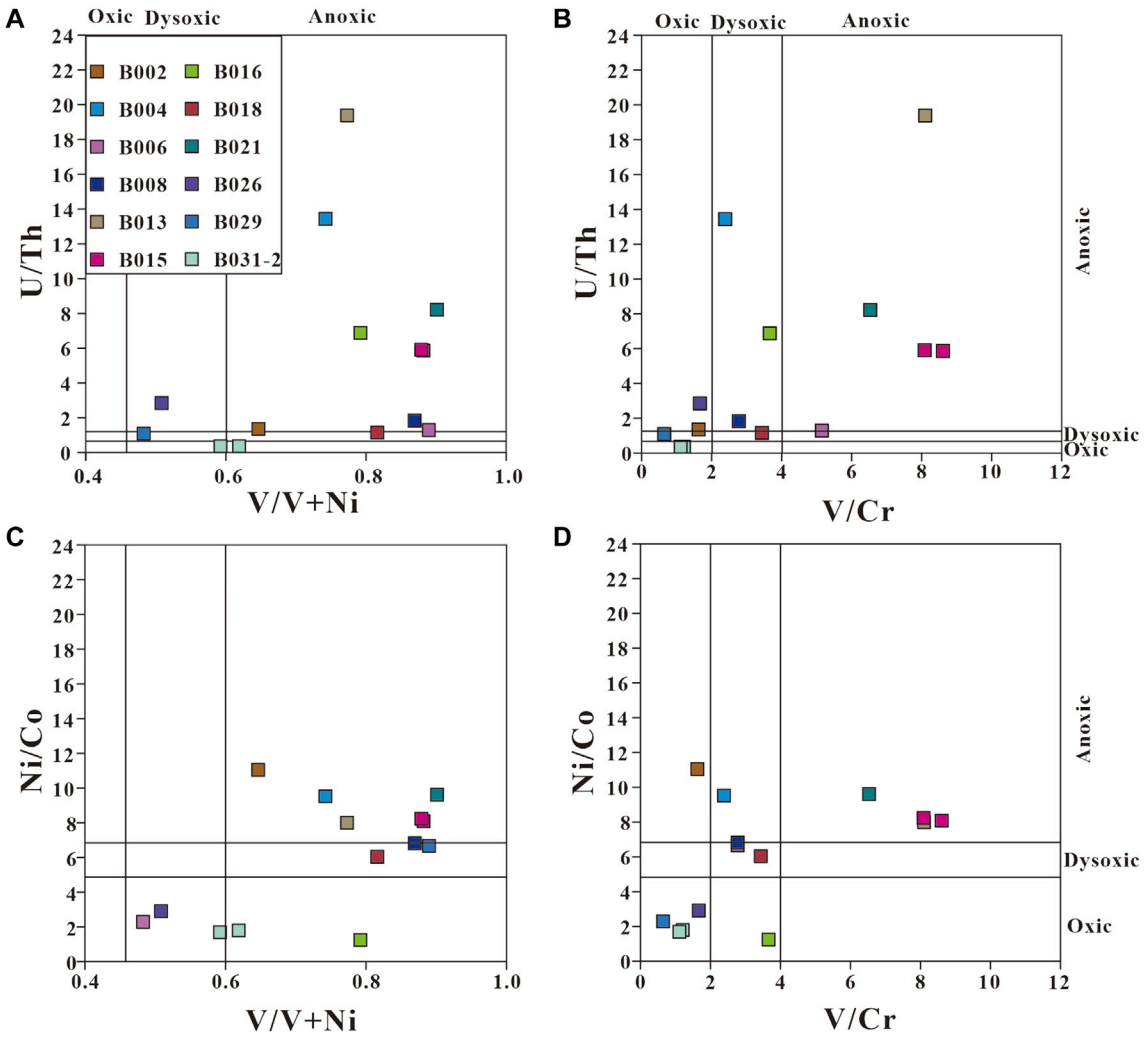

FIGURE 6
Crossplots of Ni/Co, V/Cr and U/Th ratios of samples of the Dalong Formation takin in Longfeng Quarry, Northwest Township, Guangyuan. **(A)** U/Th *vs.* V/(V + Ni). **(B)** U/Th *vs.* V/Cr. **(C)** Ni/Co *vs.* V/(V + Ni). **(D)** Ni/Co *vs.* V/Cr.

weathering, which is also supported by negative mass-independent fractionation (MIF) of odd Hg isotopes. (Shen et al., 2022).Three layers of 3–5 cm thick volcanic ash were observed in the field outcrops. Volcanic ash settled from the atmosphere into certain depositional environments can be transformed into altered rocks with a high clay mineral content through burial, diagenesis, and metamorphism (Meng et al., 2013; Meng et al., 2022). The volcanic ash deposits in the study area were grayish white in color and stick-slip after wetting with water, and they exhibited heavy alteration (Shen et al., 2022). Two relatively fresh volcanic ash samples were selected for major elemental analysis and testing. The test data are shown in Table 3.

The SiO_2 content ranges from 49.34% to 56.46%, Al_2O_3 from 22.91% to 22.93%, K_2O + Na_2O from 4.23% to 4.435%, and MgO from 1.47% to 2.67% which differs by ±3.5% compared to normal igneous rock. The TiO_2/Al_2O_3 ratio ranges from 0.014 to 0.015, which is lower than the upper limit of igneous rocks (0.02), and the SiO_2/Al_2O_3 ratio ranges from 2.15 to 2.46. All these values indicate a high clay mineral content, high maturity, and heavily altered volcanic ash sediments. According to previous studies, the enrichment of nutrient elements such as Ni, Cu, Zn, Ba, and Cd in carbonate rocks indicates high paleoproductivity, and the enrichment of Ni/Co, V/Cr, U/Th, and other elements indicates reducing conditions (Francois, 1988). Similar trends in the abundance maps of Ni, Cu, Zn, Ba, and TOC indicate that they were affected to a similar degree by environmental factors (Figure 2). The trends in Ni, Cu, Zn and Ba, and elemental Ni/Co, V/Cr, and U/Th ratios (which represent a redox environment) are also similar. A peak was observed for the Ni/Co, V/Cr, and U/Th ratios. We speculate that the aggregation of the nutrient elements Ni, Cu, Zn, and Ba was related to the redox conditions, whereby they

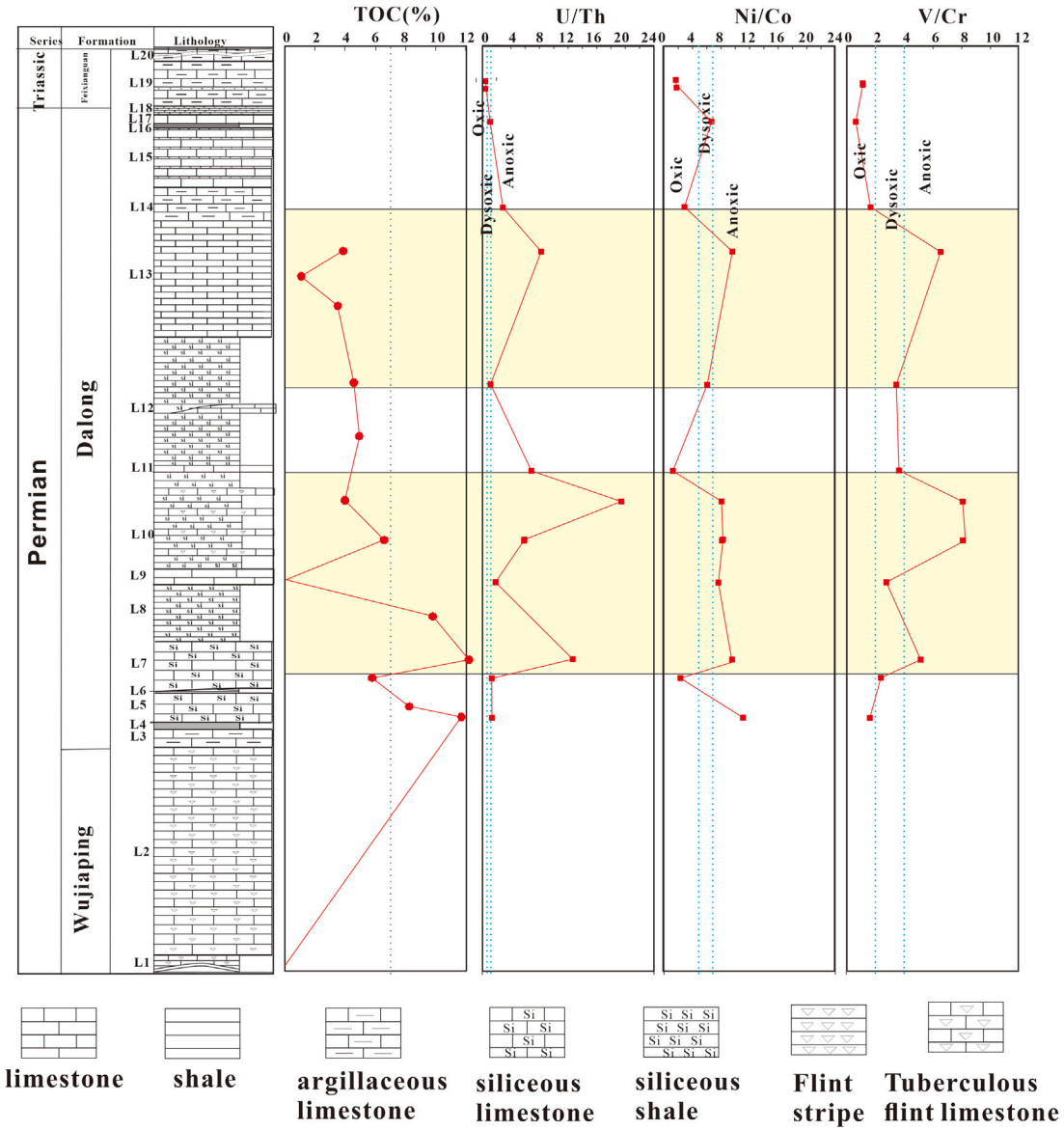

FIGURE 7
Variation in TOC, Ni/Co, V/Cr, and U/Th ratios of samples taken in Longfeng Quarry in Northwest Township, Guangyuan.

aggregated under reducing conditions. Considering that these nutrients, particularly Ba, represent ancient productivity, we speculate that the level of ancient productivity was also related to redox conditions. The nutritional elements Ni, Cu, Zn, and Ba strongly correlate with the TOC, and the redox indices, Ni/Co, V/Cr, and U/Th, show a good relationship with the TOC, reflecting that the accumulation of TOC may be affected by the level of paleoproductivity and paleo-redox conditions. There are evidences of strong control and influence from reducing conditions.

Many Upper Permian Dalong Formation sedimentary rocks with high TOC were developed at low slopes and basin bottoms. However, the sediments dominated by limestone at the top of the Changxing and Dalong Formations have obviously low TOC. Moreover, three layers of volcanic ash were observed in the field outcrops. As shown in the geochemical test data, the layers of siliceous rock and shale with high TOC were affected by hydrothermal activities. So it is inferred that high paleoproductivity has taken place in these rock layers. To elucidate the relationship between hydrothermal activity and accumulation of organic matter, we propose the following concept. The process of submarine volcanic hydrothermal activity is associated with abundant nutrients such as Mo, Pb, Ni, Zn, Ba, Sb, and P (Liu et al., 2019b; Liao et al., 2019; Li et al., 2020; Shen et al., 2022).

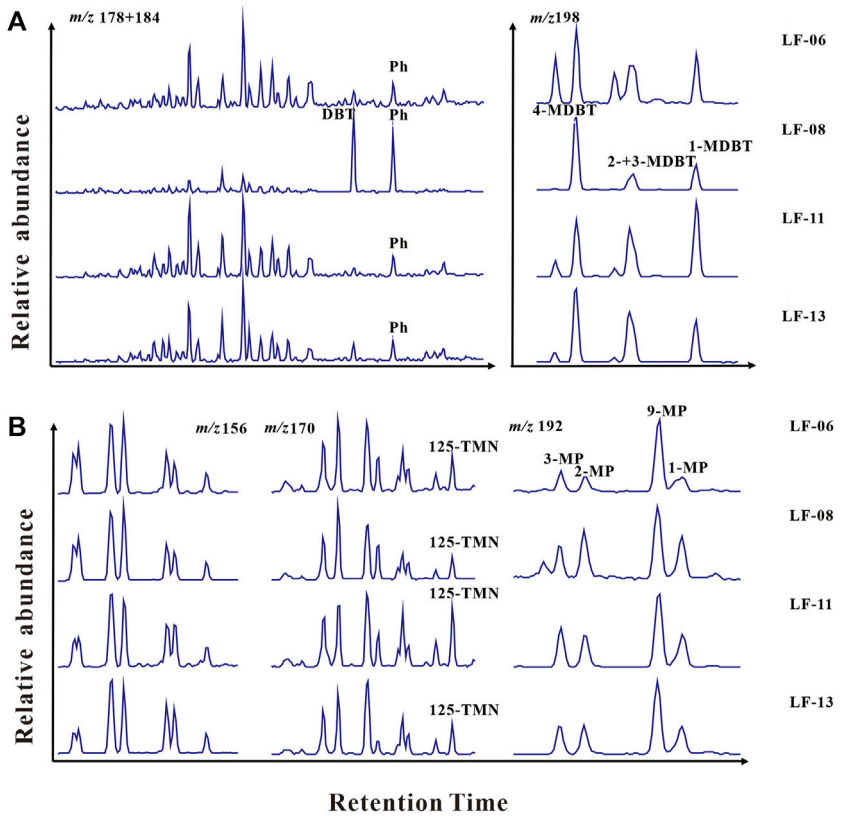

FIGURE 8
Standard biological compounds of samples 2018-LF-006, 2018-LF-008, 2018-LF-011, and 2018-LF-013. **(A)** Distribution of m/z 178 + 184, and **(B)** aromatic distribution.

TABLE 3 Major Elements of volcanic ash sedimentary rocks in Longfeng Quarry, Northwest Township, Guangyuan (Wt%).

samples	SiO_2	TiO_2	Al_2O_3	TFe_2O_3	MnO	MgO	CaO	Na_2O	K_2O	P_2O_5	LOI	TOTAL
LF-25	56.46	0.327	22.93	1.28	0.01	1.47	3.99	0.175	4.26	0.17	8.95	100.02
LF-5	49.34	0.354	22.91	5.42	0.02	2.67	1.85	0.07	4.16	0.136	12.61	99.54

In this case, the solubility of these elements rapidly increases with increasing water temperature. When Si-rich hot water meets cold seawater, Si may precipitate directly. As a result, siliceous and other biological organisms may thrive in hydrothermal environments. Biological prosperity leads to high primary productivity. However, flourishing organisms consume a large amount of free oxygen from the water, causing anoxic hypoxia in the bottom water. As the organic matter is buried deeper and deeper, anaerobic and anoxic conditions mainly control the accumulation of organic matter in the sedimentary and early diagenetic stages, providing important conditions for the preservation of organic matter in siliceous and dark shale. Therefore, we propose the following for the formation of the shale and siliceous rocks of the Upper Permian Dalong Formation in Longfeng Quarry. With submarine volcanic activities and hydrothermal (hot water) events, the paleoproductivity increased and the burial environment became reducing. In general, hydrothermal events and upwelling caused biological flourishing in the upper water body by providing nutrients, leading to an increase in primary productivity. Post-flourishing living processes consumed large amounts of free oxygen from the water, leading to the reduction of the burial conditions associated with microbial blooms at the bottom. These processes were one after the other and closely linked, and ultimately resulted in the burial of large amounts of organic matter in reducing environments that favored the formation of high-quality source rocks.

6 Conclusion

Based on microscopic observations, TOC, TS and trace element testing and analysis of shale samples from the Upper Permian Dalong Formation in Longfeng Quarry, Northwest Township, Guangyuan, the Sichuan Basin, and considering previous studies, we have the following conclusions.

The source rocks in the middle and lower members of the Dalong Formation are of high quality, and the TOC of the samples is closely related to the lithology. High TOC was tested in siliceous rock, dark shale and siliceous shale that were developed in a deep-water basin environment. In addition, high TOC is associated with the thickness of the rock layer. Generally, thinner layers have high TOC.

The Tmax-HI diagram shows that the organic matter sources are mainly types II1 and II2. The biomarker compounds and microscopic observation show that the main sources of organic matter are phytoplankton and bacteria. The Tmax values of the source rocks range from 444°C to 462°C, and the corresponding Ro is roughly 1.0%–1.5%, indicating the high-maturity stage.

The TS, V content, and trace element ratios (i.e., Ni/Co, V/Cr, U/Th, and V/[V + Ni]) indicate deposition in a closed/anoxic environment, and Pr/Ph = 0.8–1.0 also proves the depositional environment is closed and under anoxic conditions.

Submarine volcanic hydrothermal activity provides abundant nutrients and compounds, such as SiO_2, Al_2O_3, K_2O, Mo, Pb, Ni, Zn, Ba, Sb, and P, which contribute to biological prosperity and high primary productivity. This consumes large amounts of free oxygen from the water, and results in inadequate oxygen in the bottom water and better preservation of organic matter in siliceous rock and dark shale. This is conducive to the formation of high-quality source rocks.

Data availability statement

The original contributions presented in the study are included in the article/supplementary material, further inquiries can be directed to the corresponding author.

Author contributions

LW: Conceptualization, Methodology, Formal ananlysis, Data curation, Writing—original draft, Visualization. XG: Conceptualization, Writing—review, Resources, Funding acquisition, WJ: Data curation, Writing; ZS: Writing—review HX: Data curation.

Funding

This study was supported by National Scientific Funding of China (Grant No.U20B6001 and 41872164), National Key Research and Development Program (Grant No. 2019YFA0708504).

Acknowledgments

We are grateful to Meng Qingqiang for the guidance of this article, CX for assistance with the biomarker compounds operation at the Massachusetts Institute of Technology; Ding Baoming for assistance with the major element testing of whole-rock samples. The authors would like to thank to the State Key Laboratory of Biogeology and Environmental Geology, China University of Geosciences (Wuhan, China).

Conflict of interest

The authors declare that the research was conducted in the absence of any commercial or financial relationships that could be construed as a potential conflict of interest.

Publisher's note

All claims expressed in this article are solely those of the authors and do not necessarily represent those of their affiliated organizations, or those of the publisher, the editors and the reviewers. Any product that may be evaluated in this article, or claim that may be made by its manufacturer, is not guaranteed or endorsed by the publisher.

References

Bowker, K. A. (2007). Barnett shale gas production, fort worth basin: Issues and discussion. *Am. Assoc. Pet. Geol. Bull.* 91, 523–533. doi:10.1306/06190606018

Chen, H., Xie, X., Hu, C., Huang, J., and Li, H. (2012). Geochemical characteristics of late permian sediments in the Dalong Formation of the Shangsi section, northwest Sichuan basin in south China: Implications for organic carbon-rich siliceous rocks formation. *J. Geochem. Explor.* 112, 35–53. doi:10.1016/j.gexplo.2011.06.011

Curtis, J. B., and Montgomery, S. L. (2002). Recoverable natural gas resource of the United States: Summary of recent estimates. *AAPG Bull.* 86, 1671–1678.

Dai, J., Yunyan, N. I., Qin, S., Huang, S., and Han, W. (2018). Geochemical characteristics of ultra-deep natural gas in the Sichuan Basin. *SW China* 45, 619–628.

Dong, D., Gao, S., Huang, J., Guan, Q., Wang, S., and Wang, Y. (2015). Discussion on the exploration & development prospect of shale gas in the Sichuan Basin. *Nat. Gas. Ind. B* 2, 9–23. doi:10.1016/j.ngib.2015.02.002

Francois, R. (1988). A study on the regulation of the concentrations of some trace metals (Rb, Sr, Zn, Pb, Cu, V, Cr, Ni, Mn and Mo) in Saanich Inlet Sediments, British Columbia, Canada. *Mar. Geol.* 83, 285–308. doi:10.1016/0025-3227(88)90063-1

Guo, C., Li, G., Wei, H., Xia, F., and Xie, F. J. a. J. O. G. (2016)., 9. China, 359. doi:10.1007/s12517-016-2348-3Stratigraphic architecture and platform evolution of the Changxing formation (upper permian) in the yuanba gas field, northeastern Sichuan basin, China*Arab. J. Geosci.*

Isozaki, Y., Shimizu, N., Yao, J., Ji, Z., and Matsuda, T. (2007). End-Permian extinction and volcanism-induced environmental stress: The Permian-Triassic boundary interval of lower-slope facies at Chaotian, South China. *Palaeogeogr. Palaeoclimatol. Palaeoecol.* 252, 218–238. doi:10.1016/j.palaeo.2006.11.051

Jin, Y. G., Wang, Y., Wang, W., Shang, Q. H., Cao, C. Q., and Erwin, D. H. (2000). Pattern of marine mass extinction near the Permian-Triassic boundary in South China. *Science* 289, 432–436. doi:10.1126/science.289.5478.432

Li, L., Liao, Z., Lei, L., Lash, G. G., Chen, A., and Tan, X. (2020). On the negative carbon isotope excursion across the wuchiapingian–changhsingian transition: A regional event in the lower Yangtze region, south China? *Palaeogeogr. Palaeoclimatol. Palaeoecol.* 540, 109501. doi:10.1016/j.palaeo.2019.109501

Li, Y., Chen, S., Wang, Y., Qiu, W., Su, K., He, Q., et al. (2019). The origin and source of the Devonian natural gas in the Northwestern Sichuan Basin, SW China. *J. Petroleum Sci. Eng.* 181, 106259. doi:10.1016/j.petrol.2019.106259

Liao, Z., Hu, W., Cao, J., Wang, X., Hu, Z. J. M., and Geology, P. (2019). Petrologic and geochemical evidence for the formation of organic-rich siliceous rocks of the Late Permian Dalong Formation, Lower Yangtze region, southern China. *Mar. Petroleum Geol.* 103, 41–54. doi:10.1016/j.marpetgeo.2019.02.005

Liu, Q., Jin, Z., Bing, Z., Zhu, D., and Meng, Q. J. J. O. N. G. G. (2017)., 2. China, 81–97.Main factors for large accumulations of natural gas in the marine carbonate strata of the Eastern Sichuan Basin

Liu, Q., Jin, Z., Wang, X., Yi, J., Meng, Q., Wu, X., et al. (2018). Distinguishing kerogen and oil cracked shale gas using H, C-isotopic fractionation of alkane gases. *Mar. Petroleum Geol.* 91, 350–362. doi:10.1016/j.marpetgeo.2018.01.006

Liu, Q., Zhu, D., Jin, Z., Meng, Q., and Li, S. (2019a). Influence of volcanic activities on redox chemistry changes linked to the enhancement of the ancient Sinian source rocks in the Yangtze craton. *Precambrian Res.* 327, 1–13. doi:10.1016/j.precamres.2019.02.017

Liu, Q., Zhu, D., Meng, Q., Liu, J., Wu, X., Zhou, B., et al. (2019b). The scientific connotation of oil and gas formations under deep fluids and organic-inorganic interaction. *Sci. China Earth Sci.* 62, 507–528. doi:10.1007/s11430-018-9281-2

Mei, Y., Liu, W., Wang, J., and Bentley, Y. (2022). Shale gas development and regional economic growth: Evidence from Fuling, China. *Energy* 239, 122254. doi:10.1016/j.energy.2021.122254

Meng, Q., Pang, Q., Hu, G., Jin, Z., Zhu, D., Liu, J., et al. (2022). Rhyolitic ash promoting organic matter enrichment in a shallow carbonate platform: A case study of the maokou Formation in eastern Sichuan basin. *Front. Earth Sci. (Lausanne).* 10. doi:10.3389/feart.2022.879654

Meng, Q. Q., Zhu, D. Y., Hu, W. X., and Jin, Z. J. (2013). Dissolution-filling mechanism of atmospheric precipitation controlled by both thermodynamics and kinetics. *Sci. China Earth Sci.* 56, 2150–2159. doi:10.1007/s11430-013-4711-5

Mingyi, H., Zhonggui, H., Guoqi, W., Wei, Y., and Mancang, L. (2012). Sequence lithofacies paleogeography and reservoir potential of the maokou Formation in Sichuan basin. *Petroleum Explor. Dev.* 39, 51–61. doi:10.1016/s1876-3804(12)60014-7

Nie, H., He, F., and Bao, S. (2011). Peculiar geological characteristics of shale gas in China and its exploration countermeasures. *Nat. Gas. Ind.* 31, 111–116.

Peng, H., Yin, C., Zhong, Y., Yang, Y. M., Xu, L., Luo, Y., et al. (2021). A new scale shoal-forming model and natural gas exploration implications in Feixianguan Formation, northwestern Sichuan Basin, China. *Energy Explor. Exploitation* 39, 1857–1877. doi:10.1177/01445987211005219

Qiao, Z., Janson, X., Shen, A., Zheng, J., Zeng, H., Wang, X. J. M., et al. (2016). Lithofacies, architecture, and reservoir heterogeneity of tidal-dominated platform marginal oolitic shoal: An analogue of oolitic reservoirs of Lower Triassic Feixianguan Formation, Sichuan Basin, SW China. *Mar. Pet. Geol.* 76, 290–309. doi:10.1016/j.marpetgeo.2016.05.030

Shao, T., Cheng, N., and Song, M. (2016). Provenance and tectonic-paleogeographic evolution: Constraints from detrital zircon U-Pb ages of Late Triassic-Early Jurassic deposits in the northern Sichuan basin, central China. *J. Asian Earth Sci.* 127, 12–31. doi:10.1016/j.jseaes.2016.05.027

Shen, J., Algeo, T. J., Planavsky, N. J., Yu, J., Feng, Q., Song, H., et al. (2019). Mercury enrichments provide evidence of Early Triassic volcanism following the end-Permian mass extinction. *Earth-Science Rev.* 195, 191–212. doi:10.1016/j.earscirev.2019.05.010

Shen, J., Yin, R., Zhang, S., Algeo, T. J., Bottjer, D. J., Yu, J., et al. (2022). Intensified continental chemical weathering and carbon-cycle perturbations linked to volcanism during the Triassic-Jurassic transition. *Nat. Commun.* 13, 299. doi:10.1038/s41467-022-27965-x

Shen, S. Z., Zhu, M. Y., Wang, X. D., Li, G. X., Cao, C. Q., and Zhang, H. (2010). A comparison of the biological, geological events and environmental backgrounds between the Neoproterozoic-Cambrian and Permian-Triassic transitions. *Sci. China Earth Sci.* 53, 1873–1884. doi:10.1007/s11430-010-4092-y

Song, D. F., Wang, T. G., and Li, M. J. (2016). Geochemistry and possible origin of the hydrocarbons from wells Zhongshen1 and Zhongshen1C, Tazhong Uplift. *Sci. China Earth Sci.* 59, 840–850. doi:10.1007/s11430-015-5226-z

Song, D., Li, M., Shi, S., Han, Z., and Meng, B. (2019). Geochemistry and possible origin of crude oils from Bashituo oil field, Tarim Basin. *Am. Assoc. Pet. Geol. Bull.* 103, 973–995. doi:10.1306/10031817403

Wei, Z., Wang, Y., Wang, G., Sun, Z., and Xu, L. (2018a). Pore characterization of organic-rich late permian da-long Formation shale in the Sichuan basin, southwestern China. *Fuel* 211, 507–516. doi:10.1016/j.fuel.2017.09.068

Wei, Z., Wang, Y., Wang, G., Sun, Z., Zhang, T., Xu, L., et al. (2018b). Paleoenvironmental conditions of organic-rich upper permian Dalong Formation shale in the Sichuan basin, southwestern China. *Mar. Petroleum Geol.* 91, 152–162. doi:10.1016/j.marpetgeo.2017.12.003

Xia, M., Wen, L., Wang, Y., Hong, H., Fan, Y., and Wen, Y. (2010). High quality source rocks in trough facies of upper permian Dalong Formation, Sichuan basin. *Petroleum Explor. Dev.* 37, 654–662. doi:10.1016/s1876-3804(11)60002-5

Xiao, D., Cao, J., Luo, B., Tan, X., Xiao, W., He, Y., et al. (2021). Neoproterozoic postglacial paleoenvironment and hydrocarbon potential: A review and new insights from the Doushantuo Formation Sichuan basin, China. *Earth-Science Rev.* 212, 103453. doi:10.1016/j.earscirev.2020.103453

Xiao, Y., Suzuki, N., and He, W. (2017). Water depths of the latest Permian (Changhsingian) radiolarians estimated from correspondence analysis. *Earth-Science Rev.* 173, 141–158. doi:10.1016/j.earscirev.2017.08.012

Xiaoyan, R., Genming, L., Shouzhi, H., Feng, C., Si, S., Wenjun, W., et al. (2008). Molecular records of primary Producers and sedimentary environmental conditions of late permian rocks in Northeast sichuan, China. *J. China Univ. Geosciences* 19, 471–480. doi:10.1016/s1002-0705(08)60052-7

Xie, S., Algeo, T. J., Zhou, W., Ruan, X., Luo, G., Huang, J., et al. (2017). Contrasting microbial community changes during mass extinctions at the Middle/Late Permian and Permian/Triassic boundaries. *Earth Planet. Sci. Lett.* 460, 180–191. doi:10.1016/j.epsl.2016.12.015

Xie, S., Pancost, R. D., Huang, J., Wignall, P. B., Yu, J., Tang, X., et al. (2007). Changes in the global carbon cycle occurred as two episodes during the Permian-Triassic crisis. *Geol.* 35, 1083–1086. doi:10.1130/g24224a.1

Yin, H. F., and Song, H. J. (2013). Mass extinction and Pangea integration during the Paleozoic-Mesozoic transition. *Sci. China Earth Sci.* 56, 1791–1803. doi:10.1007/s11430-013-4624-3

Yin, H., Xie, S., Luo, G., Algeo, T. J., and Zhang, K. (2012). Two episodes of environmental change at the Permian-Triassic boundary of the GSSP section Meishan. *Earth-Science Rev.* 115, 163–172. doi:10.1016/j.earscirev.2012.08.006

Zou, C., Dong, D., Wang, Y., Li, X., Huang, J., Wang, S., et al. (2016). Shale gas in China: Characteristics, challenges and prospects (II). *Petroleum Explor. Dev.* 43, 182–196. doi:10.1016/s1876-3804(16)30022-2

frontiers | Frontiers in Earth Science

TYPE Original Research
PUBLISHED 13 January 2023
DOI 10.3389/feart.2022.1070924

OPEN ACCESS

EDITED BY
Juan Teng,
Yangtze University, China

REVIEWED BY
Saipeng Huang,
Northeast Petroleum University, China
Zhixing Ru,
SINOPEC Petroleum Exploration and Production Research Institute, China

*CORRESPONDENCE
Junping Huang,
cnhjp2007@163.com

SPECIALTY SECTION
This article was submitted to Geochemistry, a section of the journal Frontiers in Earth Science

RECEIVED 15 October 2022
ACCEPTED 31 October 2022
PUBLISHED 13 January 2023

CITATION
Huang J, Li X, Tan K, Xiang N and Zhang Y (2023), Discovery of solid bitumen in the Cambrian reservoirs and its geological implications in the Ordos Basin, China.
Front. Earth Sci. 10:1070924.
doi: 10.3389/feart.2022.1070924

Discovery of solid bitumen in the Cambrian reservoirs and its geological implications in the Ordos Basin, China

Junping Huang[1,2]*, Xiangbo Li[1], Kaijun Tan[1], Nijiao Xiang[1] and Yan Zhang[1]

[1]Research Institute of Petroleum Exploration & Development-Northwest PetroChina, Lanzhou, China, [2]Key Laboratory of Reservoir Description of China National Petroleum Corporation, Lanzhou, China

This study reports a comprehensive geochemical analysis of several samples of the solid bitumen recently discovered in the Cambrian reservoirs in drillings and outcrops in the Ordos Basin. The results show that the solid bitumen in the reservoir features intergranular pores and micro-fractures, with mineral particle surfaces of dolomite and limestone, and relatively clear and flat boundaries. The D and G peaks in the laser Raman spectrum were prominent. According to distributions of shapes of the D and G peaks and the relevant parameters of the laser Raman spectrum, the vitrinite equivalent reflectance (*Roeq*) values were from 2.12% to 3.46% in the solid bitumen. This indicates that the solid bitumen in the reservoirs had undergone significant thermal evolution and was mainly composed of pyrobitumen. Moreover, it mainly consisted of four types of atoms, C, O, Ca, and Mg, which confirms the hypothesis of the significant thermal evolution of the samples. In addition, the analysis of the origin of the Cambrian natural gas and the correlation between the solid bitumen and the potential source rocks show that the solid bitumen in the Cambrian reservoirs of the Southern Basin had features similar to those of the Lower Cambrian source rocks, except for the samples from well T59. All evidence suggests that the high-abundance source rocks of the Lower Cambrian have made considerable contributions to the Cambrian natural gas and the solid bitumen in the Cambrian reservoirs of the Southern Basin. The work here provides a new scientific basis for exploring natural gas in the Cambrian reservoirs and deep strata of the Ordos Basin.

KEYWORDS

solid bitumen in the reservoirs, geochemical characteristics, geological implications, Cambrian, Ordos Basin

Introduction

In recent years, our extensive observations of core samples and reconnaissance of field outcrops have led to the discovery of solid bitumen in the Cambrian reservoirs of the Ordos Basin. Horizontally, they are chiefly distributed in the Southern Basin (Figure 1A); vertically, the samples of solid bitumen in the reservoirs are mainly distributed in the Middle–Upper Cambrian (Figure 1B). Most samples of solid bitumen in the reservoirs were found in dolomite or limestone, with a few in sandstones. In general, the solid bitumen cannot be easily identified in field outcrops or drilling cores (Peters et al., 2005; Yang Hua et al., 2010; Shifa, Z et al., 2016), yet some fresh samples have an "oily" smell. The solid bitumen can be better identified using experimental approaches, such as environmental scanning electron microscopy, energy-dispersive spectrometry, and laser Raman spectroscopy.

With the discovery the of low-rate natural gas stream from the Cambrian reservoirs in the Southern Basin, the Cambrian reservoir has attracted increasing attention from explorationists. In the Middle and Late Proterozoic, a series of rift troughs that were striking north and northeast direction were developed in the Ordos Basin (YANG Junjie, 2002). During the depositional period of the Early Paleozoic, due to the influence of the inherited development of rift troughs, a number of deep-water bays were developed in the Western and Southern basins, and most of the basins were uplift. Transgression occurred in the late of the early Cambrian, and littoral deposits were developed in the Western and Southern basins. The transgression continued to expand until the middle Cambrian, the platform margin, and deep-water trough deposits were developed in the Western and Southern basins. During the late Cambrian, the sea regressed, and slope and deep-water trough deposits continued to develop in the Western and Southern basins, while constrained platform deposits were in most areas of the basin (Bai et al., 2014; Dai. 2005; Du et al., 2019). The paleogeographical framework of the Cambrian makes the distribution of the Cambrian strata particularity in the Ordos Basin. The Cambrian strata are the thickest in the Western and Southern basins but thinner in the interior of the basin (Figure 1A). Moreover, due to the Caledonian orogeny, the Ordos Basin was subjected to uplifting and erosion to different degrees during the Cambrian Period (Du et al., 2019; Hu, W. et al., 2021; Zhao, T. et al., 2021) because of which the drillings and outcrops in the basin cannot fully reveal the complete Cambrian sedimentary sequence. In addition, no large-scale reservoirs of oil and gas have yet been discovered, owing to the poor exploration of the Cambrian system. The latest research on Cambrian source rocks in the Ordos Basin shows a set of high-abundance marine source rocks that developed in the Southern Basin during the Early Cambrian (ϵ_1), with a highest *TOC* of 11.18% (Du et al., 2019). In addition to that there is the lighter carbon isotopic composition of kerogen (−31.6 to −27.4‰) (Huang et al., 2020a) and relatively high

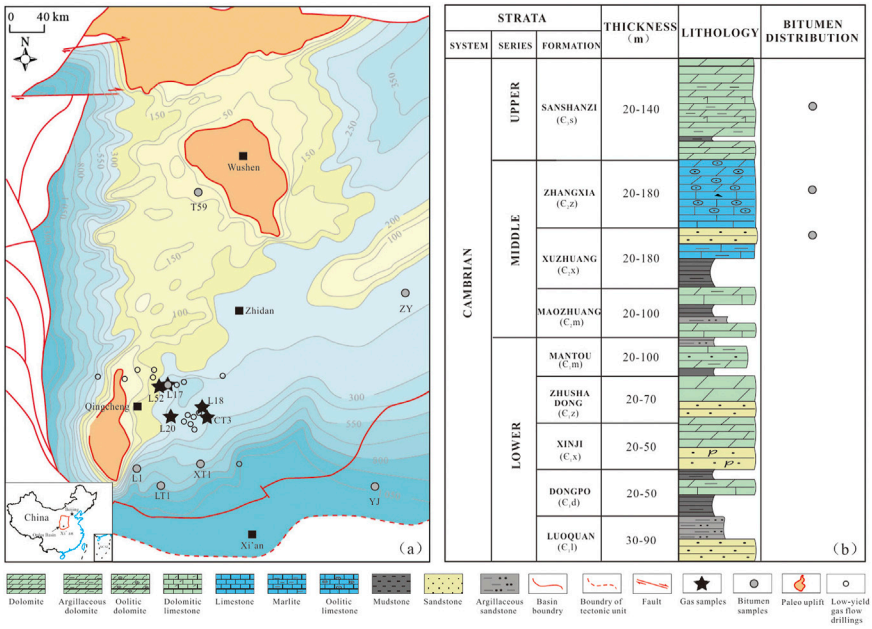

FIGURE 1
Thickness of Cambrian strata and sampling locations **(A)** and comprehensive stratigraphic column; **(B)** of the Cambrian at the southern part of the Ordos basin.

sterane/hopane ratios (S/H) (0.50–1.36) and tricyclic terpene/hopane ratios (TT/H) (0.70–1.13) (Huang et al., 2020b) in the Lower Cambrian source rocks of the Ordos Basin, which indicates that the source of the organic matter was dominated by lower algae. According to the organic matter type classification of kerogen carbon isotopic composition (Dai et al., 2005), the organic matter types of the Lower Cambrian source rocks are mainly type II, and some are type I. However, the Lower Cambrian source rocks are at high degrees of thermal evolution (Du et al., 2019; Huang et al., 2020a). Moreover, this set of source rocks has two stages of hydrocarbon generation and expulsion: the first large-scale hydrocarbon generation and expulsion period was in the Late Permian to the Middle Triassic, and then, the hydrocarbon generation stopped due to the uplift and denudation caused by the Indosinian Movement. In the Mesozoic and Cenozoic, the Ordos Basin subsides again, and there may be secondary hydrocarbon generation (Huang et al., 2020a). Thus, it has good prospects for natural gas exploration.

The solid bitumen in the Cambrian reservoirs provides direct evidence of hydrocarbon accumulation, and its presence is generally considered to indicate paleo-oil reservoirs or processes of hydrocarbon accumulation occurring through geological times. The reflectance of the Ordovician bitumen in the Ordos Basin is between 1.4% and 3.8% (Liu et al., 2009), demonstrating a highly mature stage. Generally, thermal maturity increases as burial depth increases. Also, the solid bitumen in the Cambrian reservoirs is buried deeper than the Ordovician bitumen, which indicates that the degree of thermal evolution of solid bitumen in the Cambrian reservoirs is higher than that of the Ordovician bitumen. Hence, it is critical to clarify the geochemical characteristics of the solid bitumen in the Cambrian reservoirs at a high and over-mature stage to correctly understand the Cambrian system in the Ordos Basin. This paper discusses the origin and source of the solid bitumen in the Cambrian reservoirs of the Ordos Basin based on a comprehensive analysis of its geochemical characteristics and the origin of the Cambrian natural gas.

The Ordos Basin is located in the middle and west of China, which is one of the largest petroliferous sedimentary basins in China, with an area of about 250,000 km^2 (Cai et al., 2005). During the middle and upper Proterozoic, the Ordos Basin is characterized by rifted marine deposits (Bai et al., 2014). Until the early Paleozoic, the basin was passive continental margins. The Cambrian and Ordovician are mainly carbonate platform deposits. From the end of the Ordovician to the middle of the Carboniferous, the entire basin was uplifted and denuded due to the influence of the Caledonian Movement. Transgression occurred in the middle Carboniferous, so the Carboniferous–Permian was deposited a set of alternating marine and terrestrial coal-bearing strata. The Triassic-Lower Cretaceous is characterized by lacustrine and fluvial deposits. After that, no deposition has occurred (Cai et al., 2005).

Samples and methods of analysis

The solid bitumen samples in the Cambrian reservoirs of the Ordos Basin were collected from drillings and outcrops, and the sampling location is shown in Figure 1A. The gaseous samples were mainly collected from the Qingcheng area in the Southern Basin (Figure 1A). The solid bitumen samples were subjected to environmental scanning electron microscopy (ESEM), energy-dispersive spectroscopy, laser Raman spectroscopy, and trace element analysis. In the field-emission environmental SEM analysis, the solid bitumen samples were first cut into 1 m^3 cubes or irregular blocks. A relatively flat and fresh section was selected and observed under the FEI ESEM Quanta™ 450 FEG equipped with an energy spectrometer. The energy-dispersive spectroscopic analysis of the area of interest was carried out using the Genesis Apollo XL instrument after correcting the energy spectrometer using cadmium or gold.

A LabRAM HR Evolution Confocal Raman microspectroscope was used for Raman spectroscopic measurement of samples. Main experimental conditions for Raman analysis include the following: a solid laser device of 532 nm/50 mW, confocal pinhole of 400 μm, raster slit of 100 μm, exposure time of 3–8 s, scanning wave number range 100–4000 cm^{-1}, and a silicon wafer to be used for the wave number calibration of the Raman spectroscope. The samples were ground into powder less than 200 mesh for trace element (element composition) analysis based on the ZSX Primus II X-ray fluorescence spectrometer.

Results

Geochemical characteristics of the solid bitumen in the reservoirs

Microscopic observations showed that the solid bitumen in the Cambrian reservoirs featured micro-fractures and intergranular pores in the form of strips (Figure 2A) and rings (Figures 2B,C). Moreover, most of the samples had clear boundaries, which indicates that the bitumen may mainly consist of pyrobitumen subjected to heat-induced alteration. Compared with bitumen from different origins, pyrobitumen usually has a clearer and straighter boundary (Stasiuk, 1997; Hwang et al., 1998; Hao F et al., 2011). Most of the samples were sheet-like, and some were observed on the surfaces of mineral particles in the SEM images (Figures 2D–F), which may demonstrate the process of cracking and coking of crude oil. This is because during the high-temperature cracking and coking of crude oil, small mesophase spheroids with optic anisotropy first emerge from the isotropic mother liquor; then, with progressive evolution, the mesophase spheroids continuously grow and deform and eventually change into sheet-like heterogeneous textures (Liu et al., 2009; Hao Bin et al., 2016).

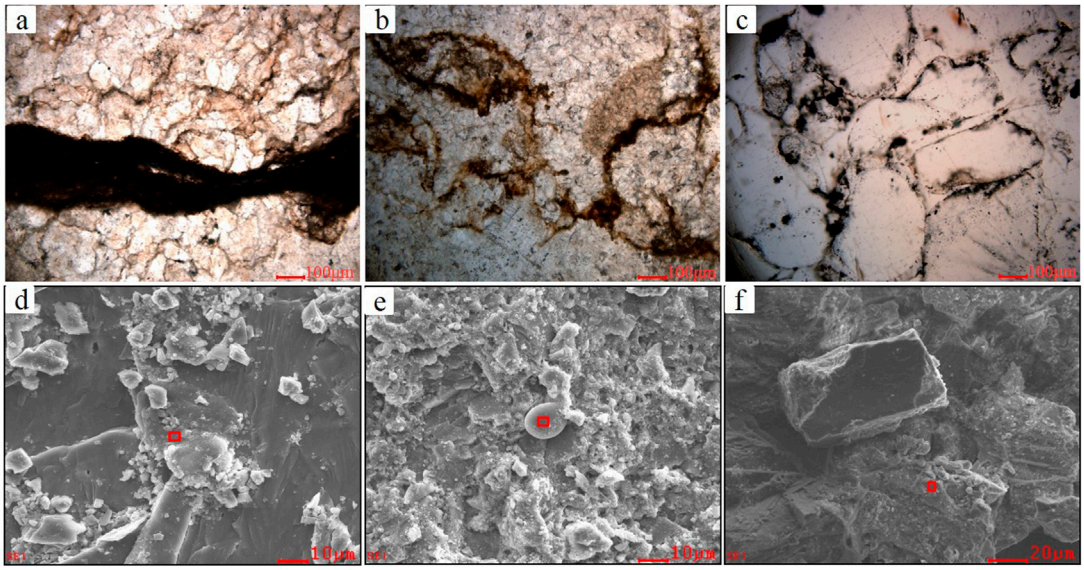

FIGURE 2
Examples of microscopic images showing the optical characteristics of solid bitumen in the Cambrian reservoirs of the Ordos Basin. **(A)** Bitumen in fractured dolomite, ϵ_2z, 4190.3 m, well L17; **(B)** bitumen in intergranular pores of limestone, ϵ_2z, ZY outcrop in Shanxi province; **(C)** bitumen in the intercrystalline pores of sandstone, ϵ_2x, 4348.0 m, well T59; **(D)** bitumen in dolomite, ϵ_2z, 4720.1m, well LT1; **(E)** bitumen in oolitic limestone, ϵ_2x, YJ outcrop in Shanxi province; **(F)** bitumen in dolomite, ϵ_1s, 3982.0 m, well L1.

The energy spectrum (Figure 3) showed that the solid bitumen in the Cambrian reservoirs of the Ordos Basin was mainly composed of C, O, Ca, and Mg atoms, where this can be attributed to the host minerals (chiefly dolomite and limestone) of the solid bitumen in the reservoirs. The mass fraction of Au atoms in the samples was high (up to 21.47% in some samples), yet it was artificially plated onto samples prior to the analysis, which means that this mass fraction was a background value. Moreover, the mass fraction of C atoms was 8.99%–45.68%, corresponding to even higher atomic fractions (15.19%–59.49%), and the mass fraction of O atoms was 19.67%–47.26%, with atomic fractions of 27.98%–59.70%. This indicates that the solid bitumen in the reservoirs had undergone carbonization and high thermal evolution.

The laser Raman spectrum presented two characteristic peaks of solid bitumen in the reservoirs (Olivier Beyssac et al., 2002, 2003; Lahfid et al., 2010), i.e., a "defect peak" (also known as the "D-peak", usually at 1320–1330 cm^{-1}) and a "graphite peak" (also known as the "G-peak," often within 1590–1650 cm^{-1}) (Kostova et al., 2012) (Figure 4). The existence of these characteristic peaks confirmed that the analyzed samples were in fact bitumen from the reservoirs. In general, with increasing maturity of bitumen, the peaks D and G of the samples become more pronounced and sharper, with peak G higher than peak D (Quirico et al., 2005).

The wavelengths of D and G peaks and the wavelength difference between D and G peaks in the laser Raman spectrum parameters are commonly used to quantitatively characterize the thermal evolution degree of solid bitumens (Wang et al., 2015). The laser Raman parameters of solid bitumen in the Cambrian reservoirs of the Ordos Basin are shown in Table 1. According to the wavelength difference between the D and G peak positions, the solid bitumen reflectance (*Rb*) in the Cambrian reservoirs can be calculated (Wang et al., 2015), which is between 1.98% and 3.39%. According to the conversion formulas in different publications (Jacob, 1989; Landis and Castano, 1995; Schoenherr et al., 2007), the bitumen reflectance (*Rb*) can be converted to the vitrinite equivalent reflectance (*Roeq*) (Table 1). However, both calibrations of the vitrinite equivalent reflectance (*Roeq*) differ from each other (Table 1). The *Rb* data on the solid bitumen in the Cambrian reservoirs of the Ordos Basin have their maximum at 3.39% (Table 1), and the regression equation of Jacob (1989) only includes the *Rb* value with a maximum of up to 2.7%, which caused the calibration small. However, the calibration of Landis and Castano (1995) is bigger than that of Jacob (1989), which may be either the high maturity of the selected samples or the fact that the formula itself has a certain scope of application. The calibration results of Schoenherr (2007) are used in this paper. Because the regression equation of Schoenherr (2007) combined the datasets of Jacob (1989) and Landis and Castano (1995), in which both samples with *Rb* values less than 2.7% and samples with *Rb* values greater than 4.0% are considered. The vitrinite equivalent reflectance (*Roeq*) of solid bitumen in the Cambrian

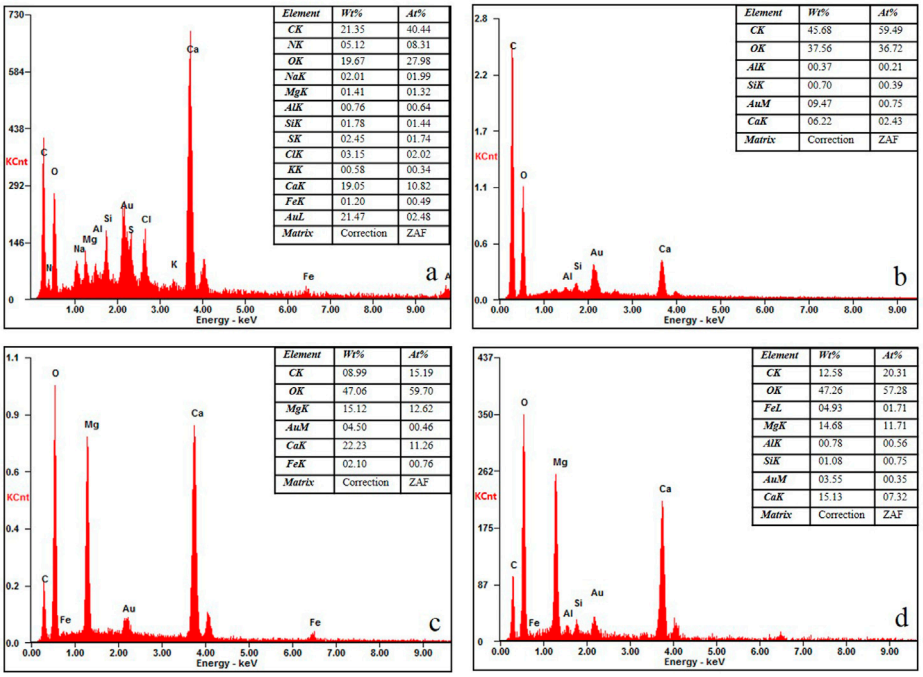

FIGURE 3
Characteristics of the energy spectrum of the solid bitumen in the Cambrian reservoirs. **(A)** ϵ_2z, 4720.1 m, well LT1. The energy spectrum shows that it mainly included C, O, Ca, and N. A higher content of C atoms occurred primarily due to the interference of the background (e.g., solid reservoir bitumen); **(B)** ϵ_2x, YJ outcrop in Shanxi province, with the energy spectrum indicating the bitumen; **(C)** ϵ_2z, ZY outcrop in Shanxi province. The energy spectrum shows that it included O, Mg, Ca, and C. Higher contents of Mg and Ca atoms indicate that the bitumen had occurred in dolomite; **(D)** ϵ_1s, 3982.0 m, well L1, with the energy spectrum indicating bitumen.

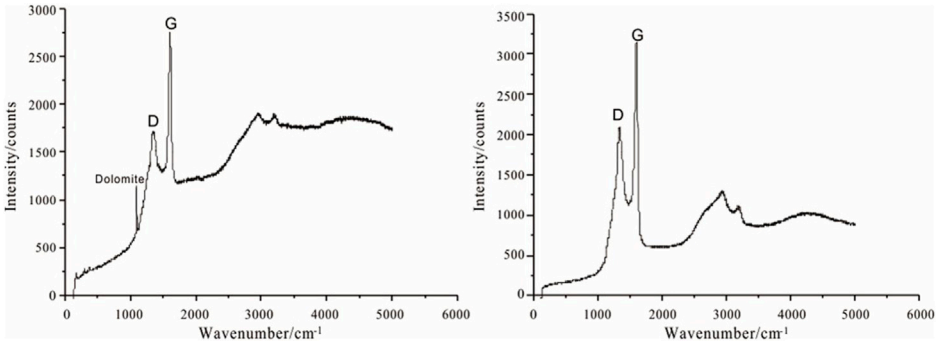

FIGURE 4
Laser Raman spectrogram of solid bitumen in the Cambrian reservoirs. Left–bitumen in dolomite, ϵ_2z, 4190.3 m, well L17; Right–bitumen in dolomite with intercrystalline pores, ϵ_2z, 3920.2 m, well XT1.

reservoirs of the Ordos Basin is calculated to be 2.12%–3.46% (Schoenherr et al., 2007), indicating that the solid bitumens in the Cambrian reservoir of the Ordos Basin had undergone a high thermal evolution process and is at the over-mature stage.

As shown in Figure 2, the solid bitumen in the Cambrian reservoirs of the Ordos Basin has a distinguishable optical microstructure. The solid bitumen in the reservoirs in Figures 2A–C is mainly filled with microfractures and intergranular pores. Also, the solid bitumen in the reservoirs in Figures 2D–F is mainly hosted on the surface of mineral particles. However, all the solid bitumen samples in the Cambrian reservoirs of the Ordos Basin do not display any fluorescence.

TABLE 1 Cambrian bitumen reflectance (Rb) data in the reservoirs of the Ordos Basin and their conversion into vitrinite equivalent reflectance (Roeq) values according to different authors.

Sample no./well name	Formation	D-band wavelength (cm^{-1})	G-band wavelength (cm^{-1})	Wavelength difference (G-D) (cm^{-1})	Wang et al. (2015) [a] bitumen reflectance (Rb%)	Jacob (1989) [b] (Roeq %)	Schoenherr et al. (2007) [c] (Roeq%)	Landis et al. (1995) [d] (Roeq %)
ZY-1	ϵ_2z	1338.0	1608.0	270.0	3.39	2.50	3.46	3.48
ZY-2	ϵ_2z	1350.0	1606.0	256.0	2.58	1.99	2.69	2.73
T59	ϵ_2x	1357.8	1603.5	245.7	1.98	1.62	2.12	2.18
L17	ϵ_2z	1360.9	1625.1	264.2	3.05	2.29	3.14	3.17
XT1	ϵ_2z	1330.3	1593.5	263.3	3.00	2.25	3.09	3.12

[a]Rb% = 0.058 wavelength difference (G-D) −12.27.
[b]Roeq% = 0.618 Rb%+0.40.
[c]Roeq% = (Rb%+0.2443)/1.0495.
[d]Roeq% = (Rb%+0.4)/1.09.

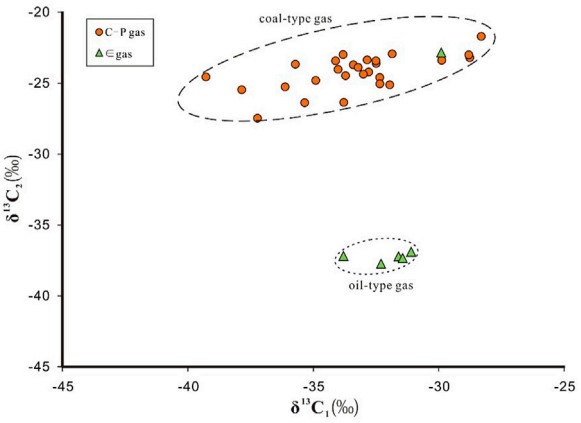

FIGURE 5
Scatter plots of $\delta^{13}C_1$ and $\delta^{13}C_2$ in the Cambrian natural gas of the Ordos Basin.

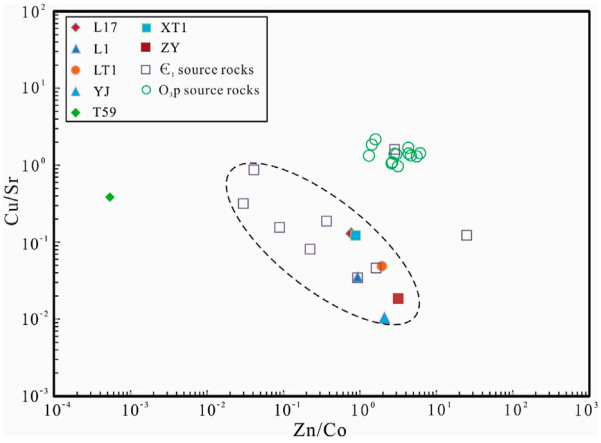

FIGURE 6
Trace element ratio scatterplot shows solid bitumen in the Cambrian reservoirs and potential source rocks of the Ordos Basin.

Correlation between solid bitumen in the reservoirs and potential source rocks

The mature bitumen had undergone a series of changes in terms of the commonly used organic geochemical indicator for bitumen–source rock correlation. This made it difficult to apply such parameters as biomarkers and stable carbon isotope ratios to the correlation to achieve the desired performance (Liang and Chen, 2005; Peters et al., 2005). Given this, the correlation between solid bitumen in the reservoirs and the source rock was investigated mainly with respect to the origin of the Cambrian natural gas and trace elements less affected by thermal maturity.

As illustrated by the cross-plot between the carbon isotope ratios of methane ($\delta^{13}C_1$) and ethane ($\delta^{13}C_2$) (Figure 5), the coal-type gas from the Upper Paleozoic Carboniferous–Permian was different from the Cambrian natural gas. Although the ranges of distribution of $\delta^{13}C_1$ for these two natural gases partially coincided, their values of $\delta^{13}C_2$ were significantly different. Overall, the content of $\delta^{13}C_2$ of the Cambrian natural gas was relatively low, mostly between −36.90% and −37.74%, exhibiting the characteristics of the oil-type gas. Only one sample contained $\delta^{13}C_2$ within the range of a coal-type gas. By comprehensively considering the planar distribution of the Cambrian natural gas samples (Figure 1A) and the source rocks (Du et al., 2019), it is inferred

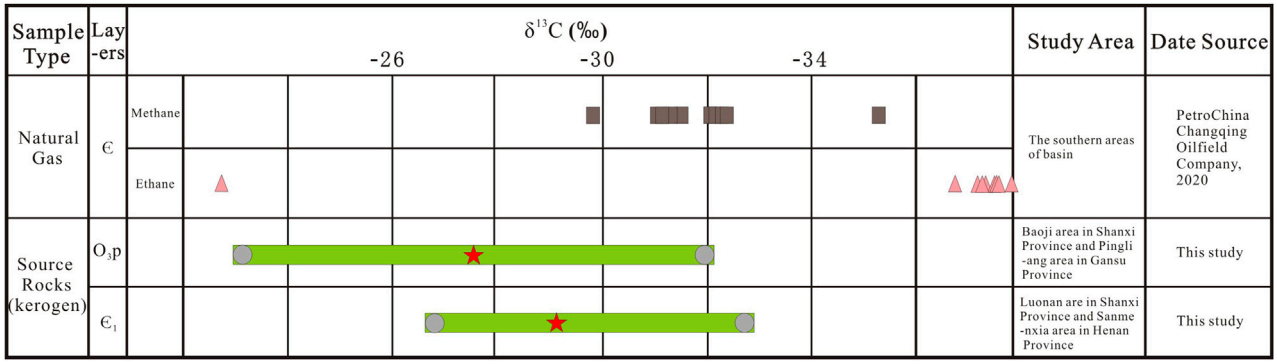

FIGURE 7
Carbon isotopic distribution of the Cambrian natural gas and the kerogen carbon isotopic distribution of the potential marine source rocks in the Ordos Basin.

that the natural gas had mainly come from the Cambrian or Ordovician marine source rocks in the Southern Basin.

The trace elements in the solid bitumen also contain genetic information on the parent rock, just like biomarkers and, more importantly, are not susceptible to hydrocarbon migration, reservoir destruction, oxidation, and biodegradation (Al-Shahristani et al., 1972; Lewan et al., 1982; Filby R H, 1994; Ramirez, 2013; Ping Gao et al., 2015; Chunhua Shi et al., 2015). Therefore, the trace elements were useful indicators to examine the correlation between bitumen in the over-mature Cambrian reservoir and the source rock of the Ordos Basin. The cross-plot of Cu/Sr versus Zn/Co for the trace elements clearly shows that most of the solid bitumen in the Cambrian reservoirs had similar characteristics of distribution to those of the Lower Cambrian source rock samples but are different from those of the Upper Ordovician Piangliang Formation source rocks (O_3p) (Figure 6). Interestingly, the trace element ratios (Cu/Sr and Zn/Co) of the solid bitumen samples in well T59 are not similar to those of the ϵ_1 and O_3p potential source rocks.

Discussion

It is worth noting that the low-yield gas flow drillings of the Cambrian are mainly distributed around the Qingyang paleo-uplift in the southwest of the Ordos Basin (Figure 1A). The ethane carbon isotope of the Cambrian in the Lower Paleozoic natural gas of the Ordos Basin is the lightest, which is lighter than the methane carbon isotope value of the Cambrian natural gas, and almost all of them are less than −36‰ (Huang et al., 2021). From the carbon isotope distribution of the Cambrian natural gas and the kerogen carbon isotopic distribution of the potential marine source rocks in the Lower Cambrian and the Upper Ordovician Pingliang Formation developed in the Western and Southern basins (Figure 7), it can be inferred that the carbon isotopic distributions of the Cambrian natural gas are similar to the kerogen carbon isotopic distributions of the Lower Cambrian source rocks. Generally, the ethane carbon isotope values of natural gas are mainly related to the type of organic matters. The ethane carbon isotope values of the oil-type natural gas are lighter, which are derived from sapropel-type organic matters. Also, the coal-type gas derived from humic-type organic matters has much heavier the ethane carbon isotope values (Huang et al., 1996).

The discovery and source of solid bitumen in the Cambrian reservoirs of the Ordos Basin provides direct evidence of hydrocarbon generation and accumulation in the Lower Cambrian source rocks. The solid bitumen in the Cambrian reservoirs is mainly located in the Western and Southern basins, and less in other places, which may be attributed to the planar distribution of the paleogeography (Dai. 2005; Bai et al., 2014; Du et al., 2019) and strata thickness (Figure 1A) of the Cambrian in the Ordos Basin. The solid bitumen in the Cambrian reservoirs was formed by over-mature pyrobitumen, which indicates that it might have been the product of cracking of crude oil. Moreover, an examination of the correlation between the solid bitumen in the reservoirs and the potential source rocks revealed similar distributions of trace elements (Cu/Sr and Zn/Co) between the solid bitumen in the Cambrian reservoirs and the Lower Cambrian source rocks in the Southern Basin, where well T59 in the basin was an exception. This shows that the solid bitumen in the Southern Basin might have primarily originated from the Lower Cambrian source rocks, while that in well T59 can be attributed to another source rock.

The structural-sedimentary evolution characteristics in the Southern Basin further show that the Caledonian Movement and Huaiyuan Movement caused the Cambrian–Ordovician strata to suffer overall uplift and denudation in the Ordos Basin, but the

original structural framework was not changed (Huang et al., 2021). Also, the Cambrian–Ordovician strata of the Qingyang paleo-uplift in the southwest of the basin still keep dipping southward. Therefore, before the Late Triassic, the Qingyang paleo-uplift in the southwest of the Ordos Basin and the surrounding areas were the oil and gas migration areas, which were favorable for oil and gas migration and accumulation in the highly abundant marine source rocks from the Lower Cambrian.

Conclusion

The presence of solid bitumen in the Cambrian reservoirs of the Ordos Basin may represent a self-generating, self-storing pattern of hydrocarbon accumulation and provides direct evidence of hydrocarbon generation and expulsion in the Lower Cambrian source rocks of the Southern Basin. The highly abundant marine source rocks of the Lower Cambrian were revealed by outcrop profiles only in the Southern Basin, which is consistent with the solid bitumen being primarily distributed in the Southern Basin. This suggests that the Lower Cambrian source rocks might have contributed to the source of solid bitumen in the Cambrian reservoirs. The analysis of the microscopic characteristics, energy spectrum, and Raman spectrum of the samples showed that the solid bitumen in the Cambrian reservoirs was formed by over-mature pyrobitumen, where this is consistent with the degree of thermal evolution of the source rocks from the Lower Cambrian. Moreover, the oil-type origin of the Cambrian natural gas in the Southern Basin and the similar characteristics of distribution of certain trace elements shared between the solid bitumen in the Cambrian reservoirs and the source rocks further support the claim that the solid bitumen in the Southern Basin mainly originated from the highly abundant source rocks from the Lower Cambrian. This study on the correlation between the solid bitumen in the Cambrian reservoirs and the Lower Cambrian source rocks provides a new frontier for exploring natural gas in the Cambrian and the deep strata of the Ordos Basin.

Data availability statement

The original contributions presented in the study are included in the article/supplementary material; further inquiries can be directed to the corresponding author.

Author contributions

JH: writing—idea, original draft, formal analysis, and methodology. XL: review and editing, and supervision. KT: resources and project administration. NX and YZ: experiments and analysis.

Funding

The authors declare that this study received funding from the Scientific Research and Technical Development of PetroChina (No.kt2021-04-01) and (2022KT0103). The funder was not involved in the study design, collection, analysis, interpretation of data, the writing of this article, or the decision to submit it for publication.

Acknowledgments

The authors thank Yuan Xiaoqi, a senior engineer with the Exploration and Development Research Institute of CNPC Changqing Oilfield Company, for his help in field work. In addition, they greatly appreciate the journal reviewers for their critical, constructive, valuable, and helpful comments, which considerably improved the clarity of the manuscript.

Conflict of interest

Author JH was employed by the China National Petroleum Corporation.

The remaining authors declare that the research was conducted in the absence of any commercial or financial relationships that could be construed as a potential conflict of interest.

Publisher's note

References

Al-Shahristani, H., and Al-Atyia, M. J. (1972). Vertical migration of oil in Iraqi oil fields: Evidence based on vanadium and nickel concentrations. *Geochimica Cosmochimica Acta* 36 (9), 929–938. doi:10.1016/0016-7037(72)90013-0

Yunlai, B., Yuhu, M., Yong, H., Jianbo, L., Xiaoguang, L., et al. (2014). Sedimentary Characteristics and hydrocarbon exploration implications on the Cambrian Aulacogen of the southern Ordos continental margin, north China. *Nat. Gas. Geosci.* 25 (11), 1706–1717. (in Chinese with English abstract).

Beyssac, Olivier, Goffe´, Bruno, Petitet, Jean-Pierre, Froigneux, Emmanuel, Moreau, Myriam, and Rouzaud, Jean-Noe¨l. (2003). On the characterization of disordered and heterogeneous carbonaceous materials by Raman spectroscopy. *Spectrochimica Acta Part A Mol. Biomol. Spectrosc.* 59, 2267–2276. doi:10.1016/s1386-1425(03)00070-2

Beyssac, Olivier, Jean-Noel, Rouzaud, Goffe´, Bruno, Brunet, Fabrice, and Chopin, Christian (2002). Graphitization in a high-pressure, low-temperature

metamorphic gradient: A Raman microspectroscopy and HRTEM study. *Contrib. Mineral. Pet.* 143, 19–31. doi:10.1007/s00410-001-0324-7

Bin, Hao, Hu, Suyun, Huang, Shipeng, Hu, J., Shi, S., Wang, K., and Liang, D. (2016). Geochemical characteristics and its significance of reservoir bitumen of longwangmiao formation in moxi area, sichuan basin. *GEOSCIENCE* 30 (3), 614–625. (in Chinese with English abstract).

Charleslandis, R., and Castano, J. O. H. N. R. (1995). Maturation and bulk chemical properties of a suite of solid hydrocarbons. *Org. Geochem.* 22, 137–149. doi:10.1016/0146-6380(95)90013-6

Cai, C. F., Hu, G. Y., He, H., Li, J., Li, J. F., and Wu, Y. S. (2005). Geochemical characteristics and origin of natural gas and thermochemical sulphate reduction in Ordovician carbonates in the Ordos Basin, China. *J. Pet. Sci. Eng.* 48, 209–226. doi:10.1016/j.petrol.2005.06.007

Dai, J. X., Liu, D. L., Qin, S. F., et al. (2005). *The Cambrian source rocks in southern margin of North China Basin*. Beijing: Petroleum Industry Press.

Du, J. H., Li, X. B., Bao, H. P., Xu, W. L., Wang, Y. T., Huang, J. P., et al. (2019). Geological conditions of natural gas accumulation and new exploration areas in the Mesoproterozoic to Lower Paleozoic of Ordos Basin, NW China. *Petroleum Explor. Dev.* 46 (5), 866–882. (in Chinese with English abstract). doi:10.1016/s1876-3804(19)60246-6

Filby, R. H. 1994. Origin and nature of trace element species in crude oils: Implications for correlation and other geochemical studies[C] Parnell J ed. Geofluids: Origin, Migration and Evolution of Fluids in Sedimentary Basins (Geological Society Special Publication). London: School of Geosciences The Queen's University of Belfast, 78: 203–221

Gao, Ping, Liu, Guangdi, Wang, Zecheng, Jia, Chengzao, Wang, Tongshan, and Zhang, Pengwei (2015). Rare Earth elements (REEs) geochemistry of sinian–cambrian reservoir solid bitumens in sichuan basin, SW China: Potential application to petroleum exploration. *Geol. J.* 95 (6), 298–316. doi:10.1002/gj.2757

Hao, F., Zhang, Z. H., Zou, H. Y., Zhang, Y., and Yang, Y. (2011). Origin and mechanism of the formation of the low-oil-saturation moxizhuang field, junggar basin, China: Implication for petroleum exploration in basins having complex histories. *Am. Assoc. Pet. Geol. Bull.* 95 (6), 983–1008. doi:10.1306/11191010114

Hu, W., Wang, Q., Zhao, R., and Ru, Z. (2021). Evaluation and application of conductivity of strike slip faults in China Shunbei reservoir, Tarim Basin. *Arab. J. Geosci.* 14, 619. doi:10.1007/s12517-021-06980-0

Huang, D. F, Xiong, C. W., Yang, J. J, et al. (1996). Gas source identification and genetic types of natural gas in the central gas field of Ordos Basin. *Nat. Gas. Ind.* 16 (6). 1-5 (in Chinese with English abstract).

Huang, J., Li, X., He, W., Wan, Y., Bao, H., Xu, Y., Wang, H., Zhang, G., Wang, J., et al. (2020a). Development characteristics of high abundance source rocks of the Lower Cambrian and dierection of oil and gas exploration in southern margin of Ordos Basin. *Mar. Orig. Pet. Geol.* 25 (4), 319–325. (in Chinese with English abstract). doi:10.3969/j.issn.1672-9854.2020.04.004

Huang, J. P., Li, X. B., He, W. X., WanYan, R., Bao, H. P., Xu, Y. H., et al. (2020b). Formation environment and development models for the Lower Cambrian source rocks of the southern North China Plate, China. *ACS OMEGA* 5, 8001–8011. doi:10.1021/acsomega.0c00077

Huang, Junping, Lin, Junfeng, Zhang, Yan, et al. (2021). The Organic geochemical characteristics of Lower Cambrian marine source rocks and its contribution to hydrocarbon accumulation in the Southern Margin of Ordos Basin. *Nat. Gas. Geosci.* (in Chinese with English abstract). doi:10.11764/j.issn.1672-1926.2021.11.007

Hwang, R. S., Teeman, S., and Carlson, R. (1998). Geochemical comparison of reservoir solid bitumens with diverse origins. *Org. Geochem.* 29, 505–517. doi:10.1016/s0146-6380(98)00078-3

Jacob, H. (1989). Classification, structure, Genesis and practical importance of natural solid oil bitumen ("migrabitumen"). *Int. J. Coal Geol.* 11 (1), 65–79. doi:10.1016/0166-5162(89)90113-4

Kostova, I., Tormo, L. K., Crespo-Feo, E., and Garcia-Guinea, J. (2012). Study of coal and graphite specimens by means of Raman and cathodoluminescence. *Spectrochimica Acta Part A Mol. Biomol. Spectrosc.* 91, 67–74. doi:10.1016/j.saa.2012.01.056

Lahfid, A., Beyssac, O., Deville, E., Negro, F., Chopin, C., and Goffe´, B. (2010). Evolution of the Raman spectrum of carbonaceous material in low-grade metasediments of the Glarus Alps (Switzerland). *Terra nova.* 22, 354–360. doi:10.1111/j.1365-3121.2010.00956.x

Lewan, M. D., and Maynard, J. B. (1982). Factors controlling enrichment of vanadium and nickel in the bitumen of organic sedimentary rocks. *Geochimica Cosmochimica Acta* 46, 2547–2560. doi:10.1016/0016-7037(82)90377-5

Liang, D., and Chen, J. (2005). Oil–source correlations for high and over matured marine source rocks in South China. *Petroleum Explor. Dev.* 32, 8–14. (in Chinese with English abstract).

Liu, D. H., Xiao, X. M., Tian, H., et al. (2009). Application of fluid inclusions and bitumen characteristics to determine the Genesis of natural gas. *Petroleum Explor. Dev.* 36 (3), 375–382. (in Chinese with English abstract).

Liu, Q. Y., Chen, M. J., Liu, W. H., Li, J., Han, P. L., and Guo, Y. R. (2009). Origin of natural gas from the Ordovician paleo-weathering crust and gas-filling model in Jingbian gas field, Ordos basin, China. *J. Asian Earth Sci.* 35, 74–88. doi:10.1016/j.jseaes.2009.01.005

Peters, K. E., Walters, C. C., and Moldowan, J. M. (2005). The biomarker guide. *Biomarkers Isotopes Petroleum Explor. Earth Hist.* 2, 475–1155. second ed. Cambridge University Press, Cambridge.

Quirico, E., Rouzaud, J-N., Bonal, L., and Montagnac, G. (2005). Maturation grade of coals as revealed by Raman spectroscopy: Progress and problems. *Spectrochimica Acta Part A Mol. Biomol. Spectrosc.* 61, 2368–2377. doi:10.1016/j.saa.2005.02.015

Ramirez-Caro, D. (2013). *Rare earth elements (REE) as geochemical clues to reconstruct hydrocarbon generation history (M.S. dissertation)*. Kansas State University, Manhattan 1–77.

Schoenherr, J., Littke, R., Urai, J. L., Kukla, P. A., and Rawahi, Z. (2007). Polyphase thermal evolution in the Infra-Cambrian Ara Group (South Oman Salt Basin) as deduced by maturity of solid reservoir bitumen. *Org. Geochem.* 38, 1293–1318. doi:10.1016/j.orggeochem.2007.03.010

Shi, Chunhua, Cao, Jian, Bao, Jianping, Zhu, Cuishan, Jiang, Xingchao, and Wu, Ming (2015). Source characterization of highly mature pyrobitumens using trace and rare Earth element geochemistry: Sinian–Paleozoic paleo-oil reservoirs in South China. *Org. Geochem.* 83-84, 77–93. doi:10.1016/j.orggeochem.2015.03.008

Shifa, Z., Xiaomin, Z., Xin, L., Dong, W., and Dongna, Z. (2016). Authigenic minerals and diagenetic evolution in altered volcanic materials and their impacts on hydrocarbon reservoirs: Evidence from the lower permian in the northwestern margin of junggar basin, China. *Arab. J. Geosci.* 9, 97. doi:10.1007/s12517-015-2201-0

Stasiuk, L. D. (1997). The origin of pyrobitumens in upper devonian leduc formation gas reservoirs, alberta, Canada: An optical and EDS study of oil to gas transformation. *Mar. Petroleum Geol.* 14, 915–929. doi:10.1016/s0264-8172(97)00031-7

Wang, Maolin, Xiao, Xianming, Qiang, Wei, et al. (2015). Thermal maturation of solid bitumen in shale as revealed by Raman spectroscopy. *Nat. Gas. Geosci.* 26 (9), 1712–1718. (in Chinese with English abstract). doi:10.11764/j.issn.1672-1926.2015.09.1712

Yang, Hua, Fu, Jinhua, and Bao, Hongping (2010). Sedimentary characteristics and gas accumulation potential along margin of ordovician trough in western and southern parts of Ordos. *Mar. Orig. Pet. Geol.* 15 (2), 1–13. (in Chinese with English abstract).

Yang, Junjie (2002). *Tectonic evolution and oil-gas reservoirs distribution in Ordos Basin*. Beijing: Petroleum Industry Press.

Zhao, T., Hu, W., Zhao, R., Yang, M., Wang, Q., Lin, H., et al. (2021). Present *in-situ* stress distribution characteristics of strike-slip in SH Oilfield, Tarim Basin. *Arab. J. Geosci.* 14, 1223. doi:10.1007/s12517-021-07552-y

frontiers | Frontiers in Earth Science

TYPE Original Research
PUBLISHED 17 January 2023
DOI 10.3389/feart.2022.1071466

OPEN ACCESS

EDITED BY
Tao Hu,
China University of Petroleum, China

REVIEWED BY
Di Chen,
China University of Petroleum, China
Li Ang,
Jilin University, China

*CORRESPONDENCE
Longlong Li,
lilonglongyx@126.com

SPECIALTY SECTION
This article was submitted to Geochemistry, a section of the journal Frontiers in Earth Science

RECEIVED 16 October 2022
ACCEPTED 11 November 2022
PUBLISHED 17 January 2023

CITATION
Peng J, Li L, Du C, Liu X, Zhu J, Liang S, Qiu Q and Wang D (2023), Hydrocarbon generation and expulsion modeling of different lithological combination source rocks from the Funing Formation in the Subei Basin.
Front. Earth Sci. 10:1071466.
doi: 10.3389/feart.2022.1071466

Hydrocarbon generation and expulsion modeling of different lithological combination source rocks from the Funing Formation in the Subei Basin

Jinning Peng[1,2], Longlong Li[1,2]*, Chongjiao Du[1,2], Xu Liu[1,2], Jianhui Zhu[1,2], Shiyou Liang[1,2], Qi Qiu[1,2] and Dongyan Wang[1,2]

[1]Wuxi Research Institute of Petroleum Geology, SINOPEC Petroleum Exploration and Production Research Institute, Wuxi, China, [2]State Key Laboratory of Shale Oil and Gas Enrichment Mechanisms and Effective Development, Wuxi, China

The oil expulsion efficiency and retention efficiency of shale affect the enrichment and preservation of shale oil. Two series of semi-closed hydrous pyrolysis experiments were performed under *in situ* geological conditions on a Paleogene shale sample as a comparable analog to evaluate the generation and preservation potential of shale oil in the Funing Formation shale in the Subei Basin. The results show that 1) the oil-generation capacity evolution of different lithological combination source rocks in the Funing Formation of the Subei Basin can be roughly divided into four stages: a) relatively slow oil-generating and slow gas-generating, b) relatively fast oil-generating and slow gas-generating, c) oil cracking into gas, and d) kerogen cracking into gas; 2) different lithological combinations have different hydrocarbon generation, expulsion, and retention efficiencies. The total oil generation rate and gas generation rate of pure shale are higher than those of shale with a silty interlayer, and the exchange point between the oil expulsion rate and retention rate of pure shale is earlier than that of shale with the silty interlayer, which indicates that the pure shale experienced the expulsion and retention process earlier. Oil retention mainly occurs at an EqVRo of 0.84%–1.12%, while oil is mainly discharged to the adjacent siltstone at an EqVRo of 1.12%–1.28%. Based on the simulation under geological conditions, it is recognized that for shale oil exploration in the Subei Basin, the favorable thermal maturity is at an EqVRo of 0.84%–1.12%, and the favorable lithology is the shale with the silty interlayer. On one hand, the siltstone interlayer can provide pore space for the early generated oil, and the concentration difference of hydrocarbons between the shale and the interlayer can be formed so that the generated shale can continuously enter the interlayer. On the other hand, the shale above the interlayer can be used as a cap rock to preserve shale oil. The favorable area for shale oil exploration in the Subei Basin is the area with relatively high maturity (at a VR value of about 1.1%)

KEYWORDS

shale oil, lacustrine shale, hydrocarbon generation and expulsion, modeling, Subei Basin

1 Introduction

The successful exploration and production of Chang 7 shale oil in the Ordos Basin and the Lucaogou shale oil in the Junggar Basin have made scholars realize the promising prospective of lacustrine shale oil worldwide (Jia et al., 2012; Yang et al., 2017; Hu et al., 2018; Hou et al., 2021a; Hu et al., 2021; Jin et al., 2021; Wang et al., 2022). In 2021, the wells SD1, QY1-HF, and SY3-7HF, were drilled into the Funing Formation in the Subei Basin and harvested high oil flow reaching industrial production levels with a proven reserve exceeding 3.5 $\times 10^9$ t, making the Funing Formation another important target for shale oil exploration in China (Yao et al., 2021).

The second member (E_1f^2) and fourth member (E_1f^4) of the Paleogene Funing Formation in the Subei Basin, with abundant shale oil sources, have been highly valued. These source rocks are characterized by a medium degree of thermal maturation and TOC, good organic matter type, large thickness, and wide distribution, which provide material conditions for the occurrence and enrichment of shale oil (Ji et al., 2013). Many previous works have been conducted on organic and inorganic geochemical characteristics, sedimentary environment, physical properties, and fractures of the Funing shale in the Subei Basin (Zhang et al., 2003; Quaye et al., 2018; Cheng et al., 2019; Liu et al., 2020; Peng et al., 2020). Meanwhile, many favorable areas of shale oil exploration were proposed and implemented (Zan et al., 2021a).

However, little interest has been paid to hydrocarbon generation and expulsion at the different stages of thermal maturity for the Funing shale, which is a key issue in shale oil exploration. Significant progress has been made in the study of hydrocarbon generation and expulsion of other lacustrine shales, but they cannot directly apply to the Funing shale, which is due to its strong heterogeneity and variation in large sedimentary facies (Anyiam and Onuoha, 2014; Shi et al., 2018; Tang et al., 2018; Ma et al., 2020). The Funing shale often contains thin siltstone and a carbonate interlayer, which may have a potential impact on hydrocarbon generation and expulsion. Therefore, a detailed analysis is crucial to the hydrocarbon generation and expulsion of organic-rich shales in the Funing Formation.

Pyrolysis experiments are important methods to understand the formation and evolution processes of oil and gas (Mahlstedt and Horsfield, 2012; Uguna et al., 2016). Pyrolysis experiments have been conducted to investigate the influences of the oil expulsion efficiency on shale gas generation and occurrence (Hill et al., 2007; Jia et al., 2014; Ma et al., 2021). Hydrocarbon generation simulation experiments are of three types: open system, closed system, and semi-closed system (Hu et al., 2022). The open-system experiment is widely used because of its fast economy and real-time and online measurement of products, but it is difficult to obtain an intuitive relationship between the hydrocarbon generation rate and maturity, which has also been questioned by some scholars when applied to geological conditions (Qin et al., 2011). The closed system can not only simulate the oil generation of source rocks in different thermal evolution stages but also simulate the maximum gas generation (Lu et al., 2006), while the semi-closed system hydrous pyrolysis is supposed to be more closed to natural underground geological conditions, better than the closed-system pyrolysis in which generated petroleum cannot be expelled and consequently cracks into gaseous hydrocarbon, causing less oil to be generated than in natural conditions, and better than the open system in which generated hydrocarbons were fully expelled out and allow the reaction of hydrocarbon generation stay the course, leading to production and expulsion of more hydrocarbons than in natural conditions (Tang et al., 2015).

In this study, a semi-closed hydrous pyrolysis system was used to investigate the generation, which has proven to be a reliable instrument for investigation of hydrocarbon generation, retention, and expulsion (Zheng et al., 2009; Ma et al., 2017). In this study, by using DK-III, hydrocarbon generation, retention, and expulsion of two different lithological combinations from the E_1f^2 and E_1f^4 were investigated with increasing thermal maturity. This work may provide a comparable measure to evaluate shale gas generation, retention, and expulsion for low-thermal maturity lacustrine shales and also provide some suggestions for shale oil exploration in the Subei Basin.

2 Geological settings

The Subei Basin is in the land part of the South Yellow Sea Basin. It is a composite basin superimposed by multiple stages and types of basins (Shu et al., 2005; Qi et al., 2018). The basin is bounded by the Binhai Uplift in the north, Southern Jiangsu Uplift in the south, Shandong–Jiangsu Uplift in the west, and the Yellow Sea in the east (Figure 1). The basin has undergone multiple tectonic movements and transformation and is divided into Yanfu Depression, Jianhu Uplift, and Dongtai Depression from north to south (Chai, 2019). The study area (Jinhu Sag) is in the western part of the Dongtai Depression (Figure 1). The base in the Subei Basin is marine Paleozoic–Mesozoic deposits, and the caprock is a continental Mesozoic–Cenozoic fault depression sedimentary body, including Taizhou Formation (K_2t), Funing Formation (E_1f), Dainan Formation (E_2d), Yancheng Formation (N_2y), and other sets of strata (Shi, 2010). The thickness of Mesozoic–Cenozoic deposits is over 11,000 m.

The E_1f was deposited in the basin depression evolution stage, widely distributed in different structural parts of various depressions (Zan et al., 2021b). The thickness of E_1f is over 7,000 m including the four members (E_1f^1–E_1f^4) from the bottom to the top. The E_1f^1 and E_1f^3 consist of a set of fluvial deltaic sandstone and siltstone, while the E_1f^2 and E_1f^4 were deposited in the lacustrine and dark lake mudstone and shale are important source rock sections (Duan et al., 2020; Liu et al., 2020). The E_1f

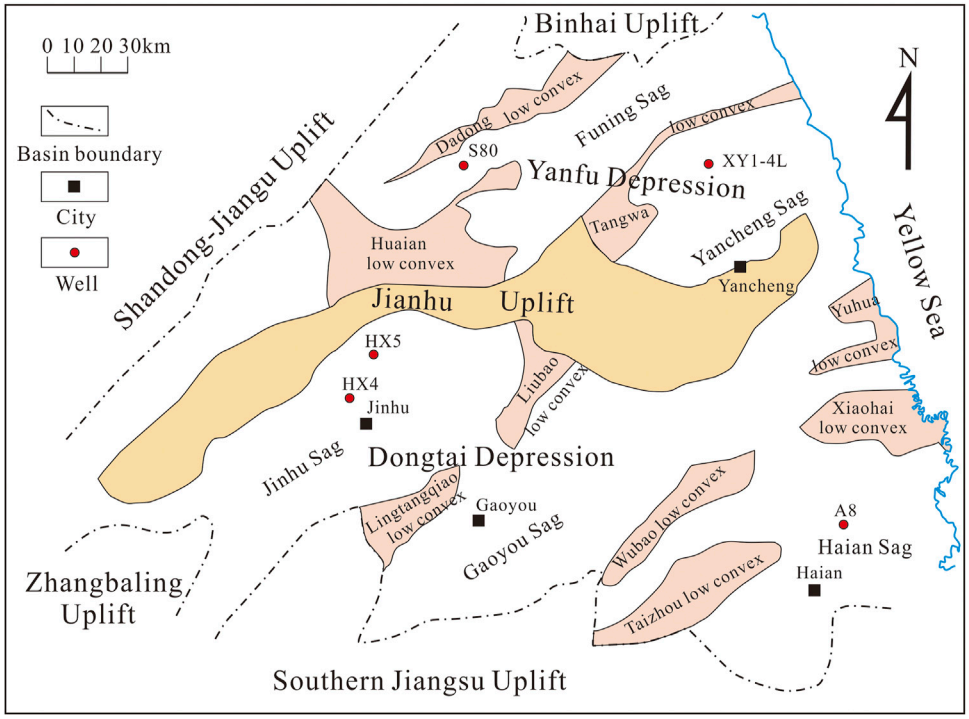

FIGURE 1
Geological setting of the Subei Basin.

was not further buried until the end of Yancheng Formation sedimentation due to the two stages of uplift and denudation, and source rocks began to enter the oil window (Liu, 2010). At present, the source rock in the E_1f^2 has reached high thermal maturity in the deep depression zone of the Subei Basin, while its maturity is lower in the slope and low uplift (Zhao et al., 2022). The thermal maturity of the source rock in the E_1f^4 is still lower owing to the shallow burial depth (Liu, 2010).

3 Samples and methods

3.1 Samples

For the pyrolysis simulation of hydrocarbon generation, the samples of immature to low-mature source rock are more representative (Ma et al., 2021). To investigate the typical hydrocarbon generation and expulsion processes of source rocks from the E_1f^2 and E_1f^4 in the Subei Basin, two samples were selected from the E_1f^2 and E_1f^4 to be prepared for the experiments according to fundamental geochemical analysis data. The total organic carbon content was detected using a carbon sulfur analyzer (CS-230) according to the Chinese standard GB/T 19145–2003 (GB/T 19145-2003, 2003); the hydrogen index and maximum pyrolysis temperature were tested using a Rock-Eval analysis; and the vitrinite reflectance (VR) was analyzed according to the Chinese standard GB/T 6948–2008 (GB/T 6948-2008, 2008).

3.2 Semi-closed hydrous pyrolysis system

Two samples are prepared to experiment different lithology combinations. Considering the fact that shale often contains silty sand and a sandy interlayer in the actual geological conditions of the Subei Basin, we designed two models to simulate the hydrocarbon generation and expulsion characteristics of shale with a silty interlayer (model 1) and pure shale (model 2).

Experiments were carried out using a high-temperature and high-pressure semi-closed hydrous pyrolysis system. The instrument is capable of conducting pyrolysis experiments under *in situ* geological conditions. It is mainly composed of a high-temperature and high-pressure reaction system, a two-way hydraulic control system, an automatic hydrocarbon expulsion product collection and fluid supplement system, a data acquisition and automatic control system, and peripheral auxiliary equipment.

The simulation experiment of hydrocarbon generation and expulsion of source rock with this instrument has the following characteristics: 1) the original cylinder sample with a diameter of

TABLE 1 Hydrocarbon generation and expulsion experiment program of source rock sample HX4 in the Jinhu Sag, Subei Basin.

Simulation temperature (°C)	Simulation time (h)	Fluid pressure (Mpa)	Static rock pressure (Mpa)	Weight of source rock (g)	Weight of overlying sandstone (g)	Weight of underlying sandstone (g)
250	48	20	36.8	60.98	20.14	20.6
275	48	21.5	39.1	60.1	20.54	20.39
300	48	23.8	43.7	60.75	20.9	20.11
310	48	25	46	60.55	20.7	20.39
320	48	27.5	50.6	59.14	20.19	20.41
335	48	30	55.2	58.28	20.72	20.36
350	48	32.5	59.8	59.85	20.27	20.15
360	48	35	64.4	59.48	20.21	20.56
370	48	40	73.6	58.6	20.96	20.55
380	48	43.8	80.5	60.32	20.78	20.71
400	48	50	92	60.49	20.48	20.36

3.8 cm and a mass of 5–150 g is drilled using a special sampling tool, and the original pore structure, composition, and organic matter occurrence state of the sample are retained as much as possible; 2) the original cylinder is sealed in the sample chamber as a whole and placed in a high-temperature autoclave. Then, the core sample is compacted by applying a static rock pressure up to 180 MPa through the oil cylinder and the middle pressure sleeve. Only a pipe with a very small inner diameter is connected with the automatic hydrocarbon expulsion product collection system. Therefore, the closed simulation of the hydrocarbon generation process is carried out in the rock pore space with almost no spare reaction space; 3) the original pore fluid of the cylinder in the sample chamber (which can supplement both formation of water and inert gas) can be supplemented in real-time through the fluid supplement system. The port of the autoclave body adopts a special sealing method combining axial self-tight static sealing and semi self-tight dynamic sealing. Therefore, the high-pressure hydrocarbon generation and expulsion simulation experiment can be conducted under the condition that the maximum pore fluid pressure reaches 150 MPa; and 4) the high-pressure valve is automatically controlled by hydrocarbon expulsion, so it can not only simulate closed hydrocarbon generation under a certain pore fluid pressure but also simulate "episodic hydrocarbon expulsion" under a higher fluid pressure. Key parameters of the instrument are introduced by Zheng et al. (2009) in detail.

3.3 Experimental procedure

According to the reconstructed burial history of the Funing Formation in the Subei Basin (Liu, 2019), the fluid pressure and static rock pressure were set (Table 1). The Funing Formation shale underwent a short-term burial before reaching a maximum depth of 3,200 m at 38 Ma and an EqVRo <1.0% (Liu, 2019). In this study, EqVRo values corresponding to different experimental temperatures were obtained from the pyrolysis experiments of immature coal samples (Table 1). The experimental temperatures were increased at a heating rate of 1°C/min and were maintained at the final temperature for 48 h. For two models, the experiment process is shown in Figure 2 and Figure 3, and experiment conditions are listed in Table 1 and Table 2.

The specific experiment steps are as follows:

1) To ensure that each temperature point simulating the experimental source rock is consistent to reduce the experimental error, the sample was crushed to the specified size (60 mesh) and divided into 11 equal parts, each about 60 g. After that, 11 small cylindrical core samples of siltstone (3.5 cm in diameter) were prepared. For model 1, the gray siltstone sample of well HX4 (2,357.6 m depth) was crushed to the same size (60 mesh); after chloroform extraction, hydrogen peroxide and other reagents are used to remove organic matter and dried. The samples are divided into 22 equal parts, and a small core sample of siltstone cylinder with a diameter of 35 mm is also prepared. Then, the prepared siltstone small cylinders, shale small cylinders, and siltstone small cylinders are loaded into the sample chamber in sequence, and the small cylinders are separated using filters (see Figure 2). For model 2, similarly, the pure shale sample XY1 is crushed to the specified size (60 meshes) and divided it into 11 equal parts, about 60 g each. The instrument is used to make a uniform-sized cylinder core sample of pure shale hydrocarbon source rock (with a diameter of 3.5 cm).
2) When the sample was loaded, a series of leak tests were performed. Helium gas was injected with a pressure of 8 MPa. This process is repeated five–six times to ensure that the reaction device is sealed and airtight.

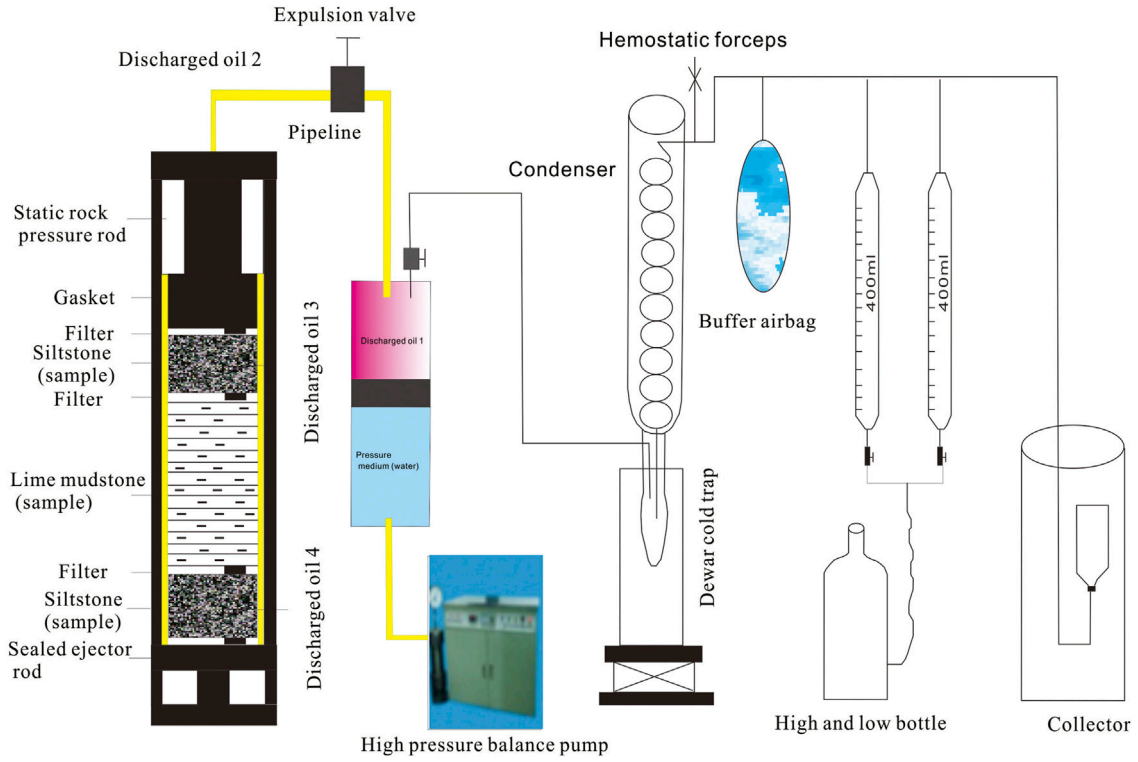

FIGURE 2
Hydrous pyrolysis system for hydrocarbon generation and expulsion of shale with a silty interlayer (model 1).

3) Distilled water was injected into the reactor with high pressure. Then, pressure is applied and the sample is heated: the two-way hydraulic press is used to apply static rock pressure to the pressure value corresponding to each temperature point through the static rock pressure rod, and then the temperature control device is used to increase the set temperature at a rate of 1°C/min, and the temperature is maintained after reaching the set temperature for 2 days (48 h). It should be noted that during the experiment, the fluid pressure in the reaction device will continue to increase as the argillaceous source rock generates hydrocarbons continually. At this time, when the fluid pressure exceeds the set hydrocarbon expulsion pressure, the hydrocarbon expulsion valve is adjusted (Figure 3) to make the fluid pressure in the reaction device consistent with the pressure of the external hydrocarbon expulsion device and it is maintained at the set pressure value.
4) After the completion of each set of simulation experiments, the discharge oil collection and quantitative research are carried out after the oil, gas, and water products in the simulation device are discharged.
5) Finally, after the experiment, the maturity analysis of the shale residual samples after the 11 groups of formation pore thermal pressure generation, expulsion, and retention of hydrocarbons is used to determine the maturity of the shale corresponding to the source rock under 11 different temperature and pressure conditions. According to Burnham's 1989 type II kerogen, the relationship between temperature and maturity was calculated using an EasyRo model (Burnhan and Sweeney, 1989).

3.4 Product analysis

Due to the different lithologies of the model settings, the products of the two models have different geological significances. For model 1, according to the simulation program of the lithological combination of shale with the silty interlayer, "discharged oil 1" shown in Figure 2 is the oil discharged due to the pressure difference between the hydrocarbon generation system and the hydrocarbon expulsion system in the experimental device, which can be regarded as a simulation of real geological conditions (the oil generated by the source rock from the source layer is discharged from the source rock through the migration channel to the oil accumulated in the reservoir outside the source layer); "discharged oil 2" refers to the oil generated from the shale discharged to the inner wall of the sample reaction device and the

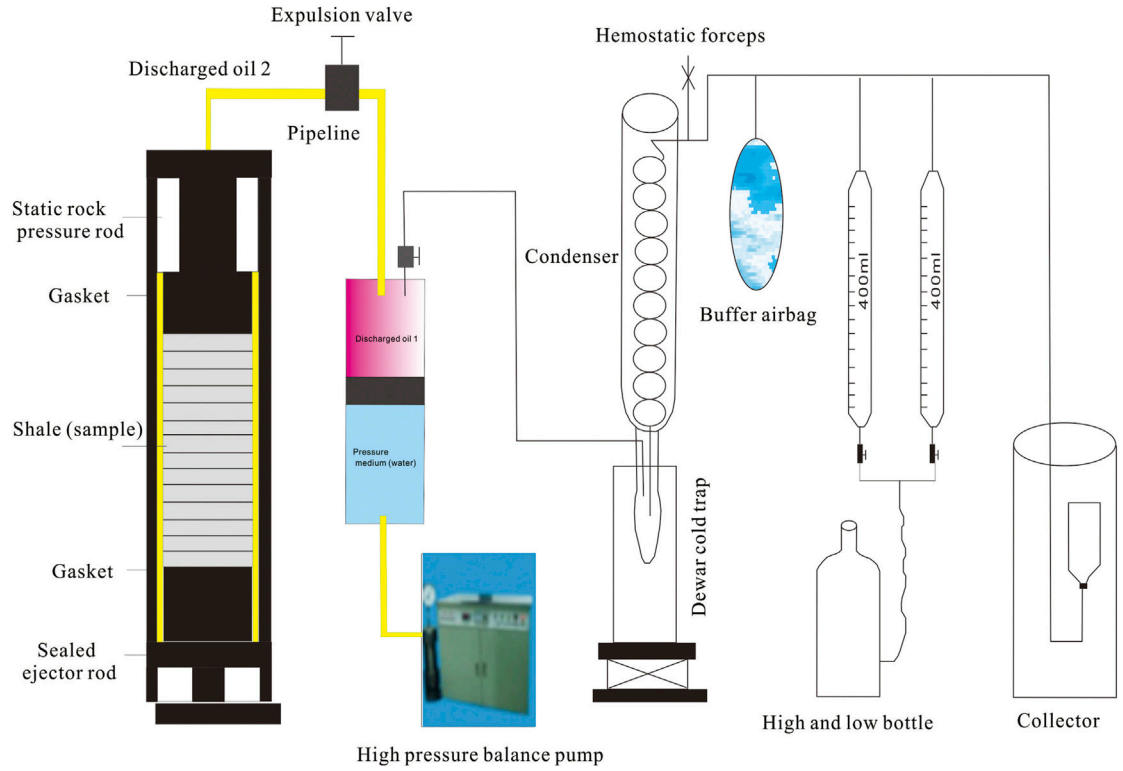

FIGURE 3
Hydrous pyrolysis system for hydrocarbon generation and expulsion of pure shale (model 2).

TABLE 2 Hydrocarbon generation and expulsion experiment program of source rock sample no. XY1-4L in the Yancheng Sag, Subei Basin.

Simulation temperature (°C)	Simulation time (h)	Fluid pressure (Mpa)	Static rock pressure (Mpa)	Weight of source rock (g)
250	48	22.1	51	60.10
275	48	26.3	60	60.10
300	48	27.9	64	60.50
325	48	30.4	70	60.18
350	48	34.1	78	60.11
375	48	36.7	84	60.00
400	48	39.3	90	59.95
425	48	41.2	95	59.63
450	48	43.5	100	58.34
475	48	47.7	110	57.79
500	48	51.9	119	60.40

inside of the dredging pipeline, which can be regarded as the oil discharged into the migration channel such as cracks under simulated real geological conditions. “Discharged oil 3” and “discharged oil 4” refer to the oil generated from the shale source rock being discharged to the core powder placed up and down due to the difference between the shale source rock and siltstone cores placed above and below. It can be regarded as the shale source rock migrated and accumulated in the siltstone in a short distance after rupture and hydrocarbon expulsion under the simulated real geological conditions. Residual oil

TABLE 3 Geochemical characterization of source rock samples used for pyrolysis.

Sample no.	Lithology	Depth (m)	Layer	S_1 mg/g	S_2 mg/g	Tmax (°C)	TOC (%)	HI mg/g	Ro (%)
HX4	Shale with a silty interlayer	1,896.3	E_1f^4	0.04	11.46	438	2.13	538	0.57
XY1-4L	Gray shale	1,613.5	E_1f^2	0.64	25.60	433	4.65	551	0.54

E_1f^4, the fourth member of the Funing Formation; E_1f^2, the second member of the Funing Formation; S_1, amount of free hydrocarbons; S_2, amount of pyrolysis hydrocarbons; Tmax, TOC, total organic carbon; HI, hydrogen index; Ro, vitrinite reflectance.

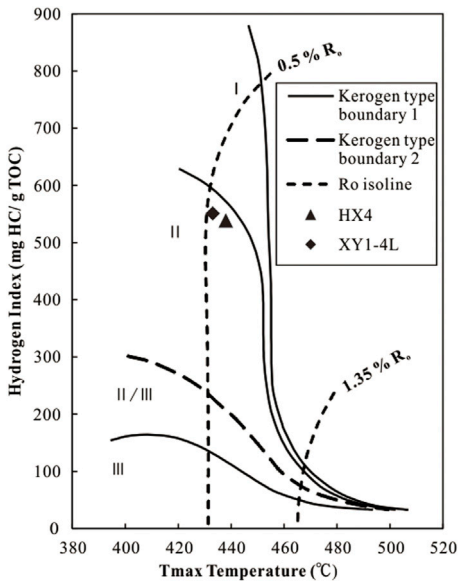

FIGURE 4
Kerogen type classification chart.

(retained oil) refers to the oil remaining in the shale source rock (existing in a free, adsorbed, and mutually soluble state) after simulation and usually refers to the bitumen "A" obtained by chloroform extraction. The total oil usually refers to the sum of the residual oil and the aforementioned discharged oil, and the total hydrocarbon usually refers to the sum of the total oil and hydrocarbon gas. Model 2 has three parts of oil and hydrocarbon gas: "discharged oil 1," "discharged oil 2," and residual oil (retained oil) (Figure 3).

4 Results

4.1 Evaluation of the geochemical parameters

Geochemical characteristics of these two samples are given in Table 3. The samples are organic-rich, low-mature, and contain type I kerogen. Total organic carbon (TOC) contents for the samples are 2.13% (HX4) and 4.65% (XY1-4L), with a hydrogen index of 538 and 551 mg HC/g TOC, respectively (Table 3). The two samples are low-mature (Ro<0.6%), and the organic matter is kerogen type II according to the Rock-Eval analysis (Figure 4) (Mukhopadhyay et al., 1995).

4.2 Oil products of model 1

4.2.1 Retained oil

The retained oil of model 1 is given in Table 4 and shown in Figure 5A. The retained oil reaches a peak of 333.53 mg/g TOC at an EqVRo of 0.84%, and there is no retained oil observed until an EqVRo of 2.0%.

4.2.2 Discharged oil

The discharged oil of model 1 is given in Table 4 and shown in Figure 5B. When the EqVRo is less than 0.74%, there is no discharged oil. With the increase in temperature, the amount of discharged oil gradually increases until Ro=1.28, reaching a maximum of 409.36 mg/g TOC; the yields then rapidly decrease to 342.1 mg/g TOC at 2.0% of EqVRo. In addition, the discharged oil consists of four parts as shown in Figure 5B. This discharged oil increased with temperature, especially discharged oil 1, and it reaches 206.49 mg/g TOC at 2.0% of EqVRo as same as discharged oil 2 of 75.27 mg/g TOC. However, discharged oils 3 and 4 form a trend of increasing first and then decreasing at 1.12% and 0.84% of EqVRo, respectively.

4.2.3 Total hydrocarbon

The hydrocarbons of model 1 are given in Table 4 and shown in Figure 5C. Before the EqVRo reaches 0.8%, the total hydrocarbon contains almost only oil with a value of 409.4 mg/g TOC. When the EqVRo reaches 1.28%, the oil yield is the highest and oil begins to crack into gas.

4.3 Oil products of model 2

4.3.1 Oil yields

The oil yields of model 2 are given in Table 5 and shown in Figure 6A. The oil yields reach the maximum 625.83 mg/g TOC

TABLE 4 Retained and discharged oil yields of model 1.

Sample	Temperature (°C)	EqVRo (%)	Oil yields (mg/g TOC)				Discharged oil (mg/g TOC)				Total hydrocarbon (mg/g TOC)		
			Total oil	Retained oil	Discharged oil	Discharged oil 1	Discharged oil 2	Discharged oil 3	Discharged oil 4	Total discharged oil	Total hydrocarbon	Total oil	Total gas
HX4-1	250	0.59	83.28	76.68	6.61	1.54	3.53	0.00	1.54	6.61	91.76	83.28	8.47
HX4-2	275	0.64	137.67	119.11	18.56	5.52	7.52	0.00	5.52	18.56	148.49	137.67	10.82
HX4-3	300	0.68	171.79	155.67	16.12	5.52	5.52	1.54	3.53	16.12	182.61	171.79	10.82
HX4-4	310	0.7	218.21	198.10	20.10	11.50	3.53	1.54	3.53	20.10	226.68	218.21	8.47
HX4-5	320	0.74	270.10	226.09	44.01	19.47	11.50	5.52	7.52	44.01	290.31	270.10	20.20
HX4-6	335	0.8	396.23	350.23	46.01	27.44	9.51	5.52	3.53	46.01	409.40	396.23	13.17
HX4-7	350	0.84	518.44	372.80	145.64	31.43	5.52	33.42	75.27	145.64	540.99	518.44	22.55
HX4-8	360	0.9	517.03	333.53	183.50	33.42	5.52	91.21	53.35	183.50	544.27	517.03	27.24
HX4-9	370	1.12	503.09	217.97	285.13	95.19	5.52	119.11	65.30	285.13	549.10	503.09	46.01
HX4-10	380	1.28	515.22	110.53	404.69	164.94	37.41	73.27	129.07	404.69	575.31	515.22	60.08
HX4-11	400	2	349.78	14.83	334.95	206.79	75.27	15.49	37.41	334.95	501.36	349.78	151.58

10.3389/feart.2022.1071466

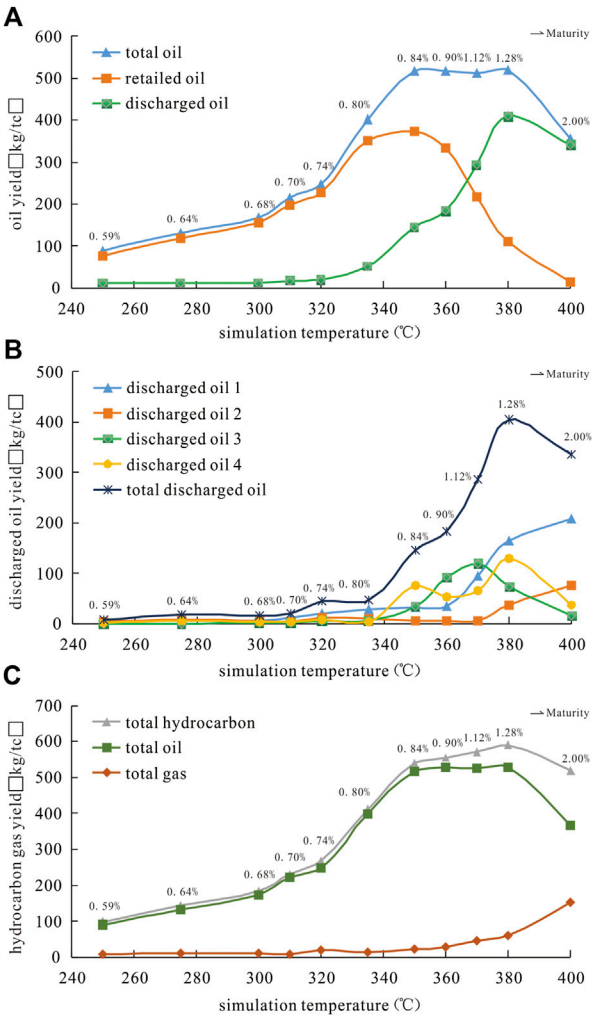

FIGURE 5
Oil yields **(A)**, discharged oil yields **(B)**, and hydrocarbon gas yields **(C)** of shale with a silty interlayer (model 1).

at an EqVRo of 0.8% as well as the discharged oil of 497.7 mg/g TOC.

4.3.2 Gas yields

The gas yields of model 2 are given in Table 5 and shown in Figure 6B. The gas yields begin to increase after an EqVRo of 0.8% and then increases quickly after an EqVRo of 1.61%, with the maximum value of 480.19 mg/g TOC at an EqVRo of 3.08%.

4.4 Stages of shale oil generation

According to the aforementioned experiments, under different temperature and pressure conditions (different thermal evolution stages), the productivity characteristics of oil generation and hydrocarbon generation, oil expulsion, and residual oil (retained oil) of lacustrine shale in the Subei Basin have a clear change rule. It can be seen that with the increase in temperature and pressure in the 11 simulation settings, the thermal evolution degree of organic matter in the source rock in the geological period increases, and the change characteristics of the discharged oil, residual oil (retained oil), and hydrocarbon gas yield of this type of source rock have gone through four stages, shown as follows.

4.4.1 Shale with a siltstone interlayer

In the first stage, the maturity of organic matter Ro increases from 0.59% to 0.74%: this is a stage of slow oil generation and a small amount of gas generation for shale with silty intercalation, and the total oil and gas yield increases slowly with the increase of maturity. At the same time, the oil discharge rate of this type is very low during this period, and the main part of the generated oil is still retained in the source rock: when Ro=0.59%, it can be seen from the total oil discharge that the oil discharged is mainly "discharged oil 1" and "discharged oil 3." When Ro=0.74%, the oil discharge rate and the oil retained (residual oil) rate are slightly increased, but the oil discharge rate is basically unchanged. The expulsion of oil is still dominated by "discharged oil 1" and " discharged oil 3," which indicates that when the evolution degree is low, the hydrocarbon source rock is mainly detained in the rock, and the main favorable expulsion direction is the upper reservoir, and the downward expulsion of the hydrocarbon source rock is basically not possible.

In the second stage, the maturity of organic matter Ro increases from 0.74% to 0.84%: this is the stage of rapid oil generation and slow hydrocarbon generation of silty intercalated shale. The total oil yield increases rapidly with the increase of maturity, but the gas yield does not change significantly, showing a slow increase. When Ro=0.80%, the discharged oil is mainly "discharged oil 1" and "discharged oil 2." However, when Ro=0.84%, the total oil yield and gas yield increase rapidly, approaching the maximum value, and the oil yield and oil discharge rate in this stage increase significantly compared with the previous stage. At this time, the proportion of discharged oil is dominated by "discharged oil 4," "discharged oil 3," and "discharged oil 1," which indicates that when the evolution degree is moderate, the source rock itself is basically saturated, and the favorable direction of hydrocarbon expulsion is to discharge to the upper part and permeate downward.

In the third stage, the maturity of organic matter Ro increases from 0.84% to 1.28%: in this stage, the amount of oil generated by the silty intercalated shale is small, and the total oil yield does not change with the increase of maturity, which is generally maintained at the level equivalent to the total oil yield value at 0.84% maturity, presenting an almost stable platform. At this stage, the gas generation capacity is significantly enhanced. When Ro=1.28%, the gas yield increases rapidly. At the same time, the

TABLE 5 Retained and discharged oil yields of model 2.

Sample	Temperature (°C)	EqVRo (%)	Oil yield (mg/g TOC)			Total hydrocarbon (mg/g TOC)		
			Discharged oil yield	Retained oil yield	Total oil yield	Hydrocarbon gas yield	Total oil yield	Total hydrocarbon yield
XY1-1	250	0.59	8.67	152.01	160.68	4.26	160.68	164.94
XY1-2	275	0.64	4.93	199.79	204.71	13.98	204.71	218.70
XY1-3	300	0.68	40.53	275.20	315.73	9.41	315.73	325.14
XY1-4	325	0.75	171.68	275.20	446.89	38.58	446.89	485.47
XY1-5	350	0.8	497.70	128.12	625.83	52.88	625.83	678.71
XY1-6	375	1.13	315.02	123.90	438.93	125.53	438.93	564.45
XY1-7	400	1.61	418.07	16.64	434.71	164.43	434.71	599.14
XY1-8	425	2.03	386.69	0.71	387.40	164.43	387.40	551.83
XY1-9	450	2.51	354.84	4.93	359.76	276.55	359.76	636.31
XY1-10	475	2.75	402.62	0.00	402.62	353.77	402.62	756.39
XY1-11	500	3.08	362.80	0.00	362.80	480.19	362.80	842.99

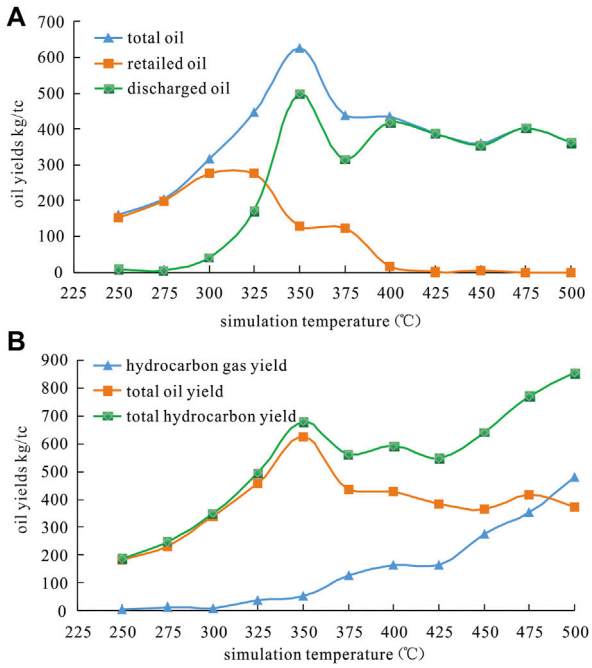

FIGURE 6
Oil yields **(A)** and hydrocarbon yields **(B)** of pure shale (model 2).

yield and rate of oil discharged in this stage increase rapidly. When Ro=1.28%, the oil discharged is dominated by "discharged oil 1," "discharged oil 4," and "discharged oil 3," which indicates that the generated oil may be lifted by gas after it starts to generate gas so that the oil in the whole system will be discharged to the upper part.

In the fourth stage, the maturity Ro > 1.28%: in this stage, the total oil yield, the output oil yield, and the residual oil yield of the silty intercalated shale decrease rapidly, while the gas yield increases rapidly. It shows that the evolution degree of organic matter Ro is more than 2.00%, and the oil generated from the source rock and the discharged oil begin to crack into gas. When Ro=2.00%, the oil drainage rate is very high, and "discharged oil 1" and "discharged oil 2" are the main ones. This shows that the oil in the source rock and its interlayer are discharged rapidly due to the expansion of generated gas, which is similar to the early high production but rapid decline characteristics of shale oil wells in high-maturity areas.

4.4.2 Pure shale

In the first stage, the maturity of organic matter Ro increases from 0.59% to 0.68%: in this stage, the pure shale generates oil slowly and will not generate gas basically. The total oil yield increases slowly with the increase of maturity, while the gas yield changes little with the increase of maturity. The yield of discharged oil in this stage is very low.

In the second stage, the maturity of organic matter Ro increases from 0.68% to 0.84%: in the stage of rapid oil generation and slow gas generation of pure shale, the total oil yield increases significantly with the increase of maturity, while the gas yield increases slowly and the output oil yield also increases rapidly in this stage.

In the third stage, the maturity of organic matter Ro increased from 0.84% to 2.00%: in this stage, the generated oil of pure shale began to crack into gas and the yield of residual oil and discharged oil decreased with the increase of maturity, while the gas yield increased significantly.

In the fourth stage, the maturity of organic matter Ro is 2.00%: in this stage, a large amount of oil generated from pure shale is cracked into gas and a large amount of kerogen is generated. With the increase of simulation temperature, the yield of hydrocarbon gas increases, while the yield of retained oil is very low, indicating that almost all the oil retained in shale is converted into hydrocarbon gas. It should be noted here that during the hydrocarbon generation simulation experiment, the oil discharged at this stage is mainly the oil discharged from the hydrocarbon generation system, so it does not participate in the evolution process of cracking to gas. Therefore, the oil discharged during the simulation process at this stage is relatively stable. Under geological conditions, it is equivalent that this part of oil has been expelled from the hydrocarbon source series and migrated to the relatively shallow conventional reservoir series.

5 Discussion

5.1 Comparisons of the generation and expulsion efficiency of two different lithological combination shales

Most hydrocarbon generation and expulsion models of lacustrine shale could be divided into four parts (Tang et al., 2018). Similarly, based on the aforementioned experimental simulation results, the evolution of the oil-generating capacity of the source rocks of the Funing Formation in the Subei Basin can be roughly divided into four stages: 1) the source rocks are relatively slow in generating oil, and the hydrocarbon gas generation is very low at this stage; 2) relatively fast oil generation and slow hydrocarbon gas generation stage of the source rock; 3) weak oil generation capacity of the source rock and significantly enhanced hydrocarbon gas generation capacity; and 4) a large amount of oil generation of the source rock to form gas and a large amount of kerogen gas generation stage.

However, the hydrocarbon generation, retention, and expulsion efficiencies of source rocks of different lithological combinations are different. Our experimental results show that the temperature of the pure shale source rock combination is 250–300°C (Ro<0.65%), the residual (retained) oil yield rate is less than 10%, and the residual (retained) amount is greater than 90%; when the temperature is 300–350°C (0.65%<Ro<0.84%), the total oil production rate of the source rock increases rapidly, the oil discharge efficiency increases rapidly, 10%<oil discharge efficiency<75%, and the residual (retained) oil efficiency declines rapidly; when the temperature is about 320°C, the yield of discharged oil is higher than the yield of residual (retained) oil. However, for the shale and thin siltstone combination, when the temperature is 250–335°C (Ro<0.84%), residual (retained) oil production hydrocarbon expulsion efficiency<10% and residual (retained) oil amount>90%; when the temperature is 335–380°C (0.84%<Ro<1.20%), the total oil production rate of the source rock increases rapidly, the oil discharge efficiency increases rapidly, 10%<oil discharge efficiency<75%, and the residual (retained) oil efficiency decreases rapidly; when the temperature is about 360°C, the yield of discharged oil is higher than the yield of residual (retained) oil (Figure 7).

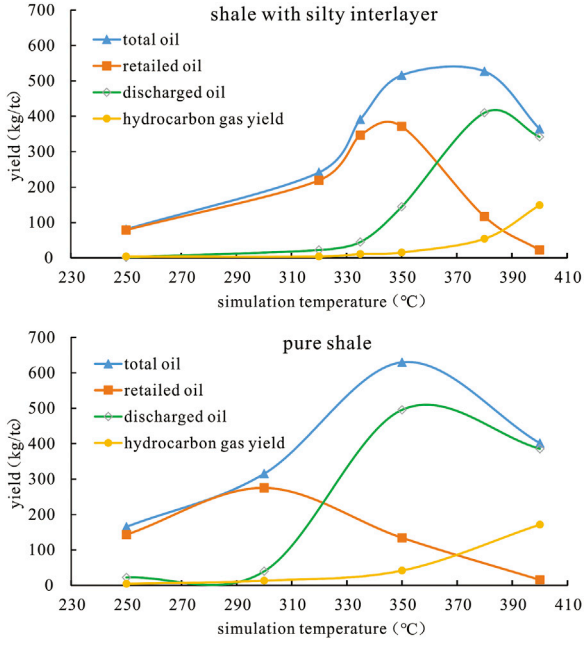

FIGURE 7
Correlation of hydrocarbon generation, expulsion, and retention of different lithological combinations.

Many factors may be involved in hydrocarbon generation, retention, and expulsion between the two lithologies. The very low porosity and permeability of pure thick pure shale allow for high oil retention and weak expulsion, despite its high hydrocarbon capacity (Li et al., 2015; Liang et al., 2017). Brittle minerals also have an effect on oil retention and expulsion. Compared with pure shale, the limestone and siltstone combination has higher carbonate. A large number of organic acids produced during earlier hydrocarbon generation (Ro < 0.84%) dissolve it to form pores, which is conducive to the retention of oil (Hou et al., 2021b). Meanwhile, the siltstone closely adjacent to source rocks provides a channel for the outflow of organic acid-dissolved carbonates, avoids secondary precipitation, and is conducive to the preservation of pores (Li et al., 2018). Pure shale with TOC may generate a large amount of oil rapidly, which may lead to the formation of high pressure in the pores, resulting in the earlier discharge of oils. For the source rocks of shale with more brittle minerals, a large amount of oil can be retained until a certain pressure is formed and then discharged.

Based on the physical models of hydrocarbon generation and expulsion established based on the aforementioned two types of

lithological combinations, combined with the tight oil accumulation conditions of the Funing Formation in the Subei Basin, "discharged oil 1 + discharge oil 2" in the physical model can be regarded as discharged to the neighboring conventional oil in the layer, "discharged oil 3 + discharged oil 4" is regarded as the tight oil discharged into the adjacent layer and the source rock interbedded tight sandstone or carbonate rock, and the rest retained in the source rock shale strata are regarded as retained shale oil in shale.

Therefore, according to this model, the shale oil reservoirs of the Funing Formation in the Subei Basin can be divided into two categories: one is the internal source type, which is discharged into the sandstone or carbonate interlayer within the source rock series to form reservoirs; the other is the source external type in which oil is discharged into the adjacent tight sandstone to form a reservoir or the source rock layer is discharged through faults to form a fault-sand body system to form a reservoir.

5.2 Implications for shale oil exploration in the Subei Basin

The generation and accumulation of shale oil is commonly related to lithofacies (sedimentary environment), maturity (chemical process), and preservation boundary (physical process) (Li et al., 2019). Thermal maturity of source rocks not only controls hydrocarbon generation but also affects the pore system and pressure system, which is a key parameter in the exploration potential of lacustrine shale oil (Zhang et al., 2012). Rui et al. (2020) conducted hydrocarbon generation pyrolysis simulation experiments of the Lucaogou shale and found that the discharge efficiency of hydrocarbons is low during the stage of low maturity of shale, thus proposing that the favorable maturity of shale for shale oil is Ro = 1.0–1.2%. Li et al. (Jarvie, 2012) proposed that at an Ro of 0.84–1.30%, the hydrocarbon expulsion efficiency of lacustrine argillaceous dolomite source rock is the highest, and the discharged oil is mainly accumulated in adjacent sandstone or carbonate reservoirs, which is a favorable maturity range for lacustrine argillaceous dolomite shale oil exploration. However, the previous standards are not recommended to be directly applied to the shale oil exploration of the Funing Formation, and a favorable mature interval should be evaluated considering the geological background.

The hydrocarbon generation and expulsion model of the shale with a silty interlayer combination suggests that at the thermal maturity of Ro =0.84–1.12%, the generated oil is mainly discharged toward adjacent siltstones or carbonate rocks in the formation to form the internal source (Figure 4). For pure shale, oil retention mainly occurs at a maturity of Ro=0.68–0.74, but oil yield is lower in this period. When the maturity is higher than 0.74, the oil yield and oil expulsion efficiency increase rapidly, which indicates that the oil is easy to be filled into the adjacent sandstone along the fault system to form a conventional reservoir, such as a sandstone reservoir in the third member of the Funing Formation (E_1f^3). Most of the E_1f^2 source rocks in the Subei Basin have moderate maturity (Ro = 0.8–1.0%), and the source rocks in the deep depression zone in the Gaoyou Sag and Qingtong Sag can reach Ro = 1.2%. Most of the E_1f^4 source rocks in the Subei Basin have low maturity (Ro = 0.5–0.7%), and the source rocks in the deep depression zone in the Gaoyou Sag, Qintong Sag, and Jinhu Sag can reach high maturity (Ro= 0.7–1.2%) (Fan and Shi, 2019). There are 455 wells in the Subei Basin showing oil and gas in shale, and an obtained industrial oil flow which shows good shale oil exploration prospects (Zan et al., 2021a). Zan et al. (2021a) proposed that the organic-rich silty shale and marlstone with a thermal maturity of Ro >1.1% is divided into favorable area I, the laminated shale and marlstone with a thermal maturity of Ro = 0.9–1.1% is divided into favorable area II, and the massive shale with a thermal maturity of Ro = 0.7–0.9 is divided into favorable area III. Types II and III are mainly composed of shale with a silty interlayer and pure shale, respectively. This classification is consistent with our experimental simulation results. Therefore, the multi-lithology combined shale such as shale with a silty or calcareous interlayer with a thermal maturity of Ro = 0.84–1.12% is suggested to be the favorable maturity range of the Funing Formation, and the deep depression zone with higher thermal maturity (Ro ≈1.1%) in the Sag is a favorable area for shale oil exploration.

6 Conclusion

1) The oil-generation capacity evolution of different lithological combination source rocks in the Funing Formation from the Subei Basin can be roughly divided into four stages: a) relatively slow oil generation and slow gas generation, b) relatively fast oil-generation and slow gas generation, c) oil cracking into gas, and d) kerogen cracking into gas.
2) Different lithological combinations have different oil generation, hydrocarbon expulsion, and retention efficiencies: the total oil generation rate and gas generation rate of pure shale are higher than those of shale with a silty interlayer, and the exchange point between the oil expulsion rate and residual (retention) rate of pure shale is earlier than that of shale with the interlayer. Oil retention mainly occurs when the source rock maturity is Ro=0.84–1.12%, while the discharged oil is mainly accumulated in the adjacent siltstone.
3) Hydrocarbon generation and expulsion models suggest that the favorable maturity of shale oil exploration in the Subei Basin is Ro=0.84–1.12%, the multi-lithofacies combination source rock is the favorable target, and the deep depression zone in the Sag is the favorable area.

Data availability statement

The original contributions presented in the study are included in the article/Supplementary Material; further inquiries can be directed to the corresponding author.

Author contributions

JP: conceptualization and writing—original draft; LL: writing—review and editing, and investigation; CD: visualization; XL: methodology; JZ: project administration; SL: data curation; QQ: formal analysis; and DW: validation and supervision.

Acknowledgments

This research was financially supported by the National Science and Technology Major Project (Nos. 2016ZX05002-006 and 2017ZX05005-003). The editor and two reviewers are acknowledged for providing comments and suggestions which helped improve this manuscript.

Conflict of interest

The authors declare that the research was conducted in the absence of any commercial or financial relationships that could be construed as a potential conflict of interest.

Publisher's note

All claims expressed in this article are solely those of the authors and do not necessarily represent those of their affiliated organizations, or those of the publisher, the editors, and the reviewers. Any product that may be evaluated in this article, or claim that may be made by its manufacturer, is not guaranteed or endorsed by the publisher.

References

Anyiam, O. A., and Onuoha, K. M. (2014). A study of hydrocarbon generation and expulsion of the Nkporo Shales in Anambra Basin, Nigeria. *Arab. J. Geosci.* 7, 3779–3790. doi:10.1007/s12517-013-1064-5

Burnhan, A. K., and Sweeney, J. J. (1989). A chemical kinetic model of vitrinite maturation and reflectance. *Geochem. Cosmochem.* 3, 6–11.

Chai, F. (2019). Study on Paleozoic sedimentary facies and favorable area evaluation in lower Yangtze basin. *Petroleum Reserv. Eval. Dev.* 9 (02), 7–12. doi:10.13809/j.cnki.cn32-1825/te.2019.02.002

Cheng, Q., Zhang, M., and Li, H. (2019). Anomalous distribution of steranes in deep lacustrine facies low maturity-maturity source rocks and oil of Funing formation in Subei Basin. *J. Petroleum Sci. Eng.* 181, 106190. doi:10.1016/j.petrol.2019.106190

Duan, H., Liu, S., and Fu, Q. (2020). Characteristics and sedimentary environment of organic-rich shale in the second member of Paleogene Funing Formation, Subei Basin. *Petroleum Geol. Exp.* 42 (04), 612–617. doi:10.11781/sysydz202004612

Fan, B., and Shi, L. (2019). Deep-lacustrine shale heterogeneity and its impact on hydrocarbon generation, expulsion, and retention: A case study from the upper triassic yanchang formation, Ordos Basin, China. *Nat. Resour. Res.* 28, 241–257. doi:10.1007/s11053-018-9387-2

GB/T 19145-2003 (2003). *Determination of total organic carbon in sedimentary rock*. China: General Administration of Quality Supervision, Inspection and Quarantine of the People's Republic of China.

GB/T 6948-2008 (2008). ISO 7404-5:1994, methods for the petrographic analysis of bituminous coal and anthracite-Part 5: Method of determining microscopically the reflectance of vitrinite, MOD.Standardization administration.

Hill, R. J., Zhang, E., Katz, B. J., and Tang, Y. (2007). Modeling of gas generation from the barnett shale, fort worth basin, Texas. *Am. Assoc. Pet. Geol. Bull.* 91 (4), 501–521. doi:10.1306/12060606063

Hou, L., Luo, X., Lin, S., Zhao, Z., and Li, Y. (2021). Quantitative Measurement of Retained Oil in Organic-Rich Shale—A Case Study on the Chang 7 Member in the Ordos Basin, China. *Front. Earth Sci.* 9, 662586. doi:10.3389/FEART.2021.662586

Hou, L., Ma, W., Luo, X., Liu, J., Liu, S., and Zhao, Z. (2021). Hydrocarbon generation-retention-expulsion mechanism and shale oil producibility of the permian lucaogou shale in the Junggar Basin as simulated by semi-open pyrolysis experiments. *Mar. Petroleum Geol.* 125, 104880. doi:10.1016/J.MARPETGEO.2020.104880

Hu, T., Pang, X., Jiang, S., Wang, Q., Zheng, X., Ding, X., et al. (2018). Oil content evaluation of lacustrine organic-rich shale with strong heterogeneity: A case study of the middle permian lucaogou Formation in jimusaer sag, Junggar Basin, NW China. *Fuel* 221, 196–205. doi:10.1016/j.fuel.2018.02.082

Hu, T., Pang, X., Jiang, S., Wang, Q., Liu, X., Wang, Z., et al. (2021). Movable oil content evaluation of lacustrine organic-rich shales: Methods and a novel quantitative evaluation model. *Earth-Science Rev.* 214, 103545. doi:10.1016/J.EARSCIREV.2021.103545

Hu, T., Wu, G., Xu, Z., Pang, X., Liu, Y., and Yu, S.(2022). Potential resources of conventional, tight, and shale oil and gas from Paleogene Wenchang Formation source rocks in the Huizhou Depression. *Adv. Geo-Energy Res.*6(5), 402–414. doi:10.46690/ager.2022.05.05

Jarvie, D. M. (2012). Shale resource systems for oil and gas: Part 2: shale-oil resource systems. *AAPG Mem.* 97, 89–119. doi:10.1306/13321447M973489

Ji, Y., Liu, Y., and Feng, W. (2013). Source rock study and accumulation pattern of Funing Formation in Yancheng sag, northern Jiangsu basin. *Petroleum Geol. Exp.* 35 (4), 449–452. doi:10.11781/sysydz201304449

Jia, C., Zou, C., Li, J., Li, D., and Zheng, M. (2012). Assesment criteria, main types, basic features and resource prospects of the tight oil in China. *Acta Pet. Sin.* 33 (3), 333–350. doi:10.7623/syxb201203001

Jia, W., Wang, Q., Liu, J., Peng, P., Li, B., and Lu, J. (2014). The effect of oil expulsion or retention on further thermal degradation of kerogen at the high maturity stage: A pyrolysis study of type II kerogen from pingliang shale, China. *Org. Geochem.* 71, 17–29. doi:10.1016/j.orggeochem.2014.03.009

Jin, Z., Zhu, R., Liang, X., and Shen, Y. (2021). Several issues worthy of attention in current lacustrine shale oil exploration and development. *Petroleum Explor. Dev.* 48 (6), 1471–1484. doi:10.1016/s1876-3804(21)60303-8

Li, J., Wang, W., Cao, Q., Shi, Y., Yan, X., and Tian, S. (2015). Impact of hydrocarbon expulsion efficiency of continental shale upon shale oil accumulations in eastern China. *Mar. Petroleum Geol.* 59, 467–479. doi:10.1016/j.marpetgeo.2014.10.002

Li, Z., Zheng, L., Jiang, Q., Ma, Z., Tao, G., Xu, E., et al. (2018). Simulation of Hydrocarbon generation and expulsion for lacustrine organic-rich argillaceous dolomite and its implications for shale oil exploration. *Earth Sci.* 43 (2), 566–576. doi:10.3799/dqkx.2018.025

Li, M., Jin, Z., Dong, M., Ma, X., Li, Z., Jiang, Q., et al. (2019). Advances in the basic study of lacustrine shale evolution and shale oil accumulation. *Petroleum Geol. Exp.* 42 (4), 489–505. doi:10.11781/sysydz202004489

Liang, C., Cao, Y., Jiang, Z., Wu, J., Song, G., and Wang, Y. (2017). Shale oil potential of lacustrine black shale in the eocene dongying depression: implications for geochemistry and reservoir characteristics. *Am. Assoc. Pet. Geol. Bull.* 101 (11), 1835–1858. doi:10.1306/01251715249

Liu, X., Lai, J., Fan, X., Shu, H., Wang, X., Shu, H., et al. (2020). Insights in the pore structure, fluid mobility and oiliness in oil shales of Paleogene Funing Formation in Subei Basin, China. *Mar. Petroleum Geol.* 114, 104228. doi:10.1016/j.marpetgeo.2020.104228

Liu, D. (2010). Analysis on structural evolution of northern jiangsu-south Yellow Sea basin. *J. Oil Technol.* 32 (6), 27–31. doi:10.3969/j.issn.1000-9752.2010.06.006

Liu, L. (2019). *Recovery of paleopressure and paleo-fluid potential of Funing Formation in Gaoyou sag*. Beijing: China University of petroleum.

Lu, S., Wang, M., Wang, Y., Xu, L., Xue, H., and Li, J. (2006). Comparison of simulation results from the closed and open experimental system and its significance. *Acta Sedimentol. Sin.* 24 (2), 282–288.

Ma, Z., Zheng, L., Xu, X., Bao, F., and Yu, X. (2017). Thermal simulation experiment of organic matter -rich shale and implication for organic pore formation and evolution. *Petroleum Res.* 2 (4), 347–354. doi:10.1016/j.ptlrs.2017.04.005

Ma, W., Hou, L., Luo, X., Liu, J., Tao, S., Guan, P., et al. (2020). Generation and expulsion process of the Chang 7 oil shale in the Ordos Basin based on temperature-based semi-open pyrolysis: Implications for *in-situ* conversion process. *J. Petroleum Sci. Eng.* 190, 107035. doi:10.1016/j.petrol.2020.107035

Ma, Z., Tan, J., Zheng, L., Shen, B., Wang, Z., Shahzad, A., et al. (2021). Evaluating gas generation and preservation of the Wufeng-Longmaxi Formation shale in southeastern Sichuan Basin, China: Implications from semi-closed hydrous pyrolysis. *Mar. Petroleum Geol.* 129, 105102–105112. doi:10.1016/J.MARPETGEO.2021.105102

Mahlstedt, N., and Horsfield, B. (2012). Metagenetic methane generation in gas shales I. Screening protocols using immature samples. *Mar. Petroleum Geol.* 31 (1), 27–42. doi:10.1016/j.marpetgeo.2011.06.011

Mukhopadhyay, P. K., Wade, J. A., and Kruge, M. A. (1995). Organic facies and maturation of Jurassic/Cretaceous rocks, and possible oil-source rock correlation based on pyrolysis of asphaltenes, Scotian Basin, Canada. *Org. Geochem.* 22 (1), 85–104. doi:10.1016/0146-6380(95)90010-1

Peng, J., Qi, Q., Wang, D., Li, Z., Zhu, J., Liang, S., et al. (2020). Occurrence and recoverability of tight oil in Paleogene Funing Formation, Subei Basin. *Petroleum Geol. Exp.* 42 (1), 53–59. doi:10.11781/sysydz202001053

Qi, K., Zhao, X., Liu, L., Su, Y., Wang, H., Tan, C., et al. (2018). Hierarchy and subsurface correlation of muddy baffles in lacustrine delta fronts: a case study in the X oilfield, Subei Basin, China. *Pet. Sci.* 15, 451–467. doi:10.1007/s12182-018-0239-9

Qin, L., Zhang, Z., Zhu, L., Liu, H., and Xi, W. (2011). Productions of closed system experiments for middle permian source rock in southern Junggar Basin. *Nat. Gas. Geosci.* 22 (5), 860–865. doi:10.11764/j.issn.1672-1926.2011.05.860

Quaye, J., Jiang, Z., and Zhou, X. (2018). Bioturbation influence on reservoir rock quality: A case study of well bian-5 from the second member paleocene Funing Formation in the Jinhu sag, Subei basin, China. *J. Petroleum Sci. Eng.* 172, 1165–1173. doi:10.1016/j.petrol.2018.09.026

Rui, X., Zhou, Y., Li, Z., and Zhang, Q. (2020). Characteristics of source rocks and reservoirs of the Funing Formation in the Subei Basin and their bearing on future shale oil exploration. *Mar. Geol. Quat. Geol.* 40 (6), 133–145. doi:10.16562/j.cnki.0256-1492.2020010301

Shi, C., Cao, J., Tan, X., Luo, B., Zeng, W., Hong, H., et al. (2018). Hydrocarbon generation capability of Sinian–Lower Cambrian shale, mudstone, and carbonate rocks in the Sichuan Basin, southwestern China: Implications for contributions to the giant Sinian Dengying natural gas accumulation. *Am. Assoc. Pet. Geol. Bull.* 102, 817–853. doi:10.1306/0711171417417019

Shi, S. (2010). Characteristics and spatial distribution of the mesozoic-paleozoic strata in the Yanfu area, north Jiangsu. *J. Stratigr.* 34 (01), 106–111.

Shu, L., Wang, B., Wang, L., and He, G. (2005). Analysis of northern Jiangsu prototype basin from late cretaceous to neogene. *Geol. J. China Univeristies* 04, 534–543. doi:10.3969/j.issn.1006-7493.2005.04.009

Tang, X., Zhang, J., Jiang, Z., Zhao, X., Liu, K., Zhang, R., et al. (2015). Characteristics of solid residue, expelled and retained hydrocarbons of lacustrine marlstone based on semi-closed system hydrous pyrolysis: Implications for tight oil exploration. *Fuel* 162, 186–193. doi:10.1016/j.fuel.2015.09.009

Tang, X., Zhang, J., Jiang, Z., Zhang, R., Lan, C., Zhao, W., et al. (2018). Heterogeneity of organic-rich lacustrine marlstone succession and their controls to petroleum expulsion, retention, and migration: A case study in the shulu sag, bohai bay basin, China. *Mar. Petroleum Geol.* 96, 166–178. doi:10.1016/j.marpetgeo.2018.05.031

Uguna, C. N., Carr, A. D., Snape, C. E., and Meredith, W. (2016). Retardation of oil cracking to gas and pressure induced combination reactions to account for viscous oil in deep petroleum basins: Evidence from oil and n -hexadecane pyrolysis at water pressures up to 900bar. *Org. Geochem.* 97, 61–73. doi:10.1016/j.orggeochem.2016.04.007

Wang, X., Liang, Q., Gao, C., Xue, P., Yin, J., and Hao, S. (2022). Hydrocarbon accumulation model influenced by"three elements (source-storage-preservation)"in lacustrine shale reservoir-A case study of Chang 7 shale in Yan'an area, Ordos Basin. *Front. Earth Sci.* 10. doi:10.3389/feart.2022.1012607

Yang, H., Liang, X., Niu, X., Feng, S., and You, Y. (2017). Geological conditions for continental tight oil formation and the main controlling factors for the enrichment: A case of Chang 7 member, triassic yanchang formation, Ordos Basin, NW China. *Petroleum Explor. Dev.* 44 (1), 11–19. doi:10.1016/s1876-3804(17)30003-4

Yao, H., Zan, L., Gao, Y., Hua, C., Yu, W., Luo, W., et al. (2021). Main controlling factors for the enrichment of shale oil and significant discovery in second member of Paleogene Funing Formation, Qintong Sag, Subei Basin. *Petroleum Geol. Exp.* 43 (5), 776–783. doi:10.11781/sysydz202105776

Zan, L., Luo, W., Yin, Y., and Jing, X. (2021). Formation conditions of shale oil and favorable targets in the second member of Paleogene Funing Formation in Qingtong sag, Subei Basin. *Petroleum Geol. Exp.* 43 (2), 233–241. doi:10.11781/sysydz202102233

Zan, L., Chai, F., and Yin, Y. (2021). Physical properties, geochemical characteristics and origins of crude oils in the QintongSag slope. *Acta Sedimentol. Sin.* 39 (5), 1068–1077. doi:10.14027/j.issn.1000-0550.2020.088

Zhang, J., Liu, B., Mao, F., and Chang, X. (2003). Clastic diagenesis and reservoir characteristics of Funing formation in north slope of Gaoyou Depression in Subei Basin. *Acta Pet. Sin.* 24 (2), 43–49. doi:10.3321/j.issn:0253-2697.2003.02.009

Zhang, J., Lin, L., Li, Y., Tang, X., Zhu, L., Xing, Y., et al. (2012). Classification and evaluation of shale oil. *Geosci. Front.* 19 (05), 322–321.

Zhao, S., Fu, Q., Luo, W., Huang, J., and Teng, J. (2022). The hydrocarbon accumulation regularity and the model of hydrocarbon accumulation along the fault ridges in the slope zone of the continental fault basin. *J. Petroleum Sci. Eng.* 208, 109188. doi:10.1016/j.petrol.2021.109188

Zheng, L., Qin, J., He, S., Li, G., and Li, Z. (2009). Preliminary study of formation porosity thermocompression simulation experiment of hydrocarbon generation and expulsion. *Petroleum Geol. Exp.* 31 (3), 296–302. doi:10.3969/j.issn.1001-6112.2009.03.017

frontiers | Frontiers in Earth Science

TYPE Review
PUBLISHED 18 January 2023
DOI 10.3389/feart.2022.1011598

OPEN ACCESS

EDITED BY
Jun Wang,
Yunnan University, China

REVIEWED BY
Ramanathan Alagappan,
Jawaharlal Nehru University, India
Dawei Lv,
Shandong University of Science and Technology, China

*CORRESPONDENCE
Bo Ran,
Ranbo08@cdut.cn

SPECIALTY SECTION
This article was submitted to Geochemistry, a section of the journal Frontiers in Earth Science

RECEIVED 04 August 2022
ACCEPTED 08 November 2022
PUBLISHED 18 January 2023

CITATION
Xu H, Ran B, Liu S, Sun T, Luo C, Li Y and Zhu Y (2023), A review of possible mechanisms for mercury migration in diagenesis: Clay to pyrite.
Front. Earth Sci. 10:1011598.
doi: 10.3389/feart.2022.1011598

A review of possible mechanisms for mercury migration in diagenesis: Clay to pyrite

Huan Xu[1], Bo Ran[1]*, Shugen Liu[1], Tong Sun[1], Chao Luo[2], Yi Li[2] and Yiqing Zhu[2]

[1]State Key Laboratory of Oil and Gas Reservoir Geology and Exploitation, Chengdu University of Technology, Chengdu, China, [2]Petrochina Southwest Oil and Gasfield Company, Chengdu, China

Though sedimentary mercury in marine sediments has been regarded as a geological indicator of volcanic activity based on volcanism activity is the dominant natural source of Hg to the oceans, the influence of diagenesis on mercury cannot be dismissed. Marine mudstone has been selected to explore the migration of mercury from the syn-sedimentary stage to the diagenetic stage in this review. Marine mudstones undergo a series of significant transformation processes, including the illitization of smectite and the formation of framboidal pyrite aggregates during the diagenetic stage. This process makes the adsorption capacity of minerals change significantly that clay minerals are weakened, while pyrites are enhanced. In this reason, it is inferred that the sedimentary mercury may re-migrate from clay minerals to pyrite. This at least means that the indication of volcanic activity by mercury enrichment in marine mudstone need to be re-evaluated.

KEYWORDS

mercury, diagenesis, smectite, illite, framboidal pyrite

Introduction

In the Phanerozoic Earth, there is a correlation between volcanic activity and several major biological extinction events, such as in the Ordovician/Silurian, Permian/Triassic and Cretaceous/Paleogene (Font et al., 2016; Grasby et al., 2016; Sial et al., 2016; Shen et al., 2019a; Shen et al., 2019b). Mercury has been widely recognized as tracer evidence of volcanic activity in sedimentary records from Large Igneous Provinces (LIPs), and so the enrichment of sedimentary mercury before and after biological extinctions has been used to assess regional/global volcanic activity (Grasby et al., 2019; Shen et al., 2020).

Mercury is mainly present in various inorganic species in marine sediments (>98% of total Hg; Morel et al., 1998; Boszke et al., 2003). The retention of mercury in sediments usually should require attachment to the mineral surfaces, including organic matter, clay minerals, sulfides, and other phases (Krupp, 1998; Oliveri et al., 2016; Ravichandran, 2004; Sanei et al., 2012; Selin, 2009). Organic matter mainly exists in form of organic-mercury complex (Ravichandran, 2004). Clay minerals can also adsorb mercury because of its high surface area, moderate to high cation exchange capacity and high negative surface charge (Farrah and Pickering, 1978; Horowitz, 1991). Sulfide minerals may be the main hosts of

Hg in anoxic environments due to the high affinity of Hg for sulfide (Bower et al., 2008; Shen et al., 2019c). Other phases (such as metal oxides) also have certain adsorption capacity for mercury, but they do not play an absoulute role in mercury adsorption (Gobeil and Cossa, 1993; Feyte et al., 2010). According to the modern and ancient mercury sedimentary hosts, the main hosts of mercury include organic matter, clay minerals and pyrite (Shen et al., 2020).

In Mcneal and Rose (1974), mercury content in unconsolidated sediments was much higher than those in sedimentary rocks, suggesting that mercury is lost during diagenesis. Furthermore, when sediment undergoes redox changes because of organic matter mineralization (Froelich et al., 1979), the Hg bound to organic matter can be released in pore water (Cossa and Gobeil, 2000; Gagnon et al., 1997). All of the above suggest that mercury remigration may occur after entering the sediment.

Because most minerals are transformed during the diagenetic stage, the possibility that Hg may move after entering sediments cannot be ignored (Young et al., 1973). This problem has also led to intensive debate about whether the core profiles of Hg enrichment at the sediment surface reflect digenesis (Rasmussen, 1994). However, the specific change mechanism of mercury in the diagenetic stage is still unclear. For this reason, based on previous studies on diagenesis of marine mudstones, we propose a remobilization mechanism of mercury that mercury migration from clay minerals to pyrite. Finally, when this migration reaches a certain extent, mercury is no longer suitable as an effective tracer for the volcanic activity of the same fire province.

Properties of mercury

Mercury is a toxic heavy metal that exists in nature with a variety of sources, including soils and surface volatilization of water bodies, geothermal and volcanic activities, forest fires, spontaneous combustion of coal and degassing of the Earth's crust (Lindberg and Stratton, 1998; Gustin, 2003; Obrist, 2007). Among which, volcanic eruption is the main natural source of mercury (Pirrone et al., 2010).

There are three main types of atmospheric mercury, including gaseous elemental mercury (Hg^0), active mercury ion (Hg^{2+}) and Hg^{2+} compounds associated with particles ($Hg_{(P)}$) (Schroeder and Munthe, 1998). It usually settles to the sea surface, soils or plant surface through dry or wet deposition (dry deposition: settling or uptake the surface without precipitation; wet deposition: removel from the atmosphere through precipitation; Mason et al., 1994; Selin, 2009). Hg^0 can remain in the atmosphere for a long-time period (0.5–1 year; Selin, 2009), and be responsible for long-distance transportation and exchange, based on its low water solubility and dry deposition rate (Lamborg et al., 2002; Selin, 2009), but also is the main occurrence state, accounting for 97%–99% of the total mercury content (Fitzgerald, 1995). Compared to Hg^0, the content of Hg^{2+} is less than 3% and it is soluble in water (Lindberg and Stratton 1998).

In the atmosphere-ocean system (Figure 1), Hg^0 can be oxidized to Hg^{2+}, which is removed from the atmosphere by the oxidation by halogen, ozone and other free radicals (Schroeder and Munthe, 1998; Selin, 2009). Some Hg^{2+} arriving at the seawater surface could be transformed through photochemical reduction and then re-emitted to the atmosphere (Ravichandran, 2004). Under biotic and abiotic action, Hg^{2+} can convert into methylmercury (Me-Hg) and mercury sulfide complex (HgS), respectively (Ravichandran, 2004). Me-Hg can then be used as an intermediate to form organic mercury complex (Hg-OM), which is deposited into sediments or adsorbed by clay and pyrite, while HgS would be precipitated in an environment rich in hydrogen sulfide (Percival et al., 2015).

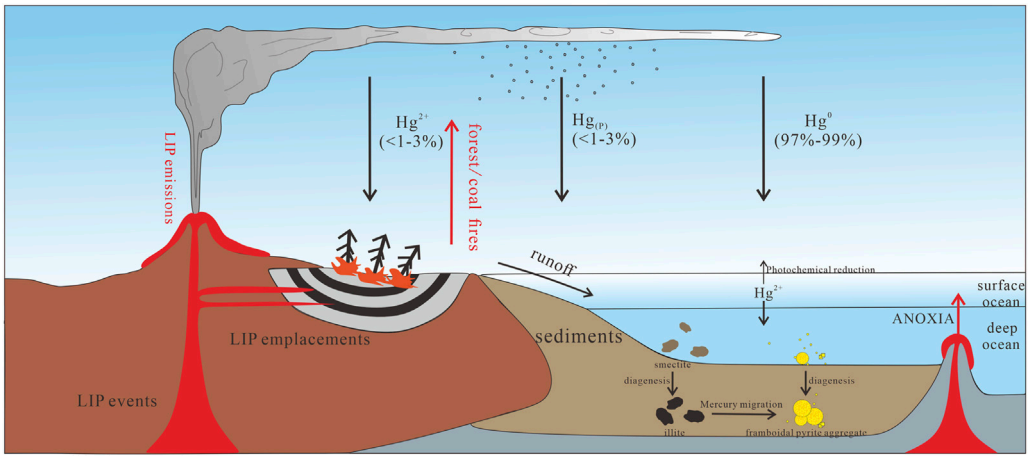

FIGURE 1
Circulation, transport and form of mercury in nature (modified from Percival et al., 2015).

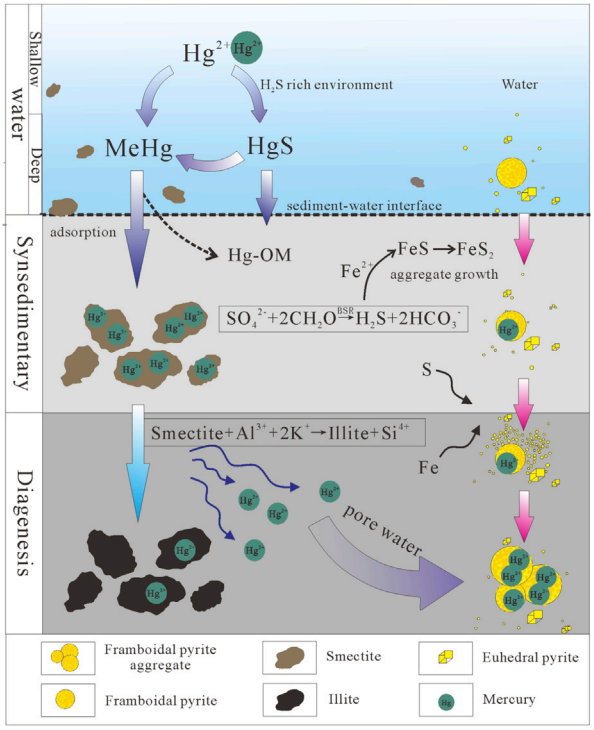

FIGURE 2
Migration and occurrence mode of mercury in syn-sedimentary and diagenetic stages.

Migration of mercury

Generally, the transportation of mercury from volcanic activity to sediments is the main focus, but the migration in the diagenetic stage has been rarely studied previously. Due to the influence of diagenesis, mercury may undergo significant migration (Smit et al., 2016). Based on the mobility of mercury in mineral transformation, we propose a migration mechanism from clay minerals to pyrite during diagenesis. Therefore, it is of interest to explore the migration processes of mercury in water bodies, and during syn-sedimentary, and diagenesis stages (Figure 2). This will affect the effectiveness of mercury as an indicator of volcanic activity.

In water bodies

The mercury derived from the atmosphere or terrigenous debris before entering the water mass is mainly $Hg_{(P)}$ and Hg^{2+} ions (Lin and Pehkonen, 1999). After entering a water body, particulate mercury can be directly adsorbed by porous media, such as organic matter, clay minerals and pyrite (Ravichandran, 2004; Holmes et al., 2009). Under the biotic and abiotic actions, most Hg^{2+} would form Me-Hg and be adsorbed by organic matter, clay minerals and framboidal pyrite (Amyot et al., 1997; Holmes et al., 2009). Some Hg^{2+} reacts with sulfide to form HgS in anoxic water which could be directly precipitated when the water column becomes saturated (Ravichandran, 2004). Unsaturated in concentration, it is methylated to form Me-Hg which would endure the transformation to migration to precipitation process (Niessen et al., 2003).

Syn-sedimentary stage

At this stage, there are mainly three kinds of porous media for mercury adsorption, including organic matter, clay minerals dominated by smectite and framboidal pyrite (Shen et al., 2020), although other hosts (iorn and manganese oxides) can also have an important role (Gobeil and Cossa, 1993; Feyte et al., 2010). Organic matter and clay minerals mainly come from terrestrial weathering products (Singer, 1984), while framboidal pyrite is a syn-sedimentary authigenic mineral formed in anoxic water columns (Wilkin and Barnes, 1997). The formation of sedimentary pyrite is mainly related to bacterial sulfate reduction (BSR) (Berner, 1984). In anoxic water, organic matter is used as reducing agent and energy source to form sulfide (mainly hydrogen sulfide) (Eq. 1), which combines with free active iron to form iron monosulfide microcrystals (Eq. 2) (Wilkin et al., 1996). The microcrystals react to form greigite (Fe_3S_4) and aggregate, and finally form framboidal pyrite (Wilkin et al., 1996). Then framboidal pyrite monomer can be accumulated and preserved in sediments after gathering (Wilkin and Barnes, 1997).

$$SO_4^{2-} + 2CH_2O \xrightarrow{BSR} 2HCO_3^- + H_2S \quad (1)$$

$$H_2S + Fe^{2+} \rightarrow FeS + 2H^+ \quad (2)$$

Diagenetic stage

There are three main groups of clay minerals, namely smectite, illite and kaolinite. During the diagenetic stage, transformations take place, including illitzation of smectite and kaolinite (Curtis, 1985). The transformation of smectite to illite is a most important diagenetic chemical transformation in mudstone with increasing burial depth (Pollastro, 1993; Schicker et al., 2021).

During diagenesis, the petroleum generation process can theoretically release a large quantity of organic acid and carbon dioxide (CO_2) (Barth and Bjorlykke, 1993; Seewald, 2003). This process can promote the dissolution of minerals (mainly feldspar and mica), and then release a large quantity of potassium ions, which would enhance the transformation of smectite to illite (Eq. 3) (Berger et al., 1999). Among the clay minerals, smectite not only has the largest specific surface area

(Passey et al., 2010), but also is the only mineral that has a significant correlation with mercury (Kongchum et al., 2011). Undergoing transformation of smectite to illite, the adsorption capacity of clay minerals is substantially reduced, which could lead to mercury that was adsorbed by smectite in the syn-sedimentary stage entering into pore water to find a new host (Loukola-Ruskeeniemi et al., 2003). However, because of the Hg-OM have relatively high stability constants (10^{22}–10^{28}) (Ravichandran, 2004) and the strong reducing environment of marine mudstones, the mineralization organic matter contributes little to the mercury content in pore water.

$$\text{Smectite} + Al^{3+} + 2K^{+} \rightarrow \text{Illite} + Si^{4+} \quad (3)$$

At the same time, pyrite also undergoes significant transformation in mudstone. The single particle (diameter <6 μm) framboidal pyrite monomer formed during syn-sedimentary deposition has a certain adsorption capacity (Wilkin et al., 1996; Wilkin and Barnes, 1997). Under certain conditions, because of a large quantity of sulfur and iron sources enriching, the individual framboidal pyrite crystals began to form framboidal pyrite aggregates, which could greatly improve the specific surface areas (Wilkin and Barnes, 1997). At this time, with the increase of the specific surface area, the adsorption capacity of pyrite can be greatly improved (Pugh et al., 1981). Furthermore, mercury is associated with abundant pyrite in Shen et al. (2019c), which commonly has a stonger affinity for Hg than other potential host phases (e.g., organic matter, clay minerals; Ravichandran, 2004; Bower et al., 2008). Therefore, free mercury being released by smectite can enter the framboidal pyrite aggregate.

Previous studies have demonstrated that clay minerals are one of the main hosts of mercury (Selin, 2009; Kalvoda et al., 2019; Shen et al., 2019d). However, in the Jiaoye section of the Ordovician/Silurian in South China, it is found that there is almost no mercury in the clay minerals, while a large amount of mercury is enriched in the framboidal pyrite aggregates (Shen et al., 2019c). This also demonstrates that the re-migration of mercury from clay minerals to pyrite during diagenesis. Furthermore, mercury isotope mass-independent fractionation (Hg-MIF) generally occurs in special photochemical processes, such as photoreduction or photooxidation (Blum et al., 2014). Therefore, the Hg-MIF can effectively identify the source of mercury. However, photochemical processes are not involved in the diagenesis process, so the isotopic mass-independent fractionation of mercury did not change significantly during this migration process. In other words, the isotopes do not distinguish whether the source of mercury is diagenetic re-migration. Therefore, when the amount of sedimentary mercury that migrates between layers is large enough, it means that the sedimentary mercury cannot be used as an effective indicator of volcanic activity in LIPs.

Conclusion

According to previous studies, it is found that the diagenetic transformation of the main host of mercury has a great influence on the retention of mercury. In addition, there is a phenomenon in the marine Ordovician/Silurian boundary in South China that a large quantity of mercury is enriched in framboidal pyrite aggregates, but almost lost in clay minerals. These aspects support the assumption of sedimentary mercury migration. For this reason, a diagenetic re-migration model of mercury based on mineral transformation is proposed that migration from clay minerals to pyrite. However, mercury is not suitable as an effective tracer of volcanic activity in large igneous provinces when the interlayer flow of mercury occurs and the mobility is sufficient to limit the reconstruction of the paleoenvironment by mercury. Therefore, inferences about volcanic mercury inputs associated with LIP may need to be re-evaluated. Finally, future research needs to better understand the influence of diagenesis on the migration of mercury are recommended.

Author contributions

BR and SL conceived and designed the study. HX and BR wrote the first draft of the manuscript. TS provided constructive suggestions for improving the work. CL, YL, and YZ edited and reviewed the manuscript.

Funding

The article is supported by the National Scientific Fund Project “Fundamental Study on Marine Deep-Layer Oil and Gas Enrichment Mechanism and Key Engineering Technologies” (No. U19B6003) and the National Natural Science Foundation of China (NSFC, Project NO. 42072129).

Conflict of interest

The authors CL, YL, and YZ were employed by Petrochina Southwest Oil and Gasfield Company.

The remaining authors declare that the research was conducted in the absence of any commercial or financial relationships that could be construed as a potential conflict of interest.

Publisher’s note

References

Amyot, M., Gill, G. A., and Morel, F. M. (1997). Production and loss of dissolved gaseous mercury in coastal seawater. *Environ. Sci. Technol.* 31 (12), 3606–3611. doi:10.1021/es9703685

Barth, T., and Bjørlykke, K. (1993). Organic acids from source rock maturation: generation potentials, transport mechanisms and relevance for mineral diagenesis. *Appl. Geochem.* 8 (4), 325–337. doi:10.1016/0883-2927(93)90002-X

Berger, G., Velde, B., and Aigouy, T. (1999). Potassium sources and illitization in Texas Gulf Coast shale diagenesis. *J. Sediment. Res.* 69 (1), 151–157. doi:10.2110/jsr.69.151

Berner, R. A. (1984). Sedimentary pyrite formation: an update. *Geochimica Cosmochimica Acta* 48 (4), 605–615. doi:10.1016/0016-7037(84)90089-9

Blum, J. D., Sherman, L. S., and Johnson, M. W. (2014). Mercury isotopes in Earth and environmental sciences. *Annu. Rev. Earth Planet. Sci.* 42, 249–269. doi:10.1146/annurev-earth-050212-124107

Boszke, L., Kowalski, A., Glosifiska, G., Szarek, R., and Siepak, J. (2003). Environmental factors affecting speciation of mercury in the bottom sediments; an overview. *Pol. J. Environ. Stud.* 12, 5.

Bower, J., Savage, K. S., Weinman, B., Barnett, M. O., Hamilton, W. P., and Harper, W. F. (2008). Immobilization of mercury by pyrite (FeS_2). *Environ. Pollut.* 156, 504–514. doi:10.1016/j.envpol.2008.01.011

Cossa, D., and Gobeil, C. (2000). Mercury speciation in the Lower st. Lawrence estuary. *Can. J. Fish. Aquat. Sci.* 57, 138–147. doi:10.1139/f99-237

Curtis, C. D. (1985). Clay mineral precipitation and transformation during burial diagenesis. *Philosophical Trans. R. Soc. Lond. Ser. A. J. Math. Phys. Sci.* 315 (1531), 91–105. doi:10.1098/rsta.1985.0031

Farrah, H., and Pickering, W. F. (1978). The sorption of mercury species by clay minerals. *Water Air Soil Pollut.* 9 (1), 23–31. doi:10.1007/bf00185744

Feyte, S., Tessier, A., Gobeil, C., and Cossa, D. (2010). *In situ* adsorption of mercury, methylmercury and other elements by iron oxyhydroxides and organic matter in lake sediments. *Appl. Geochem.* 25 (7), 984–995. doi:10.1016/j.apgeochem.2010.04.005

Fitzgerald, W. F. (1995). Is mercury increasing in the atmosphere? The need for an atmospheric mercury network (AMNET). *Water Air Soil Pollut.* 80 (1), 245–254. doi:10.1007/BF01189674

Font, E., Adatte, T., Sial, A. N., de Lacerda, L. D., Keller, G., and Punekar, J. (2016). Mercury anomaly, Deccan volcanism, and the end-Cretaceous mass extinction. *Geology* 44 (2), 171–174. doi:10.1130/G37451.1

Froelich, P. M., Klinkhammer, G. P., Bender, M. L., Lurdtke, N. A., Heath, G. R., Cullen, D., et al. (1979). Early oxidation of organic matter in pelagic sediments of the eastern equatorial atlantic: suboxic diagenesis. *Geochimica Cosmochimica Acta* 43, 1075–1090. doi:10.1016/0016-7037(79)90095-4

Gagnon, C., Pelletier, E., and Mucci, A. (1997). Behaviour of anthropogenic mercury in coastal marine sediments. *Mar. Chem.* 59, 159–176. doi:10.1016/S0304-4203(97)00071-6

Gobeil, C., and Cossa, D. (1993). Mercury in sediments and sediment pore water in the Laurentian Trough. *Can. J. Fish. Aquat. Sci.* 50 (8), 1794–1800. doi:10.1139/f93-201

Grasby, S. E., Beauchamp, B., Bond, D. P., Wignall, P. B., and Sanei, H. (2016). Mercury anomalies associated with three extinction events (Capitanian crisis, latest Permian extinction and the Smithian/Spathian extinction) in NW Pangea. *Geol. Mag.* 153 (2), 285–297. doi:10.1017/S0016756815000436

Grasby, S. E., Them, T. R., Chen, Z., Yin, R., and Ardakani, O. H. (2019). Mercury as a proxy for volcanic emissions in the geologic record. *Earth-Science Rev.* 196, 102880. doi:10.1016/j.earscirev.2019.102880

Gustin, M. S. (2003). Are mercury emissions from geologic sources significant? A status report. *Sci. Total Environ.* 304 (1-3), 153–167. doi:10.1016/S0048-9697(02)00565-X

Holmes, C. D., Jacob, D. J., Mason, R. P., and Jaffe, D. A. (2009). Sources and deposition of reactive gaseous mercury in the marine atmosphere. *Atmos. Environ.* 43 (14), 2278–2285. doi:10.1016/j.atmosenv.2009.01.051

Horowitz, A. J. (1991). *A primer on sediment-trace element chemistry*, 2. Chelsea: Lewis Publishers.

Kalvoda, J., Kumpan, T., Qie, W., Frýda, J., and Bábek, O. (2019). Mercury spikes at the devonian-carboniferous boundary in the eastern part of the rhenohercynian zone (central europe) and in the South China block. *Palaeogeogr. Palaeoclimatol. Palaeoecol.* 531, 109221. doi:10.1016/j.palaeo.2019.05.043

Kongchum, M., Hudnall, W. H., and Delaune, R. D. (2011). Relationship between sediment clay minerals and total mercury. *J. Environ. Sci. Health Part A* 46 (5), 534–539. doi:10.1080/10934529.2011.551745

Krupp, R. (1988). Physicochemical aspects of mercury metallogenesis. *Chem. Geol.* 69 (3-4), 345–356. doi:10.1016/0009-2541(88)90045-9

Lamborg, C. H., Fitzgerald, W. F., O'Donnell, J., and Torgersen, T. (2002). A non-steady-state compartmental model of global-scale mercury biogeochemistry with interhemispheric atmospheric gradients. *Geochimica Cosmochimica Acta* 66 (7), 1105–1118. doi:10.1016/S0016-7037(01)00841-9

Lin, C. J., and Pehkonen, S. O. (1999). The chemistry of atmospheric mercury: a review. *Atmos. Environ.* 33 (13), 2067–2079. doi:10.1016/S1352-2310(98)00387-2

Lindberg, S. A., and Stratton, W. J. (1998). Atmospheric mercury speciation: Concentrations and behavior of reactive gaseous mercury in ambient air. *Environ. Sci. Technol.* 32 (1), 49–57. doi:10.1021/es970546u

Loukola-Ruskeeniemi, K., Kantola, M., Halonen, T., Seppänen, K., Henttonen, P., Kallio, E., et al. (2003). Mercury-bearing black shales and human Hg intake in eastern Finland: impact and mechanisms. *Env. Geol.* 43 (3), 283–297. doi:10.1007/s00254-002-0625-9

Mason, R. P., Fitzgerald, W. F., and Morel, F. M. (1994). The biogeochemical cycling of elemental mercury: anthropogenic influences. *Geochimica Cosmochimica Acta* 58 (15), 3191–3198. doi:10.1016/0016-7037(94)90046-9

Mcneal, J. M., and Rose, A. W. (1974). The geochemistry of mercury in sedimentary rocks and soils in Pennsylvania. *Geochimica Cosmochimica Acta* 38 (12), 1759–1784. doi:10.1016/0016-7037(74)90160-4

Morel, F. M., Kraepiel, A. M., and Amyot, M. (1998). The chemical cycle and bioaccumulation of mercury. *Annu. Rev. Ecol. Syst.* 29, 543–566. doi:10.1146/annurev.ecolsys.29.1.543

Niessen, S., Foucher, D., Clarisse, O., Fischer, J. C., Mikac, N., Kwokal, Z., et al. (2003). Influence of sulphur cycle on mercury methylation in estuarine sediment (seine estuary, france). *J. Phys. IV Fr.* 107, 953–956. doi:10.1051/jp4:20030456

Obrist, D. (2007). Atmospheric mercury pollution due to losses of terrestrial carbon pools? *Biogeochemistry* 85 (2), 119–123. doi:10.1007/s10533-007-9108-0

Oliveri, E., Manta, D. S., Bonsignore, M., Cappello, S., Tranchida, G., Bagnato, E., et al. (2016). Mobility of mercury in contaminated marine sediments: biogeochemical pathways. *Mar. Chem.* 186, 1–10. doi:10.1016/j.marchem.2016.07.002

Passey, Q. R., Bohacs, K. M., Esch, W. L., Klimentidis, R., and Sinha, S. (2010). "From oil-prone source rock to gas-producing shale reservoir–geologic and petrophysical characterization of unconventional shale-gas reservoirs," in International oil and gas conference and exhibition in China, Beijing, China, 8-10 June 2010. doi:10.2118/131350-MS

Percival, L. M. E., Witt, M. L. I., Mather, T. A., Hermoso, M., Jenkyns, H. C., Hesselbo, S. P., et al. (2015). Globally enhanced mercury deposition during the end-pliensbachian extinction and toarcian OAE: A link to the karoo–ferrar Large igneous province. *Earth Planet. Sci. Lett.* 428, 267–280. doi:10.1016/j.epsl.2015.06.064

Pirrone, N., Cinnirella, S., Feng, X., Finkelman, R. B., Friedli, H. R., Leaner, J., et al. (2010). Global mercury emissions to the atmosphere from anthropogenic and natural sources. *Atmos. Chem. Phys.* 10 (13), 5951–5964. doi:10.5194/acp-10-5951-2010

Pollastro, R. M. (1993). Considerations and applications of the illite/smectite geothermometer in hydrocarbon-bearing rocks of Miocene to Mississippian age. *Clays Clay Minerals* 41 (2), 119–133. doi:10.1346/CCMN.1993.0410202

Pugh, C. E., Hossner, L. R., and Dixon, J. B. (1981). Pyrite and marcasite surface area as influenced by morphology and particle diameter. *Soil Sci. Soc. Am. J.* 45 (5), 979–982. doi:10.2136/sssaj1981.03615995004500050033x

Rasmussen, P. E. (1994). Current methods of estimating atmospheric mercury fluxes in remote areas. *Environ. Sci. Technol.* 28 (13), 2233–2241. doi:10.1021/es00062a006

Ravichandran, M. (2004). Interactions between mercury and dissolved organic matter––a review. *Chemosphere* 55 (3), 319–331. doi:10.1016/j.chemosphere.2003.11.011

Sanei, H., Grasby, S. E., and Beauchamp, B. (2012). Latest Permian mercury anomalies. *Geology* 40 (1), 63–66. doi:10.1130/G32596.1

Schicker, A., Gier, S., Schieber, J., and Krois, P. (2021). Diagenesis of the malmian mikulov formation source rock, vienna basin: Focus on matrix and pores. *Mar. Petroleum Geol.* 129, 105082. doi:10.1016/j.marpetgeo.2021.105082

Schroeder, W. H., and Munthe, J. (1998). Atmospheric mercury—An overview. *Atmos. Environ.* 32 (5), 809–822. doi:10.1016/S1352-2310(97)00293-8

Seewald, J. S. (2003). Organic–inorganic interactions in petroleum-producing sedimentary basins. *Nature* 426 (6964), 327–333. doi:10.1038/nature02132

Selin, N. E. (2009). Global biogeochemical cycling of mercury: a review. *Annu. Rev. Environ. Resour.* 34 (1), 43–63. doi:10.1146/annurev.environ.051308.084314

Shen, J., Algeo, T. J., Planavsky, N. J., Yu, J., Feng, Q., Song, H., et al. (2019a). Mercury enrichments provide evidence of Early Triassic volcanism following the end-Permian mass extinction. *Earth-Science Rev.* 195, 191–212. doi:10.1016/j.earscirev.2019.05.010

Shen, J., Chen, J., Algeo, T. J., Yuan, S., Feng, Q., Yu, J., et al. (2019b). Evidence for a prolonged Permian–Triassic extinction interval from global marine mercury records. *Nat. Commun.* 10 (1), 1563–1569. doi:10.1038/s41467-019-09620-0

Shen, J., Algeo, T. J., Chen, J., Planavsky, N. J., Feng, Q., Yu, J., et al. (2019c). Mercury in marine Ordovician/Silurian boundary sections of South China is sulfide-hosted and non-volcanic in origin. *Earth Planet. Sci. Lett.* 511, 130–140. doi:10.1016/j.epsl.2019.01.028

Shen, J., Yu, J., Chen, J., Algeo, T. J., Xu, G., Feng, Q., et al. (2019d). Mercury evidence of intense volcanic effects on land during the Permian-Triassic transition. *Geology* 47 (12), 1117–1121. doi:10.1130/G46679.1

Shen, J., Feng, Q., Algeo, T. J., Liu, J., Zhou, C., Wei, W., et al. (2020). Sedimentary host phases of mercury (Hg) and implications for use of Hg as a volcanic proxy. *Earth Planet. Sci. Lett.* 543, 116333. doi:10.1016/j.epsl.2020.116333

Sial, A. N., Chen, J., Lacerda, L. D., Frei, R., Tewari, V. C., Pandit, M. K., et al. (2016). Mercury enrichment and Hg isotopes in Cretaceous–Paleogene boundary successions: Links to volcanism and palaeoenvironmental impacts. *Cretac. Res.* 66, 60–81. doi:10.1016/j.cretres.2016.05.006

Singer, A. (1984). The paleoclimatic interpretation of clay minerals in sediments—A review. *Earth-Science Rev.* 21 (4), 251–293. doi:10.1016/0012-8252(84)90055-2

Smit, J., Koeberl, C., Claeys, P., and Montanari, A. (2016). Mercury anomaly, Deccan volcanism, and the end-Cretaceous mass extinction:Comment. *Geology* 44 (3), 381. doi:10.1130/G37683C.1

Wilkin, R. T., and Barnes, H. L. (1997). Formation processes of framboidal pyrite. *Geochimica Cosmochimica Acta* 61 (2), 323–339. doi:10.1016/S0016-7037(96)00320-1

Wilkin, R. T., Barnes, H. L., and Brantley, S. L. (1996). The size distribution of framboidal pyrite in modern sediments: an indicator of redox conditions. *Geochimica Cosmochimica Acta* 60 (20), 3897–3912. doi:10.1016/0016-7037(96)00209-8

Young, D. R., Johnson, J. N., Soutar, A., and ISAACS, J. D. (1973). Mercury concentrations in dated varved marine sediments collected off Southern California. *Nature* 244 (5414), 273–275. doi:10.1038/244273a0

frontiers | Frontiers in Earth Science

TYPE Mini Review
PUBLISHED 26 January 2023
DOI 10.3389/feart.2022.1065875

OPEN ACCESS

EDITED BY
Tao Hu,
China University of Petroleum, Beijing, China

REVIEWED BY
Chao Liang,
China University of Petroleum, Huadong, China
Wenyang Wang,
Institute of Geology and Geophysics (CAS), China

*CORRESPONDENCE
Youbin He,
heyb122@163.com
Qiao Deng,
3191181788@qq.com

SPECIALTY SECTION
This article was submitted to Geochemistry, a section of the journal Frontiers in Earth Science

RECEIVED 10 October 2022
ACCEPTED 05 December 2022
PUBLISHED 26 January 2023

CITATION
Tao Y, He Y, Zhao Z, Wu D and Deng Q (2023), Sealing of oil-gas reservoir caprock: Destruction of shale caprock by micro-fractures.
Front. Earth Sci. 10:1065875.
doi: 10.3389/feart.2022.1065875

Sealing of oil-gas reservoir caprock: Destruction of shale caprock by micro-fractures

Ye Tao[1,2], Youbin He[1,2]*, Zhongxiang Zhao[1,2], Dongsheng Wu[1,2] and Qiao Deng[3,4,5]*

[1]Key Laboratory of Exploration Technologies for Oil and Gas Resources, Ministry of Education, Yangtze University, Wuhan, China, [2]School of Geoscience, Yangtze University, Wuhan, China, [3]Cooperative Innovation Center of Unconventional Oil and Gas, Yangtze University Ministry of Education & Hubei Province, Wuhan, China, [4]Hubei Key Laboratory of Drilling and Production Engineering for Oil and Gas, Yangtze University, Wuhan, China, [5]Carbon Hydrogen Epoch Technology, Co., Ltd, Wuhan, China

The sealing ability of caprock is affected by many factors, such as cap thickness, displacement pressure, fracture development, and lithology of caprock. Shale is one of the ideal materials for oil and gas sealing cap formation due to its low porosity and permeability. Microfractures can destroy the sealing property of shale caprock. When buried deep enough, shale will change from toughness to brittleness. In general, the greater the brittleness of shale, the more developed the fractures will be. In areas with high tectonic stress, such as the anticline axis, syncline axis and stratum dip end, the strata stress is high and concentrated, and it is easier to generate fractures. When the stress state of the caprock changes, new micro-cracks are formed or previously closed cracks are re-opened, reducing the displacement pressure of the caprock. These micro-fractures are interconnected to form microleakage spaces, which reduces the sealing capacity of the caprock.

KEYWORDS

caprock, shale, microfractures, sealing ability, oil-gas reservoir, petroleum migration

Introduction

In recent years, the demand for oil and gas resources has been increasing daily, and the oil and gas exploration and exploitation scale at home and abroad is increasing gradually. The study of oil and gas accumulation conditions plays a vital role in oil and gas exploration. With the deepening of the research on reservoir-forming conditions of significant oil and gas fields, people gradually realize that the effectiveness of caprock plays a crucial role in reservoir-forming. Among the hydrocarbon accumulation elements, hydrocarbon generation is the basis and, trap is the condition, preservation is the key (Li et al., 1997). The caprock is the core content of the study of oil and gas preservation conditions (Xiao et al., 2006), the quality of caprock directly affects the formation, scale and preservation of the oil-gas reservoir. Caprock lithology determines its sealing ability. The caprock lithology of some large oil and gas fields is mainly evaporite and shale (Nederlof & Mohler., 1981). As a dense caprock, shale is characterized by low porosity and permeability, so it is one of the ideal materials for oil

and gas sealing caprock and plays a crucial role in the accumulation and preservation of oil and gas (Jin et al., 2014).

So far, fruitful research results have been obtained, and a relatively mature theoretical foundation has been formed on the sealing property of shale caprock research. The thickness of caprock (Zieglar, 1992; Lv et al., 2005), faults development extent (Skerlec, 2002; Fu et al., 2015) and diagenetic evolution (Lu et al., 2021) have direct or indirect effects on the sealing ability of shale caprock. Most scholars at home and abroad research shale fractures mainly focus on fractured oil-gas reservoirs (Fu et al., 2022). However, the research on "micro fracture damage of mudstone caprock" has not yet formed a mature theoretical system.

Research progress on sealing of caprock

The rapid development of the global petroleum industry promotes the continuous updating and improvement of petroleum geological theories. The study of oil-gas reservoir caprock has been paid more and more attention by scholars at home and abroad. The study of cap sealing can be roughly divided into four stages, as shown in Table 1. In 1966, Smith introduced the concept of cap and fault sealing (Smith, 1966). In 1987 Watts proposed the capillary sealing mechanism and hydraulic sealing mechanism of caprock, which promoted the qualitative evaluation of caprock and fault sealing mechanism (Watts et al., 1987). In 1996, Lu put forward the overpressure sealing mechanism and hydrocarbon concentration sealing mechanism, and the method of using displacement pressure, effective stress and tensile strength to evaluate the sealing ability according to different sealing mechanisms, and established the industry standard for sealing evaluation of caprock (Lv et al., 1996). In 2013, Jin put forward the evaluation method of the dynamic evolution process of the sealing capacity of shale caprock.

Factors affecting sealing ability of caprock

The displacement pressure mainly determines the sealing ability of caprock. The greater the displacement pressure, the stronger the sealing ability of the caprock is (Dewhurst et al., 1998). There is no direct relationship between cap thickness and capillary sealing ability, so some scholars, such as Hubbert (1953), believe that cap thickness has no significance on capillary sealing ability.

However, some scholars believe that although there is no direct functional relationship between caprock thickness and capillary sealing capacity, it does not mean that caprock thickness does not affect sealing capacity (Nederlof & Mohler., 1981; Fu et al., 2003). The thicker the cap is, the more difficult it is to be damaged by fracture. The thinner the cap thickness is, the easier it is to be damaged by fracture and lose the continuity of transverse distribution. Lv (2005) believed that the thicker the caprock thickness, the larger the spatial distribution area, the stronger the ability of caprock to seal gas, and the more conducive to the accumulation and preservation of gas. Yuan (2011) believes that the displacement pressure of caprock has nothing to do with the thickness, but the height of the enclosed gas column of caprock is related to the thickness; that is, the larger the cap rocks thickness, the higher the height of the enclosed oil and gas column, and the sealing ability of caprock is stronger. Lou (2021) found that the influence of clay minerals on rock sealing performance was related to plasticity and water absorption. The excellent or medium caprock was predominantly clayey mudstone, while the inferior caprock was mainly silty mudstone. Due to the influence of tectonic changes, most caprocks are destroyed in two ways. One way is the tectonic uplift of denuded caprock, which makes the thickness of the caprock thin or even exhausted at the denuded place; Another way is that faults destroy the caprock (Fu et al., 2003). Once the fault dislocates the caprock, the continuous capping range of the caprock will be reduced, and the sealing capacity of the caprock will change. If the length of the fault is greater than the thickness of the caprock, the caprock will be broken through by the fault, losing the ability to seal oil and gas (Wibberley et al., 2008). If the caprock is thick enough, the possibility of complete dislocation of the fault can be reduced.

The sealing property of caprock is closely related to the diagenetic evolution stage. The porosity and permeability of mudstone decrease with the increase in burial depth, indicating that it can effectively seal oil and gas only when it reaches a certain burial depth. When the burial depth of mudstone increases continuously and reaches a specific diagenetic stage, the plasticity of the rock will decrease, and

TABLE 1 Development history of cap sealing research.

Development stage	Lithology	Theory
Establishment of oil and gas sealing concept (before 1966)	mudstone	Anticline oil accumulation theory
Exploration of the sealing mechanism of caprock (1966–1996)	Shale, evaporite	The standard for evaluating caprock has been established
Quantitative evaluation of Caprock Sealing (1997–2012)	Shale, evaporite, limestone	A complete idea of caprock evaluation is established
Study on the dynamic evolution of sealing capacity of caprock (2013-)	Shale, evaporite, limestone	Dynamic evolution of sealing capacity of caprock

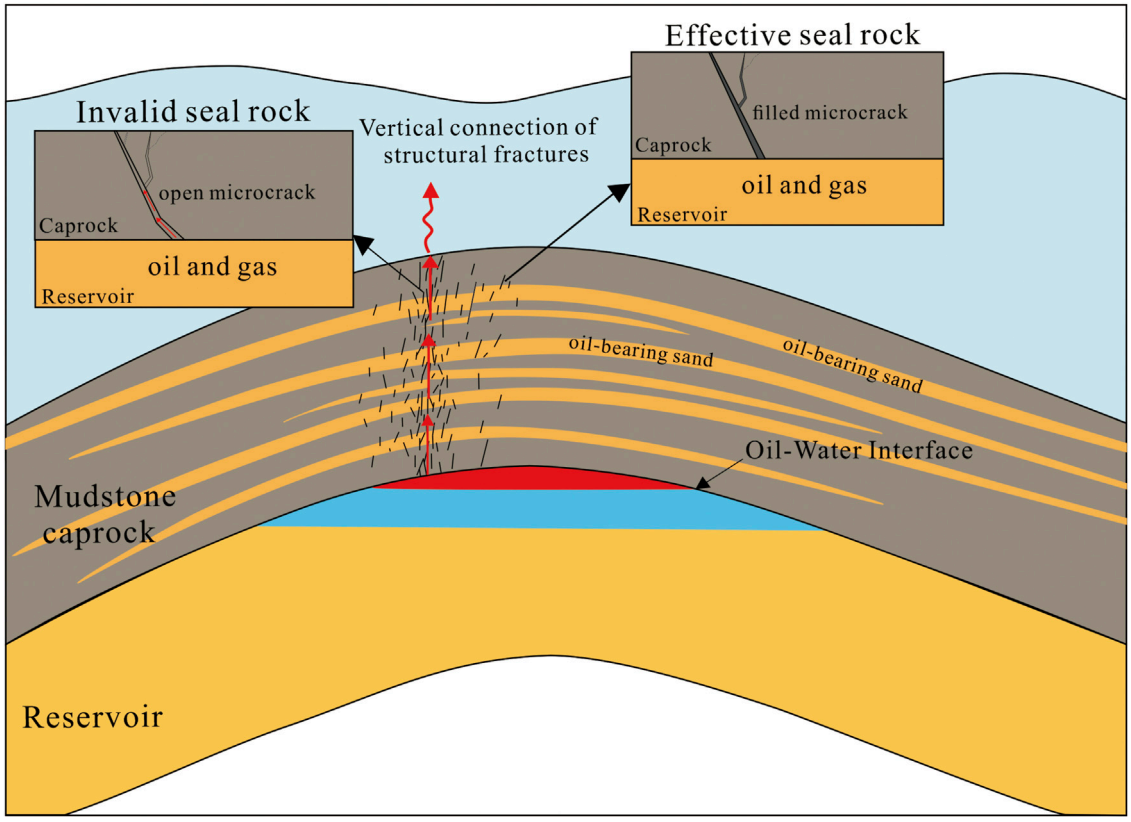

FIGURE 1
Schematic diagram of micro-crack damage to caprock.

the brittleness will increase. Under the action of over-pressure and other geostress, the shale caprock is prone to produce micro-fractures, thus reducing the displacement pressure. Therefore, the vertical evolution of the effective caprock capacity of mudstone caprock is from poor to good to poor. The main reason for the poor sealing of deep, dense mudstone is fracture (Lu, 2021).

Destruction of shale caprock by microfractures

The degree of fracture development is generally positively correlated with the content of brittle minerals in rocks (De Paola et al., 2009; Alqahtani et al., 2013). The more brittle minerals such as quartz, feldspar and carbonates are contained, the more brittle shale and the more uncomplicated fractures are to develop (Ding, 2012). With the increase of burial depth and the enhancement of the degree of compaction diagenesis (late diagenetic stage), shale will undergo a process from toughness to brittleness. When the burial depth of shale is deep enough, the brittleness is enhanced, and cracks are easily produced due to the influence of tectonic stress, thus reducing the capillary sealing capacity. Corcoran and Dore used the density and strain at fracture to quantitatively judge the transformation process of shale from brittleness to toughness. In the brittle stage, the density of shale is greater than 2.5 g/cm^3, and the strain before fracture is less than 3%. In the transition stage, the density of shale is 2.5–2.25 g/cm^3, and the strain is 5%–8%. In the ductile stage, the density of shale is less than 2.25 g/cm^3, and the strain is more than 8%.

Shale caprock usually contains a large number of micro-fractures. In areas with high tectonic stress, such as anticline axis, syncline axis and stratum dip end, stratum stress is high and concentrated, and fractures are developed (Brantut et al., 2011; Raduha et al., 2016). These micro-fractures are often isolated and closed under regular stress. When the stress state of the caprock changes, new micro-cracks would form or previously closed cracks would re-open, reducing the displacement pressure (Mildren et al., 2002). These micro-cracks are interconnected to form micro-leakage Spaces, which will reduce the sealing capacity of the caprock (Wu, 2020). Even locally continuous shale intervals can fail due to excessive fractures in local areas, as shown in Figure 1. The main mechanisms that cause the change of caprock stress include tectonic extrusion, tectonic uplift and

abnormally high-pressure fluid (Lamarche et al., 2012; Orlic & Wassing., 2013). Among them, the caprock failure caused by faults belongs to the category of vertical sealing of faults, and its evaluation method has been relatively mature. However, since cracks are "invisible", there is still a lack of effective evaluation methods.

Expectations

1) We can subdivide diagenetic stages by combining the formation and evolution of faults and fractures. In this way, the dynamic evolution process of the sealing capacity of caprock can be further studied
2) The rock mechanics of the caprock has changed dramatically during burial and uplift, and the condition of brittle-ductile transition is still a complex problem. Perhaps we can establish a quantitative characterization method for the transition from brittleness to toughness through a triaxial compression test, acoustic emission characteristics, micro deformation mechanism and deformation characteristics of the cap structure.
3) The existence of a large number of microcracks in the caprock is not necessarily a bad thing. When there is no large fault in the basin as the bottom oil and gas transportation channel, many micro-fractures developed in mudstone, shale and siltstone can be connected to form a vertical migration channel of oil and gas. When the stress field of the local layer changes, micro-cracks are easily produced at the high part of the trap. Oil and gas migrate to the upper reservoir along the vertical channel composed of fractures. Corcoran and Doré, 2002, Downey, 1984, Lv et al., 1996, Smith, 1966, Watts, 1987.

Author contributions

YT was responsible for the preliminary literature research, the writing of the whole manuscript and the drawing of the figure. YH and DW were responsible for the late revision and submission of the manuscript. QD and ZZ were responsible for providing inspiration and ideas for the manuscript.

Funding

National Natural Science Fund: 42002165.

Conflict of interest

QD was employed by Carbon Hydrogen Epoch Technology Co., Ltd

The remaining authors declare that the research was conducted in the absence of any commercial or financial relationships that could be construed as a potential conflict of interest.

Publisher's note

References

Alqahtani, A. A. (2013). Effect of mineralogy and petrophysical characteristics on acoustic and mechanical properties of organic rich shale[C]//Proceedings of the Unconventional Resources Technology Conference(URTEC), Richardson, TX, United States, 199–411.

Brantut, N., Schubnel, A., and Guéguen, Y. (2011). Damage and rupture dynamics at the brittle-ductile transition:The case of gypsum[J]. Journal of Geophysical Research. *Solid earth.* 116, B11404

Corcoran, V., and Doré, A. (2002). *Top seal assessment in exhumed basin settings-some insights from Atlantic Margin and borderland basins Koestler A G, Hunsdale R. Hydrocarbon Seal Quantification*. NPF Special Publication, Iran, 89–107.

De Paola, N., Faulkner, D. R., and Collettini, C. (2009). Brittle versus ductile deformation as the main control on the transport properties of low-porosity anhydrite rocks. *J. Geophys. Res.* 114 (B6), B06211–B06266. doi:10.1029/2008jb005967

Dewhurst, D. N., Aplin, A. C., Sarda, J. P., and Yang, Y. (1998). Compaction - driven evolution of porosity and permeability in natural mudstones: An experimental study. *J. Geophys. Res.* 103 (B1), 651–661. doi:10.1029/97jb02540

Ding, W., Li, C., Li, C., Xu, C., Jiu, K., and Zeng, W. (2012). Dominant factor of fracture development in shale and its relationship to gas accumulation. *Earth Sci. Front.* 19 (2), 212–220. CNKI:SUN:DXQY.0.2012-02 -031.

Downey, M. (1984). Evaluating seals for hydrocarbon accumulations. *AAPG Bull.* 68, 1752–1763.

Fu, G., and Xu, F. (2003). Quantitative research on controlling of thickness to seal abilities of caprock. *Nat. Gas. Geosci.* 3, 186–190. doi:10.3969/j.issn.1672-1926.2003.03.006

Fu, X., Jia, R., Wang, H., Wu, T., Meng, L., and Sun, Y. (2015). Quantitative evaluation on the fault-caprock sealing capacity of Dabei-kelasu structural belt in Kuqa depression, Tarim basin, NW China. *Petroleum Explor. Deveopment* 42 (3), 300–309. doi:10.11698/PED.2015.03.06

Fu, X., Lv, D., Huang, J., Wang, G., Meng, L., Wang, H., et al. (2022). Fault-caprock coupling sealing mechanism and fault trap hydrocarbon accumulation model. *Nat. Gas. Ind.* 42 (03), 21–28. doi:10.3787/j.issn.1000-0976.2022.03.003

Lamarche, J., Lavenu, A. P., Gauthier, B. D., Guglielmi, Y., and Jayet, O. (2012). Relationships between fracture patterns, geodynamics and mechanical stratigraphy in Carbonates (South-East Basin, France). *Tectonophysics* 581, 231–245. doi:10.1016/j.tecto.2012.06.042

Li, M., Li, W., Cai, F., and Sun, D. (1997). Integrative study of preservation conditions of oil and gas pools. *Acta Pet. Sin.* 2, 44–51. doi:10.7623/syxb199702007

Lou, M., Yang, X., You, L., Dai, L., Wang, N., and Qiu, L. (2021). The main factors affecting the quality of mudstone caprock and a new idea for its evaluation. *J. Chengdu Univ. Technol. Technol. Ed.* 48 (01), 82–93. doi:10.3969/j.issn.1671-9727.2021.01.09

Lu, X., Liu, S., Tian, H., Ma, X., Yu, Z., Fan, J., et al. (2021). An evaluation method for the integrity of mudstone caprock in deep anticlinal traps and its application: A

case study of the sinian gas reservoirs in the central sichuan basin. *Acta Pet. Sin.* 42, doi:10.7623/syxb202104001

Lv, Y., Fu, G., and Gao, D. (1996). *Study on the cap rock of reservoir*. Beijing: Petroleum Industry Press, 118–120.

Lv, Y., Fu, G., and Yu, D. (2005). Comprehensive evaluation of sealing ability of cap rock in China's large and medium gas fields and their contribution to gas accumulation. *Oil Gas Geol.* 6, 742–745+753. doi:10.3321/j.issn:0253-9985.2005.06.007

Mildren, S. D., and Hillis, R. R. (2002). Fast: a new approach to risking fault reactivation and related seal breach[J]. *AAPG Bulletin*, 2, 101–103.

Nederlof, M. H., and Mohler, H. P. (1981). Quantitative investigation of trapping effect of unfaulted caprock. *AAPG Bull.* 65 (5), 964–965.

Orlic, B., and Wassing, B. B. T. (2013). A study of stress change and fault slip in producing gas reservoirs overlain by elastic and viscoelastic caprocks. *Rock Mech. Rock Eng.* 46 (3), 421–435. doi:10.1007/s00603-012-0347-6

Raduha, S., Butler, D., Mozley, P. S., Person, M., Evans, J., Heath, J. E., et al. (2016). Potential seal bypass and caprock storage produced by deformation band to opening mode fracture transition at the reservoir/caprock interface. *Geofluids* 16 (4), 752–768. doi:10.1111/gfl.12177

Skerlec, G. (2002). *Hydrocarbon traps exploration*. Beijing: PetroleumIndustry Press, 395–444.

Smith, D. (1966). Theoretical consideration of sealing and nonsealing faults. *AAPG Bull.* 50 (2), 363–374.

Watts, N. (1987). Theoretical aspects of cap rock and fault seals for single-and two-phase hydrocarbon columns. *Mar. Petroleum Geol.* 4 (4), 274–307. doi:10.1016/0264-8172(87)90008-0

Wibberley, C. A. J., Yielding, G., Toro, G. D., Kurz, W., and Imber, J. (2008). The internal structure of fault zones , implications for mechanical and fluid-flow properties. *Recent Adv. Underst. fault zone Intern. Struct. a Rev.* 299, 5–33.

Wu (2020). *Study on the dynamic evolution of sealing capacity of mudstone and gypsum caprocks*. Northeast Petroleum University. Daqing, China, doi:10.26995/d.cnki.gdqsc.2020.000934

Xiao, K., Wo, Y., Zhou, Y., and Tian, H. (2006). Petroleum reservoiring characteristics and exploration direction in marine strata in southern China. *Oil Gas Geol.* 3, 316–325. doi:10.11743/ogg20060305

Zieglar, D. (1992). Hydrocarbon columns, buoyancy pressures, and seal efficiency: Comparisons of oil and gas accumulations in California and the rocky mountain area. *Am. Assoc. Pet. Geol. Bull.* 76 (4), 501–508.

frontiers | Frontiers in Earth Science

TYPE Original Research
PUBLISHED 02 February 2023
DOI 10.3389/feart.2023.1059869

OPEN ACCESS

EDITED BY
Xiaomin Xie,
Yangtze University, China

REVIEWED BY
Wei Dang,
Xi'an Shiyou University, China
Yanyan Chen,
Research Institute of Petroleum Exploration and Development (RIPED), China

*CORRESPONDENCE
Kun Jiao,
jiaokun@foxmail.com

SPECIALTY SECTION
This article was submitted to Geochemistry, a section of the journal Frontiers in Earth Science

RECEIVED 02 October 2022
ACCEPTED 10 January 2023
PUBLISHED 02 February 2023

CITATION
Xie G, Jiao K, Deng B, Hao W and Liu S (2023), Pore characteristics and preservation mechanism of over-6000-m ultra-deep shale reservoir in the Sichuan Basin.
Front. Earth Sci. 11:1059869.
doi: 10.3389/feart.2023.1059869

Pore characteristics and preservation mechanism of over-6000-m ultra-deep shale reservoir in the Sichuan Basin

Guoliang Xie[1,2], Kun Jiao[2]*, Bin Deng[2], Weiduo Hao[3,4] and Shugen Liu[2,5]

[1]School of Civil Engineering and Architechure, Tongling University, Tongling, China, [2]State Key Laboratory of Oil and Gas Reservoir Geology and Exploitation, Chengdu University of Technology, Chengdu, China, [3]Department of Earth and Atmospheric Sciences, University of Alberta, Edmonton, AB, Canada, [4]Department of Geology, Northwest University, Xi'an, China, [5]Xihua University, Chengdu, China

Investigation of pore characteristics and their preservation mechanism of over 6000 m ultra-deep shale reservoirs is of significance for shale gas exploration and development in the Sichuan Basin. In this study, the pores structure and multifractal characteristics of pores for the Longmaxi shale and Qiongzhusi shale in the Sichuan Basin are well studied by using field emission scanning electron microscopy (FE-SEM), gas adsorption and multifractal analysis. The results show that: (1) Extremely strong mechanical compaction resulting from ultra-deep burial depth can lead to the homogenization of pore structure, which is characterized by the change of bubble-like OM pores to silt or fracture shape pores and the higher average pore diameter (APD) value. (2) The Longmaxi shale and Qiongzhusi shale reservoirs have the obvious multifractal nature for different pore sizes. Samples from the Longmaxi shale and Qiongzhusi shale in well CS#1 demonstrate the higher average H values and smaller average ΔD values compared with those samples in well MS#1, indicating that shale reservoir in over-pressure condition has higher connectivity and less heterogeneity. The pore preservation in over 6000 m ultra-deep shale reservoirs are influenced by several geological factors, including 1) quartz is beneficial for the preservation of pores especially for OM pores due to its supporting effect; 2) the shale reservoirs in over-pressure show many more OM pores and higher surface porosity than those in normal pressure; 3) the direct floor of Qiongzhusi shale is likely the critical geological factor affecting the pores preservation. Therefore, the Longmaxi shale with both over-pressure condition and high quartz content is likely the best target zone for deep shale gas exploration in the Sichuan Basin.

KEYWORDS

shale gas, pore characteristics, over-pressure, multifractal analysis, preservation mechanism, ultra-deep shale reservoir

Introduction

Recently, great progress in shale gas exploration and development has been made in China, especially in revealing the mechanisms of shale gas generation and accumulation (Guo and Zhang., 2014; Borjigin et al., 2017; Guo et al., 2017; Wang et al., 2019; Shu et al., 2020; Xi et al., 2022), the formation and preservation of organic matter (OM) pores in shales (Liang et al., 2017; Dong et al., 2021; Ma et al., 2022; Teng et al., 2022; Yu K et al., 2022), and the characteristics of shale gas in China (Zou et al., 2010; Zou et al., 2016; Zou et al., 2019; Li et al.,

2021; Feng et al., 2022; Nie et al., 2022). Shale gas production in China exceeded 230×10^8 m^3 by the end of 2021, most of which was distributed in marine Longmaxi shale reservoirs in the Sichuan Basin and its surrounding area. Deep-shale gas with a buried depth of more than 3500 m has become an important potential resource for further shale gas exploration in the Sichuan Basin. He et al. calculated that the distribution area (12.6×10^4 km^2) of the Longmaxi shales with burial depth exceeding 3500 m in the Sichuan Basin is more than twice as large as those with burial depth less than 3500 m (He et al., 2021). The Longmaxi shale with burial depth ranging from 3500 to 4500 m in the southern Sichuan Basin covers an area of about 8.37×10^{12} m^3 (Liu et al., 2021a). Deep shale gas in the Sichuan Basin has displayed a huge potential; for example, the test production of shale gas in well L203 and platform W204 (four sub-wells) reaches 138×10^4 m^3/d and 214.4×10^4 m^3/d, respectively. Moreover, progress has been made in porosity evolution of deep gas shale reservoirs and the enrichment characteristics of deep shale gas. For instance, laminated organic-rich siliceous shale and laminated organic-rich mixed shale of deep shale reservoirs have better shale gas resource potential due to their abundant OM pores (Wang et al., 2022), and OM pores appear to be well preserved in deep shale reservoirs with TOC less than 5.5% (Gao et al., 2022; Zheng et al., 2022). However, the pore characteristics and preservation mechanism of ultra-deep (over 6000 m) shale reservoirs remain unclear.

The pore structure of shale reservoirs is the key factor affecting the transportation and storage properties of shales, further controlling shale gas content (Loucks et al., 2012; Gou et al., 2019; Zheng et al., 2022). Pore size can be divided into micropore (<2 nm), mesopore (2–50 nm), and macropore (>50 nm) (Sing et al., 1985). To evaluate the pore characteristics of shale reservoirs, a series of quantitative methods—such as high-pressure Hg intrusion and low-pressure N_2, CO_2, and Ar gas adsorption (Loucks et al., 2012; Zhang et al., 2017; Zheng et al., 2022)—and visual qualitative methods such as field emission scanning electron microscopy (FE-SEM) and CT have been widely used to obtain information about pores, including porosity, specific surface area (SSA), pore volume (PV), and pore size distribution (PSD), and to provide a visual of pore geometries and distribution (Mastalerz et al., 2013; Yu Y. X et al., 2022; Zheng et al., 2022).

In recent years, a series of ultra-deep wells has been drilled in the Sichuan Basin, for example, well MS#1 (total vertical depth 8418 m) and well CS#1 (total vertical depth 8448 m). These two wells provide an unparalleled opportunity to study the pore characteristics of over- 6000-m ultra-deep shale reservoirs. Huang et al. (2020) reported that formation temperature becomes dominant in over-3200-m shale reservoirs. In other words, the gas adsorption capacity in over-6000-m ultra-deep buried shale reservoirs will decrease significantly due to the high formation temperature. The term "ultra-deep" refers to strata deeper than 25,000 feet (approximately 4572 m), which were widely used in deep continental drilling programs in the last century (Dyman et al., 2003).

In this study, FE-SEM, SEM image processing, and low-pressure CO_2 and N_2 adsorption were used to investigate the pore characteristics of over-6000-m ultra-deep shale reservoirs. Moreover, multifractal analysis was performed to study pore connectivity and heterogeneity and their controlling factors. Finally, we concluded by studying the preservation mechanism of OM pores in over-6000-m ultra-deep shale reservoirs.

Materials and methods

Sampling

Ultra-deep shale samples, including those from Lower Cambrian Qiongzhusi and Lower Silurian Longmaxi shale, were collected from well MS#1 and well CS#1 in the Sichuan Basin. Well MS#1 was drilled on the structural high part of the Malubei anticline within the Tongnanba tectonic belt in the northeastern Sichuan Basin (Figure 1). Thirty-two shale samples from the Longmaxi Formation (6601–6926 m) and Qiongzhusi Formation (7690–8044 m) were collected from well MS#1, with their paleo-burial depths exceeding 8000 m and 11,000 m, respectively (Jiao et al., 2018). The lithology of the Longmaxi shale in well MS#1 consists of gray and dark gray shale with TOC ranging from 0.36% to 4.22% (average 1.32%) and ER_o ranging from 1.77% to 2.17% (average 1.98%). The ER_o refers to the equivalent vitrinite reflectance that is converted from the bitumen reflectance (BR_o) using the formula $ER_o=0.4+0.618\times BR_o$ (Feng, 1988). The lithology of the Qiongzhusi Formation comprises light gray to dark gray silty shale, dark gray shale, and carbonaceous shale with TOC ranging from 0.4% to 8.95% (average 3.25%) and ER_o ranging from 3.05% to 3.27% (average 3.15%).

Well CS#1 is located on the Boya nose structure in the northern slope of the central Sichuan uplift in the northern Sichuan Basin (Figure 1). Thirty shale samples from the Longmaxi Formation (6940–7152 m) and Qiongzhusi Formation (7719–8146 m) were collected from this well, with paleo-burial depths exceeding 9000 m and 12,000 m (Xie, 2020). The Longmaxi shale consists of dark gray and black carbonaceous shale with TOC ranging from 2.05% to 4.38% (average 3.56%) and ER_o ranging from 2.09% to 2.14% (average 2.11%). The Qiongzhusi shale mainly comprises gray and carbonaceous shale with TOC ranging from 0.42% to 4.13% (average 2.0%) and ER_o ranging from 2.08% to 2.22% (average 2.15%). To the best of our knowledge, wells MS#1 and CS#1 are among the deepest boreholes exposing the Cambrian Qiongzhusi Formation and Silurian Longmaxi Formation in Asia, and they provide important information about the pore characteristics of over-6000-m ultra-deep shale reservoirs.

In this study, a total of 62 samples with burial depths exceeding 6000 m were collected. The TOC, ER_o, and mineral composition of these shales are shown in Supplementary Table S1. It is noted that the relatively low value of ER_o for the shales from well CS#1, compared with those from well MS#1, are due to the low geothermal value of the western Sichuan depression (Richardson et al., 2008; Zhu et al., 2015).

Methods

In total, 8–10 large fragments from each cutting sample were selected for optical microscopic and FE-SEM observation. The remaining smaller fragments of samples were ground to 40–60 mesh with an agate mortar. Then, 2 g of 40–60 mesh samples were weighed for low-pressure CO_2 and N_2 adsorption. The remaining samples were ground to less than 200 mesh for XRD and organic geochemistry analysis. TOC and XRD tests were conducted using the LECO C230 Elemental Analyzer and D8 Advance X-ray diffractometer, respectively.

10.3389/feart.2023.1059869

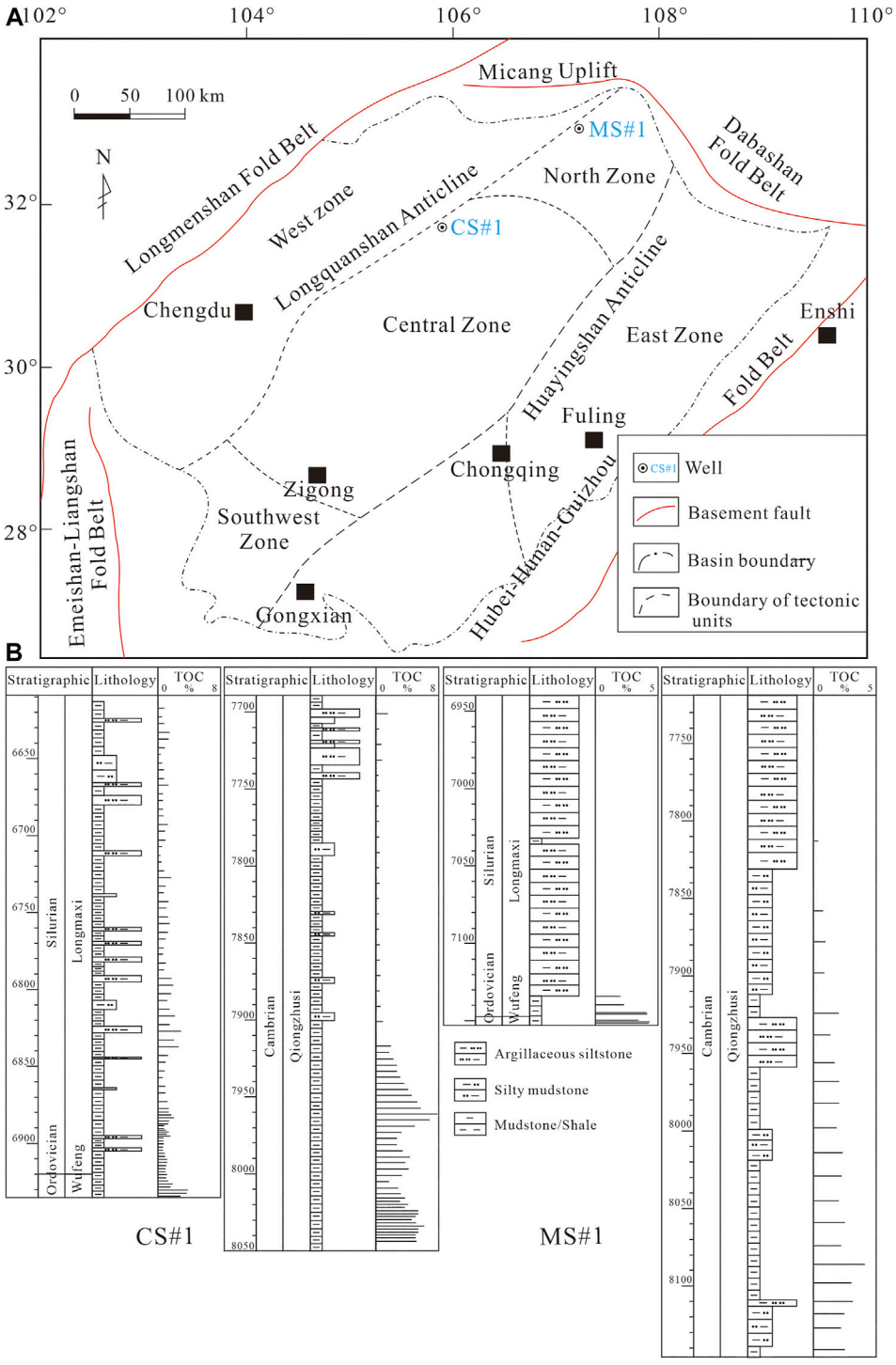

FIGURE 1
Structural units of Sichuan Basin and the studied wells' locations.

FE-SEM observation

Three samples from well MS#1 and seven samples from well CS#1 were selected for SEM observation. Each sample was cut to a size of 8×8×3 mm^3 and wet-polished with ultrathin emery papers with a sequence of 30 μm, 15 μm, 9 μm, 6 μm, 3 μm, and 1 μm to decrease the surface roughness for better performance in argon ion milling. FE-SEM observation was conducted on a Hitachi su8220 scanning electron microscope. Before observation, the surface of sample was coated with a layer of platinum. In total, 80–100 SEM images for each sample were obtained at magnifications varying from 1k× to 200k×. Then, these images were processed with Pores (Particles) and Cracks Analysis System (PCAS) software to acquire quantitative information about the

pores, including their morphological and statistical parameters. The details of the processing procedures for the PCAS can be found in Liu et al. (2011) and Jiao et al. (2018).

CO_2 and N_2 adsorption

Combined low-pressure CO_2 and N_2 adsorption can accurately quantify pore structure over the nanopore range (0.33–100 nm) (Zhang et al., 2017). Samples were degassed at 110°C for 8 hours under vacuum to remove residual moisture and volatile matter before testing (Mastalerz et al., 2013). Low-pressure CO_2 adsorption was performed using ASAP 2020 at 273 K under a relative pressure (P/P_0) ranging from 0.0004 to 0.03. The density functional theory (DFT) method was used to obtain information about pores, including the SSA, PV, and PSD. In fact, the actual detectable pore size ranges approximately from 0.03 to 0.9 nm using the DFT model (Zhang et al., 2017; Jiao et al., 2018).

N_2 adsorption is an efficient method for acquiring pore parameters across the overall nanopore range (0.33–100 nm) (Thommes et al., 2006; Sun et al., 2016; Zhang et al., 2017). The DFT model was performed to provide more accurate information about pore sizes ranging from approximately 0.9 nm to 30 nm (Jiao et al., 2018).

Multifractal analysis

Multifractal theory was first proposed by Mandelbrot to study turbulent flow and was then used to characterize the pore connectivity and heterogeneity of soil and shale (Paz Ferreiro et al., 2010; Paz Ferreiro et al., 2013; Liu et al., 2019). The data sets measured by N_2 or CO_2 adsorption were studied by multifractal analysis using the box counting method (Halsey et al., 1986). The box counting method was applied to CO_2 or N_2 adsorption data to study multifractal characteristics (Lopes and Betrouni, 2009). To implement multifractal analysis for pores of shale, a set of boxes with equal length ε are divided. The boxes are defined as index i, and $N(\varepsilon)$ represents the total number of boxes (size ε) that cover the PSD curve. Thus, the ith box of size ε is specified as ui (ε). For the N_2 or CO_2 adsorption isotherm, the relative pressure P/P_o was taken as the length ε. The probability mass function for the ith box can be calculated as

$$p_i(\varepsilon) = N_i(\varepsilon)/N_T, \tag{1}$$

where $N_i(\varepsilon)$ refers to the volume of adsorbed N_2 or CO_2 for the ith box and $N_i(\varepsilon)$ represents the total volume of adsorbed Ar. $P_i(\varepsilon)$ is defined by an exponential function for each box of size ε as

$$Pi(\varepsilon) \sim \varepsilon^{a}, \tag{2}$$

where a_i represents the singularity exponent that represents how singularities of the system tend to be infinite as ε approaches 0 (Halsey et al., 1986). For multifractal distribution properties of sections of size ε, $N(\varepsilon)$ shows an increase with decreasing ε, following a power law function:

$$N_a(\varepsilon) \sim \varepsilon^{-f(a)}, \tag{3}$$

where $N_a(\varepsilon)$ represents the number of boxes for the probability mass function of the ith box, and $P_i(\varepsilon)$, which has singularity strength between α and $\alpha+d\alpha$. $f(a)$ is the spectrum of the fractal dimension that characterizes abundance in the set with α singularity. $a(q)$ and $f(a)$ are calculated based on the following formula (Chhabra and Jensen, 1989):

$$\mathrm{a}(q) \propto \frac{\sum_{i=1}^{N(\varepsilon)} u_i(q,\varepsilon)\log[p_i(\varepsilon)]}{\log(\varepsilon)}, \tag{4}$$

$$f[a(q)] \propto \frac{\sum_{i=1}^{N(\varepsilon)} \mu_i(q,\varepsilon)\log[\mu_i(q,\varepsilon)]}{\log(\varepsilon)}, \tag{5}$$

where

$$u_i(q,\varepsilon) = \frac{p_i(\varepsilon)^q}{\sum_{i=1}^{N(\varepsilon)} p_i(\varepsilon)^q}. \tag{6}$$

Here, q refers to the exponent that characterizes the fractal properties at different scales of the pore size. a and $f(a)$ can be calculated by linear regression using Formulas (4), (5), whereas q varies from −5 to 5 for successive unit steps. For multifractal theory, the probability distribution function is defined as

$$u(q,\varepsilon) = \sum_{i=1}^{N(\varepsilon)} P_i(\varepsilon)^q \sim \varepsilon^{\tau(q)}, \tag{7}$$

where τ_q refers to the mass scaling function of order q and can be calculated as

$$\tau(q) = \lim_{\varepsilon \to 0} \left[\ln \sum_i P_i(\varepsilon)^q \Big/ \ln(1/\varepsilon)\right]. \tag{8}$$

The generalized dimension (D_q) can be calculated as (Halsey, et al., 1986)

$$D_q = \tau_q \Big/ (q-1), \tag{9}$$

where for q=1, D_q can be expressed as

$$D_1 = \lim_{\varepsilon \to 0} \left(\sum_{i=1}^{N(\varepsilon)} p_i(\varepsilon) \ln p_i(\varepsilon) \Big/ \ln(\varepsilon) \right). \tag{10}$$

The association of D_q and q can reflect the fractal characteristics. ΔD is calculated as $(D_q)_{max}$ - $(D_q)_{min}$, which can be used to characterize the heterogeneity of porosity distribution over the pore size range. The H value, calculated as $(D_2+1)/2$, is known as the Hurst exponent (Holmes et al., 2017). H exponent, ranging from 0.5 to 1, reflects the degree of the positive auto-correlation. Therefore, H can be applied to characterize the pore connectivity and permeability of shales (Martínez et al., 2010). A low H value represents poor pore connectivity.

Results

SEM analysis and PCAS processing

About 1000 SEM images were processed using PCAS analysis. The geometric parameters of pores (e.g., perimeter, area, length, and width) and the statistical parameters of pore systems (e.g., form factor and probability entropy) were obtained through PCAS processing. The form factor refers to the regularity of pores; a value of 1.0 refers to a perfect circle whereas a value of 0.785 represents a square in 2D. A high form factor value indicates complexity in the pore boundary. Probability entropy can describe a pore's directionality in 2D, the value of which ranges from 0 to 1. Pores

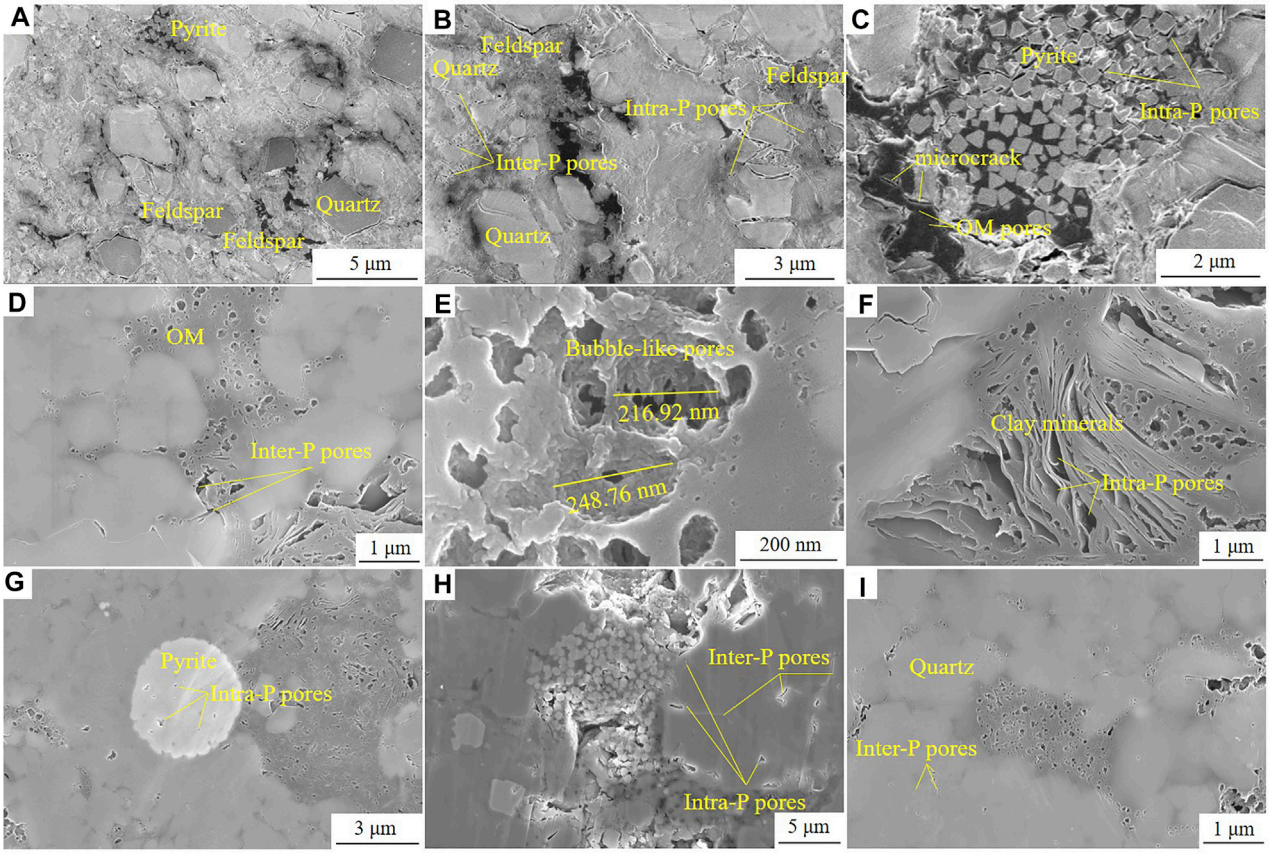

FIGURE 2
Pore types in the Longmaxi and Qiongzhusi shales from wells MS#1 and CS#1. **(A,B)** OM is closely associated with minerals like pyrite and quartz; **(C)** OM is developed within pyrite; **(D)** OM pores; **(E)** bubble-like OM pores; **(F)** OM pores developed in clay minerals; **(G)** intra-P pores developed in pyrite; **(H)** inter-P pores and intra-P pores; **(I)** intra-P pores within quartz.

tend toward the same direction with decreasing values of probability entropy (Soroushian and Elzafraney, 2005). The definition of form factor and probability entropy can be seen in Liu et al. (2011) and Jiao et al. (2018).

Pores can be divided into organic matter (OM) pores and mineral-associated pores, including intraparticle (intra-P) and interparticle (inter-P) pores, based on the pore classification by Loucks et al. (2012). The dimension of OM usually ranges from tens of nanometers to tens of micrometers in the Longmaxi and Qiongzhusi shale from well MS#1 (Figure 2). Most OM particles are crushed and show irregular shapes. OM usually occurs in association with minerals like pyrite (Figure 2A) and quartz (Figure 2B). In general, pores resulting from hydrocarbon generation are often circular or elliptical in shape (Loucks et al., 2009). Figure 2C shows that very few pores are observed in the Longmaxi and Qiongzhusi shale from well MS#1 and that these pores are irregular, silt-like, and microcrack in shape. Intra-P pores occur mainly as intercrystalline pores within pyrite framboid (Figure 2C) and can also develop in quartz (Figure 2B). Moreover, many intra-P pores can be observed within feldspar (Figure 2B), and these are known as dissolved pores. Inter-P pores can be observed between the boundary of quartz and feldspar or other minerals like pyrite (Figure 2B). Mineral-associated pores, including inter-P pores and intra-P pores, contribute up to 95% of the total surface porosity of the shales from well MS#1, based on PCAS analysis (Table 1). Table 1 shows that the mean size of OM pores is 75 nm, whereas the mean size of mineral-associated pores is close to 110 nm. Moreover, the probability entropies of OM and mineral-associated pores are relatively high in all cases, with average values ranging from 0.813 to 0.956, implying that the mineral-associated and OM pores in samples from well MS#1 are more directional. In addition, the higher form factor value of the OM pores demonstrates that OM pores are more regular than mineral-associated pores.

OM pores are very common in the Longmaxi and Qiongzhusi shale from well CS#1. The dimensions of OM particles range from hundreds of nanometers to tens of micrometers (Figure 2D). OM pores in these shales are generally bubble-like in shape and can be up to 50–250 nm (Figures 2D, E). Intra-P pores within clay minerals (Figure 2F) and pyrites (Figure 2G) are dominant, whereas inter-P pores are mainly developed between OM and quartz (Figure 2D) and/or between quartz (Figure 2H). Intra-P pores within quartz show triangle and slit shapes (Figure 2I). OM pores in these samples can contribute to 60%–90% of total surface porosity (Table 1). Additionally, Table 1 shows that the mean size of OM pores in the Longmaxi shale ranges from 34 to 37 nm, whereas the mean size of mineral-associated pores is in the range of 55–85 nm. For the Qiongzhusi shale, the mean size of OM pores is about 29 nm, whereas the mean size of mineral-associated pores is about

TABLE 1 PCAS processing results.

Formation	Sample	Depth/m	Total surface porosity/%	Pore type	Surface porosity/%	Pore size/nm		Form factor	Probability entropy
						Max.	Ave.		
Longmaxi	C4	7143	3.19	OM pores	4.95	657	37	0.64	0.966
				Mineral-associated pores	0.27	2270	85	0.54	0.821
	C7	7149	2.50	OM pores	6.05	502	34	0.65	0.969
				Mineral-associated pores	0.19	525	55	0.54	0.742
Qiongzhusi	C26	8110	2.78	OM pores	5.51	414	29	0.61	0.946
				Mineral-associated pores	0.35	211	26	0.55	0.801
	C28	8127	1.80	OM pores	3.37	535	29	0.60	0.928
				Mineral-associated pores	1.02	654	57	0.53	0.898
	M18	7940	1.25	OM pores	0.26	203	75	0.58	0.813
				Mineral-associated pores	1.31	976	110	0.53	0.956

26–57 nm. The probability entropy of OM pores in all cases is close to 1, whereas that of mineral-associated pores ranges from 0.742 to 0.898, demonstrating that the mineral-associated pores are more directional than OM pores. Moreover, higher form factor values in OM pores indicate that they are more regular in shape compared with mineral-associated pores (Table 1).

Pore volume, specific surface area, and average pore diameter

The DFT method based on CO_2 and N_2 adsorption isotherms is a suitable method for exploring pores with sizes ranging from 0.33 to 100 nm (Thommes et al., 2006; Zhang et al., 2017). In this study, the DFT method for CO_2 and N_2 adsorption data was used to investigate the nanopore structure characteristics of the Longmaxi shale and Qiongzhusi shale from wells MS#1 and CS#1, and the calculated PV and SSA results are presented in Supplementary Table S2. The PV values derived from N_2 adsorption ($PV_{N2\text{-}DFT}$) in the Longmaxi and Qiongzhusi shale from well MS#1 are in the range of 0.0234–0.0356 cm^3/g (average 0.0289 cm^3/g) and 0.0272–0.0439 cm^3/g (average 0.0379 cm^3/g), respectively. Their SSA values derived from N_2 adsorption ($SSA_{N2\text{-}DFT}$) are in the range of 7.80–11.00 m^2/g (average 9.31 m^2/g) and 8.58–14.94 m^2/g (average 12.44 m^2/g), respectively. For the samples from CS#1, the $PV_{CO2\text{-}DFT}$ values for Longmaxi and Qiongzhusi shale range from 0.0021 to 0.0027 cm^3/g (average 0.0024 cm^3/g) and 0.0009–0.0022 cm^3/g (average 0.0016 cm^3/g), respectively, whereas their $SSA_{CO2\text{-}DFT}$ values are 15.76–17.38 m^2/g (average 16.31 m^2/g) and 9.40–15.26 m^2/g (average 12.27 m^2/g), respectively. In addition, the $PV_{N2\text{-}DFT}$ values for the Longmaxi and Qiongzhusi shale from well CS#1 are in the range of 0.0225–0.0453 cm^3/g (average 0.0299 cm^3/g) and 0.0058–0.0434 cm^3/g (average 0.0240 cm^3/g), respectively, whereas the $PV_{N2\text{-}DFT}$ values of these shales range from 13.03 to 17.20 m^2/g (average 14.69 m^2/g) and 2.41–16.02 m^2/g (average 9.46 m^2/g), respectively.

The APD derived from the N_2 adsorption isotherm was also obtained (Supplementary Table S2). The APD of the Longmaxi and Qiongzhusi shale from well MS#1 ranges from 15.73 to 20.37 nm (average 17.91 nm) and 11.92–21.46 nm (average 15.88 nm), respectively. Meanwhile, the APD of samples from well CS#1 is in the range of 8.75–14.09 nm (average 11.44 nm) and 9.45–15.04 nm (average 12.83 nm), respectively.

The ratios of mesopore/micropore volume (Me/MiPV) and mesopore/micropore surface area (Me/MiSSA), derived from N_2 adsorption data, are suitable parameters for describing the pore structure of ultra-deep shales (Jiao et al., 2018). The results of Me/MiPV and Me/MiSSA ratios for the samples are presented in Supplementary Table S2. The ratio of Me/MiPV of the Longmaxi and Qiongzhusi shale from well MS#1 is in the range of 16.93–24.44 (average 20.26) and 13.47–25.22 (average 18.95), respectively, whereas their Me/MiSSA ratio ranges from 2.33 to 2.98 (average 2.60) and 1.73–3.25 (average 2.47), respectively. For the samples from well CS#1, the Me/MiPV ratio of the Longmaxi and Qiongzhusi shales is 4.78–17.34 (average 8.72) and 6.05–37.49 (average 13.79), respectively, whereas their Me/MiSSA ratio is in the range of 0.72–2.55 (average 1.32) and 1.14–7.57 (average 2.54), respectively.

Multifractal characteristics

Multifractal analysis based on CO_2 and N_2 adsorption isotherms is a more suitable method for characterizing the multifractal characteristics of micropores and meso-macropores (Liu, 2018). In general, a non-linear correlation between $\tau(q)$ and q indicates the existence of fractal characteristics (Liu, 2018). Therefore, a non-linear correlation between $\tau(q)$ and q in our samples (Supplementary Figures

S1A–C) indicates that all shale samples have multifractal characteristics in their pores.

Supplementary Figures S1E, F demonstrate that D_q decreases rapidly with an increase of q, while $q < 0$ and D_q decrease slowly with an increase of q, where $q > 0$. The decreasing trend of D_q indicates the non-uniformity degree of micropores, mesopores, and macropores in shales. The multifractal parameters of all samples are shown in Supplementary Table S3. Among them, values of ΔD and H are widely used to characterize the connectivity and heterogeneity of shale pores (Liu et al., 2019). The ΔD value derived from the CO_2 adsorption isotherm (ΔD_{CO2}) of Longmaxi and Qiongzhusi shale from well CS#1 is in the range of 1.08–1.23 (average 1.17) and 0.59 to 1.47 (0.95), respectively, whereas their H values derived from the CO_2 adsorption isotherm (H_{CO2}) range from 0.88 to 0.90 (average 0.89) and 0.88–0.92 (average 0.89), respectively.

The ΔD_{N2} values of Longmaxi and Qiongzhusi shale from well MS#1 are 1.39–1.86 (average 1.66) and 1.23–1.89 (average 1.63), respectively, whereas their H_{N2} values range from 0.75 to 0.79 (average 0.78) and 0.76 to 0.85 (average 0.80), respectively. For the samples from well CS#1, the ΔD_{N2} values of Longmaxi and Qiongzhusi shale are in the range of 0.89–1.43 (average 1.24) and 0.83 to 1.71 (average 1.29), respectively. Meanwhile, their H_{N2} values range from 0.77 to 0.84 (average 0.80) and 0.65 to 0.86 (average 0.81), respectively.

Discussion

Differences in pore characteristics of shales from wells MS#1 and CS#1

We compare the Longmaxi and Qiongzhusi shale from well MS#1 and CS#1 to better understand the effects of pressure coefficient and shale burial depth on pore characteristics because the two wells are ultra-deep and have obvious differences in pressure coefficients.

1) There are some similarities in the two shales. For example, all samples in over-6000-m ultra-deep shale reservoirs show higher APD and Me/MiSSA values and higher Me/MiPV values compared to non-superdeep shales (Jiao et al., 2018). Moreover, type IV and H3 hysteresis loop patterns of the N_2 adsorption isotherm were observed in our samples (Supplementary Figure S2).
2) More pores (especially OM pores) are developed in the Longmaxi and Qiongzhusi shale from well CS#1 based on SEM observation, compared to those of well MS#1, indicating that the shales in well CS#1 may have better OM pore-preservation conditions. The OM pores are more regular than the mineral-associated pores, as mentioned previously, which means that the surfaces of OM pores are more complex. Generally, the surfaces of OM pores show harbor-like shapes, whereas the surfaces of mineral-associated pores are smooth (Figures 2E, F). Interestingly, the OM pores have many higher values of probability entropy compared to mineral-associated pores for the two shales from well CS#1, whereas the mineral-associated pores show higher values of probability entropy for the shales from well MS#1 (Table 1). This may indicate that mineral-associated pores in ultra-deep shales are easily compacted under over-pressure conditions, compared to OM pores, because the OM pores likely contain large amounts of gas to maintain their over-pressure. In normal pressure conditions, extremely strong compaction can lead to orientation of OM pores in ultra-deep shale. Meanwhile, many microfractures are generated among minerals with no discernible orientation, further resulting in a decrease in probability entropy.

The Longmaxi shale and Qiongzhusi shale are at the over-mature stage and contain a high TOC, indicating that they have considerable shale gas generation potential. A consensus was reached that silica minerals like quartz can provide a supporting framework for the preservation of OM pores (Clarkson et al., 2013; Cao et al., 2022), whereas carbonate cementation can reduce the PV of shale reservoirs (Zheng et al., 2018; Zheng et al., 2022). Quartz is very common in our samples, especially in the Longmaxi shales from well CS#1 (average 63.7%). OM pores are mainly distributed in pyrobitumen surrounded by quartz for the two shales from well CS#1 (Figures 2E, F), suggesting that quartz can protect these OM pores from compaction. For example, a high-quartz sample (C7) has the highest OM pore surface porosity, 6.05%, whereas the lower-quartz samples C26 and C28 have lower OM pore surface porosity (5.51% and 3.37%), despite their similar TOC contents, and are in over-pressure conditions (Supplementary Table S1). This indicates that shales with higher quartz have better pore preservation conditions.

Despite the similar hydrocarbon generation potentials and quartz content, the shales from well CS#1 were found to have higher OM-pore surface porosity than the shales from well MS#1. For example, the samples M18 and C26 have similar TOC values and quartz contents (Supplementary Table S1); however, the latter has a higher surface porosity for OM pores (Table 1). The current results of shale gas exploration and development in the Sichuan Basin show that the pressure coefficient can be used as a good indicator of the preservation condition of shale gas (Guo and Zhang, 2014). A higher pressure coefficient generally indicates better preservation (Gao et al., 2019; Wang et al., 2020). Therefore, pressure coefficient seems to be the main factor for OM pore preservation because the pressure coefficients of the two shales from well CS#1 (1.77–1.89) are higher than those of the shales from well MS#1 (1.01–1.46); that is, well CS#1 has better OM pore preservation than well MS#1. This further indicates that the differences in the development of OM pores within shales from wells MS#1 and CS#1 are mainly controlled by the pressure coefficient and quartz content. In addition, carbonate cementation has little effect on OM pore development in our shale samples due to their low carbonate content (average 9.30%) (Zheng et al., 2022).

3) The APD values of the Longmaxi and Qiongzhusi shale in our samples are much higher than in previous studies showing that the APD value of shallow-buried shales ranges from 3–7 nm (Hou et al., 2014; Jiao et al., 2018). Statistical results show that the APD value of most gas-producing shales generally ranges from 3 to 7 nm (Xie, 2020). The APD value of our samples is in the range of 8.75–21.46 (average 14.51 nm). Specifically, the APD values of the Longmaxi and Qiongzhusi shale from well CS#1 range from 8.75 to 14.09 nm (average 11.44 nm) and 9.45–15.98 nm (average 12.83 nm), respectively, which is lower than the Longmaxi (15.73–20.37 nm, average 17.91 nm) and Qiongzhusi shale (11.92–21.46 nm, average 15.88 nm) from well MS#1 (Figure 3). The results of PCAS processing show that the size of mineral-associated pores is much higher than that of OM pores. Notably,

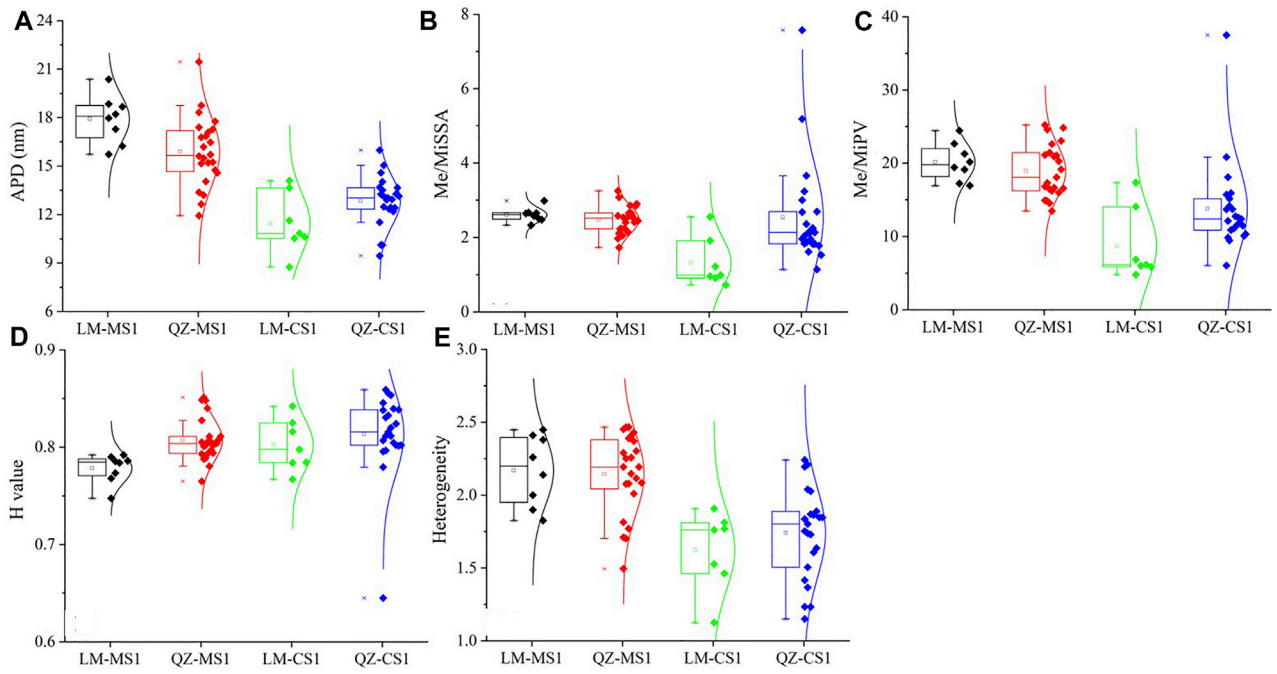

FIGURE 3
Comparison of pore structural parameters including **(A)** APD, **(B)** Me/MiSSA, **(C)** Me/MiPV, **(D)** H value and **(E)** Heterogeneity of shale samples.

the APD value of the Longmaxi shale is clearly smaller than that of the Qiongzhusi shale, whether from well CS#1 or MS#1, indicating that the OM pores with smaller sizes are easily developed in Longmaxi shale. Therefore, it is reasonable to believe that the smaller pore size of the Longmaxi shale is due to the development of OM pores.

4) The PSD of pores in over-6000-m ultra-deep shale reservoirs is characterized by multiple peaks (Supplementary Figure S3), which is different from previous studies showing that bimodal peaks are dominant in shallow shale reservoirs (Jiao et al., 2018). In addition, the ratios of Me/MiSSA and Me/MiPV in our samples exceed 1 and 5 (Figure 3). In addition, the ratios of Me/MiPV for the Longmaxi and Qiongzhusi shale in well MS#1 are significantly higher than those in well CS#1, implying that the two shales in well MS#1 have higher mesopore proportions. Therefore, we suggest that the high proportion of mesopores is a common feature of ultra-deep shale reservoirs.

Potential factors influencing pore connectivity and heterogeneity

CO_2 adsorption is a suitable method for studying the micropore range of pore size of organic-rich shales (0.33–2 nm), whereas N_2 adsorption can be used to characterize the wide range of pore sizes (2–200 nm) (Zhang et al., 2017; Jiao et al., 2018; Liu et al., 2019). Thus, multifractal analysis based on CO_2 and N_2 adsorption isotherms was used to study the connectivity and heterogeneity of micropores and meso-macropores (2–200 nm).

The heterogeneity comparison of micropores and meso-macropores in samples from well CS#1 shows that micropores have lower heterogeneity and higher H values as compared with meso-macropores (Supplementary Figures S4A, B). Moreover, no clear correlation is obtained between the micropore connectivity and meso-macropore connectivity of the two shales (Supplementary Figures S4C, D), indicating that the connectivity of shale micropores and meso-macropores needs to be studied separately.

The influence of PV and SSA

The correlation of PV, SSA, and the ΔD and H values of shales from well CS#1 is plotted in Figure 4 to determine whether pore structure parameters affect the heterogeneity and connectivity of pores. Figure 4A shows that there is a moderate positive correlation between ΔD value and micropore volume, whereas a moderate negative relationship is obtained between micropore volume and H value. This indicates that micropores in shale can increase the heterogeneity and reduce the connectivity of pores. Therefore, we inferred that the micropores in these samples may be widely distributed within the micropore aperture range. Remarkably, similar linear relationships are observed between the SSA of micropores and the ΔD and H values (Figure 4B). Notably, no obvious correlation is obtained between the PV and SSA of meso-macropores and the values of ΔD and H (Supplementary Figure S5), indicating that the meso-macropores have no obvious control over the heterogeneity and connectivity of pores in shale. This is consistent with the previous study by Liu (2018).

The influence of shale mineral composition

Given the difference in mineral composition, Pearson correlation analysis was performed to illustrate whether mineralogy or TOC could

10.3389/feart.2023.1059869

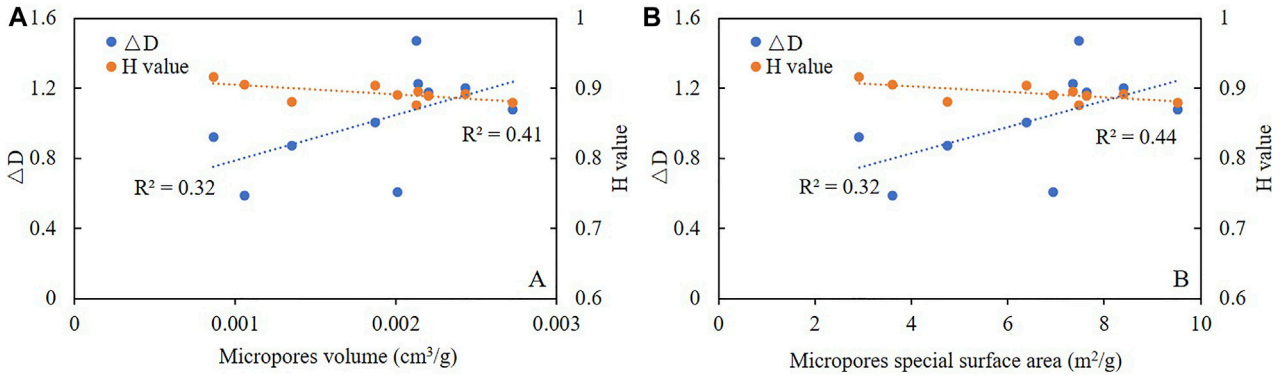

FIGURE 4
Correlation of micropores **(A)** and meso-macropore **(B)** volume and Δ*D* and *H* values.

TABLE 2 Relationship between mineral composition and values of △D and H for shales from well MS#1.

Parameter	TOC	Quartz	Feldspar	Calcite	Dolomite	Pyrite	Clays	$\Delta D_{Me\text{-}macro}$	$H_{Me\text{-}macro}$
TOC	1	0.09	.56**	−0.29	0.09	.74**	−.42*	0.16	0.18
Quartz		1	−0.01	−.72**	−.37*	−0.10	0.18	.46**	−.62*
Feldspar			1	−0.10	.42*	.62**	−.79**	0.08	0.24
Calcite				1	0.21	−0.11	−.39*	−0.22	.37*
Dolomite					1	.40*	−.47**	0.12	−0.07
Pyrite						1	−.65**	0.15	0.24
Clays							1	−0.15	−0.24
$\Delta D_{Me\text{-}macro}$								1	−.52**
$H_{Me\text{-}macro}$									1

Notes: * numbers indicate values > the critical correlation coefficient at the 95% significance level; ** numbers indicate values > the significant correlation coefficient at the 99% significance level.

TABLE 3 Relationship between mineral composition and values of △D and H for shales from well CS#1.

Parameter	TOC	Quartz	Feldspar	Calcite	Dolomite	Pyrite	Clays	ΔD_{Mi}	H_{Mi}	$\Delta D_{Me\text{-}macro}$	$H_{Me\text{-}macro}$
TOC	1	.50**	−0.27	−0.28	0.00	0.09	−0.34	0.26	0.30	−.42*	−0.12
Quartz		1	−.64**	−0.10	−0.09	−.51**	−.85**	0.62	−0.16	0.00	−0.05
Feldspar			1	−.46*	−.41*	.56**	0.35	−0.23	0.38	−0.04	0.17
Calcite				1	0.25	−0.25	0.12	−0.06	−0.51	0.26	−0.01
Dolomite					1	−0.32	0.02	−0.31	−0.35	−0.17	−.60**
Pyrite						1	.425*	−0.04	0.42	−0.06	0.05
Clays							1	−0.58	0.36	−0.06	0.19
ΔD_{Mi}								1	−0.39	−0.02	−0.39
H_{Mi}									1	−0.48	0.51
$\Delta D_{Me\text{-}macro}$										1	0.22
$H_{Me\text{-}macro}$											1

Notes: ditto.

control the pore heterogeneity and connectivity of shale. The quartz content of shales from well MS#1 is positively correlated with the ΔD value of meso-macropores, and a negative correlation between the quartz content and H value for meso-macropores was obtained (Table 2). This indicates that higher quartz content does lead to higher heterogeneity and lower connectivity for meso-macropores in shales from well MS#1. In addition, the calcite content is positively correlated with the H value of meso-macropores (Table 2), also indicating a higher connectivity of shale meso-macropores with high calcite content.

The correlation between mineral composition and ΔD and H values of micropores and meso-macropores in the two shales from well MS#1 differs from those from well CS#1 (Table 3). The TOC content is negatively correlated with the ΔD value of meso-macropores. This negative correlation also holds for the dolomite content *versus* H value of meso-macropores (Table 3). This indicates that lower TOC content can lead to less heterogeneity in meso-macropores and that higher dolomite content does lead to less connectivity of meso-macropores.

The quartz content has no obvious correlation with TOC, implying that quartz in shales from well MS#1 may be terrigenous. The effect of terrigenous quartz on the preservation of pores mainly provides a rigid framework to resist compaction and deformation (Thyberg et al., 2010; Ye et al., 2022). The dominance of mineral-associated pores in these shales (Table 1) indicates that these pores have relatively poor connectivity and further increases the heterogeneity of meso-macropores. The calcite content in the shales is in the range of 0%–21.1% (average 7.81%), and dissolved pores are observed within them. Notably, these dissolved pores are not filled with pyrobitumen, indicating that they may form after the generation of amounts of oil and gas and may be caused by the leaching of meteoric water. Therefore, these dissolved pores are conducive to increasing the connectivity of meso-macropores.

OM pores are profound and ubiquitous in shales from well CS#1 (Figures 2E, F), and they are mainly 20–250 nm, based on SEM observation. Therefore, the increase of TOC content can reduce the heterogeneity of meso-macropores because of their concentrated distribution. Carbonate cementation in carbonate-rich shale (carbonate content >10%) is common (Zheng et al., 2018; Zheng et al., 2022). Because of the extensive carbonate dissolution and subsequent re-precipitation, amounts of primary inter-P pores in carbonate-rich shale samples can be filled with carbonate cements. For example, high-carbonate sample C13 (calcite 6%, dolomite 21%) and sample C30 (calcite 4%, dolomite 19%) show much lower H values. This indicates that shales with higher carbonate content (including calcite and dolomite) have poorer pore connectivity.

Preservation mechanism of pores in over-6000-m ultra-deep shale reservoirs

The abundance of OM in shales is an important factor affecting pore development (Mastalerz et al., 2013; Zheng et al., 2022). Zheng et al. (2022) reported that with increasing TOC content, the PV of micropores, mesopores, and macropores in shales clearly increases. This phenomenon has been observed in our samples from well MS#1. A weakly positive relationship between TOC content and the PV and SSA of meso-macropores is obtained (Figure 5). The SEM images show that only a few OM pores are developed in these shales (Figures 2B, C). It is also clear that the OM in shales from well MS#1 contains more mesopores than macropores (Figure 2C). In addition, an obvious negative correlation between TOC content and the PV and SSA of meso-macropores in shales from well CS#1 is obtained (Figures 5B, C). This is quite distinct from previous studies (Zheng et al., 2018; Zheng et al., 2022). Milliken et al. (2013) and Zheng et al. (2022) reported that Devonian Marcellus shale and Silurian Longmaxi shale samples with TOC >5.5% demonstrate little or no contribution to the porosity of shale reservoirs with increasing TOC content. The ultra-deep Longmaxi shale and Qiongzhusi shale from well CS#1 suffered strong compaction. OM in ultra-deep burial is plastic mineral and susceptible to compaction at high temperature and pressure; this is why OM pore surface porosity in ultra-deep shale is clearly lower than in shallow-deep shale reservoirs (Xie, 2020). The negative correlation between TOC content and the PV and SSA of meso-macropores of the shale reservoir from well CS#1 also indicates this. Notably, the shale samples with TOC <2.0% contain many more PV of meso-macropores than those with TOC exceeding 2.0%, which does not accord with our SEM images showing that many OM pores are developed (Figures 2D, E). A careful comparison shows that the shale samples with high TOC content and low PPV and SSA all are from the Lower Qiongzhusi Formation (samples C23–C30). As is known, the direct floor of the Qiongzhusi Formation is a karst reservoir of the Late Sinian Dengying Formation that consists of dolomite, and the Tongwan unconformity between the Dengying Formation and Qiongzhusi Formation is widely distributed in most areas of the Sichuan Basin (Liu et al., 2021a). The Tongwan unconformity is an important channel for hydrocarbon migration in the Lower Paleozoic strata of the Sichuan basin (Liu et al., 2015; Liu et al., 2021a). The CS#1 well area is located on the eastern side of the Mianyang–Changning sag, and the efficiency of hydrocarbon emission is high (Liu et al., 2021a; Liu et al., 2021b). Thus, the Qiongzhusi shale close to the Tongwan unconformity is hard to maintain in over-pressure conditions, leading to decreasing pore size and further decreasing the PV and SSA of the shale reservoir. For the shales from well MS#1 close to the Tongwan unconformity, the PV and SSA are similar to the other samples. Consequently, the direct floor of the Qiongzhusi shale is an important factor controlling pore preservation in shale. After this factor was excluded, we found that TOC content is positively correlated with the PV of meso-macropores of shale with TOC <2.5%, whereas shale samples with TOC >2.5% show obvious decreases in meso-macropores with further increases in TOC (Figure 5C).

OM maturity is of great significance in the formation and development of pores, especially for OM pores (Curtis et al., 2012a; Curtis et al., 2012b; Zhang et al., 2020). Previous studies showed that Longmaxi shale has higher PV, SSA, and total porosity than Qiongzhusi shale and that Longmaxi shale has better pore connectivity (Zhang et al., 2020). The Longmaxi shale in this study has lower OM maturity compared to the Qiongzhusi shale, which shows much higher PV, SSA, and surface porosity. Marine shale reservoirs in the Sichuan Basin with ER_o ranging from 2.0% to 3.5% have considerable shale gas generation potential (Xie, 2020; Zheng et al., 2022). This further suggests that the differences in pore development (especially in OM pores) between the Longmaxi and Qiongzhusi shales and between the two wells have other, more important, causes than OM maturity.

Overall, geological factors affecting the pore development between the two shales and between the two wells can be summarized as follows.

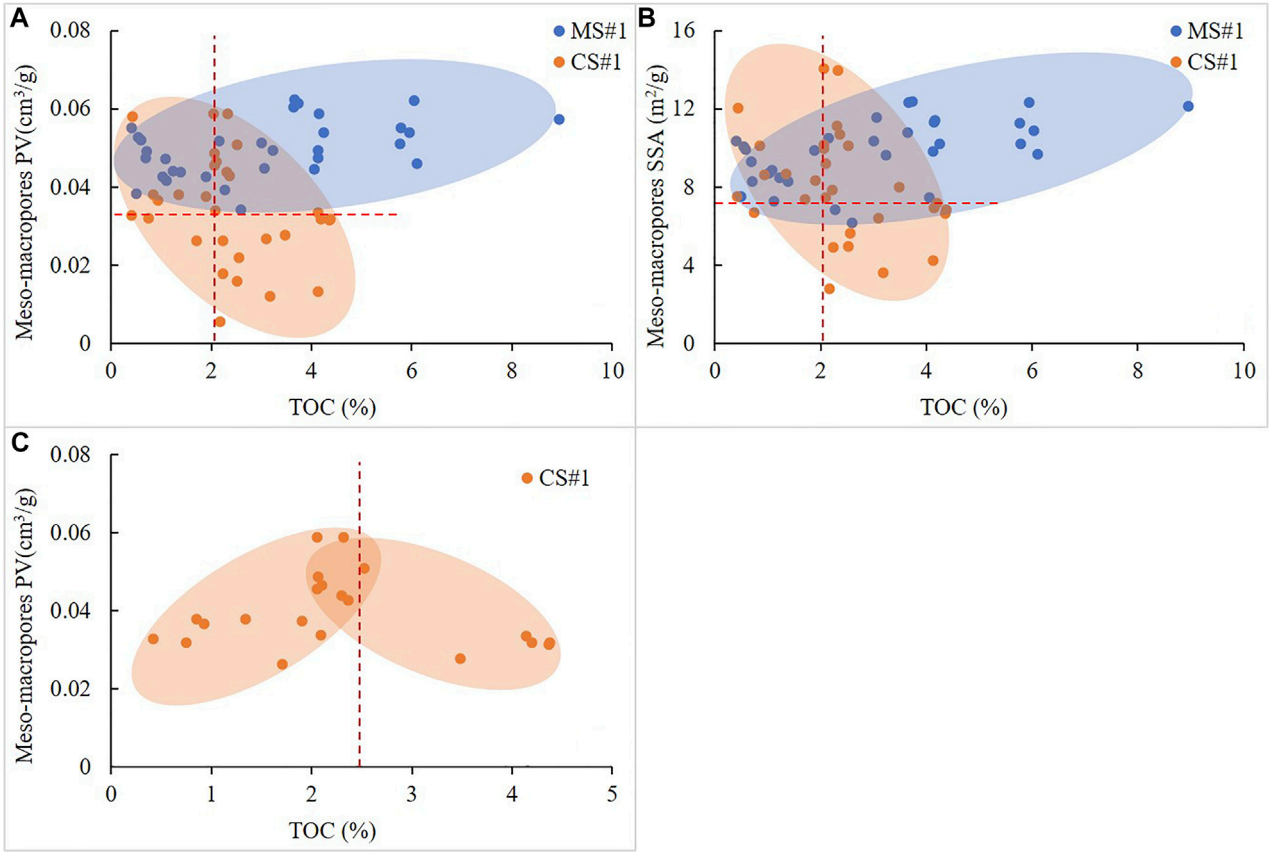

FIGURE 5
Relationship between TOC content and PV and SSA of meso-macropores of shales.

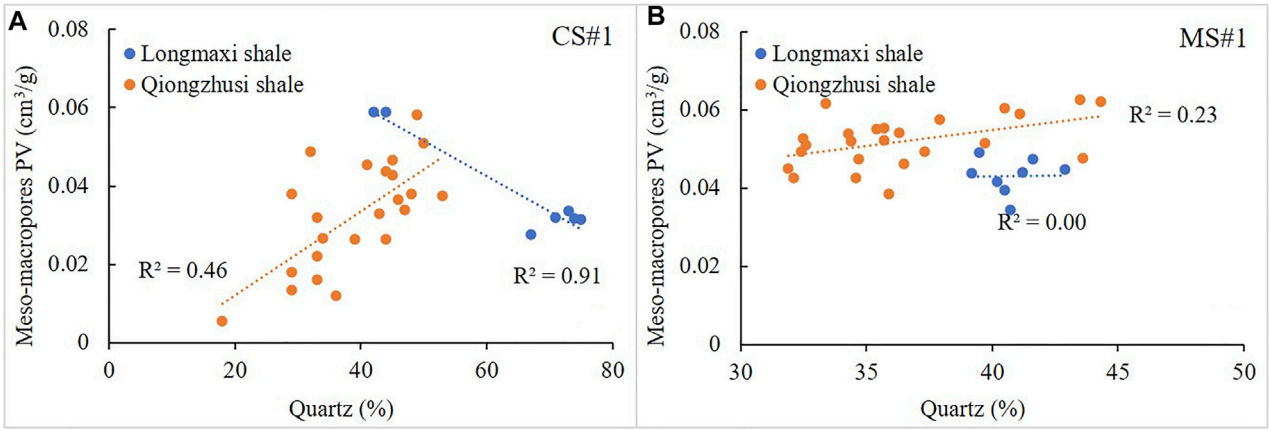

FIGURE 6
Correlation between quartz content and PV of meso-macropores. **(A)** CS#1 well; **(B)** MS#1 well.

1) The differences in the mineral composition and floor between the Longmaxi and Qiongzhusi shales are likely the critical factors controlling pore preservation. FE-SEM images show that OM pores are usually developed in shales with high quartz content (e.g., C4 and C7). A positive relationship exists between the PV of mesopores and quartz content for the Qiongzhusi shales from well CS#1 (Figure 6A). This is consistent with previous findings that quartz is conducive to the development of pores, especially OM pores (Dong et al., 2021; Guan et al., 2021). Notably, quartz content is negatively correlated with the PV of meso-macropores for the

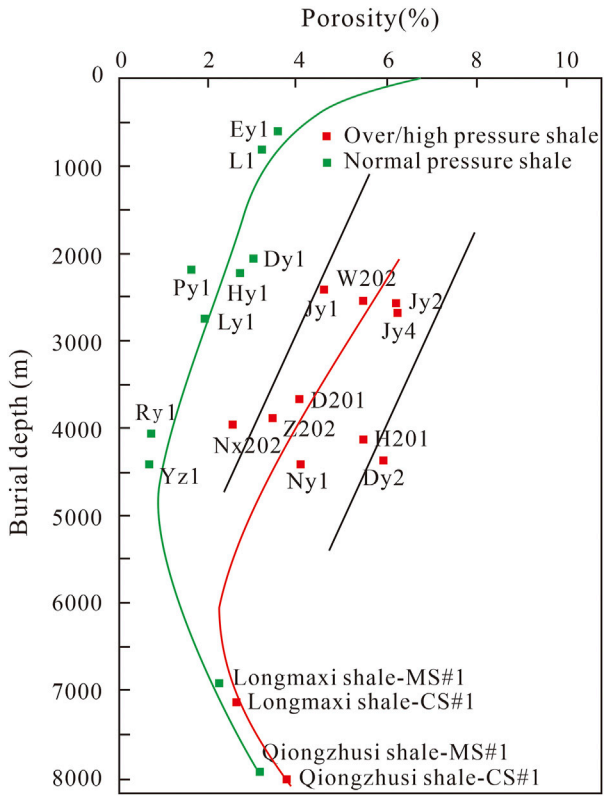

FIGURE 7
Relationship between porosity of the shale reservoir and burial depth.

Longmaxi shale from well CS#1 (Figure 6A), which is not in accordance with SEM observation. Further analysis showed that the samples with low PV of meso-macropores have high TOC content (e.g., C3–C7). Shales with high TOC content (>5%) are not favorable for the preservation of pores (Milliken et al., 2013). Interestingly, the relevance of quartz content and meso-macropore PV for shales from well MS#1 is very weak (Figure 6B), showing the obvious differences in pore structure of shales between the two wells. In addition, the floor of shale is critical for pore preservation, especially in the lower Qiongzhusi Formation, as mentioned previously.

2) The difference in the coefficient of shale between wells CS#1 and MS#1 is likely one such critical factor controlling pore development. Figure 3 shows obvious differences in pore structure, including the APD, Me/MiSSA, Me/MiPV, and H and ΔD values. In general, the shales from well MS#1 show higher APD values and higher proportions of mesopores, which do lead to greater heterogeneity. SEM observation showed that the shales from well CS#1 in over-pressure condition contain many more OM pores and have higher surface porosity than those from well MS#1 in normal pressure conditions (Xie, 2020). Statistics showed that the shales in over-pressure or high-pressure conditions have higher porosity than those in normal pressure conditions at different burial depths (Figure 7). Therefore, we have reason to believe that the coefficient of shale is the critical factor controlling the pore preservation in over-6000-m ultra-deep shale reservoirs.

Implications for deep-shale gas exploration

A better understanding of the pore preservation of ultra-deep shale may assist in the determination of favorable deep shale intervals and shale gas fields in the Sichuan Basin. Compared with Qiongzhusi shale, the higher quartz content (and the associated supporting effects) of the Longmaxi shales is one important factor positively affecting their pore development and preservation. In addition, the direct floor of the Qiongzhusi shale (and the associated Tongwan unconformity) is likely the critical geological factor negatively affecting their pore preservation and pressure coefficient and, ultimately, their gas contents. There is a threshold for the TOC content in shales, which favors OM pore development. The threshold of TOC is about 5.0% in shallow shale (Zheng et al., 2022) and even lower in deep shale reservoirs. Although the Qiongzhusi shale in the Sichuan Basin (MS#1) contains a high-quality shale interval of 80 m thickness, the low quartz content and Tongwan unconformity are not favorable for their pore preservation. Therefore, Longmaxi shale with both over-pressure or high pressure and high quartz content is likely the best target zone for deep shale gas exploration in the Sichuan Basin.

Conclusion

Samples from two ultra-deep wells, MS#1 and CS#1, were collected to study the pore characteristics and preservation mechanism of over-6000-m ultra-deep shale reservoirs in the Sichuan Basin. The conclusions are drawn as follows.

1) Ultra-deep shale reservoirs with burial depths of more than 6000 m have an obvious multifractal nature with different pore sizes. Compared with the two shales from well MS#1, the shales from well CS#1 contain relatively higher H values and lower ΔD values. This indicates that shale reservoirs in over-pressure conditions have better connectivity and less meso-macropore heterogeneity. Pearson correlation analysis indicated that quartz in the shales from well MS#1 can likely promote the preservation of pores (particularly mineral-associated pores in shales from well MS#1), further increase the heterogeneity of meso-macropores, and decrease the connectivity of meso-macropores. Meanwhile, calcite can increase the meso-macropore connectivity. In addition, for shales from well CS#1 with numerous bubble-like OM pores, TOC content can decrease meso-macropore heterogeneity. Calcite is conducive to increasing the meso-macropore connectivity of shales from well CS#1, particularly because the dissolved pores developed in these calcites are filled by pyrobitumen in OM pores.
2) The Longmaxi and Qiongzhusi shales in wells MS#1 and CS#1 have considerable shale gas generation potential because they contain high TOC contents and appropriate OM maturity. The Qiongzhusi shale in both wells, however, has relatively lower surface porosity and OM pore development degree than the Longmaxi shale. This further indicates that the surface porosity and development of OM pores are not only controlled by TOC contents and OM maturity but also by their quartz-supporting effect and pressure coefficient. Compared with Qiongzhusi shale, Longmaxi shale has a much higher quartz content and commonly has higher OM surface porosity and total surface porosity. The supportive effects of quartz seem to be a constructive factor that has promoted the preservation of OM pores. In addition, over-pressure conditions in the two shales in

well CS#1 likely lead to better OM pore preservation compared to those in well MS#1 that are under normal pressure conditions. Notably, the direct floor of the Qiongzhusi shale is also likely a critical geological factor affecting the pore structure and total surface porosity, and it seems to be a destructive factor that has decreased the PV and SSA of the shales. Based on this study, Longmaxi shale with both over-pressure or high-pressure conditions and high quartz content is likely the best target zone for deep-shale gas exploration in the Sichuan Basin.

Data availability statement

The original contributions presented in the study are included in the article/Supplementary Material; further inquiries can be directed to the corresponding authors.

Author contributions

GX and KJ designed the experiments and wrote the manuscript. BD performed the experiments. SL funded these experiments. WH and SL modified the manuscript. All authors contributed to the article and approved the submitted version.

Funding

This work was financially supported by the Natural Science Foundation of Anhui Province (Grant 2208085QD110), the National Natural Science Foundation of China (No. 42207293), the Key Scientific Research Foundation of the Education Department of the Province Anhui (No. 2022AH051748), the Key Programs of the Tongling University (No. 2021tlxyZD03), the Tongling University Starting Research Project (No. 2021tlxyrc16), and the Anhui University Excellent Research and Innovation Project (No. 2022AH010094). Natural Science Foundation of Sichuan Province (No. 2023NSFC0262).

Conflict of interest

The authors declare that the research was conducted in the absence of any commercial or financial relationships that could be construed as a potential conflict of interest.

Publisher's note

All claims expressed in this article are solely those of the authors and do not necessarily represent those of their affiliated organizations, or those of the publisher, the editors, and the reviewers. Any product that may be evaluated in this article, or claim that may be made by its manufacturer, is not guaranteed or endorsed by the publisher.

Supplementary material

The Supplementary Material for this article can be found online at: https://www.frontiersin.org/articles/10.3389/feart.2023.1059869/full#supplementary-material

References

Borjigin, T., Shen, B. J., Yu, L. J., Yang, Y. F., Zhang, W. T., Tao, C., et al. (2017). Mechanisms of shale gas generation and accumulation in the ordovician wufeng-longmaxi formation, Sichuan Basin, SW China. *Mar. Pet. Geol.* 44 (69), 69–78. doi:10.1016/s1876-3804(17)30009-5

Cao, T. T., Liu, H., Pan, A. Y., Fu, Y. T., Deng, M., Cao, Q. G., et al. (2022). Pore evolution in siliceous shales and its influence on shale gas-bearing capacity in eastern Sichuan-Western Hubei, China. *J. Pet. Sci. Eng.* 208, 109597. doi:10.1016/j.petrol.2021.109597

Chhabra, A., and Jensen, R. V. (1989). Direct determination of the f(α) singularity spectrum. *Phys. Rev. Lett.* 62, 1327–1330. doi:10.1103/PhysRevLett.62.1327

Clarkson, C. R., Solano, N., Bustin, R. M., Bustin, A. M. M., Chalmers, R. G. L., He, L., et al. (2013). Pore structure characterization of North American shale gas reservoirs using USANS/SANS, gas adsorption, and mercury intrusion. *Fuel* 103, 606–616. doi:10.1016/j.fuel.2012.06.119

Curtis, M. E., Cardott, B. J., Sondergeld, C. H., and Rai, C. S. (2012a). Development of organic porosity in the Woodford Shale with increasing thermal maturity. *Int. J. Coal Geol.* 103, 26–31. doi:10.1016/j.coal.2012.08.004

Curtis, M. E., Sondergeld, C. H., Ambrose, R. J., and Rai, C. S. (2012b). Microstructural investigation of gas shales in two and three dimensions using nanometer-scale resolution imaging. *AAPG Bull.* 96 (4), 665–677. doi:10.1306/08151110188

Dong, T., He, Q., He, S., Zhai, G. Y., Zhang, Y. R., Wei, S. L., et al. (2021). Quartz types, origins and organic matter-hosted pore systems in the lower cambrian Niutitang Formation, middle yangtze platform, China. *Mar. Pet. Geol.* 123, 104739. doi:10.1016/j.marpetgeo.2020.104739

Dyman, T. S., Wyman, R., Kuuakraa, V., Lewan, M., and Cook, T. A. (2003). Deep natural gas resources. *Nat. Resour. Res.* 12 (1), 41–56. doi:10.1023/A:1022656421803

Feng, Z. Q., Hao, F., Tian, J. Q., Zhou, S. W., Dong, D. Z., and Huang, S. (2022). Shale gas geochemistry in the Sichuan Basin, China. *Earth-Sci Rev.* 232, 104141. doi:10.1016/j.earscirev.2022.104141

Feng, G. X. (1988). Relationship between reflectance of bitumen and vitrinite in rock. *Nat. Gas. Ind.* 8 (8), 20–25. (In Chinese with English Abstract).

Gao, J., Zhang, J. K., He, S., Zhao, Z. L., He, Z. L., Wo, Y. J., et al. (2019). Over-pressure generation and evolution in Lower Paleozoic gas shales of theJiaoshiba region, China: Implications for shale gas accumulation. *Mar. Pet. Geol.* 102, 844–859. doi:10.1016/j.marpetgeo.2019.01.032

Gao, P., Xiao, X. M., Hu, D. F., Lash, G. G., Liu, R. B., Cai, Y. D., et al. (2022). Effect of silica diagenesis on porosity evolution of deep gas shale reservoir of the Lower Paleozoic Wufeng-Longmaxi formations, Sichuan Basin. *Mar. Pet. Geol.* 145, 105873. doi:10.1016/j.marpetgeo.2022.105873

Gou, Q. Y., Xu, S., Hao, F., Yang, F., Zhang, B. Q., Shu, Z. G., et al. (2019). Full-scale pores and micro-fractures characterization using FE-SEM, gas adsorption, nano-CT and micro-CT: A case study of the silurian Longmaxi Formation shale in the fuling area, Sichuan Basin, China. *Fuel* 253, 167–179. doi:10.1016/j.fuel.2019.04.116

Guan, Q. Z., Dong, D, Z., Zhang, H. L., Sun, S. S., Zhang, S. R., and Guo, W. (2021). Types of biogenic quartz and its coupling storage mechanism in organic-rich shales: A case study of the upper ordovician wufeng formation to lower silurian Longmaxi Formation in the Sichuan Basin, SW China. *Pet. Explor. Dev.* 48 (4), 813–823. doi:10.1016/S1876-3804(21)60068-X

Guo, T. L., and Zhang, H. R. (2014). Formation and enrichment mode of Jiaoshiba shale gas field, Sichuan Basin. *Pet. Explor. Dev.* 41 (1), 31–40. doi:10.1016/S1876-3804(14)60003-3

Guo, X. S., Hu, D. F., Li, Y. P., Wei, Z. L., Wei, X. F., and Liu, Z. J. (2017). Geological factors controlling shale gas enrichment and high production in Fuling shale gas field. *Pet. Explor. Dev.* 44 (4), 513–523. doi:10.1016/S1876-3804(17)30060-5

Halsey, T. C., Hensen, M. H., Kadanoff, L. P., Procaccia, I., and Shraiman, B. I. (1986). Fractal measures and their singularities: The characterization of strange sets. *Phys. R. A* 33 (2), 1141–1151. doi:10.1103/PhysRevA.33.1141

He, Z. L., Nie, H. K., and Jiang, T. X. (2021). Challenges and countermeasures of effective development with large scale of deep shale gas in Sichuan Basin[J]. *Reserv. Eval. Dev.* 11 (2), 1–11. (In Chinese with English Abstract).

Holmes, R., Rupp, E. C., Vishal, V., and Wilcox, J. (2017). Selection of shale preparation protocol and outgas procedures for applications in low-pressure analysis. *Energy fuels.* 31 (9), 9043–9051. doi:10.1021/acs.energyfuels.7b01297

Hou, Y. G., He, S., Yi, J. Z., Zhang, B. Q., Chen, X. F., Wang, Y., et al. (2014). Effect of pore structure on methane sorption capacity of shales. *Pet. Explor. Dev.* 41 (2), 248–256. doi:10.11698/PED.2014.02.17

Huang, H. X., Li, R. X., Jiang, Z. X., Li, J., and Chen, L. (2020). Investigation of variation in shale gas adsorption capacity with burial depth: Insights from the adsorption potential theory. *J. Nat. Gas Sci. Eng.* 73, 103043. doi:10.1016/j.jngse.2019.103043

Jiang, Z. X., Song, Y., Tang, X. L., Li, Z., Wang, X. M., Wang, G. Z., et al. (2020). Controlling factors of marine shale gas differential enrichment in southern China. *Pet. Explor. Dev.* 47 (3), 661–673. doi:10.1016/S1876-3804(20)60083-0

Jiao, K., Ye, Y. H., Liu, S. G., Ran, B., Deng, B., Li, Z. W., et al. (2018). Characterization and evolution of nanoporosity in superdeeply buried shales: A case study of the Longmaxi and Qiongzhusi shales from MS well #1, north Sichuan basin, China. *Energy fuels.* 32 (1), 191–203. doi:10.1021/acs.energyfuels.7b02932

Li, X. S., Zhu, H. J., Zhang, K. X., Li, Z., Yu, Y. X., Feng, X. Q., et al. (2021). Pore characteristics and pore structure deformation evolution of ductile deformed shales in the Wufeng-Longmaxi Formation, southern China. *Mar. Pet. Geol.* 127, 104992. doi:10.1016/j.marpetgeo.2021.104992

Liang, M., Wang, Z., Gao, L., Li, C. L., and Li, H. J. (2017). Evolution of pore structure in gas shale related to structural deformation. *Fuel* 197, 310–319. doi:10.1016/j.fuel.2017.02.035

Liu, C., Shi, B., Zhou, J., and Tang, C. S. (2011). Quantification and characterization of microporosity by image processing, geometric measurement and statistical methods: Application on SEM images of clay materials. *Appl. Clay Sci.* 54 (1), 97–106. doi:10.1016/j.clay.2011.07.022

Liu, K. Q., Ostadhassan, M., Sun, L. W., Zou, J., Yuan, Y. J., Gentzis, T., et al. (2019). A comprehensive pore structure study of the Bakken Shale with SANS, N_2 adsorption and mercury intrusion. *Fuel* 245, 274–285. doi:10.1016/j.fuel.2019.01.174

Liu, S. G., Yang, Y., Deng, B., Zhong, Y., Wen, L., Sun, W., et al. (2021a). Tectonic evolution of the Sichuan Basin, southwest China. *Earth-Sci Rev.* 213, 103470. doi:10.1016/j.earscirev.2020.103470

Liu, S. G., Li, Z. Q., Deng, B., Sun, W., Li, Z. W., Ding, Y., et al. (2021b). Occurrence morphology of bitumen in Dengying Formation deep and ultra-deep carbonate reservoirs of the Sichuan Basin and its indicating significance to oil and gas reservoirs[J]. *Nat. Gas. Ind.* 41 (8), 102–112. (In Chinese with English Abstract).

Liu, S. G., Sun, W., Zhao, Y. H., Wang, G. Z., Song, L. K., Deng, B., et al. (2015). Differential accumulation and distribution of natural gas and their maincontrolling factors in the Upper Sinian Dengying Fm, Sichuan Basin. *Natural Gas Industry* 35 (1), 10–23.

Liu, K. Q. (2018). *Microstructures and nanomechanical properties of the Bakken shale*. Grand Forks: University of North Dakota.

Lopes, R., and Betrouni, N. (2009). Fractal and multifractal analysis: A review. *Med. Image Anal.* 13, 634–649. doi:10.1016/j.media.2009.05.003

Loucks, R. G., Reed, R. M., Ruppel, S. C., and Jarvie, D. M. (2009). Morphology, genesis, and distribution of nanometer-scale pores in siliceous mudstones of the mississippian barnett shale. *J. Sediment. Res.* 79 (12), 848–861. doi:10.2110/jsr.2009.092

Loucks, R. G., Reed, R. M., Ruppel, S. C., and Hammes, U. (2012). Spectrum of pore types and networks in mudrocks and a descriptive classification for matrix-related mudrock pores. *AAPG Bulletin* 96 (6), 1071–1098. doi:10.1306/08171111061

Ma, Z. J., Tang, X., Deng, E. D., Liu, Y., Wang, Y. F., Zhang, J. Z., et al. (2022). Lithofacies and its controls on the organic matter-hosted pores in the Cambrian gas-rich Niutitang shale in upper Yangtze Plate, China. *J. Pet. Sci. Eng.* 218, 111052. doi:10.1016/j.petrol.2022.111052

Martínez, F. S., Martin, M. A., Caniego, F. J., Tuller, M., Guber, A., Pachepsky, Y., et al. (2010). Multifractal analysis of discretized X-ray CT images for the characterization of soil macropore structures. *Geoderma* 156, 32–42. doi:10.1016/j.geoderma.2010.01.004

Mastalerz, M., Schimmelmann, A., Drobniak, A., and Chen, Y. (2013). Porosity of devonian and mississippian new albany shale across a maturation gradient: Insights from organic petrology, gas adsorption, and mercury intrusion. *AAPG Bull.* 97 (10), 1621–1643. doi:10.1306/04011312194

Milliken, K. L., Rudnicki, M., Awwiller, D. N., and Zhang, T. W. (2013). Organic matter hosted pore system, Marcellus Formation (Devonian), Pennsylvania. *AAPG Bull.* 97 (2), 177–200. doi:10.1306/07231212048

Nie, H. K., Li, P., Dang, W., Ding, J. H., Sun, C. X., Liu, M., et al. (2022). Enrichment characteristics and exploration directions of deep shale gas of Ordovician-Silurian in the Sichuan Basin and its surrounding areas, China. *Pet. Explor. Dev.* 49 (4), 744–757. doi:10.1016/S1876-3804(22)60307-0

Paz-Ferreiro, J., Miranda, J. G. V., and Vidal Vázqueq, E. (2010). Multifractal analysis of soil porosity based on mercury injection and nitrogen adsorption[J]. *Vadose Zone J.* 9, 325–335. doi:10.2136/vzj2009.0090

Paz-Ferreiro, J., Da Luz, L. R. Q. P., Lado, M., and Vázquez, E. V. (2013). Specific surface area and multifractal parameters of associated nitrogen adsorption and desorption isotherms in soils from santa catarina, Brazil. *Vadose Zone J.* 6, vzj2012.0203–14. doi:10.2136/vzj2012.0203

Richardson, N. J., Densomore, A. L., Seward, D., Fowler, A., Wipf, M., Ellis, M. A., et al. (2008). Extraordinary denudation in the Sichuan Basin: Insights from lowtemperature thermochronology adjacent to the eastern margin of the Tibetan Plateau. *J. Geophys.l Res.* 113, B04409. doi:10.1029/2006JB004739

Shu, Y., Lu, Y. C., Chen, L., Wang, C., and Zhang, B. Q. (2020). Factors influencing shale gas accumulation in the lower Silurian Longmaxi formation between the north and South Jiaoshiba area, Southeast Sichuan Basin, China. *Mar. Pet. Geol.* 111, 905–917. doi:10.1016/j.marpetgeo.2019.06.029

Sing, K. S. W., Everett, D. H., Haul, R. A. W., Moscou, L., Pierotti, R. A., Rouquérol, J., et al. (1985). Physical and biophysical chemistry division commission on colloid and surface chemistry including catalysis. *Pure Appl. Chem.* 57, 6031–6036. doi:10.1351/pac198557040603

Soroushian, P., and Elzafraney, M. (2005). Morphological operations, planar mathematical formulations, and stereological interpretations for automated image analysis of concrete microstructure. *Compos* 27 (7-8), 823–833. doi:10.1016/j.cemconcomp.2004.07.008

Sun, M. D., Yu, B. S., Hu, Q. H., Chen, S., Xia, W., and Ye, R. C. (2016). Nanoscale pore characteristics of the lower cambrian niutitang formation shale: A case study from well yuke #1 in the southeast of chongqing, China. *Int. J. Coal Geol.* 154-155, 16–29. doi:10.1016/j.coal.2015.11.015

Teng, J., Liu, B., Mastalerz, M., and Schieber, J. (2022). Origin of organic matter and organic pores in the overmature ordovician-silurian wufeng-longmaxi shale of the Sichuan Basin, China. *Int. J. Coal Geol.* 2022, 103970. doi:10.1016/j.coal.2022.103970

Thommes, M., Smarsly, B., Groenewolt, M., Ravikovitch, P. I., and Neimark, A. V. (2006). Adsorption hysteresis of nitrogen and argon in pore networks and characterization of novel micro- and mesoporous silicas. *Langmuir* 22, 756–764. doi:10.1021/la051686h

Thyberg, B., Jahren, J., Winje, T., Bjørlykke, K., Faleide, J. I., and Marcussen, Ø. (2010). Quartz cementation in Late Cretaceous mudstones, northern North Sea: Changes in rock properties due to dissolution of smectite and precipitation of micro-quartz crystals. *Mar. Pet. Geol.* 27 (8), 1752–1764. doi:10.1016/j.marpetgeo.2009.07.005

Wang, H., He, Z. L., Zhang, Y. G., Bao, H. Y., Sun, K., Shu, Z. H., et al. (2019). Dissolution of marine shales and its influence on reservoir properties in the Jiaoshiba area, Sichuan Basin, China. *Mar. Pet. Geol.* 102, 292–304. doi:10.1016/j.marpetgeo.2018.12.017

Wang, M., Chen, Y., Bain, W., Song, G. Q., Liu, K. Y., Zhou, Z. Z., et al. (2020). Direct evidence for fluid over-pressure during hydrocarbon generation and expulsion from organic-rich shales. *Geology* 48, 374–378. doi:10.1130/G46650.1

Wang, E. Z., Guo, T. L., Li, M. W., Li, C. R., Dong, X. X., Zhang, N. X., et al. (2022). Exploration potential of different lithofacies of deep marine shale gas systems: Insight into organic matter accumulation and pore formation mechanisms. *J. Nat. Gas. Sci. Eng.* 102, 104563. doi:10.1016/j.jngse.2022.104563

Xi, Z. D., Tang, S. H., Zhang, S. H., Lash, G. G., and Ye, Y. P. (2022). Controls of marine shale gas accumulation in the eastern periphery of the Sichuan Basin, South China. *Int. J. Coal Geol.* 215, 103939. doi:10.1016/j.coal.2022.103939

Xie, G. L. (2020). *Pore structure characteristics of the Lower Paleozoic marine shale in the Sichuan Basin and their relationships with burial depth of shale*. Chengdu: Chengdu University of Technology.

Ye, Y. P., Tang, S. H., Xi, Z. D., Jiang, D. X., and Duan, Y. (2022). Quartz types in the Wufeng-Longmaxi Formations in southern China: Implications for porosity evolution and shale brittleness. *Mar. Pet. Geol.* 137, 105479. doi:10.1016/j.marpetgeo.2021.105479

Yu, K., Zhao, K. D., and Ju, Y. W. (2022). A comparative study of the permeability enhancement in coal and clay-rich shale by hydraulic fracturing using nano-CT and SEM image analysis. *Appl. Clay Sci.* 218, 106430. doi:10.1016/j.clay.2022.106430

Yu, Y. X., Wang, Z. X., Zhang, K. X., Feng, X. Q., and Cheng, M. (2022). Effects of shear on development characteristics of organic matter pores in shale: A case study of shale in the niutitang formation of the well XAD1. *J. Pet. Sci. Eng.* 211, 110166. doi:10.1016/j.petrol.2022.110166

Zhang, L., Xiong, Y. Q., Li, Y., Wei, M. M., Jiang, W. M., Lei, R., et al. (2017). DFT modeling of CO_2 and Ar low-pressure adsorption for accurate nanopore structure characterization in organic-rich shales. *Fuel* 204, 1–11. doi:10.1016/j.fuel.2017.05.046

Zhang, Y. F., Yu, B. S., Pan, Z. J., Hou, C. H., Zou, Q. W., and Sun, M. D. (2020). Effect of thermal maturity on shale pore structure: A combined study using extracted organic matter and bulk shale from Sichuan Basin, China. *J. Nat. Gas. Sci. Eng.* 74, 103089. doi:10.1016/j.jngse.2019.103089

Zheng, Y. J., Liao, Y. H., Wang, Y. P., Xiong, Y. Q., and Peng, P. A. (2018). Organic geochemical characteristics, mineralogy, petrophysical properties, and shale gas prospects of the Wufeng-Longmaxi shales in Sanquan Town of the Nanchuan District, Chongqing. *AAPG Bull.* 102 (11), 2239–2265. doi:10.1306/04241817065

Zheng, Y. J., Liao, Y. H., Wang, Y. P., Xiong, Y. Q., and Peng, P. A. (2022). The main geological factors controlling the Wufeng-Longmaxi shale gas content. *AAPG Bull.* 106 (10), 2073–2102. doi:10.1306/07132218243

Zhu, C. Q., Qiu, N. S., Jiang, Q., Hu, S. B., and Zhang, S. (2015). Thermal history reconstruction based on multiple paleo-thermal records of the yazihe area, western sichuan depression, SW China. *Chin. J. Geophys.* 58 (10), 599–610. doi:10.1002/cjg2.20198

Zou, C. N., Dong, D. Z., Wang, S. J., Li, J. Z., Li, X. J., Wang, Y. M., et al. (2010). Geological characteristics and resource potential of shale gas in China. *Pet. Explor. Dev.* 37 (6), 641–653. doi:10.1016/S1876-3804(11)60001-3

Zou, C. N., Dong, D. Z., Wang, Y. M., Li, X. J., Huang, J. L., Wang, S. F., et al. (2016). Shale gas in China: Characteristics, challenges and prospects (II). *Pet. Explor. Dev.* 43 (2), 182–196. doi:10.1016/S1876-3804(16)30022-2

Zou, C. N., Zhu, R. K., Chen, Z. Q., Ogg, J. G., Wu, S. T., Dong, D. Z., et al. (2019). Organic-matter-rich shales of China. *Earth-Sci Rev.* 189, 51–78. doi:10.1016/j.earscirev.2018.12.002

frontiers | Frontiers in Earth Science

TYPE Original Research
PUBLISHED 15 February 2023
DOI 10.3389/feart.2023.1094434

OPEN ACCESS

EDITED BY
Senhu Lin,
Research Institute of Petroleum Exploration and Development (RIPED), China

REVIEWED BY
Yanyan Chen,
Research Institute of Petroleum Exploration and Development (RIPED), China
Wenxue Han,
Shandong University of Science and Technology, China

*CORRESPONDENCE
Zhuoheng Chen,
zhuoheng.chen@nrcan-rncan.gc.ca

SPECIALTY SECTION
This article was submitted to Geochemistry, a section of the journal Frontiers in Earth Science

RECEIVED 10 November 2022
ACCEPTED 16 January 2023
PUBLISHED 15 February 2023

CITATION
Chen Z, Jiang C, Reyes J, Liu X and Little E (2023), A method for evaluating resource potential and oil mobility in liquid-rich shale plays—An example from upper Devonian Duvernay formation of the Western Canada Sedimentary Basin. *Front. Earth Sci.* 11:1094434. doi: 10.3389/feart.2023.1094434

A method for evaluating resource potential and oil mobility in liquid-rich shale plays—An example from upper Devonian Duvernay formation of the Western Canada Sedimentary Basin

Zhuoheng Chen*, Chunqing Jiang, Julito Reyes, Xiaojun Liu and Edward Little

Geological Survey of Canada, Calgary, AB, Canada

This paper discusses methods of assessing oil and gas resources and evaluating their mobility in shale reservoirs using programed pyrolysis data in conjunction with reservoir engineering parameters derived from production data. The hydrocarbon resource is calculated from the measured free hydrocarbon by programed pyrolysis with correction of evaporative loss that occurred during coring, storage and sample preparation. The correction takes account of the loss of light hydrocarbon fluids as a result of phase change during core retrieval to the surface and evaporative loss related to storage and sample preparation. Based on their response to ramping temperature during sample pyrolysis and thermal equilibrium behavior of distinct petroleum products at different thermal maturities, the estimated oil and gas resources are divided into three categories: non-movable, restricted, and movable to characterize the mobility of the petroleum fluids. The mobility classification is compared with oil compositional grouping based on evaporative kinetics of petroleum products in rock samples to examine their affinity. Pyrolysis analysis results from naturally matured samples and production data from different fluid zones in the Duvernay Shale resource play in Western Canada Sedimentary Basin (WCSB) were used to demonstrate the application of the proposed method. While the mobility of petroleum fluids increases with thermal maturation in general, the total movable resource reaches its maximum at the end of oil generation window, then declines as a result of massive loss due to hydrocarbon expulsion towards to gas window where liquids are thermally cracked to gaseous hydrocarbons. Compositional grouping based on evaporative kinetics does not show a complete accordance with mobility grouping, suggesting composition is only one of many factors affecting hydrocarbon fluid flow in shale reservoir. More studies are required to better understand the fundamentals of oil mobility in shale reservoir.

KEYWORDS

oil compositional grouping, oil mobility, evaporative kinetics, evaporative loss, Duvernay shale

Highlights

- Lowering starting temperature in programed pyrolysis can reveal oil compositions in shale.
- Evaporative loss correction of free hydrocarbons in S1 considers fluid phase and PVT behavior.
- Petroleum compositional grouping from hydrocarbon evaporative kinetics was compared with oil mobility assessment.
- Hydrocarbon compositional grouping and oil mobility assessment provide critical information to resource development decision on shale oil plays.

1 Introduction

Shale oil and gas reservoirs are a type of self-sourced and self-retained system with mixed porous media of different origins and properties that differs significantly from conventional and tight reservoirs (Akkutlu and Fathi, 2012; Chen et al., 2017a). Petroleum fluid in shale reservoir starts from a single phase of oil in oil window (e.g., shale oil) through a transition of multiphase fluid to a single phase of gas in dry gas window (i.e., shale gas) with increasing thermal maturity. This study presents novel methods for assessing petroleum resource potential and mobility of petroleum fluid in a shale reservoir.

In shale petroleum resource appraisal, the current practice of "volume = porosity × hydrocarbon saturation" is largely based on the understanding of conventional reservoir, and the resulting estimates often yield large uncertainties in resource volume and provide no information with respect to oil mobility. Many laboratory methods designed for conventional reservoirs could be problematic for measuring porosity and water saturation in shale reservoirs (e.g., Passey et al., 2010; Bohacs et al., 2013; Hartigan, 2014). Uncertainties arise because of the presence of large amount of clay minerals (e.g., Passey et al., 2010) and multiscale porous media with different origins and physical/chemical properties in shale reservoirs (Passey et al., 2010; Akkutlu and Fathi, 2012; Bohacs et al., 2013; Hartigan, 2014; Chen et al., 2017b). For example, Passey et al., 2010 showed that there could be large discrepancies in porosity measurements from different laboratories for the same set of shale samples and discussed the possible causes for the discrepancies. Ole (2015) showed that porosity from He porosimetry is about two times of that from mercury injection porosimetry (MIP) even they were measured at the same lab. This led to a recommendation of utilizing hydrocarbon saturated porosity for resource estimation in shale resource plays by industry (e.g., Passey et al., 2010; Bahacs, et al., 2013). As a matter of fact, there are also significant shortcomings to the hydrocarbon saturation estimation approach. In addition to the evaporative loss of hydrocarbon and uncertainty in porosity measurement of the sample, the impact of phase change on hydrocarbon volume due to variation in temperature-pressure (T-P) conditions from reservoir to surface is difficult to measure. Furthermore, the properties of shale reservoir can vary from one formation to the other, and thus petrophysical porosity and saturation calculations requiring calibration from these laboratory measurements is less reliable (Sondergeld, et al., 2010). Baek and Akkutlu (2019b) showed that source rock reservoir stores oil in significantly larger volume than that obtained based on conventional oil saturated pore volume calculation due to the so-called nanopore confinement effects.

In addition to the abundance of resources and rock mechanics, movability of petroleum fluid in shale reservoir represents another key challenge for successful resource development. Shale oil production results from North America suggest that oil mobility is a key factor affecting the success of commercial production. Cander (2013) showed that high production rate in the liquid zones is related to high gas to oil ratio and optimal oil viscosity. Unlike conventional reservoirs where hydrocarbon flow shows nearly-constant composition through production, physical and chemical properties of petroleum fluids retained in shale reservoir differ from those of the produced fluids largely due to the interaction between the hydrocarbon fluids and the hosting organic-rich rock (Whitson and Sunjerga, 2012; King, 2014; Akkutlu et al., 2017; Baek and Akkutlu, 2019c), suggesting that fluid compositions play an important role in oil mobility. Furthermore, hydrocarbon molecules are more likely to be trapped in the pores that are smaller than 10 nm in size (Zhang et al., 2017). The nanopore confinement combined with oil adsorption in shale reservoir impedes the mobility of oil, thus reducing oil recovery (Akkutlu et al., 2017; Baek and Akkutlu, 2019a and c). Therefore, information on fluid compositional properties prior to production are crucial for delineation of productive sweet-spots in shale resource plays and their completion design as well as extraction optimization (Carder, 2013; King, 2014; Jarvie, 2012; Chen et al., 2022).

The state of occurrence of oil and gas in shale reservoir is primarily controlled by the thermal maturity and the type of source rock and is a good indicator of oil mobility (Chen et al., 2019a; Li et al., 2019). Bulk geochemical data from Rock-Eval analysis and other types of programed pyrolyses contain critical information related to source rock type and maturity. While the mass of petroleum fluids remains the same under reservoir and surface conditions, the phase behavior of various compositional groups can respond differently to the changes in temperature and pressure, allowing for inferences of resource potential and compositional characterization of produced fluids.

Programed pyrolysis provides a measure of free hydrocarbons (i.e., S1 peak from Rock-Eval analysis) for the amount of retained oil in the rocks, and the parameter has been used to calculate the oil filled pore volume (Jarvie, 2012; Modica and Lapierre; 2012; Li et al., 2018; Chen et al., 2019b). However, early hydrocarbon generation products contain larger amounts of high molecular weight and heteroatoms-containing components of crude oil and bitumen with properties in a transition between solid organic matter and petroleum fluids (e.g., Delveaux et al., 1990; Jarvie, 2012; Abrams, et al., 2017; Burnham, 2017), thus resulting in strong interaction between the hydrocarbon fluids and the organic-rich host rocks. The interaction is further enhanced by large specific surface area of nano-pores (Sandvik et al., 1992; Jiang et al., 2016; Chen et al., 2017a; Li et al., 2018) and lead to strong confinement effects (Akkutlu et al., 2017; Bui et al., 2018; Baek and Akkutlu, 2019a; b and c). As a result, the evaporative release of the adsorbed oil from rock sample requires higher temperature than the default 300°C of routine Rock-Eval pyrolysis, causing the so called "carry-over" phenomenon in which a large portion of oil in the adsorbed state appears within the Rock-Eval S2 peak as a front-shoulder. Thus, the S1, supposedly representing "free hydrocarbons", contains predominantly only the light components of the total oil (Delveaux et al., 1990; Jarvie, 2012; Jiang et al., 2016; Abrams et al., 2017). Furthermore, evaporative loss of volatile components (and gas components as well) from the S1 can occur during coring, sampling, storage and sample preparation. Correction of this loss has been indicated to be challenging (e.g., Jarvie, 2012; Modica and Lapierre, 2012; Michael et al., 2013; Jiang et al., 2016; Chen et al., 2018; Li et al.,

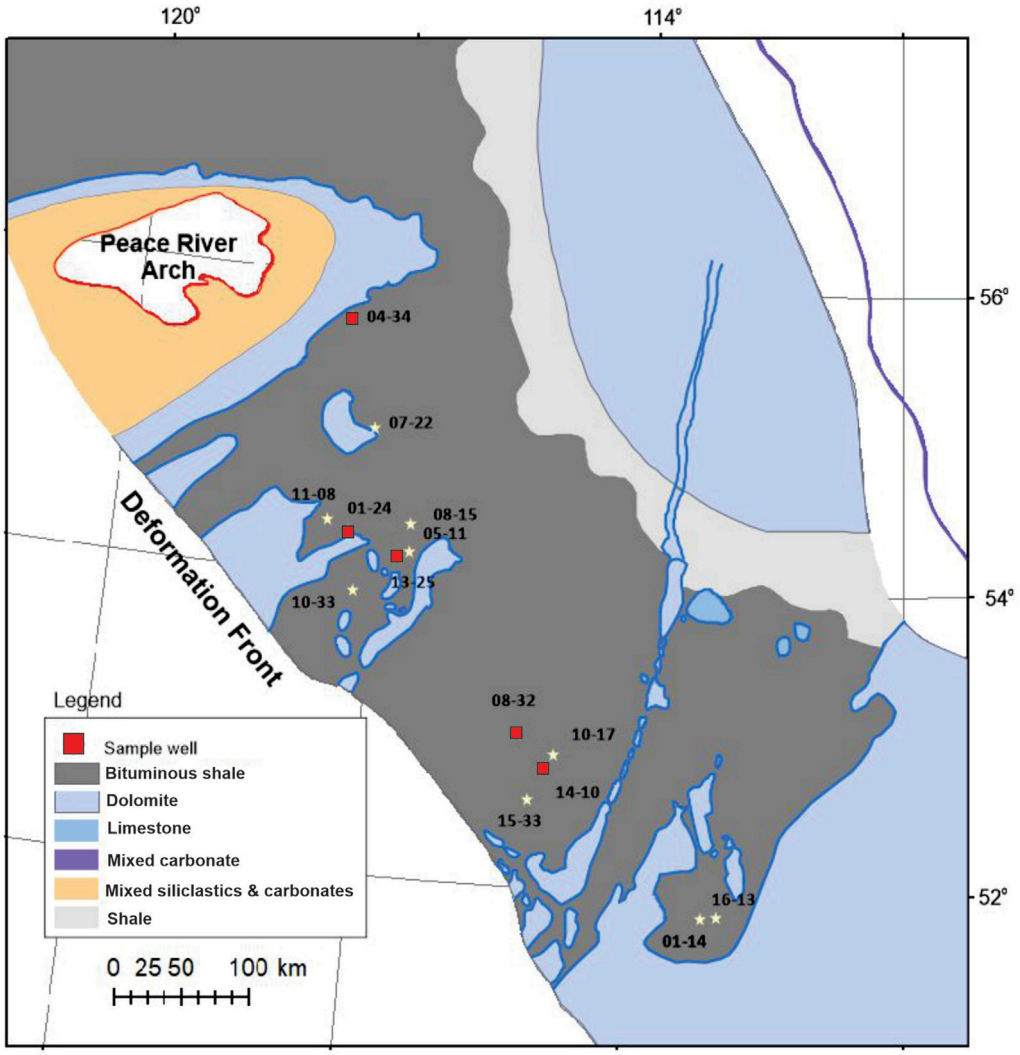

FIGURE 1
Location of the study area and core sample well locations in this study (modified from Switzer et al., 1994). Well names and major bulk geochemical features of the samples are provided in Table 1 (last column: well ID in map).

2018). Therefore, a robust estimation of shale oil resource based on Rock-Eval type programed pyrolysis requires corrections on both evaporative loss and separation of the retained oil from S2 peaks.

This paper uses the Duvernay liquid rich resource play as an example to propose an alternative approach to assess the resource potentials in different thermal maturity zones and evaluate petroleum fluid mobility and compositional grouping based on mass balance principles, phase and PVT behaviors and evaporative kinetics.

2 Data and methods

2.1 Data and analytic procedure

2.1.1 Samples

Five core samples were taken from the bituminous shale of the Upper Devonian Duvernay Formation in five wells in the Western Canada Sedimentary Basin (WCSB). The five core samples cover source rock maturity levels from early oil generation to dry gas windows (Figure 1). Table 1 presents the Rock-Eval data for the five Duvernay shale samples used in this study. As no immature sample was available in this study, the data of SAP sample from Dieckmann et al. (2004) was plotted in Figure 2B as the immature source rock for comparison.

2.1.2 Hydrocarbon distributions from programed pyrolysis

Sequential thermal desorption and pyrolysis of powdered (<250 um) bulk shale samples was used in this study to characterize the amount of hydrocarbons liberated from the shale samples in different temperature ranges. The thermal analysis was performed on a Frontier EGA/PY 3030D pyrolyzer system that was interfaced to an Agilent GC-MSD/FID for the detection of hydrocarbons and other volatile components. The furnace of the pyrolyzer was programed from 50°C to 850°C at a rate 25°C/min and then held for 3 min. Products released from the rock samples

TABLE 1 Rock-Eval analysis results of the five core samples from Upper Devonian Duvernay Formation in WCSB.

Sample ID	Well name	Sample type	Depth m)	S1 (mg HC/g rock)	S2 (mg HC/g rock	S3 (mg CO2/g rock)	TOC (%)	Tmax (°C)	HI (mg HC/ g TOC)	RC (%)	PI (%)	Well ID in map
C-590392	LONG RUN DD GVILLEE 4-34-77-23	Core	2,412.15	2.07	19.27	0.41	4.43	433	435	2.62	0.10	04-34
C-594351	SDEL PEMBINA 8-32-46-9	Core	3,137.1	8.55	9.33	0.47	5.09	454	183	3.58	0.48	08-32
C-590327	CELTIC KAYBOBS 13-25-59-19	Core	3,212.25	11.61	5.21	0.28	5.73	466	91	4.32	0.69	13-25
C-590436	CVE WILLGR 14-10-44-7	Core	3,112.35	10.12	4.52	0.35	4.91	476	92	3.68	0.69	14-10
C-590378	AOSC GRIZZLY 1-24-61-23	Core	3,725.05	0.84	1.33	0.22	3.45	517	39	3.26	0.39	01-24
E42790	SPA (Diechmann et al., 2004)	Core					8.58	420	604			

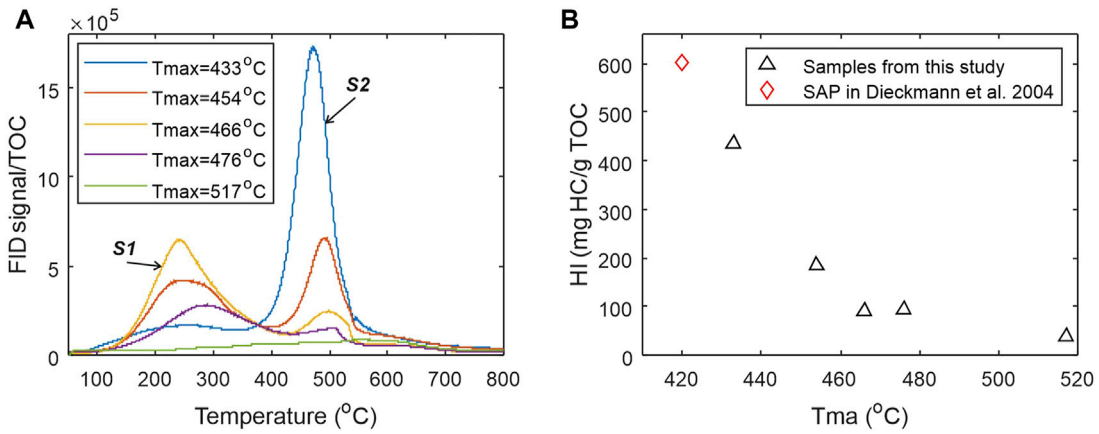

FIGURE 2
(A) Hydrocarbon pyrograms of the five shale samples from EGA pyrolyzer showing general trends of decreasing hydrocarbon generation potential represented by S2 peaks and increasing free hydrocarbon represented by S1 peaks with increasing thermal maturity represented by Tmax. Higher maturity samples do not have larger S1 peaks due to evaporative loss of gaseous and volatile hydrocarbons and the expulsion of a large part of generated hydrocarbons out of the source rocks prior to coring; **(B)** Cross-plot of Tmax-HI data from Rock-Eval analysis showing the trajectory of thermal decomposition for kerogen in Duvernay shales.

during either the thermal desorption (e.g., <350°C) or the pyrolysis (350–850°C) in the pyrolyzer furnace was immediately transferred through a short (i.e., 2.5 m) non-activated capillary column to the GC-MSD/FID detectors by helium carrier gas at 10 mL/min flow rate, so the abundances of the thermal products can be measured real time as hydrocarbon pyrograms or traces. The EGA FID pyrograms represent the real-time response of instant total amount of hydrocarbons released from the thermal analysis and are used in this work for studying the kinetics of hydrocarbon desorption and generation from the organic-rich shales. The pyrograms are also used for compositional grouping of the petroleum substances (Figure 2A). It should be noted that, the programed pyrolysis procedure using the Frontier EGA/PY 3030D pyrolyzer system differs from the routine Rock-Eval analysis heating program. The powdered shale samples were also subjected to conventional programed pyrolysis using a Vinci Technology's Rock-Eval 6 device. The basic method was used for Rock-Eval analysis to produce a Rock-Eval FID hydrocarbon pyrogram where S1 was generated at 300°C for 3 min, and S2 was then produced by increasing the furnace temperature at 25°C/min to 650°C. Details of the procedure can be found in Behar et al. (2002). Figure 2B shows the cross plot of hydrogen index (HI) versus Tmax from routine Rock-Eval 6 analysis.

2.2 Methods

For the convenience of methodology description, a raw Rock-Eval hydrocarbon pyrogram is divided into three parts (Figure 3), S1a for

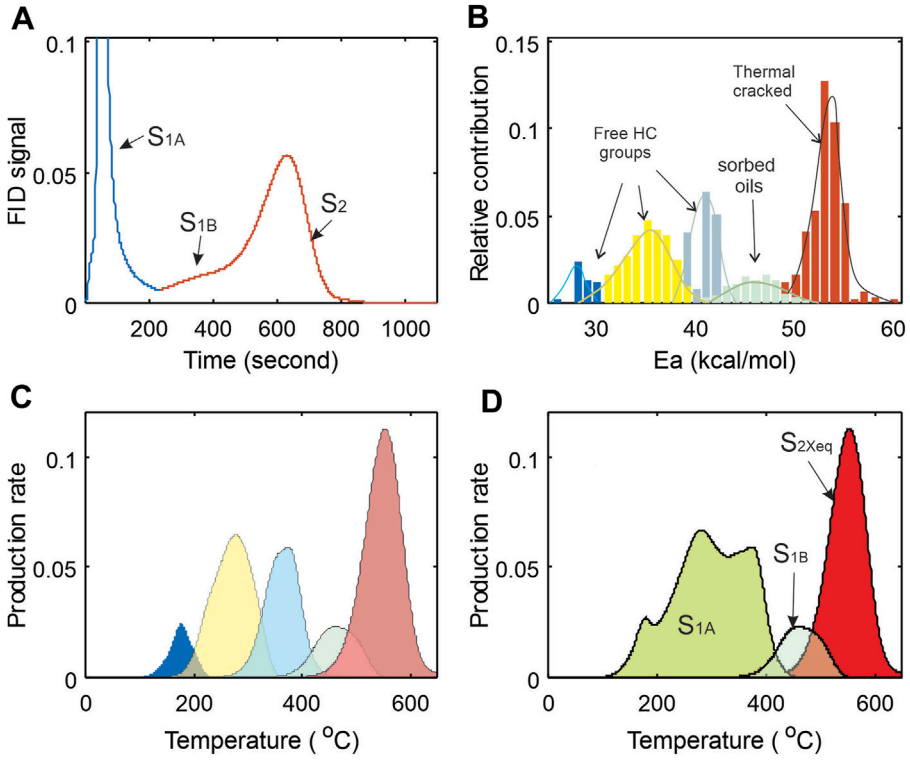

FIGURE 3
Thematic diagrams showing partition of Rock-Eval FID pyrogram and corresponding activation energy groups and thermal production make-ups. FID responses of petroleum products from pyrolysis can be plotted in different variable spaces: **(A)** FID response vs. time of thermal analysis (FID curve); **(B)** decomposed FID in activation energy space; **(C)** thermal products re-grouped in temperature domain that were converted from **(B)**; and **(D)** three categories of products re-grouped from **(C)** and defined in **(A)** in temperature domain. **(B)** and **(C)** are mathematic projections of **(A)** in Ea and T variable spaces, while **(D)** is re-grouped **(C)**.

volatile and semi-volatile petroleum components released at 300°C; S1b for high-molecular weight petroleum components with high boiling points; and S2 for kerogen thermal decomposition products. Li et al. (2018) and Chen et al. (2018) have discussed methods for separating S1b from S2 using a numerical approach based on evaporative kinetics. The present study attempts to determine the total oil yield and quantify petroleum group characteristics with respect to oil mobility and composition, and this is done by considering the various interactions between petroleum fluid and porous media including sorption, nanopore-confinement and any other factors that may impede the fluid flow in shale reservoir.

This study focuses on the petroleum substance already existing prior to pyrolysis regardless of their composition and physical states (free or adsorbed) in a source rock sample. Jarvie (2012) used the term "total oil yield" to describe the amount of petroleum in rock samples. The following terms are used to describe petroleum resource components in a shale reservoir. Similar to Jarvie (2012), total oil yield (TOY) is the quantity of petroleum already present in sample prior to pyrolysis and detected by FID during thermal analysis. Free hydrocarbon is one portion of TOY and represented by the Rock-Eval S1a peak that is thermally vaporized at or below 300°C during the thermal analysis. Sorbed oil describes the other portion of TOY that is thermally vaporized at temperatures exceeding 300°C during pyrolysis shown as S1b "carry-over" in the front of S2 peak, comprised of hydrocarbons and hydrocarbon-like substance of high molecular weight oil and bitumen (Jarvie 2012; Jiang, et al., 2016; Li et al., 2018). Please note that some of petroleum substances in S1a, particularly the gaseous and volatile components are likely lost during drilling and sampling prior to the laboratory analysis, and all these need to be taken into account for advanced resource assessment.

2.2.1 Evaporative loss of volatile hydrocarbon

The evaporative loss of free hydrocarbons in source rock samples is a well-known problem, and various methods have been proposed to address this issue. For example, Michael et al. (2013) proposed using the density index API of crude oil and the <C15 hydrocarbon content to estimate light hydrocarbon loss. Chen et al. (2018) used geochemical data to calculate the amount of light hydrocarbon loss in S1 on the basis of material balance. Based on the phase equilibrium and studies of pyrolysis light hydrocarbon loss under different temperature and pressure conditions, Chen et al. (2019b) proposed the use of oil formation volume factor (FVF) or solution gas oil ratio (GOR) to estimate evaporative loss from a sample during coring/drilling. The approach proposed by Chen et al. (2019b) is adopted in this study, using FVF to approximate light hydrocarbon loss during coring/drilling for samples from oil window and extend the evaporative loss into dry gas window in this study.

In this paper, *S1F* is defined as the free petroleum, and *S1S* the oils sorbed in the source rock corresponding to the S1b peak in

Figure 3A. Jarvie (2012) refers to the sum of the two as total oil yield (TOY):

$$TOY = S_{1F} + S_{1S} \tag{1}$$

The units are the same as the pyrolysis data (mg HC/g rock).

Here, we are interested in the free hydrocarbons only and will discuss the sorbed oils later. The total free hydrocarbon (*S1F*) is the sum of the remaining free hydrocarbon (*S1a*) in the sample as represented in Figure 3A, and the light hydrocarbons lost during coring, storage, sampling and preparation prior to analysis (*S1L*):

$$S_{1F} = S_{1a} + S_{1L} \tag{2}$$

Let *S1LS* denote the amount of light hydrocarbon loss during coring and *S1LP* the loss during storage, sampling and sample preparation prior to analysis. The total amount of light hydrocarbon loss (*S1L*) is defined as:

$$S_{1L} = S_{1LS} + S_{1LP} \tag{3}$$

For shale reservoirs still located in the oil window, the light hydrocarbon in sample can be calculated using the formation volume factor (FVF) of the crude oil:

$$S_{1F} = (S_{1LP} + S_{1a})\mathrm{FVF}\frac{\rho_{oilR}}{\rho_{oiiS}} \tag{4}$$

where *S1a* corresponds to the Rock-Eval S1 reading of normal pyrolysis procedure, representing the amount of remaining free hydrocarbons in the sample; *ρoilS* and *ρoilR* are the densities of crude oil under surface and reservoir conditions. If the difference of the two densities is smaller than the uncertainty of the density data itself, we can directly use (*S1a*+*S1LP*)×*FVF* to restore the amount of gaseous hydrocarbons lost during coring. It can be seen later that *FVF* is a power function of *Tmax*. At the end of the oil window, even a small abnormal fluctuation in T*max* value can affect the calculation of *FVF*. As such, a constraint based on conservation principle is introduced to avoid over-corrections. An upper-limit constraint is given in the following form:

$$S_{1F} \le (1 - f)(HI^{o} - HI) \times TOC/100 \tag{5}$$

where *f* (fraction) is hydrocarbon expulsion efficiency factor and *HIo* (mg HC/g TOC) is the initial hydrogen index that can be obtained using the empirical equations in Chen and Jiang (2016); Li et al. (2019). *HI* (mg HC/g TOC) and *TOC* (*w* % of rock) are measured hydrogen index and total organic carbon content from pyrolysis respectively, and their values decrease with increasing maturity.

For samples in gas window, the correction can be done on the basis of gas volume change through gas compressibility calculation. Let *moilR* denote the oil mass in shale reservoir, *φorg (=φoilR)* be the corresponding pore space storing the oil, and *ρoilR* be the oil density in reservoir. Let *VgasR* denote the volume of natural gas in reservoir, *ρgasS* be the density of natural gas at surface condition, and m_{gasS} the mass of natural gas at standard surface condition. The gas formation volume factor b_g, can be estimated from the following equation:

$$b_g = \frac{z T_r P_s}{T_s P_r} \tag{6}$$

where T_r and T_s k) are temperatures at reservoir and standard surface condition, respectively; P_s and P_r are pressures (mPa) in reservoir and surface condition respectively, and z is gas compressibility factor.

The oil volume in reservoir can be estimated by

$$V_{oilR} = m_{oilR}/\rho_{oilR} \tag{7a}$$

and the gas volume in surface condition

$$V_{gasS} = m_{gasS}/\rho_{gasS} \tag{7b}$$

by assuming that the volume of pore space occupied by oil before being thermally cracked to gas remains approximately the same, the ratio of the pore volume in reservoir (φ_{oilR}) in Eq. 7a to gas volume in surface (V_{gasS}) in Eq. 7b equals the gas formation volume factor (b_g). Re-arranging the ratio of Eq. 7a/Eq. 7b, the mass of gas in pore can be obtained by the following relation:

$$m_{gasS} = \frac{\rho_{gasS}}{\rho_{oilR}}\frac{m_{oilR}}{b_g} \tag{8}$$

From Eq. 8, the gas evaporative loss can be estimated by the difference between m_{gas} and residual gas remaining in *S1* at the surface. This is mass balanced method without dealing the mechanism of the loss.

In contrast, the amount of light hydrocarbon loss during sample storage and sample preparation are subject to many factors, such as, the type of sample (cuttings or core), oil and gas composition, source rock maturity, abundance of organic matter, state of core (complete or broken), storage conditions after coring (immediately sealed with plastic film or cryopreservation with liquid nitrogen, etc.), and whether the sample is analyzed immediately after pulverization (Jiang, etc. 2016; Michael et al., 2013; Chen, et al., 2018). In the absence of detailed information, accurate estimation of the loss of light hydrocarbons during core storage, sampling and sample preparation seem to be difficult. As such, we apply an average value from laboratory experiments, such as those from Jiang et al. (2016). This method is a mass balanced method and does not require knowing the mechanisms of light hydrocarbon loss.

2.2.2 Oil grouping from evaporative kinetics of petroleum substances

The temperature dependency of chemical reaction rate constant k_j is described using the Arrhenius equation (e.g., Chen et al., 2017b):

$$k_j = A \cdot \exp\left(-\frac{E_j}{RT}\right) \tag{9a}$$

where *A* is the pre-exponential or frequency factor, E_j is the activation energy of the *jth* compositional group, *R* is the gas constant, *T* is the absolute temperature, and a_j is the abundance of the *jth* components.

Penner (1952) showed that the temperature dependency of rate constant in chemical reaction kinetics also holds for thermal evaporation. The rate constant for evaporation (k_{Vj}) can be approximated by the following form (Penner, 1952):

$$k_{Vj} = eB \cdot \exp\left(-\frac{H_{Vj}}{RT}\right) \tag{9b}$$

where *B* is the frequency factor of evaporation, which is a function of enthalpy and molecular weight of evaporating liquid, and free volume (per molecule) in condensate state. H_{Vj} is the enthalpy for composition group *j* of the evaporating liquid, and *e* =2.71828 is a mathematical constant that is the base of the natural logarithm.

Thermal evaporation of petroleum in an open pyrolysis system is treated as pseudo thermal decomposition as the physical evaporation and chemical reaction processes are mixed at low temperature, and the

formulation in chemical reaction kinetics (Eq. 9a) is used to approximate the behavior of thermal evaporation of petroleum substances in an open pyrolysis system.

Let x denote the content of petroleum in the source rock, and $f(x)$ a mathematical function of x describing the thermal evaporation. The petroleum evaporation of a source rock sample in a pyrolysis system can be approximated by a series of independent and parallel first order pseudo-chemical reactions with a_j representing relative contribution of the *jth* component (Chen et al., 2018; Li et al., 2018).

$$\frac{dx}{dt} = \sum_{j=1}^{m} a_j k_j f(x_j) \tag{10}$$

Eq. 10 is re-written to reflect the fact of mixture of three types of thermal products during programed pyrolysis:

$$-\frac{dx}{dt} = \sum_{j=1}^{w} a_j k_j f(x_j) + \sum_{i=1}^{p} a_i k_i f(x_i) + \sum_{k=1}^{q} a_k k_k f(x_k) \tag{11}$$

The first term on the right side in Eq. 11 describes the thermally evaporated free hydrocarbons in S_{1a}; and the second term quantifies the thermally vaporized hydrocarbon residuals of bitumen and heavy oils (i.e., S_{1b}), and the third one represents the true kerogen thermal decomposition of the source rock during pyrolysis, S_2. In the equation, w is the number of pseudo-activation energies for the free hydrocarbons in S_{1a}, p is the number of pseudo-activation energy groups for the residual oils in S_{1b}, and q is the number of activation energy groups for the kerogen in S_2.

By sharing the same frequency factor A and using an activation energy distribution for the mixed physical and chemical thermal processes, the cumulative amount of hydrocarbons detected by FID at time t is the sum of each individual hydrocarbon and kerogen components specified by a corresponding activation energy (Burnham and Braun, 1999; Chen et al., 2017b and c; Chen et al., 2018):

$$x = \int_0^{\infty} \exp\left[-A\int_0^t k(T)dt\right] D(E)dE \tag{12}$$

where $D(E)$ is the density of petroleum components with specific ranges of activation energies, and $\int_0^{\infty} D(E)dE = 1$. In this study a non-parametric and discrete form of activation energy distribution is used. For the numerical integration in time domain for Eq. 12, one can break the heating processing into a series of isothermal segments,

$$x_p = x_{p-1} - k_{p-1} \cdot \mathrm{f}(x_{p-1}) \cdot (t_p - t_{p-1}) \tag{13}$$

where x_p is the fraction remaining at time p; k_{p-1} is the reaction rate at the previous time; $(t_p - t_{p-1})$ is the time interval (Chen et al., 2017a; and b).

2.2.3 Heavy and sorbed oils

Early and intermediate products of kerogen thermal degradation contain a large amount of high molecular weight bitumen and heavy crude oil components. Strong interaction between those products and the host rock makes sorption a common phenomenon for source rocks in oil window, and this oil component is often not detected and reported as free hydrocarbons with routine Rock-Eval analysis. Li et al. (2018) reported >50% of the total oil yield in sorbed sate in Eocene-Oligocene Shahejie Formation source rocks from the Jiyang Sag. Similarly, Han et al. (2015) reported 54% of the total oil being sorbed in the Barnett shale in Bend Arch-Fort Worth Basin of the United States. To tackle this issue, Jarvie (2012) suggested two separate pyrolysis analyses on the same sample, one on the whole rock sample and the other on the solvent-extracted aliquot. The adsorbed oil content (S1S) can then be estimated from the two pyrolysis results by the following relationship:

$$S_{1S} = S_2 - S_{2X} - S_{1X} \tag{14}$$

where, *S2* and *S2X* are the hydrocarbon generation potentials from the pyrolysis data before and after solvent treatment, and *S1X* is the free hydrocarbon *S1* after solvent treatment.

Alternatively, Li et al. (2018) proposed a numerical method for directly calculating the adsorbed oil based on hydrocarbon generation kinetics and the differences in the thermal evaporative and kerogen cracking products. By transforming the sample FID pyrogram (Figure 3A) into activation energy domain (Figure 3B), two activation energy distributions can be obtained, one for petroleum substances existing in the sample by thermal desorption and the other for kerogen cracking products. Transforming the activation energy distribution of the kerogen decomposition products back to temperature domain will result in a true S2 equivalent curve S2Xeq, the pyrogram equivalent of a solvent-treated sample (Figures 3C, D). The adsorbed oil can then be calculated using the following equation:

$$S_{1b} = \left(S_2 - S_{2Xeq}\right) \tag{15}$$

For details of the numerical method, readers are referred to Li et al. (2018).

3 Results

The upper Devonian Duvernay Shale is a known petroleum source rock in the Devonian conventional petroleum system of south-central Alberta in WCSB (Creaney et al., 1994) and has been studied and reported in the past (e.g., Stoakes and Creaney, 1984 and, 1985) Creaney, 1989; Creaney and Allan 1990; Allan and Creaney, 1991; Switzer et al., 1994; Chow et al., 1995 and Stasiuk and Fowler, 2002 and 2004). It is also a proven liquid-rich shale gas play in North America (AER, 2016; NEB, 2017). The Duvernay Formation was deposited under basinal and marine setting with deep-water and low-energy conditions surrounded by reefs and carbonate platforms. The Duvernay source rock is organic-rich, consisting of mostly oil prone Type II kerogen, with present day TOC values of up to 15%. Duvernay-sourced oils are low in sulphur and have pristane/phytane ratios of 1.5–2.4, indicating source deposition under normal marine salinities in an oxygen-poor environment (Creaney et al., 1994). Studies suggested that the presence of anoxic conditions, combined with slow sedimentation rates, are the main reasons for preservation of organic material in this organic-rich source rock (Chow et al., 1995). Stasiuk and Fowler (2004) and 2005 show that maturity of the organic matter varies from immature in the north and east to over-mature in the southwest close to the deformation front, with a large part of the Duvernay Shale basins lying in the wet-gas generation window. Dong et al. (2019) presented a porosity model for the Duvernay shale reservoir, documenting the porosity development with increasing thermal maturity.

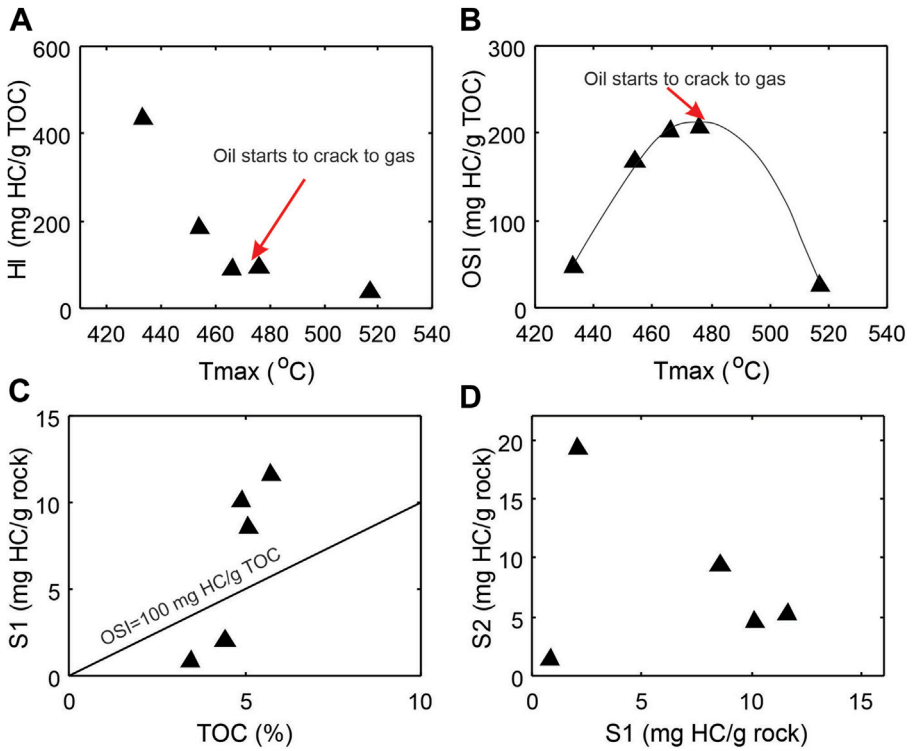

FIGURE 4
Cross-plots of Rock-Eval parameters showing general characteristics of the source rock samples and the thermal maturity overprints. **(A)** Hydrocarbon generating potential hydrogen index HI vs maturity parameter Tmax; **(B)** Oil saturation index OSI vs maturity Tmax; **(C)** S1 peak vs TOC; **(D)** S2 peak vs S1 peak. OSI=S1/TOC × 100 (oil saturation index).

3.1 Bulk geochemical characteristics of source rock samples

Five core samples from recent Duvernay Shale oil and gas pilot wells of various thermal maturities are selected for this study. They are organic rich with remaining TOC contents varying from 3.21 to 5.73% and show wide range of maturity levels from early mature (T*max* = 433°C) to over mature (T*max* = 560°C) in a depth range between 2,412 and 3725 m (Table 1). The remaining petroleum generation potential as represented by HI varies from 435 to 39 mg HC/g TOC (Table 1) and decreases with increasing thermal maturity (Figure 4A). The OSI=S1/TOCx100 (mg HC/g TOC) increase with maturity and reaches a maximum at around Tmax of 475°C (Figure 4B), then follows a decreasing trend with further thermal maturation. The samples above the OSI = 1 line in Figure 4C are those with abundant free oil. S1 versus S2 do not follow a linear correlation because of the maturity overprint (Figure 4D). When samples come from the same source rock with similar maturity in oil window, S1 and S2 show a linear relationship (e.g., Chen et al., 2018).

The EGA FID hydrocarbon pyrograms of the five naturally matured samples have been normalized to their TOC contents and overlapped one to another to show the systematic shift in the thermally evolved products from kerogen to petroleum with increasing thermal maturity (Figure 2A). The S1 peak on the left represents thermally evaporated petroleum substance already in the sample, whereas the S2 peak on the right corresponds to the remaining kerogen yet to be converted. With increase in thermal maturity, S2 peaks decrease in both height and size, accompanied by a shift in temperature at the peak generation rate. The diminishing of remaining kerogen generation potential with increasing maturity is clearly demonstrated by decreasing HI with increasing Tmax in Figure 4B. It should be noted that no special measures have been taken to prevent the evaporative loss of light hydrocarbons during coring and sample preparation for analysis of any of the five samples.

Several interesting observations can be made from Figure 2A on the change in S1 peaks. First of all, the temperature of peak valley between S1 and S2 peaks varies from around 300°C for immature source rock sample to 430°C for high maturity samples (T*max* > 460°C). The temperature shifts in both S1 and S2 curves suggest a dynamic process in kerogen conversion and show compositional changes in both kerogen and generated petroleum products through kerogen conversion to petroleum fluids. Secondly, S1 peak does not show a monotonic increase with thermal maturation and kerogen conversion to petroleum products (Figure 2A). The size and height of S1 curves reach the maximum at Tmax around 466–476°C (Figure 2A) due to oil expulsion in the source rock and evaporative loss of volatile components during coring/drilling, sampling and sample preparation in laboratory. Thirdly, change in the shape of S1 curve reflects oil compositional variation with thermal maturation. A considerable amount of light oil already in the sample seems to have disappeared, being partly expelled from the source rock as a consequence of fluid expansion and partly lost when the core was brought to the surface.

Among the five samples, the least thermal mature is C-590392 with a T*max* = 433°C, PI = 10% and vitrinite reflectance of 0.8%. To

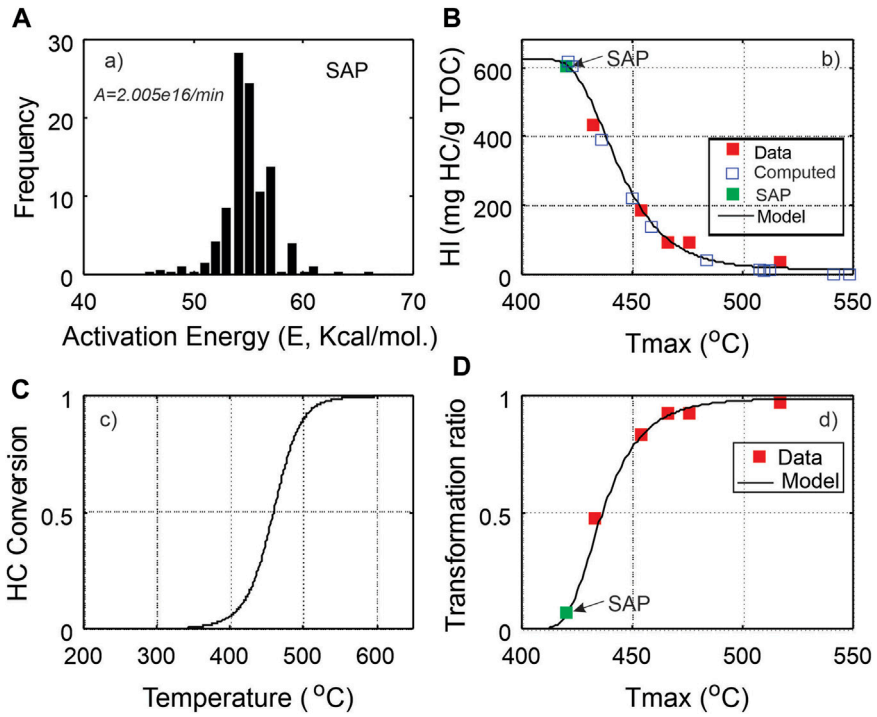

FIGURE 5
Comparison of kerogen conversion models from chemical reaction kinetic model and data-driven model. **(A)** Estimated kinetic parameters from the core sample SAP in Dieckmann et al. (2004) was used as immature source rock for hydrocarbon generation model; **(B)** Tmax-HI plot of data and computed Tmax-HI data pairs using a forward modelling (Chen et al., 2017b); **(C)** Computed kerogen conversion rate using kinetic parameters in Dieckmann et al. (2004); **(D)** Constructed empirical model of kerogen transformation ratio from data in Figure 5B).

establish a full thermal decomposition trajectory for the Duvernay Shale from immature stage, it is preferably to start from an immature sample. The pyrolysis parameters and activation energy estimation of the sample SAP (Table 1; Figure 5A) from Dieckmann et al. (2004) were taken to serve as the immature sample. The forward kinetic modeling procedure by Chen et al. (2015 and 2019) is employed to generate pseudo Tmax-HI trajectory that are then superimposed by the measured sample data points to show the thermal decomposition path of the Duvernay Shale (Figure 5B). The modeled kerogen conversion using the activation energy and frequency factor of the SAP sample is shown in Figures 5A, C transformation ratio based on empirical equation of Chen and Jiang (2016) is plotted in Figure 5D.

3.2 Petroleum resource potential and mobility grouping

3.2.1 Evaporative loss estimation

A total of 238 horizontal production wells were drilled into the Upper Devonian Duvernay Shale with multi-stage fracturing between 2011 and 2015. The proven reserves include 210 million barrels of oil and 1.2 trillion cubic feet of natural gas from 21 shale oil wells and more than 100 gas wells (AER, 2016). Production data suggest a good correlation between gas-to-oil ratio (GOR) and formation volume factor (FVF) in conventional petroleum reservoirs (PetroWiki, 2018). Similarly, initial GOR of dissolved gas in shale oil reservoirs is well correlated with FVF. Available GOR, FVF and fluid density data from the proven Duvernay shale reservoirs are plotted in Figures 6A, B. In reservoir engineering practice, it is common to use GOR from production data to estimate FVF (Figure 6A), Data analysis shows that the maturity index Tmax and GOR also have a good empirical relationship (Figure 6C). By replacing GOR from production data by a highly correlated organic geochemical indicator Tmax (source rock maturity indicator), an empirical relationship between Tmax and FVF (Figure 6D) is derived based on the relationship in Figures 6A, C (Chen and Jiang, 2020).

$$\mathrm{FVF} = 1 + \frac{1}{225} 10^{\{0.054\,(\mathrm{Tmax}-415)\}} \tag{16}$$

where FVF is the oil formation volume factor of the source rock reservoir and FVF takes a value between 1-3 in oil generation window; Tmax (a kinetic parameter) is the pyrolysis temperature corresponding to the highest hydrocarbon generation rate on a pyrogram. Eq. 16 is applicable to source rock reservoir within oil generation window only. For the Duvernay shale, the upper limit of Tmax is around 465°C (Figure 6C). Figure 6E shows the reservoir pressure of the liquid rich Duvernay shale. For different source rocks, the parameters in Eq. 16 will have to be adjusted by fitting data.

For samples from gas generation window, Rock-Eval S1 measures the adsorbed gas only and Eq. 8 can be used directly to estimate the mass of natural gas in reservoir condition with the following parameters assumed: gas density of 0.7 kg/m^3 at surface condition; oil density of 860 kg/m^3 in reservoir condition; and gas compressibility factor z = 1.1. For the calculation of bg, measured pressure and temperature gradients in the region are used to obtain empirical models of reservoir pressure and temperature, leading to an average pressure gradient of 13.5 mPa/km and temperature gradient of 0.029°C/m in this study.

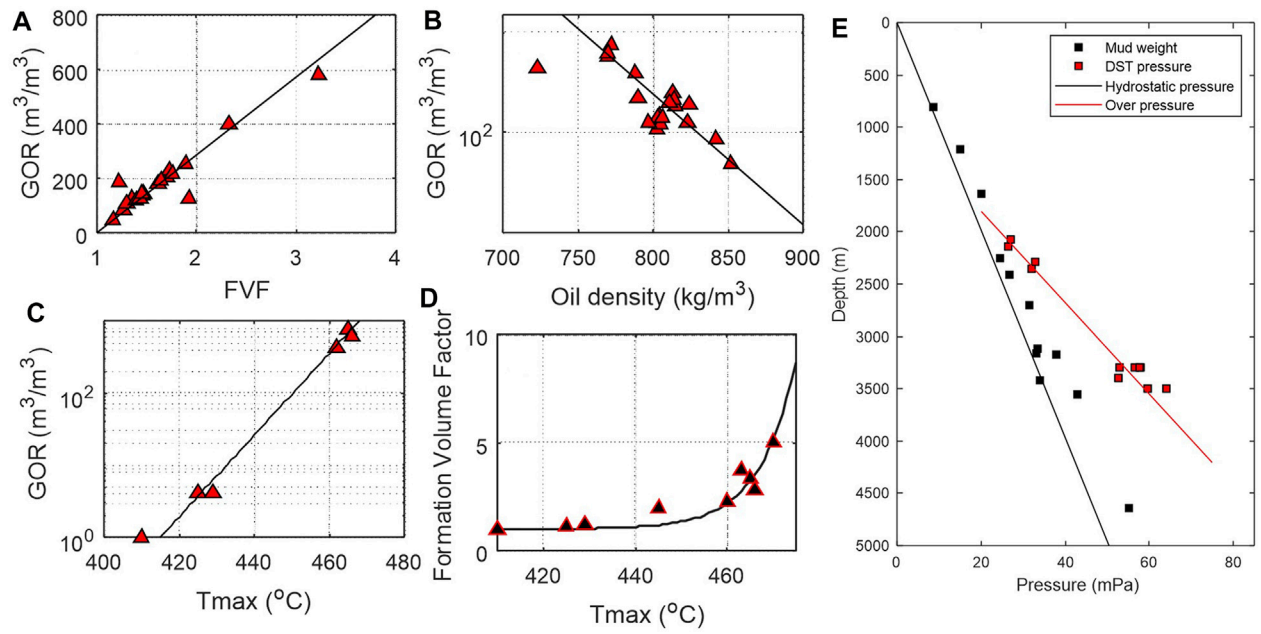

FIGURE 6
Cross-plots of reservoir parameters of the Duvernay Shale showing general characteristics of petroleum fluids at surface condition (modified from Chen and Jiang, 2020). **(A)** Gas to oil ratio GOR vs formation volume factor VFV; **(B)** GOR vs oil density; **(C)** GOR vs maturity index Tmax; **(D)** Formation volume factor FVF vs maturity index Tmax. **(E)** Reservoir pressure profile of the liquid-rich Duvernay shale.

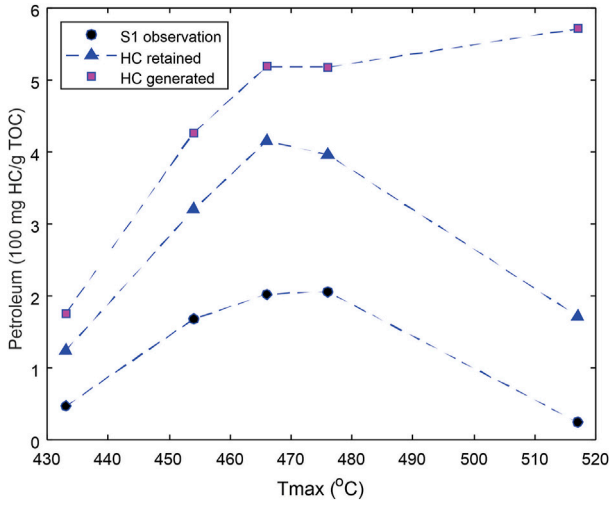

FIGURE 7
Comparison of observed S1 (free petroleum remained in samples) with retained petroleum (TOY defied by Eq. 1) that is the total quantity of petroleum corrected from light hydrocarbon loss. The total petroleum generated is shown as a reference.

The estimated evaporative loss, that is, the difference between the HC retained and HC observed (S1) is shown in Figure 7 for each sample, and compared with the computed total petroleum that has been generated from the source rock at different maturities. The difference between the HC generated and HC retained indicates the amount of petroleum that has been expelled from the source rock.

3.2.2 Estimation of heavy and sorbed oils

The numerical method by Li et al. (2018) is used in this work to transform the Rock-Eval FID pyrogram from temperature domain to activation energy domain. Figure 8 displays the activation energy (Ea) distributions of the five samples with increasing thermal maturity. Each Ea distribution can be roughly divided into two populations (groups): petroleum substances already in sample prior to analysis (yellow) and petroleum generated from kerogen during lab pyrolysis (red). With increasing maturity, the petroleum population increases while kerogen population decreases. To separate the two groups, it is assumed that each of the Ea groups can be modelled by a normal distribution (e.g., Braun and Burnham, 1987). As the two distributions could overlap in a transition zone between 47 and 54 kcal/mol, a sigmoid function is used to fit the cumulative curve of kerogen group (Figure 9), thus determining its natural extension. By adopting the sigmoid natural extension to the left side and keeping the original Ea values on the right, we obtain a corrected Ea distribution for kerogen components for each sample. The difference between the corrected and uncorrected Ea distributions for kerogen components derived from the S2 curve is considered to be the equivalent of the petroleum sorbed in the source rocks or having complex petroleum molecules requiring high temperature to evaporate. The numerically estimated sorbed oil is plotted in Figure 10A.

3.2.3 Hydrocarbon resource mobility grouping

In this study, the TOY is divided into four sub-groups: sorbed oil (Eq. 1), oil and gas with restricted mobility, movable oil, and gaseous petroleum lost prior to analysis during coring, storage and sample preparation. The movable oil is defined as a portion of petroleum substances that can flow freely in reservoir condition. Jarvie (2012) defined an oil saturation index OSI = 100 × S1/TOC, and production

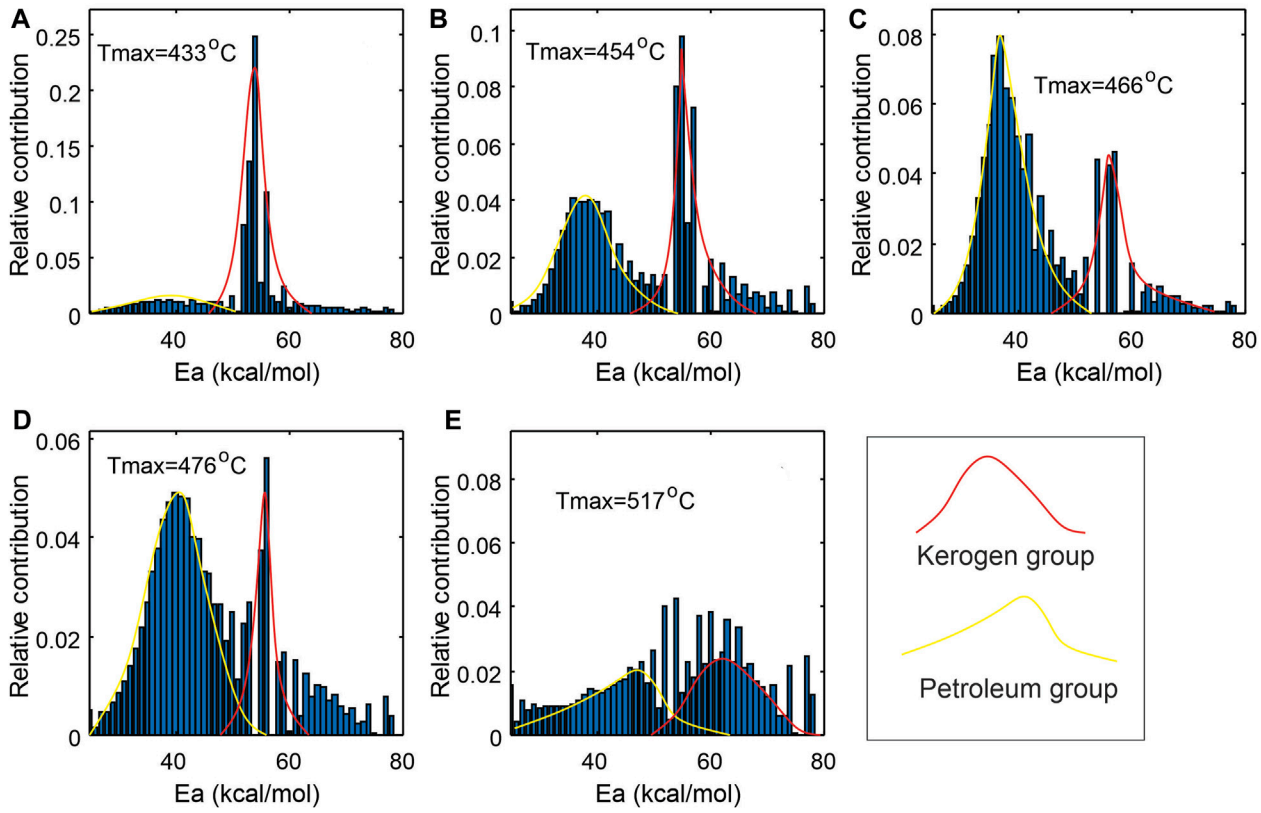

FIGURE 8
Petroleum and kerogen components grouping based on Ea values derived from Rock-Eval FID curve in an activation domain, seeing growth in petroleum and decline in kerogen components with increasing thermal maturity: **(A–E)** correspond to samples C-590392, C-594351, C-590327, C-590436 and C-590378 in Table 1.

statistics suggest that most producing shale oil intervals in North American have an OSI> 100 mg HC/g TOC, while Behar et al., 2002 called OSI > 100 "oil show" in conventional oil exploration. An OSI value greater than 100 mg HC/g TOC may suggest that the mass of petroleum fluids in the reservoir has exceeded the source rock retention capacity. We adopt the definition of movable oil as the portion of TOY that exceeds the critical threshold of the sample TOC value (Chen et al., 2019b; Li et al., 2019):

$$\varnothing_{mob} = \begin{cases} 0, & S1c \le \widetilde{TOC} \\ S1c - \widetilde{TOC}, & S1c > \widetilde{TOC} \end{cases} \quad (17)$$

where $\widetilde{TOC}$ is a discount factor with a quantity equal to the numerical value of sample TOC and has a unit of mg HC/g rock. For example, if the free hydrocarbon after correction for evaporative loss $S1_C$=10 mg HC/g rock, sample $\widetilde{TOC}$ =6%, the movable oil, $\varnothing_{mob} = S1c - \widetilde{TOC}$ = 10 − 6 = 4 (mg HC/g rock). The restricted oil and gas is the difference between petroleum in the sample after correction of evaporative loss and movable oil, that is, $\varnothing_{restricted} = S1c - \varnothing_{mob} = 10 - 4 = 6$ (mg HC/g rock). This is a numerical translation of Jarvie's observation (2012) of OSI>100 mg HC/g TOC in shale oil production interval and is applied to assessing oil mobility. In this sense, the critical threshold is equivalent to the oil saturation threshold.

The oil and gas grouping (normalized to TOC) results for the five Duvernay shale samples with respect to mobility are plotted in Figure 10, showing the variation of different mobility groups with thermal maturation. Movable petroleum resource increases with increasing thermal maturity and reaches a maximum from the peak generation to wet gas window (T*max* from 450 to 490°C) where kerogen is almost depleted and condensate dominates. Massive cracking of oil to gas accelerates expulsion from T*max* = 475°C onward, leading to continuous loss of petroleum fluids and thus decreasing resource intensity (defined as mass of hydrocarbon/reservoir volume). Figure 10 demonstrates the changes in the mass of hydrocarbon retained in shale reservoir with maturity and shows mobility level of petroleum fluids increasing from left to right.

3.2.4 Composition grouping based on evaporative kinetics

Following the steps of the proposed methods described above in Section 2.2.2, the retained petroleum substances in the analyzed sample represented by S1a and S1b can be grouped according the temperature sections in thermal analysis: 100–200°C, 200–350°C, 350–450°C, 400–650 and >650°C on the basis of evaporative kinetics (Figure 8). The corresponding Ea values in Figure 8 for each temperature interval was transformed back to temperature domain, representing evaporation/thermal desorption and chemical reaction equivalent composition (Figure 11). The first 3 groups with lower temperature in Figure 11 are the petroleum substances already generated and retained in the samples. The gaseous hydrocarbon group (<100°C) is the estimated

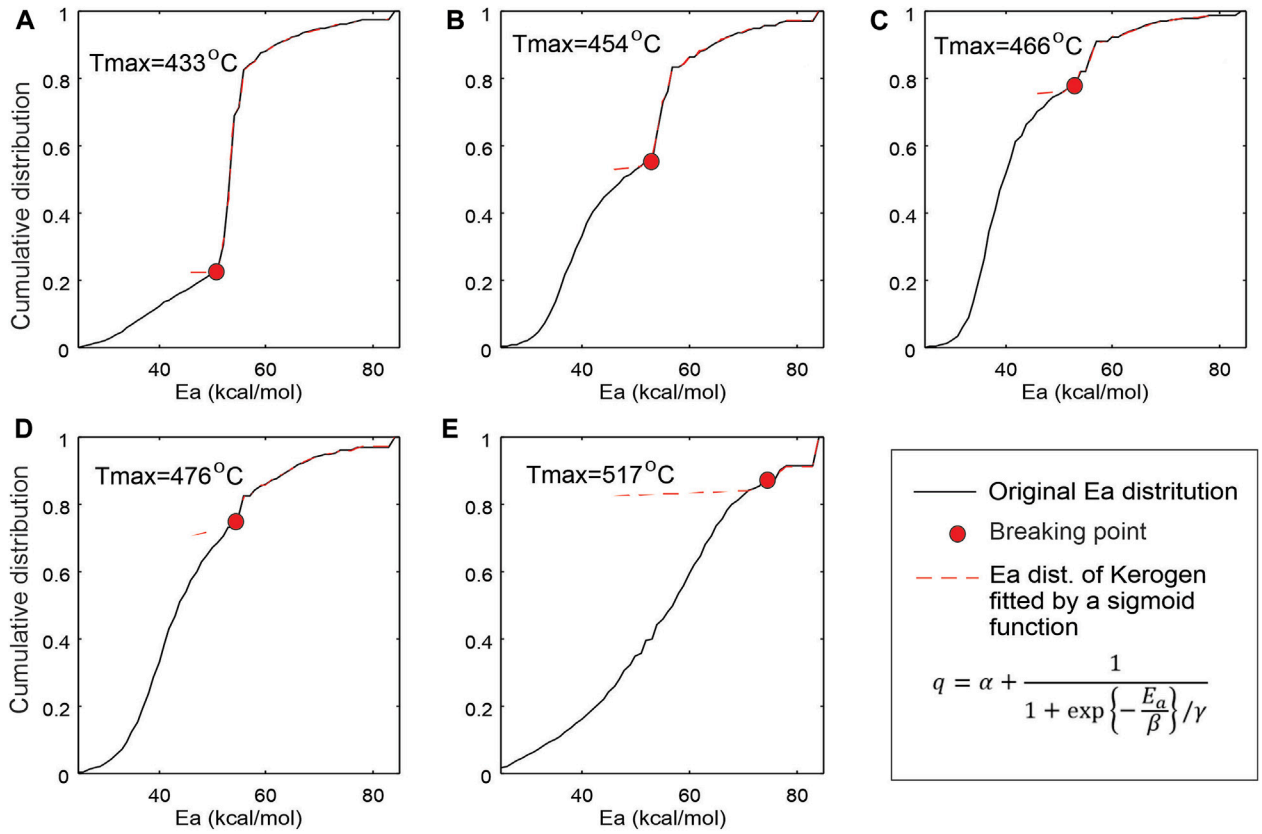

FIGURE 9
Separation of kerogen components from petroleum components in Ea domain. **(A–E)** correspond to samples C-590392, C-594351, C-590327, C-590436 and C-590378 in Table 1. Each group was fitted to a normal distribution, and separation in the mixed transitional area was achieved using a sigmoid function, in which α, β and γ are unknown parameters and obtained by fitting the S2 curve.

evaporative losses and not shown in Figure 11. Numerically, the evaporation rate of petroleum products during pyrolysis is modeled as a convolution of the Ea distribution and evaporation/reaction rate constant (Eq. 11), as such, there will be overlaps between successive oil temperature groups. The degree of overlap depends largely on the temperature ramping rate of the experiment and is shown in Figure 11. The 100–200°C group components may represent light oil components < C_{12}, corresponding to petroleum substances with boiling temperature <200°C. Those in temperature range 200–350°C may represent intermediate molecular weight components with carbon number less than C_{20}, while the 350–450°C group likely represents components of high molecular weight and high boiling point substances (Li et al., 2020). The last two groups are kerogen (chemical decomposition) components (450–650°C) and spent kerogen and pyrobitumen (>650°C) that are exhausted of side aliphatic chains.

4 Discussion

There are several observations on the relationship between mobility groups and thermal maturity. First, in general sorbed oil decreases with increasing thermal maturity, so does the restricted oil and gas group (Figure 10). This reflects the thermal decomposition processes of large molecule heavy oil and bitumen complex breaking down with increasing thermal stress. When the size of petroleum molecule becomes smaller, the interaction between petroleum fluids and host rock is weakened, while when its quality is beyond a critical threshold, the excess part becomes mobile. In gas window, the petroleum group with restricted mobility represents the gases adsorbed to the walls of organic pore and the surface of clay minerals. Secondly, the gas component and movable petroleum groups behave differently. The movable oil increase gradually from early oil generation window and reaches a maximum at the end of oil generation and the beginning of wet gas window in a Tamx zone from 465 to 480°C, where large amount of gaseous petroleum is generated before massive hydrocarbon expulsion. The movable oil group starts to decrease as oil cracking intensifies, while gaseous group appears to decline slightly in mass with increasing thermal maturity. Petroleum fluid maintains an equilibrium between volume and pressure during oil cracking as evidenced from a drastic increase in the volume of expelled petroleum fluids. Thirdly, the mobility of petroleum fluids improves at the expenses of reduced resource potential in the shale reservoir as evidenced by decreased mass of petroleum (per unit TOC) at advanced thermal maturation levels. The total petroleum in mass reaches maximum at the end of oil generation window, and then follows a decreasing trend as fluid expansion causes expulsion. The maximum retaining rate of petroleum fluids (mg HC/g TOC) in shale is in the transitional zone from late oil generation to wet gas windows. Petroleum fluid gains its mobility by converting to smaller gaseous substances, which is a trade-off for reduced resource potential *via* petroleum expulsion. When the source rock enters gas generation window, the aliphatic carbon-carbon chains becomes shorter, improving the mobility of petroleum fluids in reservoir.

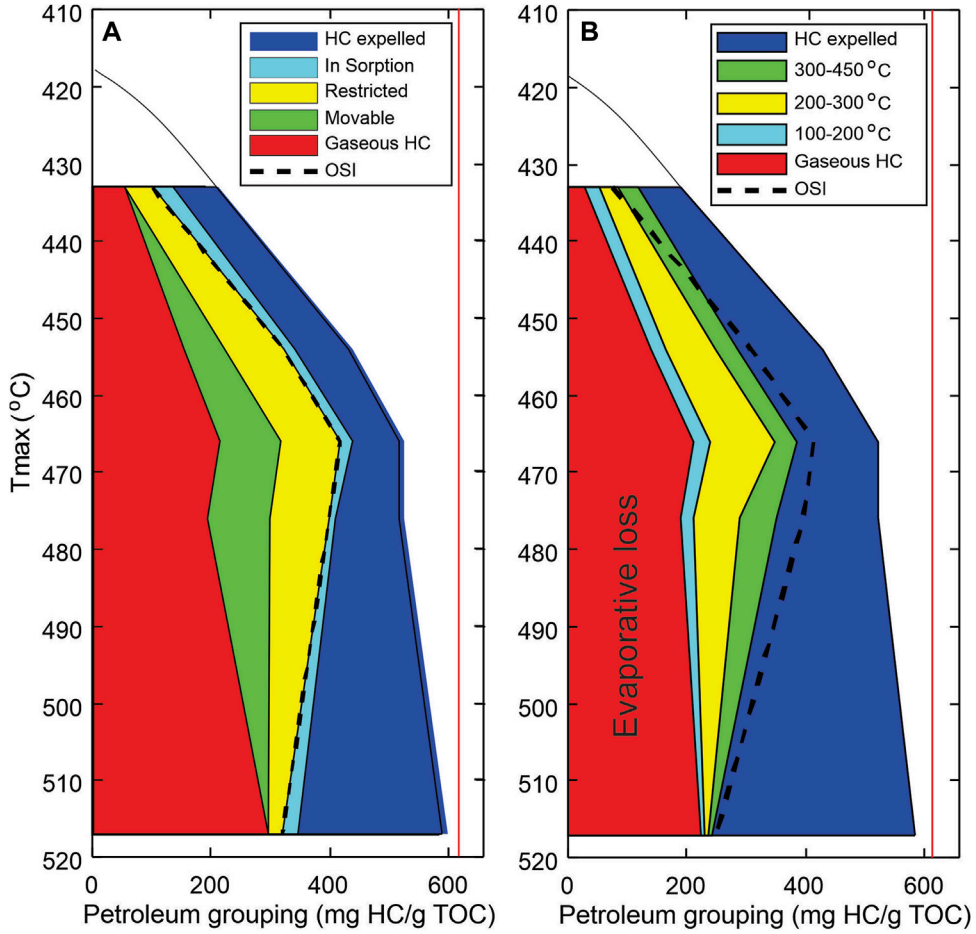

FIGURE 10
Petroleum fluid composition grouping and mobility estimation in shale petroleum reservoir, Duvernay Formation in WCSB. **(A)** resource grouping based on petroleum fluid mobility assessment in reservoir (phase behaviors and OSI); **(B)** petroleum compositional grouping (boiling temperature range equivalent) inverted from kinetic models. Oil saturation index: OSI=S1/TOCx100. The evaporative loss includes gaseous hydrocarbons and light oils that have been generated and retained in the shale, but lost prior to the sample analysis.

Figure 10 compares the grouping results by petroleum fluid mobility (Figure 10A) and by compositional evaporative kinetics (Figure 10B). The gaseous petroleum group is derived from PVT and phase behavior analysis associated with P/T changes from reservoir to surface conditions. The two low temperature petroleum groups (<350°C) (Figure 10B) appear to be comparable with the movable group determined from OSI. The calculated high molecular petroleum substances in temperature range of 350–450°C represent the groups affected by OM-mineral interaction and sorption. However, there are differences between the two types of grouping. The grouping based on evaporative kinetics of petroleum substance shows considerable amount of petroleum in low boiling temperature range at low maturity. This appears to be similar to the phenomena of "permeability jail" in tight gas reservoir, where when gas saturation is less than a critical value, the relative permeability of gas is too low to allow gas flowing to wellbore. For a shale oil reservoir with low thermal maturity, the amount of light oil is less than rock sorption capacity or is dissolved in heavy oil-bitumen, making it not movable. This is also true even in the gas generation window where there still requires a portion of available gas to saturate the active pore surfaces, making the recovery of those gas typically difficult. Thus, petroleum fluid mobility is not only a matter of its compositional characteristics, but also involves additional critical conditions due to increased complexity of interaction between the fluids and the host rock that contains mixed pore types with different physical and chemical properties. However, recent molecular thermodynamic simulation showed that petroleum fluid flow in a shale reservoir depends not only on fluid types (size of the molecule, viscosity, composition) and the pore characteristics (size distribution, type of pore, connectivity), but also the interaction between petroleum fluids and host rock (kerogen types, types and grain size of mineral contents) (e.g., Akkutlu and Fathi, 2012; Akkutlu et al., 2017; Bui et al., 2018; Baek and Akkutlu, 2019a; Baek and Akkutlu, 2019b; Baek and Akkutlu, 2019c). In addition, depending on compositional character of the petroleum fluids, hydrocarbon molecules are likely to be trapped in the pores when the pore size is smaller than a critical threshold (Zhang, et al., 2017). Oil nanopore confinement has also been shown to be a key issue in the mobility of oil, which involves pore size distribution and structure in shale reservoir. Therefore, oil mobility evaluation in shale reservoir has to consider both oil composition and pore characteristics simultaneously. In combination with pore structure and size distribution, it could provide new insights for better understanding the hydrocarbon mobility in shale reservoirs.

The above proposed method for resource estimation is a mass balanced approach that can potentially minimize the impacts of phase change on volumetric calculations of the resource. Hydrocarbons in the original samples were categorized into mobility groups largely

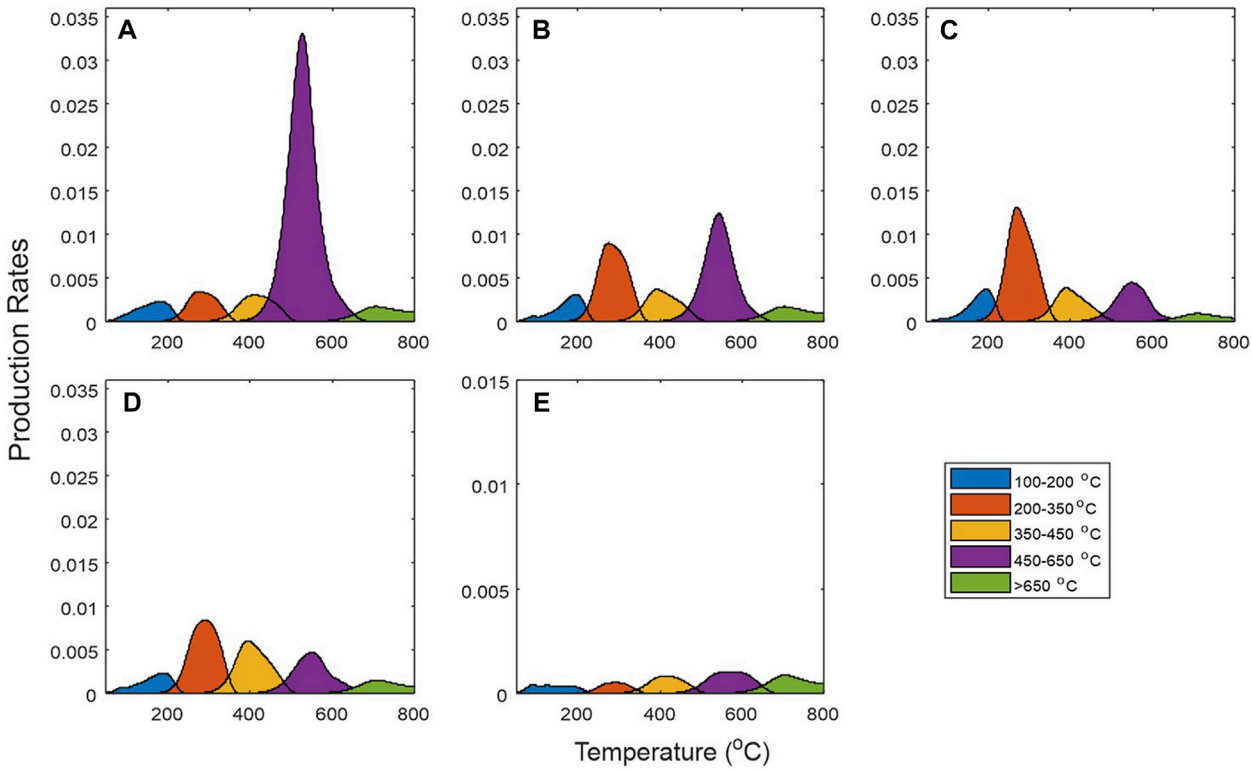

FIGURE 11
Petroleum and kerogen component grouping for the five Duvernay shale samples, showing progressive decrease in kerogen component and increase in petroleum components with increasing thermal maturity: **(A–E)** corresponding to samples C-590392, C-594351, C-590327, C-590436 and C-590378 in Table 1. Petroleum components are lost in gas generation windows due to hydrocarbon expulsion and evaporative loss of gaseous components.

based on their combined behavior of changes in phase and PVT characteristics under different physical conditions (reservoir versus surface) and responses to ramping temperature during routine pyrolysis in the laboratory. The utilization of evaporative kinetics for hydrocarbon fractional analysis avoids additional laboratory analyses, and can be directly related to chemical compositional fractions based on their boiling temperature ranges.

5 Conclusion

This study showed that PVT and phase behavior related changes in petroleum fluid volume and composition due to differences in T/P from reservoir to surface conditions can be used to estimate the amount of evaporative loss of free hydrocarbons in shale rock samples, providing additional information useful for assessing resource potential and oil mobility in shale reservoirs. In oil generation window, the oil formation volume factor is proposed for estimating the evaporative loss of dissolved gas in S1 because the dissolved gas is released due to pressure drop when core is brought to surface. In gas window, the gas volume change, quantified by gas formation volume factor as a function of temperature and pressure, is used to restore the mass of gaseous petroleum in a reservoir condition. With corrections for both evaporative hydrocarbon loss and heavy oil "carry over" in S2, the total oil yield represents better resource intensity in a shale reservoir.

While petroleum fluid mobility increases with maturity in general, the total movable resource reaches its maximum at the end of oil generation window around T*max* = 465°C, then declines towards gas generation window as a result of massive expulsion due to overpressure from thermal cracking of liquid to gaseous hydrocarbon. In this sense, increased oil mobility with thermal maturation is a trade-off with reduced resource intensity.

Evaporative kinetics-based petroleum composition grouping does not show a complete accordance with mobility grouping based on reservoir phase behavior and OSI, suggesting that composition is not the only factor controlling oil mobility. Similar to permeability jail in tight gas reservoir, oil also needs to saturate the retention capacity (including sorption, nanopore confinement and other impeding forces) of the host rock prior to flow. More studies are required to better understand the oil mobility in shale reservoirs.

Data availability statement

The datasets presented in this article are available upon request that can be directed to the corresponding author: zhuoheng.chen@nrcan-rncan.gc.ca.

Author contributions

All authors participated in the preparation of the paper. ZC: Conceptualization, mathematical method development and data processing, original draft writing and revision; CJ: Conceptualization, programmed thermal analysis design and data

interpretation, draft writing, review and revision; JR: Analytical data processing and iq16nterpretation, manuscript review and revision; XL: Mathematical method development and data processing, manuscript draft review and revision. EL: Resource and admin support of project, manuscript review.

Funding

This represents an output from Geoscience for New Energy Supply Program of Natural Resources Canada and is partly supported by PERD funding.

Acknowledgments

We thank the two journal reviewers as well as our internal reviewer J. Cesar Colmenares at Geological Survey of Canada, for their helpful comments and suggestions that improved the quality of the paper. This is Geological Survey of Canada NRCan Contribution 20220418.

Conflict of interest

The authors declare that the research was conducted in the absence of any commercial or financial relationships that could be construed as a potential conflict of interest.

Publisher's note

References

Abrams, M. A., Gong, C., Garnier, C., and Sephton, M. A. (2017). A new thermal extraction protocol to evaluate liquid rich unconventional oil in place and *in-situ* fluid chemistry. *Mar. Pet. Geol.* 88, 659–675. doi:10.1016/j.marpetgeo.2017.09.014

AER (2016). Duvernay reserves and resources report, A comprehensive analysis of alberta's foremost liquids-rich shale resource. .

Akkutlu, I. Y., Baek, S., Olorode, O. M., Wei, P., Zhang, T., and Shuang, A. (2017). Shale resource assessment in presence of nanopore confinement, URTEC-2670808-MS. Unconventional Resources Technology Conference, SPE/AAPG/SEG Unconventional Resources Technology Conference. 24. July 26, Austin, Texas, USA, doi:10.15530/URTEC-2017-2670808

Akkutlu, I. Y., and Fathi, E. (2012). Multiscale gas transport in shales with local kerogen heterogeneities. *SPE J.* 17 (04), 1002–1011. doi:10.2118/146422-PA

Allan, J., and Creaney, S. (1991). Oil families of the western Canada basin. *Bull. Can. Petroleum Geol.* 39, 107–122.

Ambrose, R. J., Hartman, R. C., Diaz-Campos, M., Akkutlu, I. Y., and Sondergeld, C. H. (2012). Shale gas-in place calculations Part I: New pore-scale considerations. *SPE J. (March)* 17, 219–229. doi:10.2118/131772-pa

Baek, S., and Akkutlu, I. Y. (2019a). CO2 stripping of kerogen condensates in source rocks. *SPE J.* 24 (03), 1415–1434. doi:10.2118/190821-PA

Baek, S., and Akkutlu, I. Y. (2019c). *Produced-fluid composition redistribution in source rocks for hydrocarbon-in-place and thermodynamic recovery calculations SPE J.* 24 (03), 1395–1414. doi:10.2118/195578-PA

Baek, S., and Akkutlu, I. Y. (2019b). "Recovery mechanisms for nano-confined oil in source rocks using lean gas injection" in. SPE (Society of Petroleum Engineers) Western Regional Meeting. San Jose, CA, April 2019. doi:10.2118/195272-MS

Behar, F., Beaumont, V., De, B., and Penteado, H. L. (2002). Rock-eval 6 technology: Performances and development, oil & gas science and Technology. *Rev. IFP* 56 (2), 111–134.

Bohacs, K. M., Passey, Q. R., Rudnicki, M., Esch, W. L., and Lazar, O. R. (2013). The spectrum of fine-grained reservoirs from "shale gas" to "shale oil"/tight liquids: Essential attributes, key controls, practical characterization. *IPTC* 16676, 1–16.

Braun, R. L., and Burnham, A. K. (1987). Analysis of chemical reaction kinetics using a distribution of activation energies and simpler models. *Energy & Fuels* 1 (2), 153–161. doi:10.1021/ef00002a003

Bui, K., Akkutlu, I. Y., Zelenev, A., and Hill, W. A. (2018). "Kerogen maturation effects on pore morphology and enhanced shale oil recovery" in. SPE Europec featured at 80th EAGE Conference and Exhibition, Copenhagen, Denmark, June 2018. doi:10.2118/190818-MS

Burnham, A. (2017). *Global chemical kinetics of fossil fuels, how to model maturation and pyrolysis*. Springer, 145–147.

Burnham, A. K., and Braun, R. L. (1999). Global kinetic analysis of complex materials. *Energy Fuels* 13 (1), 1–22. doi:10.1021/ef9800765

Cander, H. (2013). *Finding sweet spots in shale liquids and gas plays: (with lessons from the eagle ford shale). Search and discovery article #41093*, 2012–2013. Posted May 13, 2013 Available.

Chen, J., Pang, X., Pang, H., Chen, Z., and Jiang, C. (2018). Hydrocarbon evaporative loss evaluation of lacustrine shale oil based on mass balance method: Permian Lucaogou Formation in Jimusaer Depression, Junggar Basin. *Mar. Petroleum Geol.* 91, 422–431. doi:10.1016/j.marpetgeo.2018.01.021

Chen, Z., Kong, B., and Lee, H. S. (2022). Reservoir characteristics and light hydrocarbon channeling revealed by production data: A case study of liquid rich Duvernay shale play with emphasis in fox creek area, Alberta Canada. *Fuel* 392. doi:10.2139/ssrn.4093750

Chen, Z., and Jiang, C. (2016). A revised method for organic porosity estimation in shale reservoirs using Rock-Eval data: Example from Duvernay Formation in the Western Canada Sedimentary Basin. *Am. Assoc. Petroleum Geol. Bull.* 100 (3), 405–422. doi:10.1306/08261514173

Chen, Z., Jiang, C., Lavoie, D., and Reyes, J. (2016). Model-assisted rock-eval data interpretation for source rock evaluation: Examples from producing and potential shale gas resource plays. *Int. J. Coal Geol.* 165, 290–302. doi:10.1016/j.coal.2016.08.026

Chen, Z., Lavoie, D., Malo, M., Jiang, C., Sanei, H., and Haeri-Ardakani, O. (2017a). A dual-porosity model for evaluating petroleum resource potential in unconventional tight-shale plays with application to Utica Shale, Quebec (Canada). *Mar. Petroleum Geol.* 80, 333–348. doi:10.1016/j.marpetgeo.2016.12.011

Chen, Z., Li, M., Jiang, C., and Qian, M. (2019b). Shale oil resource potential and mobility assessment: A case study of upper devonian Duvernay shale in the western Canada Sedimentary Basin. *Oil Gas Geol.* 40 (6), 459–468.

Chen, Z., Li, M., Ma, X., Cao, T., Liu, X., Li, Z., et al. (2018). Generation kinetics based method for correcting effects of migrated oil on rock-eval data – An example from the Eocene qianjiang formation, jianghan basin, China. *Int. J. Coal Geol.* 195, 84–101. doi:10.1016/j.coal.2018.05.010

Chen, Z., Liu, X., Guo, Q., Jiang, C., and Mort, A. (2017c). Inversion of source rock hydrocarbon generation kinetics from Rock-Eval data. *Fuel* 194, 91–101. doi:10.1016/j.fuel.2016.12.052

Chen, Z., Liu, X., and Jiang, C. (2017b). Quick evaluation of source rock kerogen kinetics using hydrocarbon pyrograms from regular rock-eval analysis. *Energy* 31 (2), 1832–1841. doi:10.1021/acs.energyfuels.6b01569

Chen, Z., Liu, X., and Osadetz, K. E. (2019a). Petroleum generation kinetic models for late ordovician kukersite yeoman Formation source rocks, williston basin (southern saskatchewan), Canada. *Fuel* 241, 234–246. doi:10.1016/j.fuel.2018.11.154

Chow, N., Wendte, J., and Stasiuk, L. D. (1995). Productivity versus preservation controls on two organic-rich carbonate facies in the devonian of Alberta: Sedimentological and organic petrological evidence: *Bull. Can. Petroleum Geol.*, 43, 433–460.

Creaney, S., and Allan, J. (1992). "Petroleum systems in the foreland basin of Western Canada," in *Foreland basins and foldbelts*. *American Association of petroleum geologists*. Editors R. W. Macqueen and D. A. Leckie (Memoir, 55, 279–308.

Creaney, S., Allan, J., Cole, K. S., Fowler, M., Brooks, P. W., Osadetz, G. K., Snowdon, L., and Riediger, C. L. (1994). "Petroleum generation and migration in the Western Canada Sedimentary Basin[M]," in *Geological atlas of the Western Canada Sedimentary Basin, G.D. Mossop and I. Shetsen (comp.)* (Calgary: Canadian Society of Petroleum Geologists and Alberta Research Council). URLlast accessed online June 24, 2014).

Creaney, S. (1989). "Reaction of organic material to geological heat," in *Thermal history of sedimentary basins - methods and case histories*. Editors N. D. Naeser and T. H. McCulloh (Springer-Verlag), 37–52.

Delveaux, D., Martin, H., Leplat, P., and Paulet, P. (1990). Comparitive Rock-Eval pyrolysis as an improved tool for sedimentary organic matter analysis. *Orgarnic Geochem.* 16 (4-6), 1221–1229.

Dieckmann, V., Fowler, M., and Horsfield, B. (2004). Predicting the composition of natural gas generated by the Duvernay formation (Western Canada sedimentary basin) using a compositional kinetic approach. *Org. Geochem.* 35, 845–862. doi:10.1016/j.orggeochem.2004.02.010

Dong, T., Harris, N. B., McMillan, J. M., Twemlow, C. E., Nassichuk, B. R., and Bish, D. L. (2019). A model for porosity evolution in shale reservoirs: An example from the Upper Devonian Duvernay Formation, Western Canada Sedimentary Basin. *AAPG Bull.* 103 (5), 1017–1044. doi:10.1306/10261817272

Han, Y., Horsfield, B., Wirth, R., Mahlstedt, N., and Bernard, S. (2017). Oil retention and porosity evolution in organic-rich shales. *AAPG Bull.* 101, 807–827. doi:10.1306/09221616069

Han, Y., Mahlstedt, N., and Horsfield, B. (2015). The Barnett Shale: Compositional fractionation associated with intraformational petroleum migration, retention, and expulsion. *Am. Assoc. Petroleum Geol. Bull.* 99 (12), 2173–2202. doi:10.1306/06231514113

Hartigan, D. A. (2014). *The petrophysical properties of shale gas reservoirs*. UK: Ph.D thesis, the University of Leicester. .

Jarvie, D. M. (2014). "Components and processes affecting producibility and commerciality of shale resource systems,"*Geol. Acta* (December: ALAGO Special Publication), 12. 307–325. N. 12.

Jarvie, D. M. (2012). "Shale resource systems for oil and gas: part 2—shale–oil resource systems,". Editor J. A. Breyer (AAPG Memoir), 97. 89–119.*Shale reservoirs—Giant resources for the 21st century*. Tulsa: American Association of Petroleum Geologists.

Jiang, C., Chen, Z., Mort, A., Milovic, M., Robinson, R., Stewart, R., et al. (2016). Hydrocarbon evaporative loss from shale core samples as revealed by Rock-Eval and thermal desorption-gas chromatography analysis: Its geochemical and geological implications. *Mar. Petroleum Geol.* 70, 294–303. doi:10.1016/j.marpetgeo.2015.11.021

Jiang, C., Mort, A., Sanei, H., Chen, Z., Milovic, M., and Robinson, R. (2015). S1 peak of Rock-Eval analysis: What does it represent for unconventional hydrocarbon resource assessment? *GeoConcention*. .

Jiang, Q., Li, M., Qian, M., LiLiHuang, Z. Z. Z., Zhang, C., and Ma, Y. (2016). Quantitative characterization of shale oil in different occurrence state and its application. *Petroleum Geol. Exp.* 38 (6), 843–848.

King, G. E. (20142014). *Improving recovery factors in liquids-rich resource plays requires new approaches, the American oil & gas reporter*. .

Lafargue, E., Marquis, F., and Pillot, D. (1998). Rock-Eval 6 Applications in Hydrocarbon Exploration, Production, and Soil Contamination Studies. *Oil Gas Sci Technol, Rev. Fr. Petroleum Inst.* 53, 421–437. doi:10.2516/ogst:1998036

Li, M., Chen, Z., Ma, X., Cao, T., Qian, M., Jiang, Q., et al. (2019). Shale oil resource potential and oil mobility characteristics of the Eocene-Oligocene Shahejie Formation, Jiyang Super-Depression, Bohai Bay Basin of China. *Int. J. Coal Geol.* 204, 130–143. doi:10.1016/j.coal.2019.01.013

Li, M., Chen, Z., Ma, X., CaoLi, T. Z., and Jiang, Q. (2018). A numerical method for calculating total oil yield using a single routine Rock-Eval program: A case study of the Eocene Shahejie Formation in Dongying Depression, Bohai Bay Basin, China. *Int. J. Coal Geol.* 191, 191 49–65. doi:10.1016/j.coal.2018.03.004

Li, M., Chen, Z., Qian, M., Ma, X., Jiang, Q., Li, Z., et al. (2020). What are in pyrolysis S1 peak and what are missed? Petroleum compositional characteristics revealed from programed pyrolysis and implications for shale oil mobility and resource potential. *Int. J. Coal Geol.* 217, 103321. doi:10.1016/j.coal.2019.103321

Macedo, R. (2013). Duvernay Well Encouraging for Encana. *Dly. Oil Bull. April.* 24, 2013.

Michael, G. E., Packwood, J., and Holba, A. (2013). "Determination of *in-situ* hydrocarbon volumes in liquid rich shale plays," in Unconventional Resources Technology Conference (Denver, Colorado, USA, August. .

Modica, C. J., and Lapierre, S. G. (2012). Estimation of kerogen porosity in source rocks as a function of thermal transformation: Example from the Mowry Shale in the Powder River Basin of Wyoming. *Am. Assoc. Petroleum Geol. Bull.* 96, 87–108. doi:10.1306/04111110201

NEB (2017). *Duvernay resource assessment energy briefing note*. Available at:.

Ole, M. E. (2015). *Reservoir characterization of the Duvernay Formation, Alberta: A pore-to basin-scale investigation*. Vancouver: Ph.D thesis, University of British Columbia. .

Passey, Q. R., Bohacs, K. M., Esch, W. L., Klimentidis, R., and Sinha, S. (2010), "From Oil-Prone Source Rock to Gas-Producing Shale Reservoir – Geologic and Petrophysical Characterization of Unconventional Shale-Gas Reservoirs" in International Oil and Gas Conference and Exhibition, Beijing, China, June, 2010. 131350.

Penner, S, S. (1952). On the kinetics of evaporation. *J. Phys. Chem.* 56 (4), 475–479. doi:10.1021/j150496a015

PetroWiki (2018). Oil Formation Factor. Available at:.

Sandvik, E. I., Young, W. A., and Curry, D. J. (1992). Expulsion from hydrocarbon sources: The role of organic absorption. *Org. Geochem.* 19, 77–87. doi:10.1016/0146-6380(92)90028-V

Sondergeld, C. H., Newsham, K. E., Comisky, J. T., Rice, M. C., and Rai, C. S. (2010). "Petrophysical considerations in evaluating and producing shale gas resources," in Proceedings of the SPE Unconventional Gas Conference, Pittsburgh, Pennsylvania, USA, 23–25th February 2010, 1–34.*Society of petroleum engineers*.

Stasiuk, L. D., and Fowler, M. G. (2004). Organic facies in Devonian and Mississippian strata of Western Canada Sedimentary Basin; Relation to kerogen type, paleoenvironment, and paleogeography. *Bull. Can. Petroleum Geol.* 52 (3), 234–255. doi:10.2113/52.3.234

Stasiuk, L. D., and Fowler, M. G. (2002). *Thermal maturity evaluation (vitrinite and vitrinite reflectance equivalent) of Middle Devonian, Upper Devonian, and Mississippian strata in the Western Canada Sedimentary Basin*. Ottawa: Geological Survey of Canada. Open File 4341 (CD-ROM).

Stoakes, F. A., and Creaney, S. (1985). "Controls on the accumulation and subsequent maturation and migration history of a carbonate source rock," in Society of Economic Paleontologists and Mineralogists, Core Workshop Proceedings, Golden, Colorado, U.S.A., August 1985.

Stoakes, F. A., and Creaney, S. (1984). "Sedimentology of a carbonate source rock: Duvernay Formation of central Alberta," Proceedings of the 1984 Canadian Society of Petroleum Geologists Core Conference. Calgary. in *Carbonates in subsurface and outcrop*. Editor L. Eliuk, 132–147.

Switzer, S. B., Holland, W. G., Christie, D. S., Graf, G. C., Hedinger, A. S., McAuley, R. J., et al. (1994). "Devonian Woodbend-Winterburn Strata of the Western Canada Sedimentary Basin," in *Geological atlas of the Western Canada Sedimentary Basin* (Calgary: Canadian Society of Petroleum Geologists and Alberta Research Council). URLlast accessed online Available at: August 21, 2014).

Whitson, C. H., and Sunjerga, S. (2012). PVT in Liquid-Rich Shale Reservoirs, SPE-155499-MS. SPE Annual Technical Conference and Exhibition, 8-10. San Antonio, Texas, USA.

Zhang, P., Hu, L., Meegoda, J. N., and Gao, S., (2015). Micro/Nano-pore Network Analysis of Gas Flow in Shale Matrix, *Sci. Rep.* 5:13501. doi:10.1038/srep13501

Zhang, Y., Yu, W., and SepehrnooriDi, Y. (2017). Investigation of nanopore confinement on fluid flow in tight reservoirs. *J. petroleum Sci. Eng.* 150, 265–271. doi:10.1016/j.petrol.2016.11.005

frontiers | Frontiers in Earth Science

TYPE Original Research
PUBLISHED 09 May 2023
DOI 10.3389/feart.2023.1137026

OPEN ACCESS

EDITED BY
Feng Yang,
China University of Geosciences Wuhan, China

REVIEWED BY
Guangyou Zhu,
Research Institute of Petroleum Exploration and Development (RIPED), China
Zhixing Ru,
SINOPEC Petroleum Exploration and Production Research Institute, China

*CORRESPONDENCE
Jaime Cesar,
jaimerafael.cesarcol@ucalgary.ca

RECEIVED 03 January 2023
ACCEPTED 24 April 2023
PUBLISHED 09 May 2023

CITATION
Cesar J, Robinson R, Naeher S, Milovic M and H. Ardakani O (2023), Fatty acids, alkanones and alcohols from a major lower Triassic low-permeability petroleum reservoir.
Front. Earth Sci. 11:1137026.
doi: 10.3389/feart.2023.1137026

Fatty acids, alkanones and alcohols from a major lower Triassic low-permeability petroleum reservoir

Jaime Cesar[1]*, Rachel Robinson[1], Sebastian Naeher[2], Marina Milovic[1] and Omid H. Ardakani[1,3]

[1]Geological Survey of Canada, Natural Resources Canada, Calgary, AB, Canada, [2]GNS Science, Lower Hutt, New Zealand, [3]Department of Geoscience, University of Calgary, Calgary, AB, Canada

For the first time, polar organic compounds in extracted bitumen from the Lower Triassic Montney Formation have been analyzed. This stratigraphic unit is one of the most prolific low-permeability reservoirs in Western Canada. However, its organic geochemical characterization is a challenge due to low biomarker concentration in the liquids and frequent mixing of gas/condensate hydrocarbons. Since typical biomarkers were not available, this study focused on another group of molecules, polar oxygen-compounds, which were derivatized and subsequently resolved using chromatographic techniques. In the polar fractions, based on their contrasting molecular distributions, *n*-fatty acids and alkan-2-ones do not seem to share a common origin and do not have an apparent association with the n-alkanes. This study is also the first report of 1,13-, 1,14- and 1,15-diols in fossil organic matter; and in carbon number ranges of C_{15}-C_{29}, C_{16}-C_{29} and C_{17}-C_{29} respectively. The similar distributions of 1,14- 1,15-diols suggests a common origin for these compound classes, whereas theand 1,13-diols seem to derive from a different source or mechanism. A series of alkan-3-ols has also been identified in the C_{12}-C_{28} range, sharing a common distribution pattern with the *n*-fatty acids. The large variability detected in the molecular distribution of oxygen-containing aliphatic compounds introduces the question whether they may record a geochemical signature that precedes thermal degradation and hydrocarbon migration events within Montney reservoirs.

KEYWORDS

polar, diol, acid, ketone, low-permeability, Montney

1 Introduction

In the Western Canadian Sedimentary Basin, a significant amount of petroleum resources is currently produced from the Lower Triassic Montney Formation (unconventional estimated reserves at 12,719 billion m^3 of natural gas, 14,521 million barrels of natural-gas-liquids, and 1,125 million barrels of oil, BC Oil and Gas Commission, 2012; Rokosh et al., 2012). Hydrocarbons in the Montney Formation are thought to originate from thermal degradation of migrated oil. This is based on the fact that the organic matter in Montney mostly consists of pore-filling solid bitumen (Sanei et al., 2015; Wood and Sanei, 2016; Wood et al., 2018). Maximum burial and thermal maturity reached in the Late Cretaceous/Early Paleogene caused thermal cracking of accumulated hydrocarbons which led to the petroleum accumulations we know today (Wood and Sanei, 2016; Ducros et al.,

2017; Euzen et al., 2021). Primary organic matter has also been identified within Montney (Ardakani et al., 2022). However, the relative contribution from *in-situ* kerogen to the petroleum accumulations remains unknown. Source rock candidates include the Middle Triassic Doig Formation, the Lower Jurassic Gordondale Member of the Fernie Formation, and the Montney Formation (Alan and Creaney, 1991; Ejezie, 2007; Euzen et al., 2021). Nonetheless, fluid to source correlations to date (e.g., based on biomarkers) continue to be rather inconclusive.

Recent studies on gas hydrocarbons have facilitated the definition of hydrocarbon play boundaries within Montney (e.g., Cesar et al., 2020b; Cesar et al., 2021), as well as potential gas migration pathways (Wood and Sanei, 2016; Euzen et al., 2021; Wood et al., 2022) using a molecular approach. The overall geochemical signature of produced gases from these fields seems to be controlled by thermal maturity effects and fluid mixing due to migration (Cesar et al., 2020a; Cesar et al., 2021; Cesar et al., 2022; Wood et al., 2022). As a result, gas geochemical tools alone have not been successful discriminators for the identification of the source(s) of hydrocarbons.

In the liquid phase, geochemical assessment has been limited by the low abundance of biomarkers (e.g., hopanes and steranes) in the produced condensates and light oils. In the Montney Formation, little has been studied regarding the geochemistry of light hydrocarbons, which often cannot be detected in rock extracts due to volatility loss during sample handling/preparation, limiting fluid to source correlation. Research on condensate samples has suggested the possibility of mixtures of migrated hydrocarbons with hydrocarbons derived from original kerogen of the Montney Formation (Cesar et al., 2020a).

In contrast to molecules in the gas-condensate range, there is a group of compounds that have not been analyzed yet, these are polar compounds in the resin fraction of soluble bitumen. It is known that resins are scarce (or absent) in the produced condensates and light oils. However, they are preserved in the solid bitumen residue within the reservoir, and potentially record a fingerprint of the original source of migrated hydrocarbon that charged Montney productive intervals. At the same time, these polar compounds can be a source of gas/condensate, particularly when thermal alteration (cracking) takes place (e.g., Michels et al., 2000) as is the case of the Montney Formation.

In this study, and for the first time, we characterize polar compounds of extracted bitumen from the Montney Formation in order to 1) identify the main oxygen-aliphatic compound classes, 2) investigate associations between them, and 3) discuss their potential as source discriminators.

2 Geological setting

The Montney Formation (Figure 1A) deposited in the northwestern margin of the North American craton during the Lower Triassic (Davies, 1997; Davies et al., 2018; Zonneveld and Moslow, 2018) in a mixed siliciclastic-carbonate depositional environment that accumulated shoreface to offshore, and turbidite sediments (Davies, 1997; Davies et al., 2018; Zonneveld and Moslow, 2018). The lithology includes a complex succession of dolomitic siltstone, minor component of very fine-to fine-grained sandstone with local bioclastic carbonate rocks and minor shale intervals (Davies, 1997; Davies et al., 2018; Zonneveld and Moslow, 2018).

The Montney Formation is divided into three main members (Davies, 1997; Davies et al., 2018; Zonneveld and Moslow, 2018). The Lower Member corresponds to multi-cyclic very fine-grained sandstone and dolomitic siltstone. It overlies the Triassic unconformity on Permian and/or older strata, and it is overlain by the base of the Middle Member in the east (where present), and by the Upper Member in the west. The Middle Member consists of a thick succession of bituminous dolomitic siltstone with interbedded very-fine grained sandstone. It overlies the Lower Member and is marked by a boundary of reworked clasts of the underlying units. The Upper Member corresponds to multicyclic, coarsening-up siltstones and very fine sandstones dominated by storm-related fabrics, with local dolomitized coquina facies; and it is overlain by the Doig Formation. The Upper Member is primarily seen in the British Columbia section (Supplementary Figure S1). In addition, the Montney stratigraphic succession deeps towards the southwest, thus the sections in British Columbia are often more mature than those from Alberta (BC Oil and Gas Commission, 2012; Rokosh et al., 2012). The general schematic stratigraphy is illustrated in Figure 1B.

3 Materials and methods

3.1 Sample preparation

A total of 15 powdered and homogenized rock samples were solvent-extracted using dichloromethane (DCM) in a Soxhlet apparatus for 24 h. The general characteristics of the samples are listed in Table 1. The samples selected for this study correspond to core intervals from the different stratigraphic Members (Lower, Middle, and Upper), different locations, and different thermal maturity levels as indicated by rock pyrolysis (Tmax) and aromatic ratios (Table 1).

Polar fractions were obtained from the extracted bitumen using column chromatography by elution with methanol once saturate and aromatic hydrocarbon fractions had been eluted with *n*-pentane and DCM:*n*-pentane, respectively. Aliquots of the polar fractions (0.5–1 mg) were derivatized in 200 µL of pyridine and 300 µL of N,O-Bis(trimethylsilyl) trifluoroacetamide (BSTFA) at 70°C for 1 h. Then, the derivatized fractions were dried under a gentle stream of nitrogen at 35°C and re-dissolved in *n*-hexane for molecular analysis as explained below. Procedural blanks were prepared and analyzed to monitor for any contamination during sample preparation, and instrument blanks and standards were run to check for instrument carry over or any other instrumental anomalies. Nonadecanol was used as internal standard.

3.2 Molecular analysis

Derivatized fractions were analyzed via gas chromatography time-of-flight mass spectrometry (GC–QTOF-MS) on an Agilent 7890BGC - 7200 QTOF mass spectrometer equipped with a DB5-ms column (60 m × 0.25 µm i.d. × 0.25 mm f.t.), using splitless injection and helium as carrier gas (1.3 mL/min). The temperature program of the GC oven started at 80°C for 1 min, then ramped at 5°C/min to 325°C and held at the final temperature for 30 min. Compound identification was carried out using relative retention times and characteristic mass spectra.

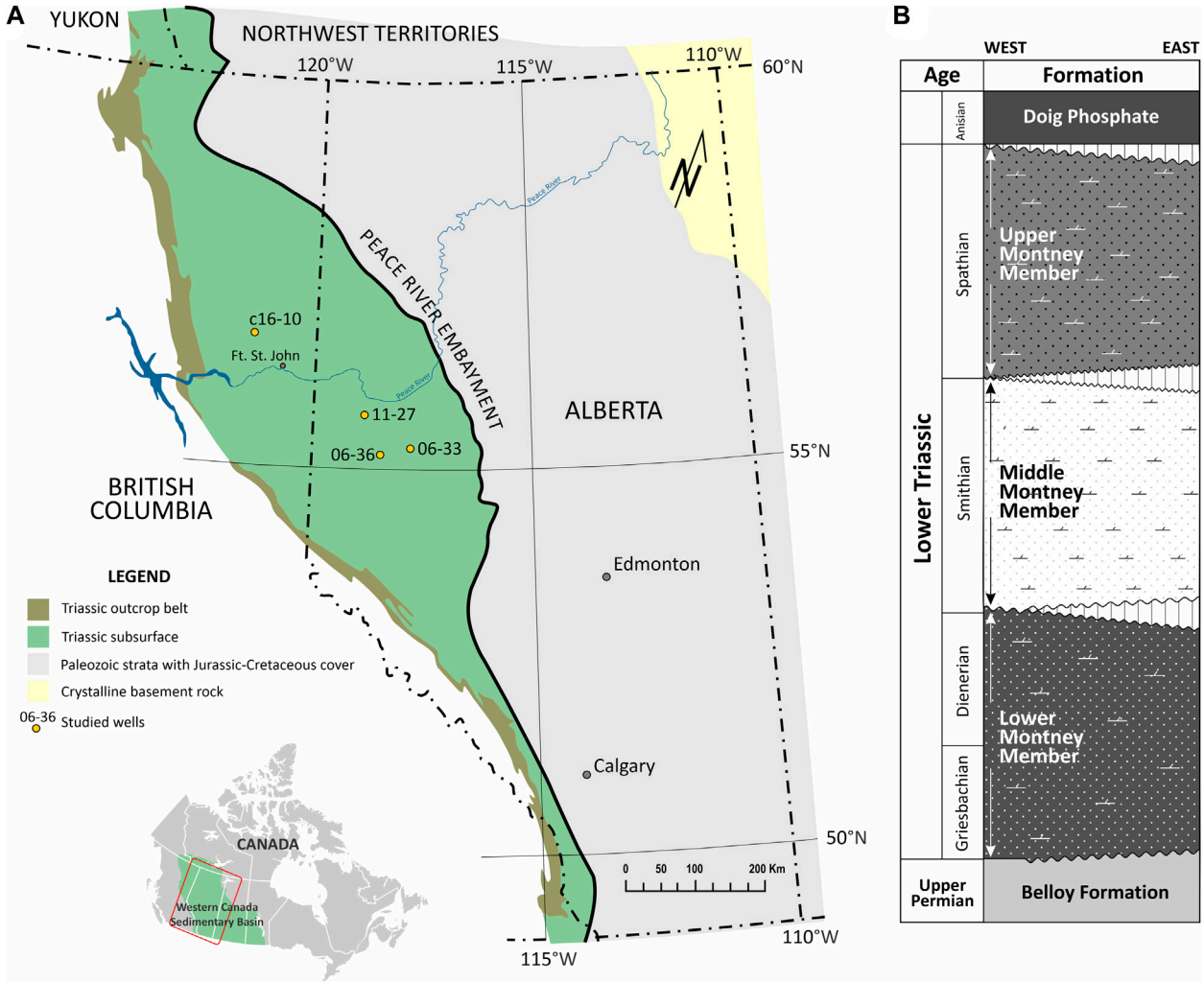

FIGURE 1
Geological context indicating **(A)** the Montney Formation and location of studied wells (modified after Ardakani et al., 2022), and **(B)** a summarized stratigraphic column (after Zonneveld and Moslow, 2018).

The distribution of *n*-alkanes in the saturate fractions were determined using GC with flame ionization detection (FID) analysis of the saturated hydrocarbon fractions on an Agilent 7890B GC-FID. A 30 m × 0.25 mm × 0.25 μm DB-1 fused silica capillary column was used, with helium as carrier gas. The samples were injected using split injection with the injector temperature set at 300°C. The temperature program of the GC oven started at 60°C, then ramped at 6°C/min to 300°C for 30 min. The FID temperature was maintained at 300°C.

4 Results

4.1 Fatty acids

C_{15}-C_{30} *n*-fatty acids (carboxylic acids) are present in all samples (Figure 2A, *m/z* 117) and typically dominated by C_{18}-C_{20} (Figure 2A; Figure 3A). However, samples X12140 and X12143 have bimodal distributions with maximum abundance at C_{18}-C_{19} and C_{22}-C_{24} (Figures 3B, D). Samples X12141 and X12148 display unimodal distributions that are to some extent flat tops between C_{19} and C_{23} (Figure 3C).

4.2 Alkanones

Alkanones, or more specifically alkan-2-ones, were identified using the *m/z* 58 as shown in Figure 2B, usually in the C_{17}-C_{27} carbon range. All the samples exhibit unimodal distributions with maximum abundance of C_{20} as illustrated in Figure 3. Predominance of even carbon numbered homologues was found in samples X12140, X12142, X12143, X12148, X12149, X12151, and X12152 (e.g., Figure 3D).

4.3 Diols

Figure 4 presents the diols detected in the studied samples, which include 1,13-diols (*m/z* 257), 1,14-diols (*m/z* 271), and 1,15-

TABLE 1 Montney Formation core rock samples included in this study. Core locations shown in Figure 1A.

Sample	Core/province	Member	T_{max} (°C)	TMNr[a]	Pr/Ph[b]	Potential source
X12139	C16-10-88-23W6/British Columbia	Upper	446	0.90	1.42	Montney migrated? (Watt et al., 2022)
X12140	C16-10-88-23W6/British Columbia	Upper	458	0.88	1.43	
X12141	06-36-071-04W6/Alberta	Middle	434	0.60	0.84	
X12142	06-36-071-04W6/Alberta	Middle	440	0.60	1.12	Montney migrated? (Watt et al., 2022) + *in-situ* Montney (Ardakani et al., 2022)
X12143	11-27-077-06W6/Alberta	Lower	441	0.56	0.80	
X12144	C16-10-88-23W6/British Columbia	Upper	447	0.90	1.48	Montney migrated? (Watt et al., 2022)
X12145	C16-10-88-23W6/British Columbia	Upper	455	0.90	1.49	
X12146	C16-10-88-23W6/British Columbia	Upper	453	0.91	1.50	
X12147	06-33-072-25W5/Alberta	Middle	428	0.61	0.79	Montney migrated? (Watt et al., 2022) + *in-situ* Montney (Ardakani et al., 2022)
X12148	06-36-071-04W6/Alberta	Middle	440	0.64	0.78	
X12149	C16-10-88-23W6/British Columbia	Upper	456	0.91	1.53	Montney migrated? (Watt et al., 2022)
X12150	C16-10-88-23W6/British Columbia	Upper	439	0.91	1.31	
X12151	C16-10-88-23W6/British Columbia	Upper	463	0.90	1.45	
X12152	06-33-072-25W5/Alberta	Middle	430	0.61	0.51	Montney migrated? (Watt et al., 2022) + *in-situ* Montney (Ardakani et al., 2022)
X12153	11-27-077-06W6/Alberta	Lower	438	0.60	0.91	

[a]TMNr: trimethylnaphthalene ratio calculated as 1,3,7-trimethylnaphthalene/(1,3,7 + 1,2,5)-trimethylnaphthalene, peak areas from the m/z 170; TMNr increases with thermal maturity (van Aarssen et al., 1999).
[b]Pr/Ph: pristane/phytane; using peak areas from the total ion chromatogram (e.g., Peters et al., 2005).

diols (*m/z* 285). These compound classes were identified in the ranges C_{15}-C_{29}, C_{16}-C_{29}, and C_{17}-C_{29}, respectively.

The main carbon number distribution patterns of the diols can be observed in Figure 5. The 1,14- and 1,15- diols (Figures 5B, C) generally decrease in abundance with increasing carbon number at variable slopes, except samples X12140 and X12143 which register higher abundances in the C_{20+} range. Another aspect to notice is the preference for odd carbon numbers in the 1,14-diols, particularly in the C_{20+} range (Figure 5B). The odd preference is less emphasized in the 1,15-diols yet observed in samples X12145, X12151 and X12152 (e.g., Figure 5C). The 1,13-diols exhibit a more variable molecular distribution though with a preference for C_{18} and odd carbon numbers after C_{20} (Figure 5A).

4.4 Alkan-3-ols

For this compound series (Figure 6A; Supplementary Figure S2), the chain length varied from C_{12} to C_{28} (sometimes C_{28+} visible). The distribution patterns were found to be very similar to those of the fatty acids (Figure 3, Figure 6B): 1) mixed/bimodal distribution (e.g., X12140, X12143), 2) flatten top (e.g., X12141, X12148), and 3) decreasing abundance with increasing carbon number after maximum peak (the rest of the samples). Certain preference for C_{20} and C_{22} was observed in samples X12140, X12142-X12146, and X12148-X12151.

5 Discussion

5.1 The significance of fatty acids in fossil organic matter from the Montney Formation

In recent sedimentary organic matter, fatty acids have typically been attributed to algal and bacterial (C_{14}-C_{20}; Perry et al., 1979; Cranwell et al., 1987; Naeher et al., 2022), aquatic macrophytes (C_{22}-C_{26}; Cranwell et al., 1987; Volkman et al., 1999; Naeher et al., 2022) and terrestrial plant sources (C_{28}-C_{32}; Rieley et al., 1991; Freeman and Pancost, 2014; Naeher et al., 2022). It is also considered that terrestrial plants synthesize longer chain fatty acids preferably (Wang and Liu, 2012; Naafs et al., 2019). However, chain length alone is not always diagnostic of the source of these compounds, particularly in environments with aquatic and terrestrial organic matter inputs (Fang et al., 2014). As well, the molecular distribution of *n*-alkanes and *n*-fatty acids are expected to be similar when the

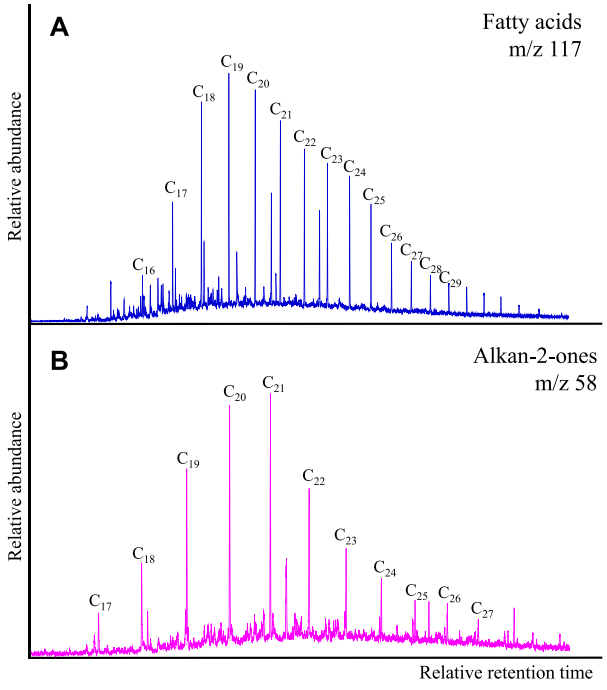

FIGURE 2
n-Fatty acids **(A)** and alkan-2-ones **(B)** identified in the samples (e.g., X12153).

n-alkanes derive from the decarboxylation of the acids during deposition/diagenesis (Barakat et al., 2000; Naafs et al., 2019).

In fossil organic matter (e.g., petroleum, bitumen), the evaluation of linear carboxylic acids is less common because of their degradation with thermal maturity and many other biomarkers being available for petroleum geochemistry studies (e.g., hopanes, steranes, aromatic markers, etc.). However, we must highlight the work by Jaffé and Gallardo (1990), Jaffé et al. (1992), Jaffé and Gallardo (1993), who suggested that most of the fatty acids identified in fossil organic matter are originally protected within more complex geo-polymer structures (later kerogen, bitumen) and released with increasing thermal maturity before the peak of oil generation. Free fatty acids, instead, would not be preserved but degrade to *n*-alkanes and/or other compounds during diagenesis. Therefore, opposite to recent environments, we may infer that in petroleum fluids and bitumen extracts from mature source rocks, the fatty acids should not be expected to have a distribution pattern similar to the *n*-alkanes as the latter would not necessarily be degradation products of the former (Jaffé and Gallardo, 1990; Jaffé et al., 1992; Jaffé and Gallardo, 1993).

This may explain why in our samples the distribution of *n*-fatty acids generally differs from the distribution of *n*-alkanes. For instance, samples X12140 and X12143, from completely different locations and stratigraphic intervals (Table 1; Figure 1), have a bimodal distribution pattern of fatty acids in common (Figures 2B, D). The same bimodality is not expressed in the *n*-alkanes distribution of these samples. It could be argued that a second group of fatty acids with highest peaks in the C_{22}-C_{24} range (Figures 2B, D) represents an additional terrestrial organic matter input. However, additional evidence is required to confirm terrestrial contribution. As well, bimodal fatty acids distribution could simply result from hydrocarbon mixing before maximum burial of the Montney Formation. Post maximum burial migration events in Montney (e.g., during the Eocene uplift) consisted of gas/condensate which unlikely carried fatty acids due to insolubility of the latter.

It is important to mention that in sample X12143, primary organic matter was identified besides solid bitumen (Ardakani et al., 2022). Therefore, we cannot rule out the possibility of fatty acids bimodality resulting from the mixture of migrated hydrocarbons and *in-situ* organic matter.

Samples X12141 and X12148 are also peculiar because they showed a flatten-top distribution pattern of *n*-fatty acids, which is different to the *n*-alkanes from the same samples. These samples come from the same well (Table 1) and Middle Montney Member although 40 m apart from each other. At this stage, it is challenging to propose source variations attributed to a flatten profile, but these samples could also represent mixtures of multiple-sourced hydrocarbons.

In the rest of the samples, fatty acids abundances generally decrease with increasing carbon number after C_{18}-C_{20} (Figure 2A; Figure 3A), similar to the *n*-alkanes. However, there is no obvious indication that the latter are degradation products of the fatty acids. For instance, if decarboxylation was taking place (loss of a COOH group), the highest peak in the *n*-alkane distribution should be displaced one carbon number less compared to the highest peak of the fatty acids, and that is not the case in any of the samples (see also Supplementary Table S4).

We must emphasize that comparisons between fatty acids and *n*-alkanes are also limited by the fact that the current distribution of *n*-alkanes in the Montney Formation has largely resulted from thermal cracking of migrated hydrocarbons during Montney's maximum burial, and additional fluid migration/mixing during the Eocene uplift (Wood and Sanei, 2016; Cesar et al., 2020a; Wood et al., 2022).

It is also possible that the distribution of fatty acids is responding to localized organic facies variations. A larger number of samples and geochemical constraints will provide light on this matter. Likewise, biodegradation cannot be ruled out although thermal maturity might have overprinted the molecular distribution ultimately.

5.2 The significance of alkan-2-ones in fossil organic matter from the Montney Formation

Alkan-2-ones are commonly present in peat and peat-forming vegetation (C_{17}-C_{35}; Puttmann and Bracke, 1995; Zheng et al., 2007; Naafs et al., 2019). In addition, bacterial and algal sources have been found to generate these compounds in a variety of depositional settings (C_{14}-C_{31}; Grimalt et al., 1990; Lopez-Dias et al., 2013; Zhang and Volkman, 2020). Although extensively studied in recent environments, alkan-2-ones have been detected in fossil organic matter of different thermal maturities with a moderate (or none) odd over even predominance of carbon chain length (Grimalt et al., 1990; George and Jardine, 1994; Leif and Simoneit, 1995; Strelnikova and Serebrennikova, 2011; Jaraula et al., 2015). Similar to the case of fatty acids, the low concentration of ketones in mature petroleum

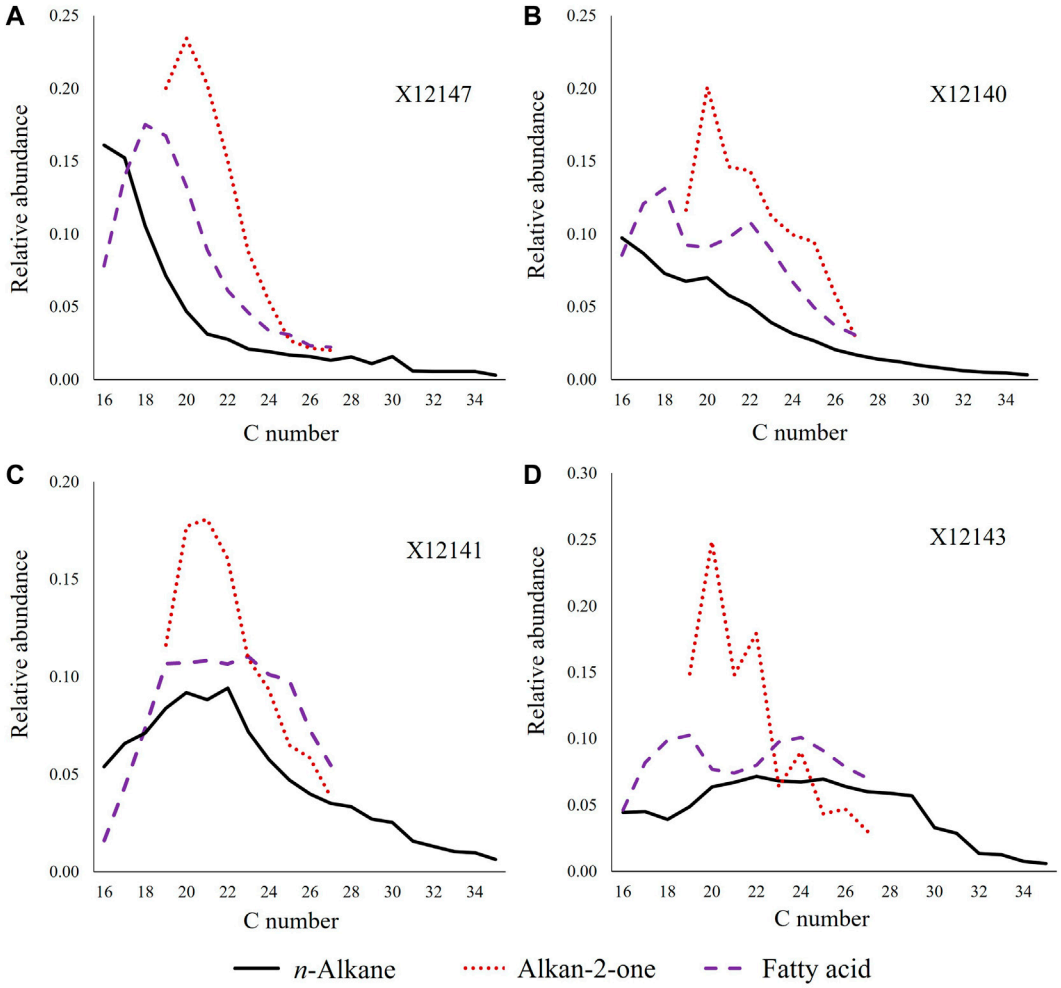

FIGURE 3
Main distribution patterns observed in the *n*-fatty acids: **(A)** unimodal distribution, **(B,D)** bimodal distribution, **(C)** flatten top; all compared with the corresponding distribution of alkan-2-ones and *n*-alkanes.

source rocks compared to other biomarkers has probably reduced the interest in the analysis of these compounds in petroleum (Alhassan and Anderson, 2013).

Zhang and Volkman (2020) reported an even over odd predominance of alkan-2-ones in a torbanite from the Sydney Basin, Australia, similar to the C-number predominance in samples from our study. The Australian torbanite contains organic matter type I and has vitrinite reflectance of 0.4 %Ro. The same authors suggested that these compounds could have derived from cleavage of C-O bonds in the kerogen and indicated the presence of long-chain alkyl moieties in green algae (Derenne et al., 1997; Zhang and Volkman, 2017). Despite the difference in maturity, this example may explain the presence and marine origin of alkan-2-ones in Montney samples since there is no reported evidence of significant terrestrial organic matter input in the Montney Formation.

We rule out alkan-2-one generation via decarboxylation of fatty acids because of their different molecular distribution patterns. Decarboxylation would have led to alkan-2-ones with one less carbon atom, switching maximum peak heights towards lower carbon chains (Puttmann and Bracke, 1995; Lopez-Dias et al., 2013). Instead, the highest alkanone peak found in our samples corresponds to a carbon chain (C_{20}) longer than the highest peaks in the fatty acid distribution (C_{18}-C_{19}) (Figure 2; Figure 3; Supplementary Tables S1, S2). In addition, oxidation of *n*-alkanes does not seem to be a potential generation pathway either because of the contrasting molecular distribution pattern of both compound classes (Figure 3, Supplementary Tables S2, S4).

5.3 The significance of alcohols in fossil organic matter from the Montney Formation

Contrary to the case of fatty acids and alkan-2-ones, to our knowledge, this is the first report ever of alkyl diols in fossil organic matter.

In recent environments, these lipids typically consist of even-numbered carbon chains with hydroxyl groups at C-13, C-14, or C-15, and 28 to 32 carbon atoms (e.g., Rodrigo-Gamiz et al., 2016; Rampen et al., 2021). In the studied samples, diol distributions are

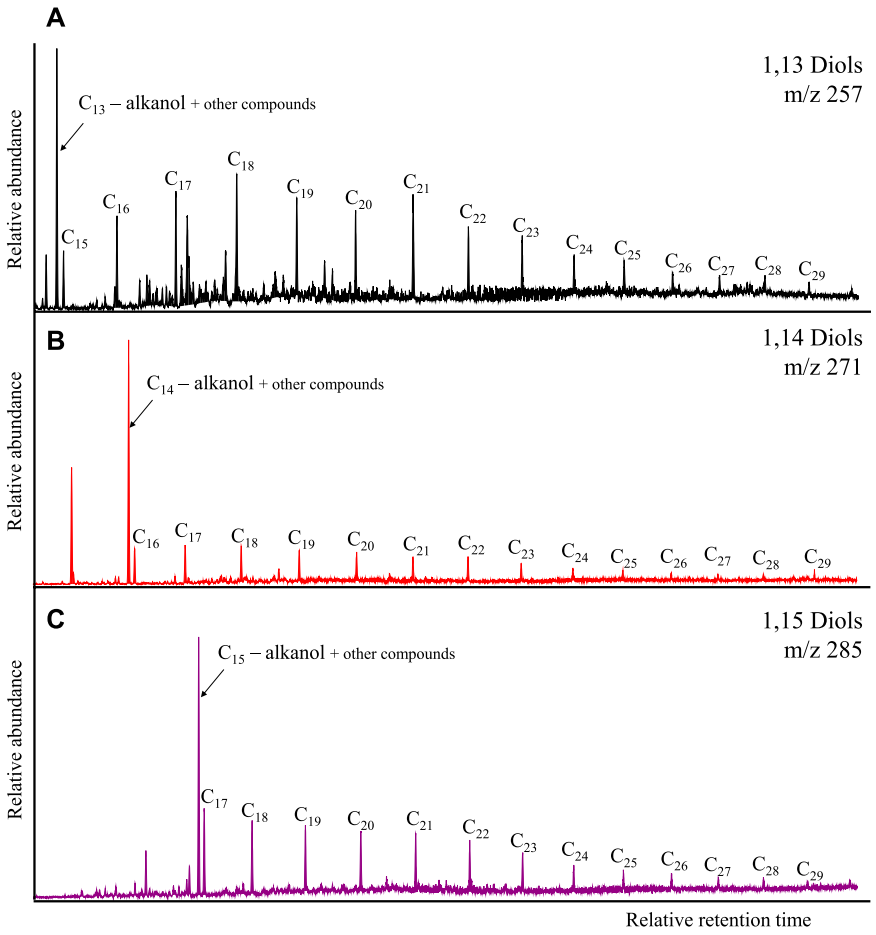

FIGURE 4
Diols identified in the samples (e.g., X12153): **(A)** 1,13-diols, **(B)** 1,14-diols, **(C)** 1,15-diols.

characterized by an odd-numbered carbon preference after C_{20}, and shorter chain length (less than 30 carbon atoms). It is possible that the diols detected in this research are thermal breakdown products of the original long-chain diols, and the loss of a methyl group by thermal cleavage has switched the carbon length preference to odd numbers.

Generally, 1,14-diols are considered to be sourced by specific diatoms and are typically associated with upwelling zones (Koning et al., 2001; Wakeham et al., 2002; Damste et al., 2003), whereas 1,15-diols have been attributed to specific marine and freshwater algae (Volkman et al., 1992, 1999) in recent organic matter. However, in our sample set, 1,14- and 1,15- diols seem to share a common source (Figures 7A, B). This is interpreted based on their markedly similar distribution. In Figure 7A, we have plotted the ratios of the C_{16}-C_{18} range to the C_{20}-C_{22} range for both compound classes and they express an almost 1:1 correlation, with no significant thermal maturity overprint (Figure 7B). Their mutual association cannot be explained by their distribution in recent environments. It is possible that in the Mesozoic, 1,14- and 1,15- diols were synthesized by a common source/organism. The samples X12147 and X12152 stand out in Figure 7 with values $[C_{16}$-$C_{18}]/[C_{20}$-$C_{22}]$ above three. They are the only two samples from the well 06-33-072-25W5 (Middle Montney, Table 1), and local organic matter type variations may be responsible for their uniqueness.

Contrary to 1,14-diols, 1,13-diols have been found to share a source with 1,15-diols in recent depositional environments (e.g., Rodrigo-Gamiz et al., 2016; Rampen et al., 2021). However, in this study, the distribution of 1,13-diols clearly differs from 1,14- and 1,15- diols (Figure 5A). Additionally, we noticed a marked preference for C_{21}1,13-diol with respect to C_{20} and C_{22} in most of the samples, and for C_{18}1,13-diol in sample X12152 (Figure 5A). Additional studies are necessary to investigate potential sources for the 1,13 homologues, but their origin most likely differ from the sources of 1,14- and 1,15- diols.

Another possibility is that the original distribution of alkyl-diols has simply been overprinted by other geochemical phenomena (e.g., mineral-catalyzed isomerization/cyclization, biodegradation), to which each compound class (1,13- versus 1,14- versus 1,15-) may have a different susceptibility. Under such condition, our interpretation of a common source for 1,14-diols and 1,15-diols would not necessarily be the case.

The presence of alkan-3-ols seems to be closely related to the fatty acids, probably sharing a common source since their molecular distributions are significantly similar (Figure 3; Figure 6; Figure 7C).

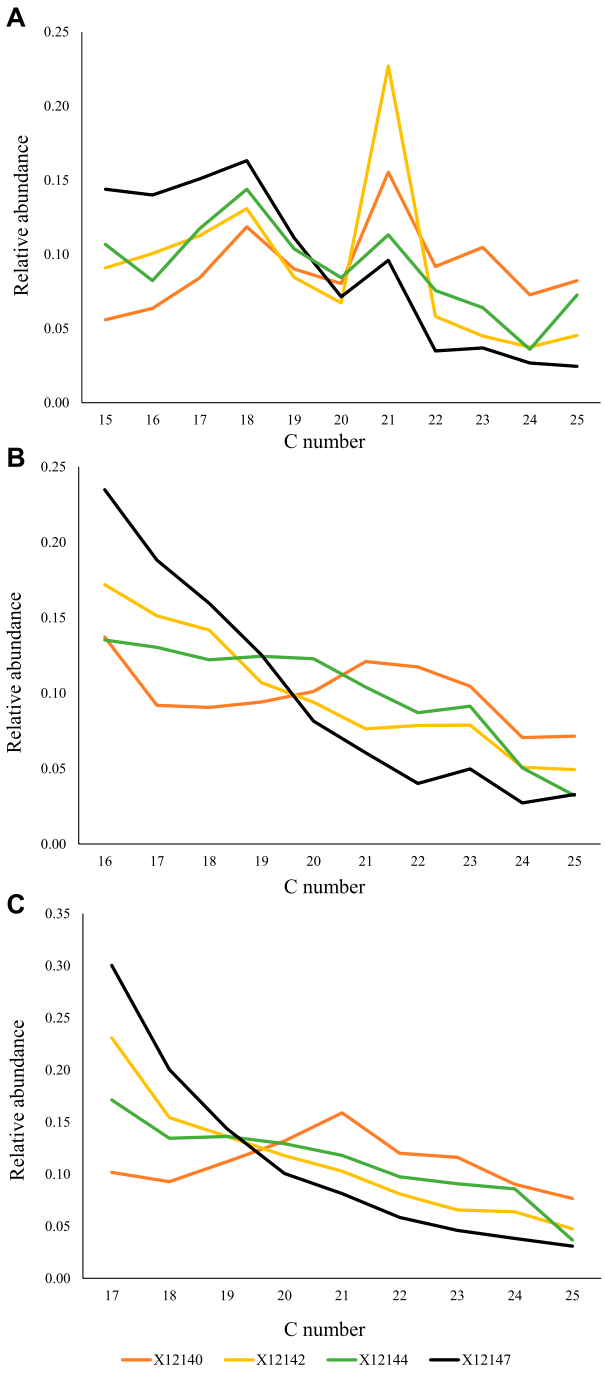

FIGURE 5
Selected samples to illustrate the main distribution patterns of **(A)** 1,13-diols, **(B)** 1,14-diols, and **(C)** 1,15-diols identified in the samples.

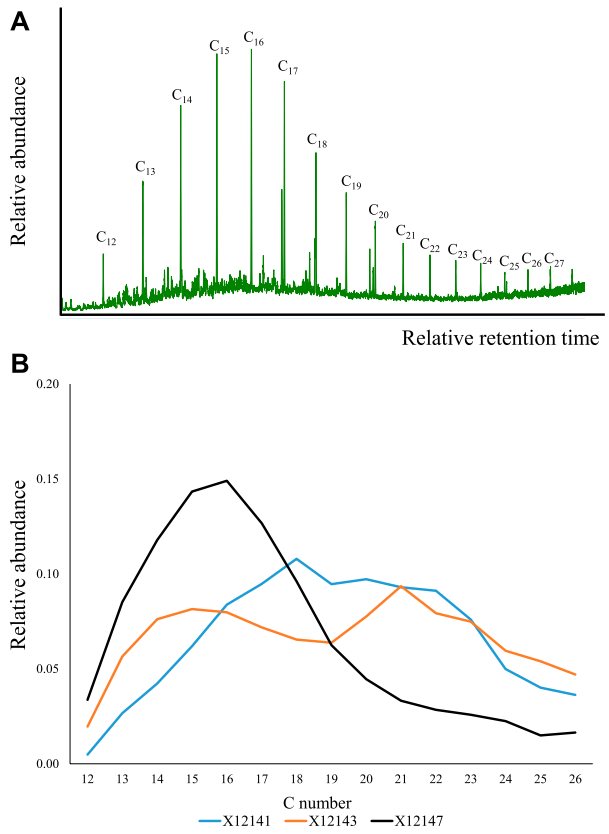

FIGURE 6
Alkan-3-ols identified in the samples. **(A)** The m/z 131 indicating carbon chain length, and **(B)** the main distribution patterns (see also, Supplementary Figure S2).

To our knowledge, this research is also the first time that alkan-3-ols are reported in fossil organic matter. In recent environments, alkan-3-ols have only been identified in surface-wax washings of Primulaceae (Radulovic and Zivkovic Stosic, 2021) or are perhaps usually not reported in studies of recent organic matter. At this stage, an association with plant contribution is challenged by the limited evidence of terrestrial organic matter contribution to Montney hydrocarbons (e.g., Ardakani et al., 2022). If we attempt to find other potential precursors based on the molecular structure, a suitable candidate may be the 3-hydroxy-fatty acid compound class, which are widely distributed in aquatic environments. These acids are known to be part of cell membranes in bacterial communities (Cranwell et al., 1987; Wakeham, 1999; Wakeham et al., 2003), and have been used for temperature reconstruction due to the sensitivity of certain bacterial groups to climate change (Wang et al., 2016; Huguet et al., 2019; Yang et al., 2021). However, the potential degradation of 3-hydroxy-fatty acids to alkan-3-ols in the study samples yet lacks supporting evidence.

5.4 Potential associations with the general Montney Formation stratigraphy

To further investigate the applicability of oxygenated aliphatic compounds as source discriminators, we divided the data in Lower, Middle, and Upper members in Figure 7. The molecular characteristics of the samples do not seem to be specific of a particular Montney Member. The samples from the Upper Member in British Columbia are more mature (Figure 7B). The lack of differentiation among Montney Members might have resulted from hydrocarbons migrating from the same source or variable combinations of two or more sources.

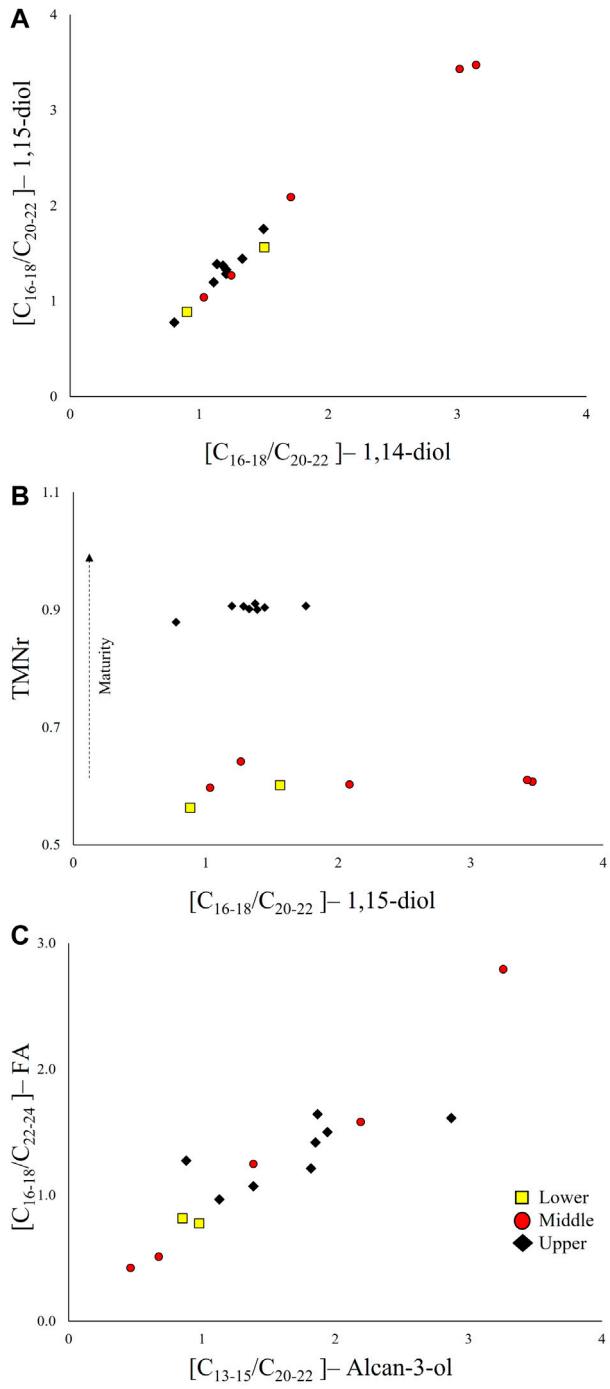

FIGURE 7
Relationship between selected alcohol parameters. **(A)** The [C_{16-18}/C_{20-22}]– 1,15-diol versus [C_{16-18}/C_{20-22}]– 1,14-diol, **(B)** TMNr versus [C_{16-18}/C_{20-22}]– 1,15-diol. **(C)** Relationship between alkan-3-ols and fatty acids expressed as the [C_{16-18}/C_{22-24}]–FA versus [C_{13-15}/C_{20-22}]–alkan-3-ol.

Although defining source discriminators of Montney petroleum fluids remains a challenge, we have made evident that oxygenated aliphatic compounds are suitable candidates to achieve such goal, not only because they have been preserved, but also because of their variability in the samples. The characteristics of polar compounds are also important because they have very unlikely been overprinted by hydrocarbons that migrated during the Eocene, which mostly consist of gas/condensate (very low concentration of polar compounds). Therefore, the polar compounds from the extracted bitumen are a closer approximation to the hydrocarbons that originally migrated into Montney intervals before its maximum burial.

From a broader perspective, it is intriguing that the molecular distributions observed herein do not indicate clear association with the generation mechanisms currently known for the synthesis of these compounds in recent sediments. Another pathway for investigation is to evaluate whether the polar compounds studied were as sensitive to climate variations as they are known to be in recent depositional environments.

A final aspect that is important for low-permeability reservoirs in the region is that the thermal degradation of polar compounds might also be affecting other rock properties such as organic porosity, which plays a key role in hydrocarbon production.

6 Conclusion

Fatty acids, alkan-2-ones, diols and alkan-3-ols have been identified in extracted bitumen from the Montney Formation. This may represent the first time that 1,13-, 1,14- and 1,15- diols as well as alkan-3-ols are reported in fossil organic matter.

Regardless of thermal maturation overprint on the original signatures of the fatty acids merely based on their distribution, we infer marine organic matter (<C_{20} range dominant) source. Exceptions include samples X12140 and 12143 where a bimodal molecular distribution was observed with additional maximum peaks in C_{22} and C_{24} respectively. Further evidence is required to suggest a terrestrial input in these samples. Both samples correspond to different stratigraphic members and thermal maturity, thus the bimodality is probably a consequence of the mixing of contrasting hydrocarbon charges within those Montney sections before maximum burial.

Based on their distinctive distribution pattern, fatty acids have not been degraded to *n*-alkanes (e.g., via decarboxylation). Likewise, the alkan-2-ones do not represent oxidation products of the *n*-alkanes. Mechanisms to explain the preference for even-numbered carbon chain of alkan-2-ones remain unknown though even-chain ketones have been identified in Australian torbanites previously.

In contrast to recent organic matter, in Montney Formation the 1,14- and 1,15- seem to share a common source or generation mechanism as expressed by their very similar molecular distribution patterns. These and the 1,13-diols could be breakdown products of their longer-chain counterparts or have otherwise precursors that have not been identified to this date. The origin of 1,13-diols is not clearly associated to the other alkyl diols as interpreted based on their different molecular patterns.

The highly similar molecular distribution of alkan-3-ols and fatty acids suggest that they are biosynthetically related and/or share a common source. Their origin from the degradation of compounds with similar structure (e.g., 3-hydroxy-fatty acids) remains unclear.

Ultimately, our research opens a new path in geochemical screening of the unconventional Lower Triassic Montney Formation and conveys renovated interest in studying oxygenated compound classes in fossil organic matter that had scarcely been considered in recent years.

Data availability statement

The original contributions presented in the study are included in the article/Supplementary Material, further inquiries can be directed to the corresponding author.

Author contributions

JC conceptualized the study, wrote the first draft, and made Figures 2–7. SN helped conceptualizing the study and identifying compounds. JC, RR, and MM generated the data. RR and OA secured funding. OA elaborated Figure 1. All authors contributed to the analysis and interpretation of the data, and to writing and reviewing the manuscript.

Funding

This research was funded by Natural Resources Canada (NRCan) and its Geoscience for New Energy Supply (GNES) program, grant number 331403. The derivatization procedure was funded by the GEM-GeoNorth program in anticipation that the methodology can be applied to future program/project research.

Acknowledgments

The authors thank the editors for organizing the special issue and acknowledge the reviewers for their contribution to enhance the quality of this work.

Conflict of interest

The authors declare that the research was conducted in the absence of any commercial or financial relationships that could be construed as a potential conflict of interest.

Publisher's note

All claims expressed in this article are solely those of the authors and do not necessarily represent those of their affiliated organizations, or those of the publisher, the editors and the reviewers. Any product that may be evaluated in this article, or claim that may be made by its manufacturer, is not guaranteed or endorsed by the publisher.

Supplementary material

The Supplementary Material for this article can be found online at: https://www.frontiersin.org/articles/10.3389/feart.2023.1137026/full#supplementary-material

References

Alhassan, A., and Anderson, J. T. (2013). Ketones in fossil materials a mass spectrometric Analysis of a crude oil and a coal tar. *ENERG FUEL* 27, 5770–5778. doi:10.1021/ef400961d

Allan, J., and Creaney, S. (1991). Oil families of the western Canada basin. *Bull. Can. Petrol. Geol.* 39, 107–122. doi:10.35767/gscpgbull.39.2.107

Ardakani, O. H., Cesar, J., Pedersen, P. K., Mackie, S. J., Reyes, J., and Wood, J. M. (2022). Occurrence and preservation of primary organic matter in a hybrid unconventional reservoir: Montney Formation, Western Canada Sedimentary Basin. *Int. J. Coal Geol.* 261, 104096. doi:10.1016/j.coal.2022.104096

Barakat, A. O., El-Gayar, M. Sh., and Mostafa, A. R. (2000). Geochemical significance of fatty acids in crude oils and related source rocks from Egypt. *Pet. Sci. Technol.* 18 (5–6), 635–655. doi:10.1080/10916460008949864

BC Oil and Gas Commission (2012). *Montney Formation play atlas NEBC*. Canada: Government of British Columbia, 36.

Cesar, J., Becker, V., and Mayer, B. (2020a). Organic and isotope geochemistry analysis of petroleum condensates from the unconventional portion of the Montney Formation, Western Canada. *Fuel* 282, 118879. doi:10.1016/j.fuel.2020.118879

Cesar, J., Nightingale, M., Becker, V., and Mayer, B. (2020b). Stable carbon isotope systematics of methane, ethane and propane from low-permeability hydrocarbon reservoirs. *Chem. Geol.* 558, 119907. doi:10.1016/j.chemgeo.2020.119907

Cesar, J., Mayer, B., Deblonde, C., Mort, A., and Ardakani, O. H. (2021). Alternative indicators to assess the distribution characteristics of methane, ethane, and propane derived from petroleum in the Montney Formation, Western Canada. *Fuel* 294, 120524. doi:10.1016/j.fuel.2021.120524

Cesar, J., Mayer, B., Becker, V., Nightingale, M., and Ardakani, O. H. (2022). Molecular and stable carbon isotope geochemistry of mud-gas-derived hydrocarbons and its application for the assessment of low-permeability reservoirs from the Montney Formation, Western Canada. *Org. Geochem* 163, 104328. doi:10.1016/j.orggeochem.2021.104328

Cranwell, P. A., Eglinton, G., and Robinson, N. (1987). Lipids of aquatic organisms as potential contributors to lacustrine sediments—II. *Org. Geochem.* 11 (6), 513–527. doi:10.1016/0146-6380(87)90007-6

Damste, J. S. S., Rampen, S., Irene, W., Rijpstra, C., Abbas, B., Muyzer, G., et al. (2003). A diatomaceous origin for long-chain diols and mid-chain hydroxy methyl alkanoates widely occurring in quaternary marine sediments: Indicators for high-nutrient conditions. *Geochim. Cosmochim. Acta* 67 (7), 1339–1348. doi:10.1016/s0016-7037(02)01225-5

Davies, G. R., Watson, N., Moslow, T. F., and Maceachern, J. A. (2018). Regional subdivisions, sequences, correlations and facies relationships of the lower triassic Montney Formation, west-central Alberta to northeastern British Columbia, Canada — With emphasis on role of paleo structure. *Bull. Can. Petrol. Geol.* 66, 23–92.

Davies, G. R. (1997). The triassic of the western Canada Sedimentary Basin: Tectonic and stratigraphic framework, paleogeography, paleoclimate and biota. *Bull. Can. Petrol. Geol.* 45, 434–460. doi:10.35767/gscpgbull.45.4.434

Derenne, S., Largeau, C., Hetényi, M., Brukner-Wein, A., Connan, J., and Lugardon, B. (1997). Chemical structure of the organic matter in a pliocene maar-type shale: Implicated botryococcus race strains and formation pathways. *Geochim. Cosmochim. Acta.* 61, 1879–1889. doi:10.1016/s0016-7037(97)00042-2

Ducros, M., Sassi, W., Vially, R., Euzen, T., and Crombez, V. (2017). "2-D basin modeling of the Western Canada sedimentary basin across the Montney-Doig system. implications for hydrocarbon migration pathways and unconventional resources potential,". *Petroleum systems analysis—case studies*. Editors M. A. AbuAli, I. Moretti, and H. M. Nordgård Bolås. Tulsa: (AAPG Memoir), 114, 117–134.

Ejezie, N. (2007). *Triassic oil families and possible source rocks, peace river embayment area, Alberta, Canada*. [dissertation/PhD thesis]. Calgary: University of Calgary.

Euzen, T., Watson, N., Fowler, M., Mort, A., and Moslow, T. F. (2021). Petroleum distribution in the Montney hybrid play: Source, carrier bed, and structural controls. *AAPG Bull.* 105, 1867–1892. doi:10.1306/12222020088

Fang, J., Wu, F., Xiong, Y., Li, F., Du, X., An, D., et al. (2014). Source characterization of sedimentary organic matter using molecular and stable carbon isotopic composition of *n*-alkanes and fatty acids in sediment core from Lake Dianchi, China. *Sci. Total Environ.* 473–474, 410–421. doi:10.1016/j.scitotenv.2013.10.066

Freeman, K. H., and Pancost, R. D. (2014). "Biomarkers for terrestrial plants and climate," in *Treatise on geochemistry*. Editor K. K. Turekian (Oxford: Elsevier), 395–416.

George, S. C., and Jardine, D. R. (1994). Ketones in a Proterozoic dolerite sill. *Org. Geochem.* 21, 829–839. doi:10.1016/0146-6380(94)90042-6

Grimalt, J. O., Angulo, L., Lopez-Galindo, A., Comas, M. C., and Albaiges, J. (1990). Lipid and mineralogical composition of the cretaceous black shale deposits of the fardes formation (southern iberian paleomargin, betic cordillera, south Spain). *Chem. Geol.* 82, 341–363. doi:10.1016/0009-2541(90)90089-p

Huguet, A., Coffinet, S., Roussel, A., Gayraud, F., Anquetil, C., Bergonzini, L., et al. (2019). Evaluation of 3-hydroxy fatty acids as a pH and temperature proxy in soils from temperate and tropical altitudinal gradients. *Org. Geochem.* 129, 1–13. doi:10.1016/j.orggeochem.2019.01.002

Jaffé, R., and Gallardo, M. T. (1993). Application of carboxylic acid biomarkers as indicators of biodegradation and migration of crude oils from the Maracaibo Basin, Western Venezuela. *West. Venezuela. Org. Geochem.* 20 (7), 973–984. doi:10.1016/0146-6380(93)90107-m

Jaffé, R., and Gardinali, P. R. (1990). "Generation and maturation of carboxylic acids in ancient sediments of the Maracaibo Basin, Venezuela,". *Advances in organic geochemistry 1989*. Editor B. Durand. Exeter, UK: (F. Behar Org. Geochem), 16, 211–218.

Jaffé, R., Gardinali, P., and Wolf, G. A. (1992). Evolution of alkanes and carboxylic acids in ancient sediments from the Maracaibo Basin. *Org. Geochem.* 18 (2), 195–201. doi:10.1016/0146-6380(92)90130-p

Jaraula, C. M. B., Schwark, L., Moreau, X., Pickel, W., Bagas, L., and Grice, K. (2015). Radiolytic alteration of biopolymers in the Mulga Rock (Australia) uranium deposit. *J. Appl. Geochem.* 52, 97–108. doi:10.1016/j.apgeochem.2014.11.012

Koning, E., van Iperen, J. M., van Raaphorst, W., Brummer, G.-J. A., and van Weering, T. C. E. (2001). Selective preservation of upwelling-indicating diatoms in sediments off Somalia, NW Indian Ocean. *Deep Sea Res. 1 Oceanogr. Res. Pap.* 48, 2473–2495. doi:10.1016/s0967-0637(01)00019-x

Leif, R. N., and Simoneit, B. R. T. (1995). Ketones in hydrothermal petroleums and sediment extracts from Guaymas Basin, Gulf of California. *Gulf Calif. Org. Geochem.* 23, 889–904. doi:10.1016/0146-6380(95)00085-2

Lopez-Dias, V., Blanco, C. G., Bechtel, A., Puttmann, W., and Borrego, A. G. (2013). Different source of *n*-alkanes and *n*-alkan-2-ones in a 6000cal. yr BP *Sphagnum*-rich temperate peat bog (Ronanzas, N Spain). *Org. Geochem.* 57, 7–10. doi:10.1016/j.orggeochem.2013.01.006

Michels, R., Burkle, V., Mansuy, L., Langlois, E., Ruau, O., and Landais, P. (2000). Role of polar compounds as source of hydrocarbons and reactive medium during the artificial maturation of Mahakam Coal. *ENERG FUEL* 14, 1059–1071. doi:10.1021/ef000046d

Naafs, B. D. A., Inglis, G. N., Blewett, J., McClymont, E. L., Lauretano, V., Xie, S., et al. (2019). The potential of biomarker proxies to trace climate, vegetation, and biogeochemical processes in peat: A review. *Glob. Planet Change* 179, 57–79. doi:10.1016/j.gloplacha.2019.05.006

Naeher, S., Cui, X., and Summons, R. (2022). Biomarkers: Molecular tools to study life, environment, and climate. *Elements* 18 (2), 79–85. doi:10.2138/gselements.18.2.79

Perry, G. J., Volkman, J. K., Johns, R. B., and Bavor, H. (1979). Fatty acids of bacterial origin in contemporary marine sediments. *Geochim. Cosmochim. Acta*. 43, 1715–1725. doi:10.1016/0016-7037(79)90020-6

Peters, K. E., Walters, C. C., and Moldowan, J. M. (2005). *The biomarker guide*. Cambridge: Cambridge University Press.

Puttmann, W., and Bracke, R. (1995). Extractable organic compounds in the clay mineral sealing of a waste disposal site. *Org. Geochem.* 23 (1), 43–54. doi:10.1016/0146-6380(94)00106-b

Radulovic, N. S., and Zivkovic Stosic, M. Z. (2021). Long-chain syn-1-phenylalkane-1,3-diyl diacetates, related phenylalkane derivatives, and sec-alcohols, all possessing dominantly iso-branched chain termini, and 2/3-methyl-branched fatty acids from Primula veris L. (Primulaceae) wax. *Phytochem* 186, 112732. doi:10.1016/j.phytochem.2021.112732

Rampen, S. W., Thomas, F., Rybalka, N., and Thiel, V. (2021). The long chain diol index: A marine palaeotemperature proxy based on eustigmatophyte lipids that records the warmest seasons. *PNAS* 119 (16), e2116812119. doi:10.1073/pnas.2116812119

Rieley, G., Collier, R. J., Jones, D. M., and Eglinton, G. (1991). The biogeochemistry of ellesmere lake, U.K.—I: Source correlation of leaf wax inputs to the sedimentary lipid record. *Org. Geochem.* 17, 901–912. doi:10.1016/0146-6380(91)90031-e

Rodrigo-Gamiz, M., Rampen, S. W., Schouten , S., and Sinninghe Damste, J. S. (2016). The impact of oxic degradation on long chain alkyl diol distributions in Arabian Sea surface sediments. *Org. Geochem.* 100, 1–9. doi:10.1016/j.orggeochem.2016.07.003

Rokosh, C., Lyster, S., Anderson, A., Berhane, H., Brazzoni, T., Chen, D., et al. (2012). "Summary of Alberta's shale- and siltstone-hosted hydrocarbon resource potential," in *Energy resources conservation board/alberta geological Survey, open file report 2012-06*.

Sanei, H., Wood, J. M., Ardakani, O. H., Clarkson, C. R., and Jiang, C. (2015). Characterization of organic matter fractions in an unconventional tight gas siltstone reservoir. *Int. J. Coal Geol.* 150–151, 296–305. doi:10.1016/j.coal.2015.04.004

Strelnikova, E. B., and Serebrennikova, O. V. (2011). Ketones of Western siberian jurassic oils. *Petrol. Chem.* 51, 264–269. doi:10.1134/s0965544111030145

van Aarssen, B. G. K., Bastow, T. P., Alexander, R., and Kagi, R. I. (1999). Distributions of methylated naphthalenes in crude oils: Indicators of maturity, biodegradation and mixing. *Org. Geochem.* 30, 1213–1227. doi:10.1016/s0146-6380(99)00097-2

Volkman, J. K., Barrett, S. M., Dunstan, G. A., and Jeffrey, S. W. (1992). C30–C32 alkyl diols and unsaturated alcohols in microalgae of the class Eustigmatophyceae. *Org. Geochem.* 18, 131–138. doi:10.1016/0146-6380(92)90150-v

Volkman, J. K., S., Barrett, S. M., and Blackburn, S. I. (1999). Eustigmatophyte microalgae are potential sources of C29 sterols, C22–C28 n-alcohols and C28–C32 n-alkyl diols in freshwater environments. *Org. Geochem.* 30, 307–318. doi:10.1016/s0146-6380(99)00009-1

Wakeham, S. G., Peterson, M. L., Hedges, J. I., and Lee, C. (2002). Lipid biomarker fluxes in the arabian sea, with a comparison to the equatorial pacific ocean. *Deep Sea Res. 2 Top. Stud. Oceanogr.* 49, 2265–2301. doi:10.1016/s0967-0645(02)00037-1

Wakeham, S. G., Lewis, C. M., Hopmans, E. C., Schouten, S., and Damste, J. S. S. (2003). Archaea mediate anaerobic oxidation of methane in deep euxinic waters of the Black Sea. *Geochim. Cosmochim. Acta* 67 (7), 1359–1374. doi:10.1016/s0016-7037(02)01220-6

Wakeham, S. G. (1999). Monocarboxylic, dicarboxylic and hydroxy acids released by sequential treatments of suspended particles and sediments of the Black Sea. *Org. Geochem.* 30 (9), 1059–1074. doi:10.1016/s0146-6380(99)00084-4

Wang, Z., and Liu, W. G. (2012). Carbon chain length distribution in n-alkyl lipids: A process for evaluating source inputs to lake qinghai. *Org. Geochem* 50, 36–43. doi:10.1016/j.orggeochem.2012.06.015

Wang, C., Bendle, J., Yang, Y., Yang, H., Sun, H., Huang, J., et al. (2016). Impacts of pH and temperature on soil bacterial 3-hydroxy fatty acids: Development of novel terrestrial proxies. *Org. Geochem.* 94, 21–31. doi:10.1016/j.orggeochem.2016.01.010

Watt, E. A., Laycock, D. P., Michael, E., Toblin, R. C., Kelly, S., and Johnston, M. N. (2022). Hydrocarbon charge and petroleum system evolution of the Montney Formation: A multidisciplinary case study of the blueberry sub-play in northeast British Columbia, Canada. *BCEG* 69, 21–50. doi:10.35767/gscpgbull.69.1.021

Wood, J., and Sanei, H. (2016). Secondary migration and leakage of methane from a major tight-gas system. *Nat. Commun.* 7 (13614), 13614–13619. doi:10.1038/ncomms13614

Wood, J., Sanei, H., Ardakani, O. H., Curtis, M., and Akai, T. (2018). Organic petrography and scanning electron microscopy imaging of a thermal maturity series from the Montney tight-gas and hydrocarbon liquids fairway. *Bull. Can. Pet. Geol.* 66 (2), 499–515.

Wood, J. M., Cesar, J., Ardakani, O. H., Rudra, A., and Sanei, H. (2022). Geochemical evidence for the internal migration of gas condensate in a major unconventional tight petroleum system. *Sci. Rep.* 12, 7931. doi:10.1038/s41598-022-11963-6

Yang, Y., Wang, C., Bendle, J. A., Luo, Z., Dang, X., Xue, J., et al. (2021). Appraisal of paleoclimate indices based on bacterial 3-hydroxy fatty acids in 20 Chinese alkaline lakes. *Org. Geochem.* 160, 104277. doi:10.1016/j.orggeochem.2021.104277

Zhang, Z., and Volkman, J. K. (2017). Algaenan structure in the microalga Nannochloropsis oculate characterized from stepwise pyrolysis. *Org. Geochem.* 104, 1–7. doi:10.1016/j.orggeochem.2016.11.005

Zhang, Z., and Volkman, J. K. (2020). Isotopically enriched n-alkan-2-ones with even chain predominance in a torbanite from the Sydney Basin, Australia. *Org. Geochem.* 144, 104018. doi:10.1016/j.orggeochem.2020.104018

Zheng, Y., Zhou, W., Meyers, P. A., and Xie, S. (2007). Lipid biomarkers in the Zoige-Hongyuan peat deposit: Indicators of Holocene climate changes in West China. *Org. Geochem.* 38, 1927–1940. doi:10.1016/j.orggeochem.2007.06.012

Zonneveld, J. P., and Moslow, T. F. (2018). Palaeogeographic setting, lithostratigraphy, and sedimentary framework of the lower Triassic Montney Formation of Western Alberta and northeastern British Columbia. *Bull. Can. Petrol. Geol.* 66, 93–127.

Frontiers in Earth Science

Investigates the processes operating within the major spheres of our planet

Advances our understanding across the earth sciences, providing a theoretical background for better use of our planet's resources and equipping us to face major environmental challenges.

Discover the latest Research Topics

See more →

Frontiers

Avenue du Tribunal-Fédéral 34
1005 Lausanne, Switzerland
frontiersin.org

Contact us

+41 (0)21 510 17 00
frontiersin.org/about/contact